Petrogenesis of the False Bay Dyke Swarm, Cape Peninsula, South Africa

Nils Rainer Backeberg

Dissertation submitted for the degree of Master of Science
Department of Geological Sciences
University of Cape Town
2012

Petrogenesis of the False Bay Dyke Swarm

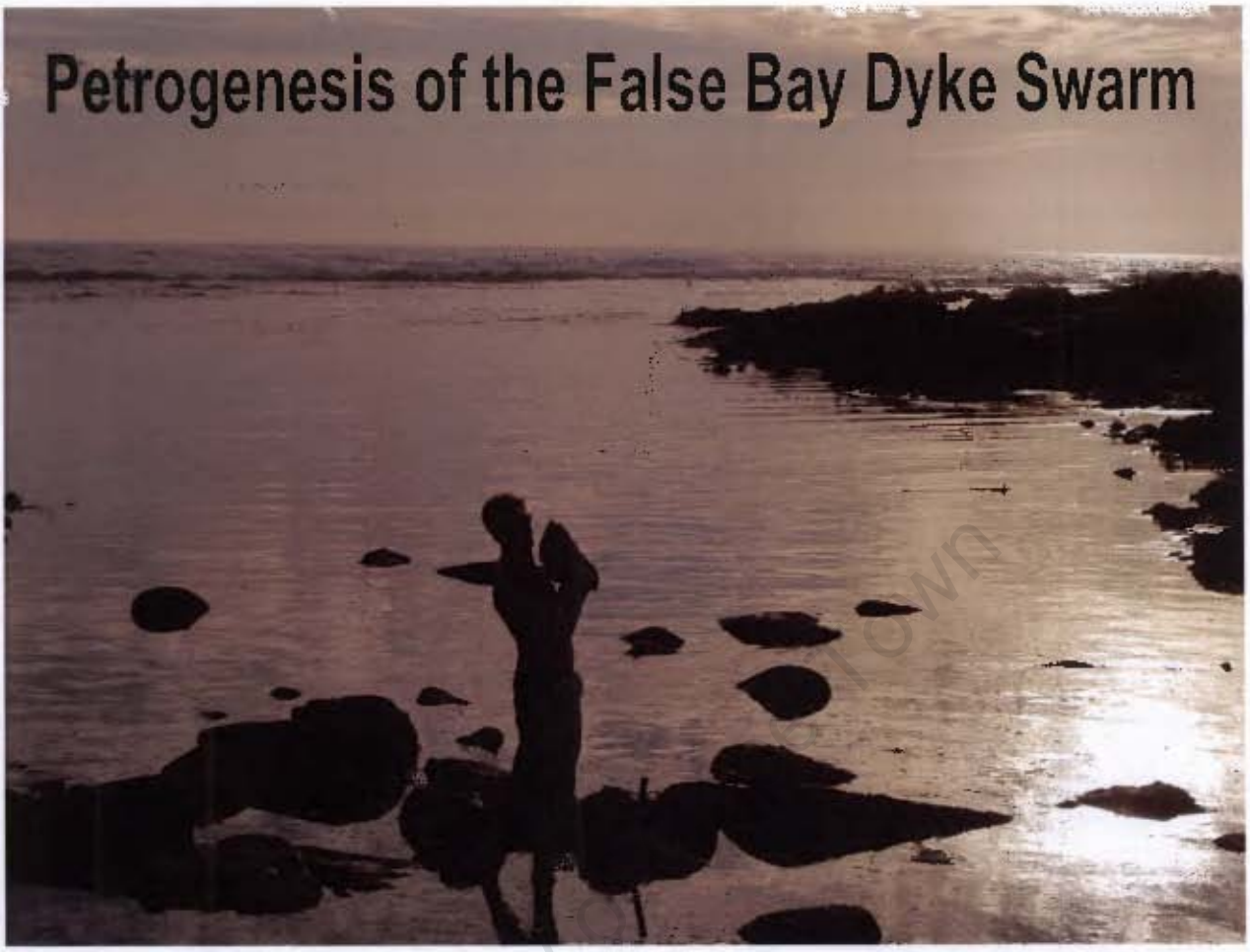

Dolerite dyke at Long Bay on Robben Island, August 2009

"That is sufficiently radical to entertain alternatives..." D L Reid

27th October, 2010; in Potsdam, Germany

University of Cape Town • iYunivesithi yaseKapa • Universiteit van Kaapstad

SPES BONA

INKABA yeAFRICA

Abstract

The False Bay dyke swarm is the southern-most set of Early Cretaceous dolerite dyke intrusions along the western margin of southern Africa associated with rifting of Gondwana and opening of the South Atlantic Ocean. Previous work highlighted the evolution of a single magma type from olivine-tholeiite basalt to ferro-tholeiite andesite. This thesis presents detailed field observations of each dyke in the False Bay - Cape Peninsula region and the focus of the study is on the finer details of the differentiation process to define combined assimilation and fractional crystallisation models.

Fractional crystallisation and assimilation trends are identified in the suite using both trace element and Sr-Nd isotope data; however, evidence of crustal assimilation is only pronounced in samples with less than 5 wt.% MgO. Initial differentiation (> 5 wt.% MgO) is characterised mainly by near closed-system fractional crystallisation, while the later stages of differentiation show a progressively larger input from assimilation. Assimilation trends of the False Bay dolerites are modelled with various assimilant sources, including the Cape Granite Suite, the Malmesbury Group and the Bushmanland Terrane. The AFC models show that the exposed country rocks of the False Bay dyke swarm, including Cape Granites and Malmesbury Group metasediments, are compositionally unfavourable for producing the observed assimilation trends in the dykes. Instead, a more suitable crustal assimilant would be Mesoproterozoic gneisses similar to those exposed in the neighbouring Namaqua Province, which may underlie the Cape Peninsula.

Acknowledgements

The study of the False Bay dyke swarm is part of the research group, Inkaba yeAfrica, and falls into the Chapter 2.1: Margins of Africa project. Inkaba yeAfrica is run through the University of Cape Town and the Geoforschungszentrum, Potsdam, and provided the funding for this thesis. Inkaba yeAfrica graciously exposed me to two conferences during the course of the project, first in Swaziland during 2009 and the second in Potsdam, Germany in 2010. These conferences provided great insight into the project as well as the academic world of geology and enriched my experience gained during the Masters thesis.

I thoroughly enjoyed working on the geology in Cape Town for my thesis and that leads me to thank my supervisor, Professor Dave Reid. He provided much guidance and mentorship, while allowing me independence and free reign in the evolution of the project and supported me along the way with any hick-ups that arose. Specifically when it came to my joy of taking the morning off for a surf and unfortunately in one occasion not coming back to the office for a whole month, due to an unexpected leg-break. A big thank you goes to Professor Chris Harris, who acted as co-supervisor and a additional source of support, including guidance through the oxygen isotope lab and resultant data as well providing me with strong confidence in completing this MSc.

Thank you to Robert Trumbull and Rolf Romer, at the Geoforschungszentrum in Potsdam, who added much value to the manuscript that evolved out of the study and broadened the scope of topics that I got to encounter.

I had much support from the entire staff and students at the Department of Geological Sciences during my 6 month recovery period and I would specifically like to thank Fayrooza Rawoot, Christel Tinguely, Shireen Govender and Petrus le Roux, who helped me through the lab work and took time out of their schedules to help process and prepare the samples for my project.

Furthermore the list of people I would like to thank is endless and there are a few I would like to single out: Thanks to Carly Faber, Pia Viglietti and Kaylan Hamel, who brought the postgraduate "family" much needed entertainment and life up on the overheated and flooded 6th floor as well as accompanying me on short field trips to collect samples and measurements.

My time as a postgraduate would have been very different if you three had not moved in.

A very special thanks to my parents in Swellendam, who supported me all the way and helped me get back on my feet during my "leg-break recovery", giving me a humble home to rest with my leg up and starting a healthy recovery. I love you so much. Then to my brother, with whom I have lived with the past three years and has been with me every step of the way, even playing geologist one day and joining me in the field. You have stimulated me with good discussion and have had a strong influence in my life.

A big thank you to the efforts from the examiners, providing critical and constructive reviews.

Finally I wish to leave with a comment (and a good scientific morale), which arose while I was sitting in Potsdam, Germany, with my supervisor, Dave, enjoying a good German Weissbier and discussing the essence of life and science late into the night. At one point in the conversation Dave suddenly commented:

"Well... that is sufficiently radical to entertain alternatives!" - A nice way of telling someone that they are talking... nonsense.

Dave Reid and myself (Nils Backeberg) standing below the Chapman's Peak view point close to the CP2 dyke, looking over Hout Bay in the background.

Supervisors

Prof. David L Reid

david.reid@uct.ac.za

Department of Geological Sciences, University of Cape Town, South Africa

Prof. Chris Harris

chris.harris@uct.ac.za

Department of Geological Sciences, University of Cape Town, South Africa

Preface

This study was initiated in July 2009 as part of Inkaba yeAfrica, a collaborative research group of the Department of Geological Sciences and AEON (Africa Earth Observation Network) at the University of Cape Town and the GeoForschungsZentrum, a German Research Centre for Geosciences at Potsdam, Germany. Inkaba yeAfrica covers all manors of geoscientific and interdisciplinary topics, with focus of the research under the following project titles:

1. Heart of Africa
2. Margins of Africa
3. Living Africa

The False Bay dyke swarm records igneous activity during the opening of the Atlantic Ocean and is related to various dyke swarms and other igneous units along the southwest African margin that were emplaced during the Cretaceous Period. Therefore, this study falls within the "Margins of Africa; Project 2.1: Magmatic processes, rifting and continental breakup". The research presented here continues from initial work done by Prof. D. L. Reid and co-authors (1990, 1991 and 2007) and other authors since the 1950s. The results have been published in a peer-reviewed journal as:

Petrogenesis of the False Bay dyke swarm, Cape Peninsula: evidence for basement assimilation. Backeberg, N.R., Reid, D.L., Trumbull R.B. and Romer, R.L. *South African Journal of Geology*, 2011, Volume 114 (3-4), pages 335-352.

Declaration

I know the meaning of plagiarism and declare that all of the work in the document, save for that which is properly acknowledged, is my own.

Signed by candidate

Nils Rainer Backeberg

2012

Contents

Chapter 1

Introduction

The South Atlantic continental margins represent the result of Cretaceous rifting during Gondwana breakup, which produced extensive magmatic activity such as the Paraná-Etendeka large igneous province (Erlank et al., 1984; Ewart et al., 1998; Marsh et al., 2001; Ewart et al., 2004). Etendeka-age dolerite dykes cutting the South Atlantic coast of Africa are mostly parallel to the continental shelf, with the exception of the Henties Bay - Outjo dyke swarm (HOD) in northwest Namibia, which, in part, follows the NE-SW trending basement structures of the Damara Belt (Trumbull et al., 2004b). The Ponta Grossa dyke swarm in Brazil, which is not included in this study, lies predominantly perpendicular to the South American eastern margin (e.g. Renne et al., 1996a). The False Bay dolerite dyke swarm (FBDS) is the southern-most extension of the coastal dykes and it intrudes within a narrow ~70 km wide band across the southwest corner of South Africa around False Bay and the Cape Peninsula. Although magnetic data published by Day (1987) suggests the presence of numerous dykes in the region, only 24 are exposed around the Cape Peninsula. Dyke outcrops are usually restricted to coastal shoreline locations, intruding all of the pre-Cretaceous rocks found on the Peninsula at a regional trend of NW-SE. The published records of the dark intrusive rocks of the Cape Peninsula are those of Nell and Brink (1944), Walker (1956), Day (1987) and Reid (1990) and in the literature the dyke swarm has been referred to as the Cape Peninsula dolerites (Walker, 1956; Reid, 1990) or the False Bay dolerites (Day, 1987; Reid et al., 1991).

Published ages for False Bay dyke swarm include a mean value of 132 ± 6 Ma with a slight

range (126 - 141 Ma) from whole rock K-Ar (Reid et al., 1991) and an Ar-Ar date of 131.3 ± 1.3 Ma measured on plagioclase (Stewart et al., 1996). This Cretaceous age links the dyke suites to the earliest tectonic evolution of the South Atlantic basin during Gondwana rifting, which at around 130 Ma had experienced initial continental stretching (Nürnerg and Müller, 1991). Initial rifting of western Gondwana until opening of the Atlantic Ocean is modelled to span from 150 Ma to 100 Ma, at which time the South Atlantic Ocean connected northward into the North Atlantic Ocean (Nürnerg and Müller, 1991).

Reid (1990) described the FBDS as containing a wide spectrum of dyke compositions indicative of differentiation, which were later compared to those in the HOD by Trumbull et al. (2007), who reported the presence of isotopic heterogeneity in the False Bay dykes, but confined their work to interpreting the least contaminated dykes to compare mantle sources along the African margin. The HOD swarm is thought to be the product of high-flux magma volumes compared to the low-flux magmas developed in the south at the Cape. The contrast in basaltic magma types and magma flux between north and south has been related by these authors to different tectonic settings and available magma sources along the margin, with the HOD being a product of active rifting driven by the Tristan Plume, while the southern dykes were described as a monogenetic system during passive rifting (Reid, 1990; Trumbull et al., 2007).

This study was aimed at extending our knowledge of the False Bay dyke intrusion event by adding modern trace element and radiogenic isotope data for key samples of the dyke swarm that cover the compositional range established in previous work. Results obtained have been incorporated into an evaluation of petrogenetic models for the evolution of the False Bay dyke magmatic system and possible interaction with its crustal host. The following two chapters will provide the necessary background to the regional and local geological settings.

Chapter 2

Regional Geological Setting

The Cape Peninsula and surrounding Western Cape are underlain by a basement consisting of the Neoproterozoic Malmesbury Group and the Cambrian Cape Granite Suite, which are unconformably overlain by the Palaeozoic Table Mountain Group (Figure 2.1). Older pre-Malmesbury basement is only exposed in the northern part of the Western Cape and in the Northern Cape, where medium to high-grade gneisses form part of the Mesoproterozoic Namaqua-Natal Province (e.g. Eglington, 2006).

2.1 Namaqua-Natal Province

Namaqua basement rocks are exposed approximately 300 km north of Cape Town along the west coast and throughout the Northern Cape of South Africa. The basement is subdivided into several terranes, interpreted to have formed and accreted over the period between 2.0 - 1.0 Ga (Moore et al., 1990; Eglington, 2006; Cornell et al., 2006). Distribution of the various Namaqua terranes are shown in Figure 2.2 and indicate the crustal blocks through which some of the Cretaceous dyke swarms traversed (e.g the Cedarberg dyke swarm, see below). To the south of the exposed Namaqua basement, the Mesoproterozoic units are unconformably overlain by sequences of similar age to the Neoproterozoic Malmesbury Group (e.g. Gresse and Scheepers, 1993). The Mesoproterozoic Namaqua basement has recently been suggested from seismic surveys to extend as far south as the Agulhas Fracture Zone (Lindeque et al., 2007, 2011) and compositionally similar crustal blocks could have interacted with the dyke

swarm magmas at depth.

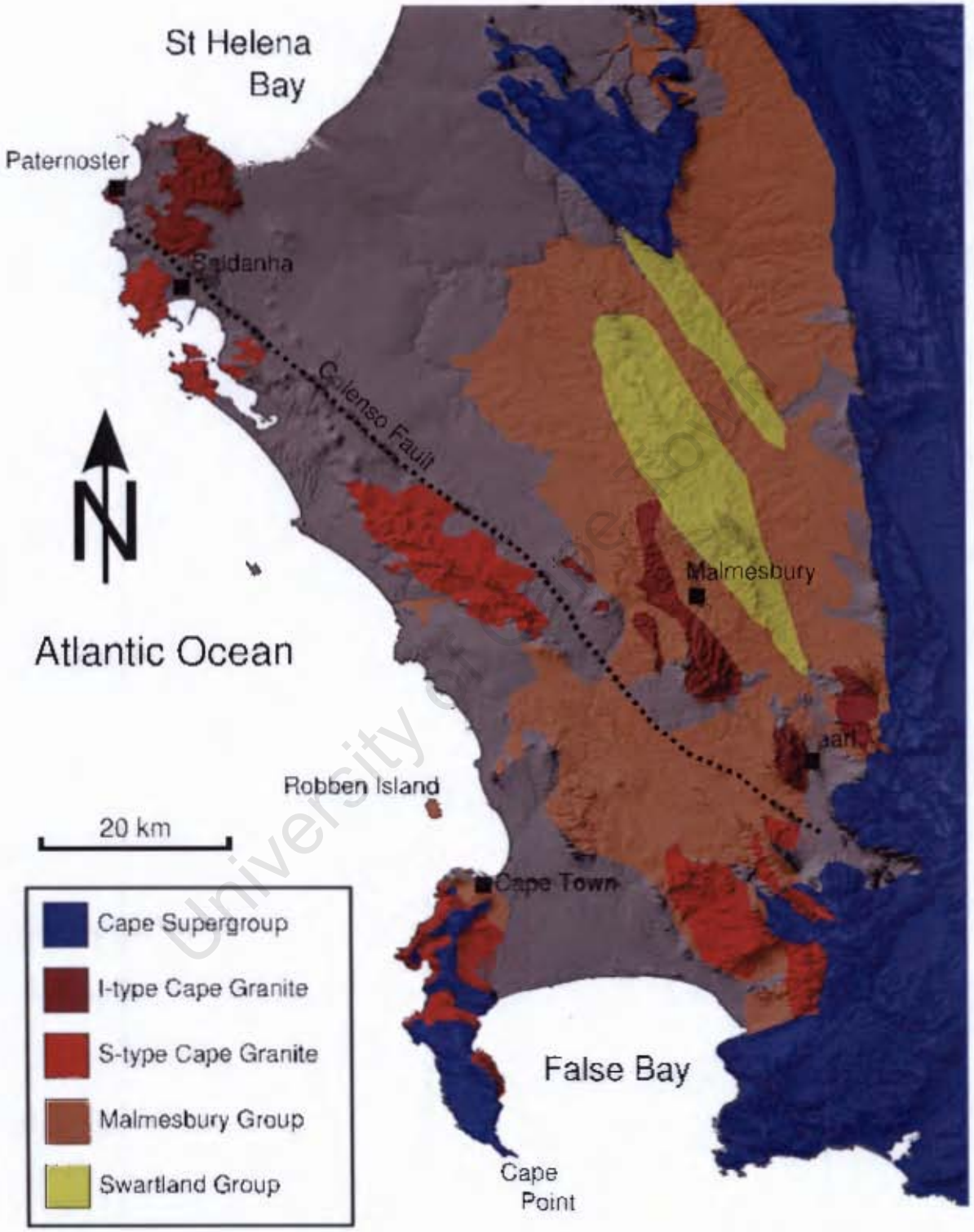

Figure 2.1: Shuttle Radar Topography Mission (SRTM, http://srtm.csi.cgiar.org) image overlain with the simplified regional basement geology of the south western Cape, with the grey areas showing recent sediment cover. Estimated extension of the Colenso Fault is shown by the dotted line.

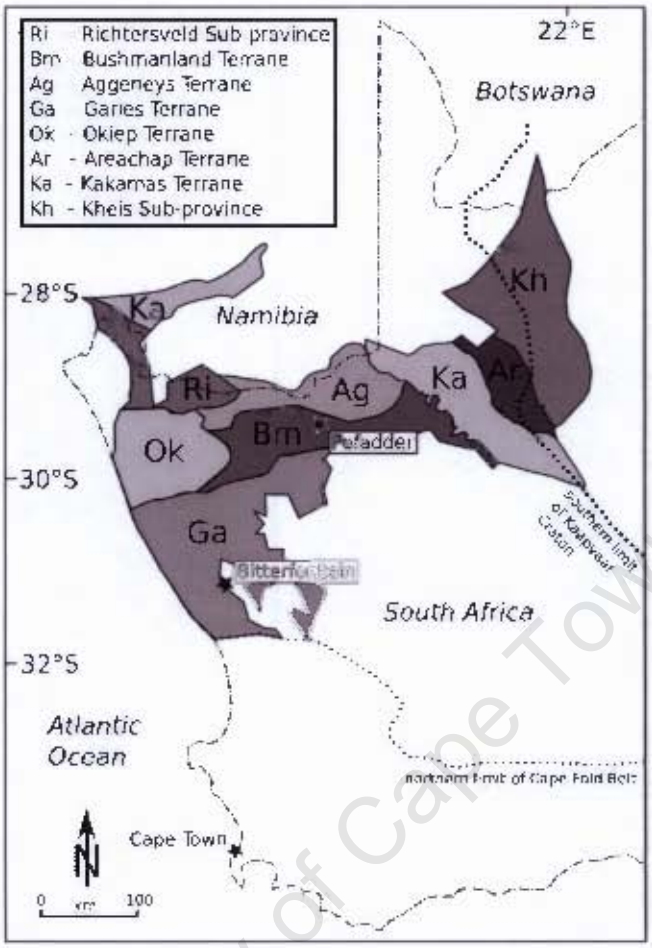

Figure 2.2: Terranes of the Namaqualand portion of Namaqua-Natal Province. Terranes are shear/thrust bounded. Terrane map redrawn from Moore et al. (1990), Eglington (2006) and Cornell et al. (2006).

2.2 Malmesbury Group

Rifting of the Mesoproterozoic basement during the Pan-African tectonic cycle led to the deposition and deformation of various belts that were formed during the closing of the Adamastor Ocean. To the north in Namibia, these include the Kaoko Belt, which records a transpressional event around 650 to 600 Ma (Goscombe et al., 2003; Goscombe and Gray, 2007), and Gariep Belt, an extensional basin that developed during 570 to 530 Ma (e.g. Frimmel and Frank, 1998; Frimmel and Frölling, 2004). Further south the Pan-African is represented by deformed Swartland and Malmesbury Group sedimentary rocks to lower green-schist facies, known as the Saldania Belt (Hartnady et al., 1974). The current outcrop patterns of the Swartland and

Malmesbury Group are shown in Figure 2.1. The Malmesbury Group is exposed along the Cape coast as the Tygerberg Formation. Sediments of the Tygerberg Formation were deposited in a closing subduction basin and the youngest deposition of the Malmesbury Group turbidites, as reported by detrital zircons, is at approximately 560 Ma (Armstrong et al., 1998). Rowe et al. (2010) describes in detail the tectonic relation between the various terranes, specifically the structures developed in the Tygerberg Formation on Robben Island, which records transpression during highly oblique subduction and final closure of the Adamastor Ocean.

2.3 Cape Granite Suite

Later stages of the Pan-African tectonic cycle were accompanied by the intrusion of the Cape Granite Suite after the deformation of the Malmesbury Group ceased. The distribution of S- and I-type granite plutons of the Cape Granite Suite are also shown in Figure 2.1. Not shown on the figure, but also found distributed in granite outcrops in close proximity to the Colenso Fault, are graintes interpreted as A-type by Scheepers (1995). The Cape Granite Suite intruded across the southwestern Cape Province, with an age progression from the older S-type intrusions at approximately 550 Ma, through the 540 - 520 Ma I-type granites (Da Silva et al., 2000), followed by the younger 520 - 500 Ma A-type granite intrusions (Scheepers, 1995; Scheepers and Armstrong, 2002). Scheepers (1995) showed that the S-type granite intrusions are exposed to the west of the Colenso fault, which separates them from the I-type granites to the east (Figure 2.1). In the Cape Peninsula the Cape Granite Suite is represented by the S-type Peninsula Granite batholith, which intruded around 540 Ma (Armstrong et al., 1998; Jordaan et al., 1995). The contact of the Peninsula Granite and the intruded Tygerberg Formation can be seen at Sea Point, Cape Town. Contact metamorphism of the Malmesbury Group rocks is restricted to the immediately adjacent exposures, whereas no thermal alteration is observed at Robben Island, 11 km north of the contact.

2.4 Cape Supergroup

Uplift and erosion of the Pan-African Saldanian sub-province took place from approximately 540 Ma until 510 Ma, the age of the youngest detrital zircons found in the basal Cape strata (Armstrong et al., 1998). The sandstone-dominated Cape Supergroup consists of the Table Mountain Group (TMG), Bokkeveld Group and Witteberg Group, covering a depositional history of a passive margin basin from the Early Ordovician (~510 Ma) to the Early Carboniferous (~330 Ma). In a few locations basal conglomerates exist, for example at Piekenierskloof Pass, whereas elsewhere the reddish Graafwater Formation generally forms the base of the TMG, followed by unit of cross-bedded sandstones, known as the Peninsula Formation, which is up to 2000 m thick (Rust, 1967). The End Ordovician period records a receding glacially-influenced palaeoenvironment, which is represented by the deformed upper 10 to 50 m of the Peninsula Formation, known as the Fold Zone, which formed during a large scale fluidization event (Rust, 1981; Backeberg and Rowe, 2009), and is associated with the Pakhuis Formation diamictites. The Cedarberg Formation forms the last shale-dominated deposition before the TMG enters its second large-scale sandstone depositional cycle: the Nardouw Subgroup, which makes up a further 700 m of sandstone (Rust, 1967; Thamm and Johnson, 2006). The later Bokkeveld and Witteberg Groups consist of interbedded marine sandstones and shales that conformably overlie the Table Mountain Group (Rust, 1967; Theron, 1972).

Farther north and east of Cape Town, the entire Cape Supergroup is deformed into variable wavelength folds by the Cape Orogeny, which occurred at around 250 Ma and is known as the Cape Fold Belt (Hälbich, 1983). In the False Bay - Cape Peninsula region only the lower Graafwater, Peninsula and Pakhuis Formations of the Table Mountain Group are preserved and although they seem mostly undeformed on the Cape Peninsula, to the east of False Bay the Peninsula Formation is clearly tilted to high angles. Distribution of the Table Mountain Group outcrops is indicated in Figure 2.1.

2.5 Gondwana Breakup

Separation of eastern and western Gondwana began around 160 Ma with the initial rifting that led to the opening of the Indian Ocean (Powell et al., 1988), although the approximately 180 Ma Karoo dyke swarm records the earliest intra-continental magmatism and associated flood basalt (Elburg and Goldberg, 2000). Intrusions of dolerite dykes across Gondwana are common during the initiation of breakup period, for example Jurassic age dykes in the West Garo Hills, India, which are related to an extensional regime (Rao, 2002). The rifting of South America from Africa is interpreted to span the period of 150 Ma to 100 Ma (Nürnerg and Müller, 1991) and marks the break up of western Gondwana. Nürnerg and Müller (1991) showed that at 150 Ma initial continental stretching occurred along with the development of margin-perpendicular basins on the flanks of the South American plate and by approximately 130 Ma, rifting begins to extend northward, while to the south of the plate the Agulhas-Falkland Fracture Zone develops. By 118 Ma the Atlantic rift reached West Africa and after 100 Ma the South Atlantic Ocean is well developed and the rift connected into the North Atlantic (Nürnerg and Müller, 1991), completely separating the African plate from South America (Figure 2.3).

Opening of the Atlantic Ocean is suspected to be accompanied by the presence of the Tristan da Cunha plume, which may have enhanced uplift (Morgan, 1981; Turcotte and Emerman, 1983; Thompson et al., 2001). The Tristan da Cunha plume was located underneath the African and South American plate boundary; however, its exact location during breakup is still uncertain (Figure 2.3). Many authors suggest the Walvis Ridge is a record of the relative position of the plume head during the continental drift period (e.g. Ernesto et al., 2002; Gibson et al., 2005), whereas others suggest that the basaltic ridge is a result of a complex extension and breakup dynamic (e.g. Peate et al., 1999). The presence of a plume (or higher heat flux) is consistent with the production of the Paraná-Etendeka continental flood basalt province including extensive intrusive magmatism (Erlank et al., 1984; Ernesto et al., 2002; Trumbull et al., 2007). The tectonic regime that governed the southwestern tip of Africa resulted in relatively less preserved magmatism, possibly related to a smaller influence by the plume (i.e. distal) and smaller heat flux. The Agulhas-Falkland fracture zone is located nearby and the large dextral strike slip offset of the fracture zone likely accommodated large portions of crustal attenuation

at the time (Ben-Avraham et al., 1997).

2.6 West Coast Dyke Swarms and Related Magmatism

The intensive Cretaceous magmatism along the southwest African margin has been recorded by a variety of dyke swarms, central complexes, continental flood basalts (CFB) and lava fields found in on- and off-shore sections. Reflection of similar intrusive and extrusive magmatism is found on the South American plate as the Paraná CFB province and the associated Cretaceous Ponta Grossa dyke swarm (e.g. Ussami et al., 1991; Renne et al., 1996a). The equivalent continental flood basalt on the African plate, although much smaller in volume and extent, is the Etendeka CFB (Erlank et al., 1984; Renne et al., 1996b; Jerram et al., 1999), which is assumed to have been connected to the Paraná CFB prior to continental separation, collectively known as the Paraná-Etendeka continental flood basalt. The Etendeka portion of the CFB has been constrained to have initiated its magmatic activity around 133 Ma, while the combined Paraná-Etendeka CFB is constrained to 138 - 128 Ma (Trumbull et al., 2007 and references therein). Figure 2.4 shows the spacial relations between the various Cretaceous igneous provinces and dyke swarms with a reconstruction of the African and South American plates at around 130 Ma. Further evidence for extrusive volcanic rocks is represented by seaward-dipping reflectors. The seaward-dipping reflectors are found all along the African margin (Gladczenko et al., 1997) and are highlighted by NE-SW seismic profiles: MAMBA-1 in Namibia (Bauer et al., 2000) and the Springbok line in South Africa (Mahanyele et al., 2004). High velocity bodies in the lower continental crust are identified in the P-wave velocity profiles by Bauer et al. (2003); Mahanyele et al. (2004), which are interpreted as mafic- (or crust with higher MgO concentrations) intruded lower crustal rocks, based on petrophysical estimates summarised in Trumbull et al. (2007).

Rift-associated Cretaceous dykes are typically parallel to the margin or regional structures (e.g. the Damara Belt), as depicted in Figure 2.4. The sections below describe the dyke swarms, which are of varying intensity and in this study the terms mega-swarm, swarm and sub-swarm are used to describe the relative intensity of dykes along the Atlantic margin from Namibia to the Cape Peninsula of South Africa.

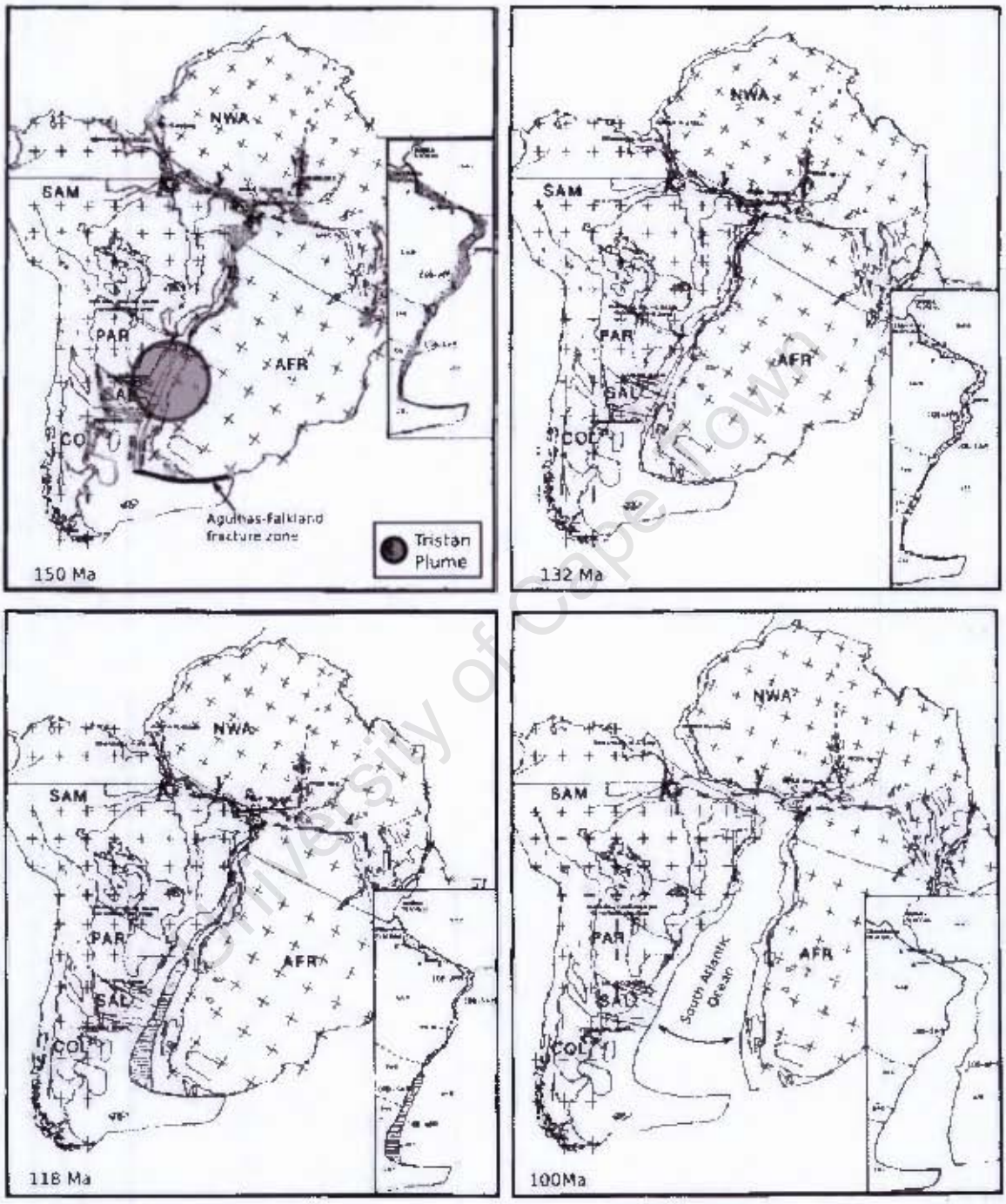

Figure 2.3: Southwestern Gondwana breakup from 150 - 100 Ma, after Nürnerg and Müller (1991). Shaded circle marks the estimated location of Tristan da Cunha mantle plume head at time of breakup (Ernesto et al., 2002).

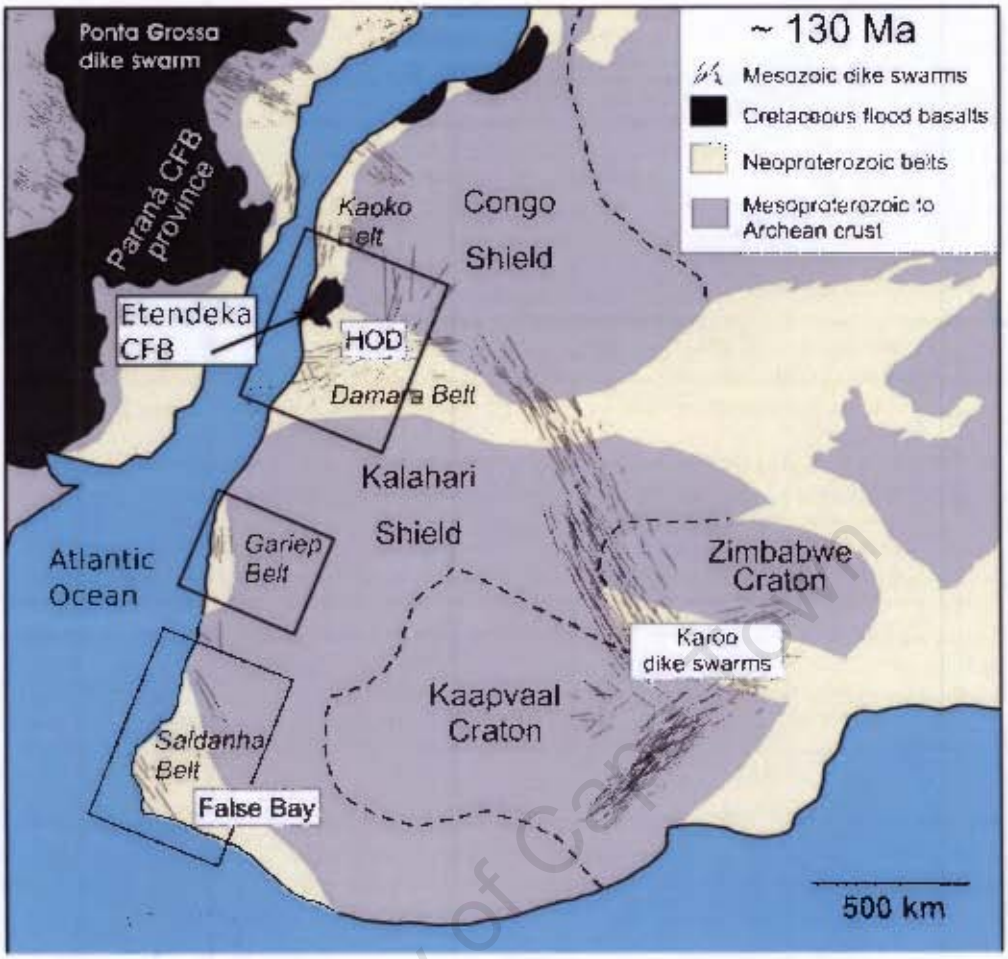

Figure 2.4: Map of Southern Africa and South America at around 130 Ma, showing flood basalt and dyke swarm distributions. The Karoo dyke swarm (180 Ma) is also shown. Figure from (Trumbull et al., 2007).

2.6.1 Henties Bay-Outjo

The Henties Bay-Outjo dyke swarm of Namibia (HOD) is the highest density dyke swarm found along the margin and is located close to the preserved Etendeka CFB to which the cretaceous magmatism is related (Figure 2.4). The HOD is considered, in this study, to be a Cretaceous mega-swarm, due to the high-density expression seen in aero-magnetics (Trumbull et al., 2004b). This high-density expression of dykes defining the HOD as a mega-swarm has been attributed to a higher magma flux in the region (Trumbull et al., 2007). The HOD mega-swarm does show some margin-parallel dykes; however, most of the dykes farther inland have intruded roughly perpendicular to the margin, parallel to the Damara Belt structural trend (Trumbull et al., 2004b). Intrusion ages from existing K-Ar data cover a range from 116 -

143 Ma (Trumbull et al., 2007 and references therein) and the geochemistry of the extensive mega-swarm can be subdivided into three different types (or swarms) based on unique mantle normalised incompatible trace element plots, suggesting different magma sources (Trumbull et al., 2007). Magma sources are divided into: (1) Tafelberg type swarm (Marsh et al., 2001), (2) Nepheline-normative type swarm (Trumbull et al., 2007) and (3) Horingbaai type swarm (Erlank et al., 1984). Trumbull et al. (2007) interpreted the variety of HOD magma sources and the high magma flux of the mega-swarm to be associated with the influence of the Tristan da Cunha mantle plume, which provided more heat to the HOD system allowing for melting of multiple source regions.

2.6.2 Mehlberg

South of the HOD mega-swarm a much smaller network of dykes is found intruding the Gariep Belt parallel to the continental margin (Figure 2.4). This sub-swarm is named after the more prominent dyke in the region, the Mehlberg Dyke, which extends south across the border of Namibia, up to 16 km into South Africa (De Villiers and Söhnge, 1959). Reid and Rex (1994) showed compositional similarities between the Mehlberg dyke and similar dolerite sills in the region, which are of Karoo age (180 Ma), but highlighted the younger intrusion age of 133 ± 4 Ma, which they dated by whole rock $^{40}Ar/^{39}Ar$. The Mehlberg dyke shows an en echelon intrusive pattern (Reid and Rex, 1994) and further dykes, mapped by aero-magnetics, have been linked to the Mehlberg dyke (see Trumbull et al., 2007) and together define the Mehlberg sub-swarm.

2.6.3 Koegel Fontein Complex

The Koegel Fontein Complex, a felsic central complex of 35 km in diameter, is linked to the Cretaceous igneous activity (De Beer and Armstrong, 1998) and is dated between 134 and 144 Ma. The central complex is situated due west of Bitterfontein and is made up a variety of granites (Rooivleitjie and Rietpoort), syenite, bostonite dykes and quartz porphyry dykes that originated from two different magma series (Curtis, 2009). The felsic complex is accompanied by a set of mafic dykes that are estimated to intrude within the same time period, prior to the

Figure 2.5: Dolerite dyke of the Garies sub-swarm cutting through the Namaqua-Natal Province gneisses at the Atlantic shoreline west of Bitterfontein. Photo by D I. Reid.

intrusion of quartz porphyry dykes and the younger Rietpoort granite (De Beer et al., 2002).

2.6.4 Cedarberg

The Cedarberg dyke swarm occurs north of the Koegel Fontein Complex close to the towns of Bitterfontein and Garies, while also extending inland into the Karoo Basin. Field mapping by De Beer et al. (2002) was further augmented by geophysical aero-magnetics published by Reeves (2000) and shows the extent of the Cedarberg swarm north of the Saldania Belt (Figure 2.4). Although no dykes of the Cedarberg swarm have been dated, they are presumed to be part of the Cretaceous age intrusions associated with Gondwana breakup, as they intrude parallel to the Atlantic margin and further inland are seen to cut Karoo dolerite sills (Chevallier and Woodford, 1999).

The Cedarberg dyke swarm is sparsely dispersed across the region and has been tentatively subdivided into various sub-swarms, which from north to south are: Garies, Knersvlakte and Doring-Tanqua sub-swarms. The Garies sub-swarm is found north of the Koegel Fontein Complex and intrudes the gneisses of the Namaqua-Natal Province (Figure 2.5). Most of the dykes of the Cedarberg swarm intrude Table Mountain Group sandstones in the Cape Fold Belt as

well as part of the Karoo sedimentary package (Petzer, 2006).

2.6.5 Saldanha

Offshore magnetic mapping by Day (1987) show a prominent margin-parallel dyke swarm at St Helena Bay off the coast of Saldanha (Figure 2.6A). The presence of dykes in this region has been supported by an unpublished aero-magnetic survey by C. de Beer (see Trumbull et al., 2007). Northwest of Saldanha at Paternoster, hornblende lamprophyre dykes intrude the local Vredenburg Granite. The lamprophyre dykes are distinctively different from the common dolerite dykes of the Cretaceous and are presumed to be an older dyke generation associated with the Cape Granite emplacement. The Saldanha dyke swarm has only been positively identified by magnetic surveys and is shown to be parallel to the Cedarberg swarm (Figure 2.6A). The correlation with the Cedarberg dyke swarm and margin-parallel pattern of the Saldanha dyke swarm is the only available information to suggest the Cretaceous age of intrusions.

2.6.6 False Bay

The southernmost expression of Cretaceous dykes is the False Bay dyke swarm, which is located in the False Bay - Cape Peninsula region near Cape Town (Figure 2.6B) and is the focus of this study. Although the magnetic data published by Day (1987) suggests the presence of numerous dykes in the False Bay region, only a few have surface exposures around the Cape Peninsula and on Robben Island (exposures shown by open circles in Figure 2.6B). Outcrops of the dykes are usually restricted to coastal shoreline locations. The dykes cut all of the pre-Cretaceous basement esposed at the Peninsula. The regional trend of the dyke swarm is NW-SE (Figure 2.6A). The False Bay dyke swarm can be correlated reasonably well along strike to the Saldanha dyke swarm, although at False Bay the dykes show a slightly more westerly trend of 300°, compared to the 320° trend of the Saldanha dyke swarm (Figure 2.6A).

Publications of the dark intrusive rocks of the Cape Peninsula are those of Nell and Brink (1944), Walker (1956), Day (1987) and Reid (1990) and in the literature the dyke swarm has been referred to as the Cape Peninsula dolerites (Walker, 1956; Reid, 1990) and the False Bay dolerites (Day, 1987; Reid et al., 1991). Nell and Brink (1944) used the term "Western Province

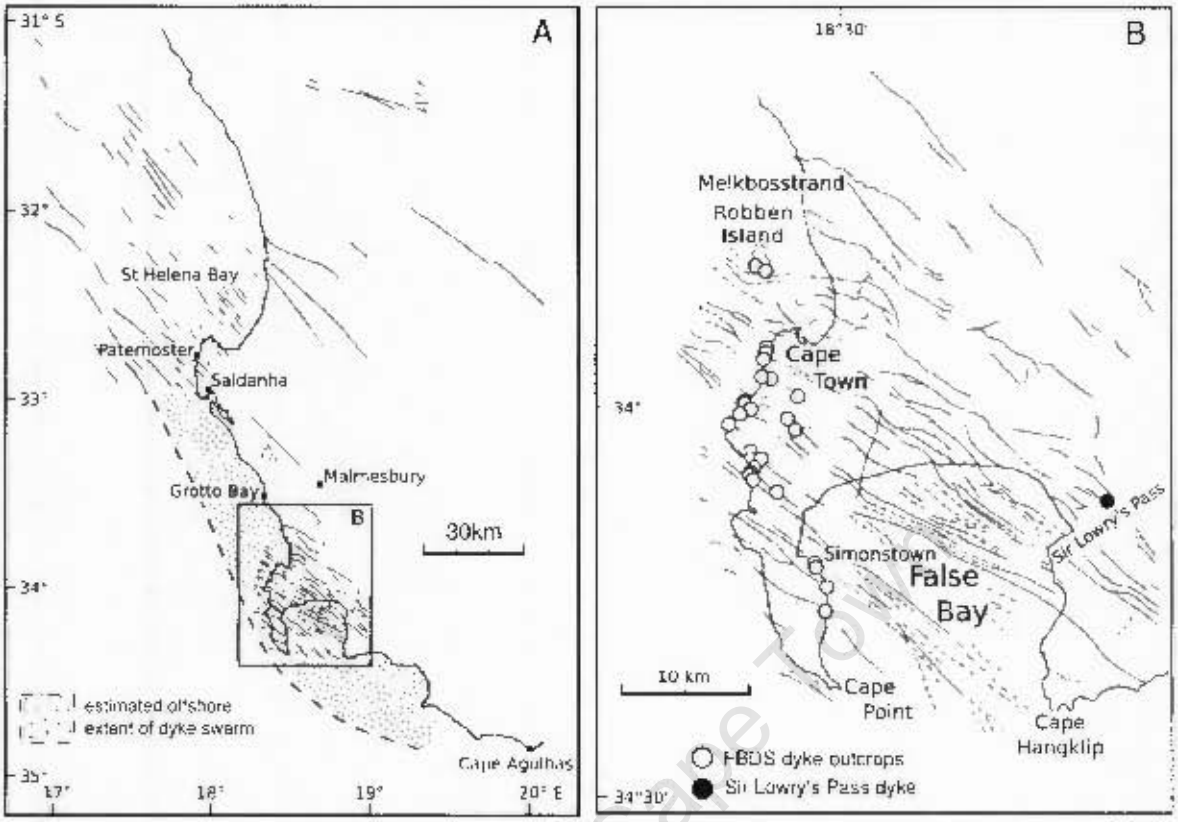

Figure 2.6: Magnetic anomaly maps published by Day (1987), highlighting the NW-SE striking dykes in the basement. A: Map including the Saldanha and False Bay dyke swarms, with an estimated extent of the dyke swarm offshore (dashed line and dotted area). B: The False Bay dyke swarm with known dyke outcrops on the Cape Peninsula and Robben Island (open circles) and the dyke at Sir Lowry's Pass (filled circle).

dolerites" to describe the dykes between the Cape Peninsula and Malmesbury, which includes both the False Bay and Saldanha dyke swarms, as defined here.

The intrusion age of the dykes was initially considered to be Karoo (~180 Ma) due to similarities drawn between geochemical comparisons of the False Bay dyke swarm with specific types of the Karoo Igneous Province (Reid, 1990). Nell and Brink (1944) had already indicated geochemical differences to distinguish between the Karoo and False Bay dykes, but believed the intrusion age of the False Bay dykes to be older than that of the Karoo igneous event. The latest and most reliable published radiometric ages for the False Bay dyke swarm include a mean emplacement age of 132 ± 6 Ma with a range from 126 - 141 Ma from whole rock K-Ar (Reid et al., 1991) and an Ar-Ar age of 131.3 ± 1.3 Ma measured on plagioclase separated from the dyke found at Millers Point (Stewart et al., 1996). The radiometric dating of the False Bay dykes confirm the Cretaceous age during which the dykes were intruded and relate the swarm

to the HOD and Mehlberg dyke swarms, which are also found along the Atlantic margin. Ages for the other dyke swarms (Saldanha and Cedarberg) remain to be established.

Chapter 3

Field Relations and Dyke Outcrops

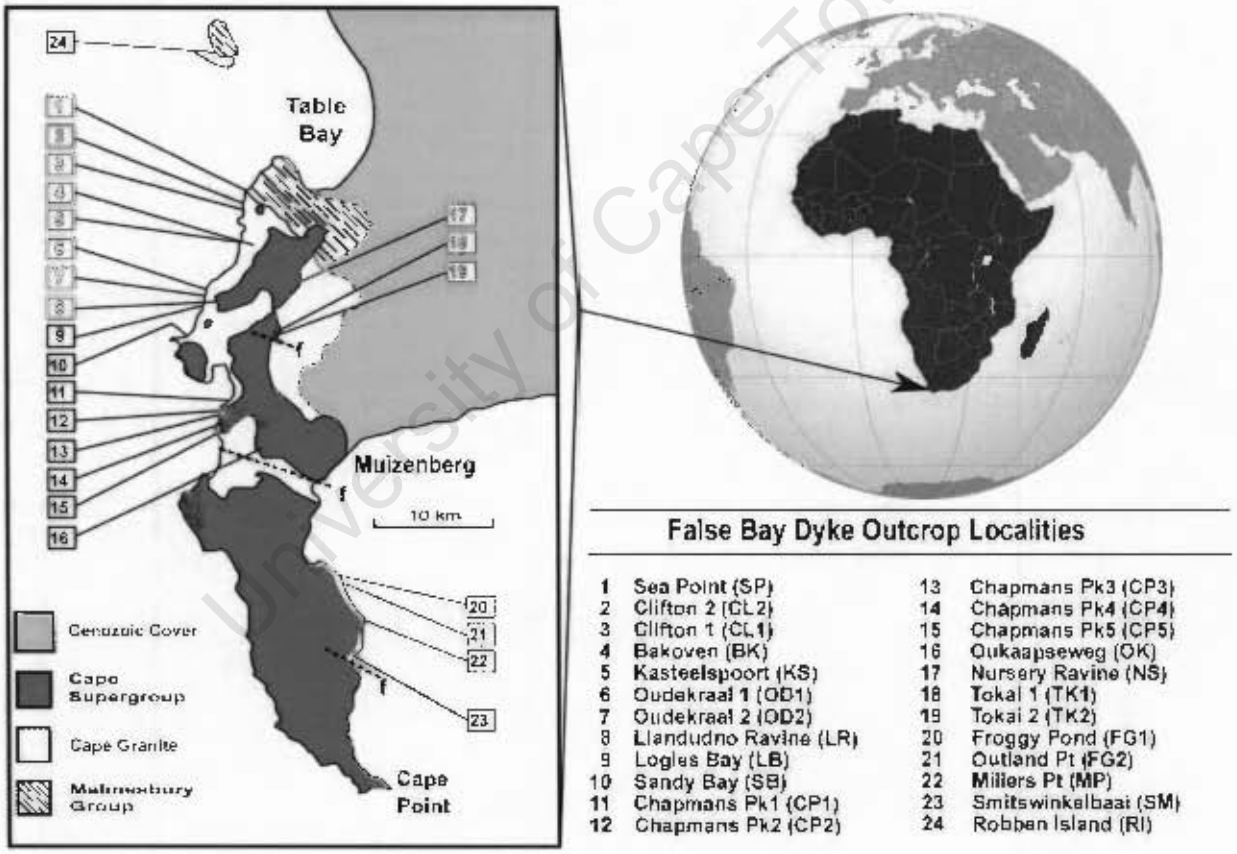

Figure 3.1: Location map of outcrops of the False Bay dyke swarm, Cape Peninsula, South Africa, adapted from Reid (1990).

The limited outcrop of the False Bay dyke swarm along shorelines, road cuts and stream beds is emphasised by the rare occurrence of dolerite schematic symbols on regional geological maps (1:50,000 Geology Sheets, Theron, 1984). The dyke outcrops are commonly situated along

Table 3.1: False Bay dyke coordinates, thicknesses and orientations. Llandudno Ravine and Sandy Bay dyke coordinates are from Google Earth.

#	Location	Abbreviation	GPS coordinates South	GPS coordinates East	dyke width (m)	strike/dip
1	Sea Point	SP	33° 55.259'	018° 22.726'	0.2	290/86S
2	Clifton 2	CL2	33° 56.017'	018° 22.652'	1.4	298/87S
3	Clifton 1	CL1	33° 56.064'	018° 22.637'	6	308/80N
4	Bakoven	BK	33° 57.845'	018° 22.394'	?	?
5	Kasteelspoort	KS	33° 58.078'	018° 22.928'	7	310/86N
6	Oudekraal 1	OD1	33° 59.545'	018° 20.652'	13	286/90
7	Oudekraal 2	OD2	34° 05.478'	018° 20.638'	1.5	300/87S
8	Llandudno Ravine	LR*	34° 00.298'	018° 21.140'	?	?
9	Logies Bay	LB1	34° 00.299'	018° 20.506'	40	314/75N
9	Logies Bay (minor dyke)	LB2	34° 00.299'	018° 20.506'	5	
10	Sandy Bay	SB*	34° 01.479'	018° 19.802'	?	?
11	Chapmans Peak 1	CP1	34° 04.195'	018° 21.953'	2	280/88S
12	Chapmans Peak 2	CP2	34° 04.776'	018° 21.449'	7	290/85S
13	Chapmans Peak 3	CP3	34° 04.992'	018° 21.408'	8	310/80N
14	Chapmans Peak 4	CP4	34° 05.423'	018° 21.107'	10	302/89N
15	Chapmans Peak 5	CP5	34° 05.548'	018° 21.087'	5	295/80S
16	Oukaapseweg	OK	34° 06.682'	018° 23.244'	>15	314/90
17	Nursery Ravine	NS	33° 59.222'	018° 25.312'	10	320/90
18	Tokai 1	TK1	34° 02.277'	018° 23.752'	?	?
19	Tokai 2	TK2	34° 02.277'	018° 23.752'	30	295/72N
20	Froggy Pond	FG1	34° 12.284'	018° 27.485'	2	290/87S
21	Oatland Point	FG2	34° 12.472'	018° 27.613'	4	330/89S
22	Millers Point	MP	34° 13.986'	018° 28.530'	6	310/85S
23	Smitswinkelbaai	SW	34° 15.802'	018° 28.095'	18	300/90
24	Robben Island west	RI	33° 49.005'	018° 21.904'	20	290/90
24	Robben Island east	RI	33° 49.073'	018° 22.531'	20	290/90

the coast, mostly within the Peninsula Granite; however, one prominent dyke outcrop is found in the Malmesbury Group on Robben Island. A map of the Cape Peninsula with simplified geology and dyke outcrop locations is shown in Figure 3.1. The locations of the dykes found around the Cape Peninsula and on Robben Island are given by their GPS coordinates in Table 3.1, which includes a summary of the dyke orientations (strike and dip) and their width.

The False Bay dyke swarm is undeformed by the Cape Orogeny and cross-cuts Cape Fold Belt structures. Walker (1956) noted that some of the dykes follow structures in the Peninsula Formation formed by Cape Fold Belt event. However, the dyke swarm maintains the regional NW-SE trend. The Cape Fold Belt structures are predominantly absent at the Cape Peninsula,

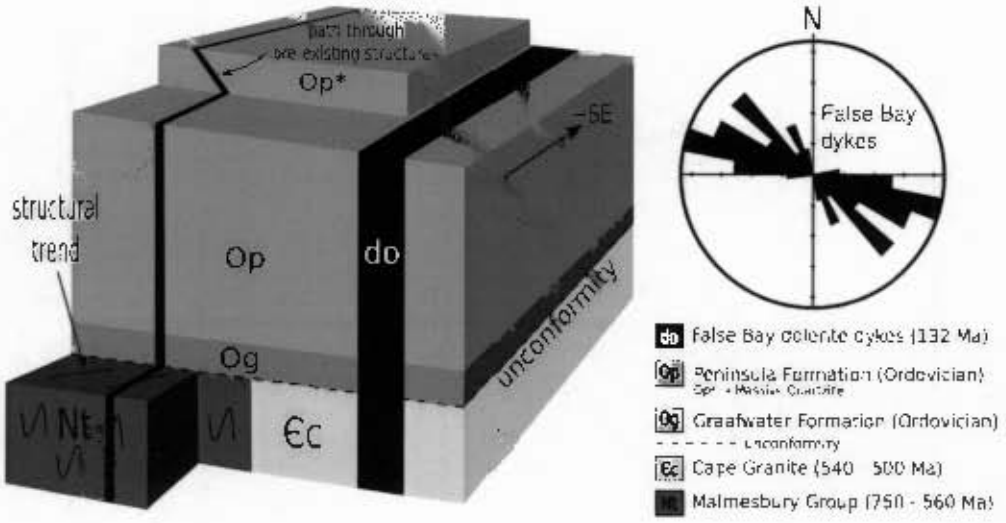

Figure 3.2: 3D block schematic showing field relation between dykes and country rocks at the Cape Peninsula. Saldanian structural trend indicated in the Malmesbury Group block and observations by Walker (1956) that dykes follow pre-Cretaceous structure where the Peninsula sandstone becomes more massive shown by smaller block (Op*) on top. Rose Diagram of dyke orientations shown in top right corner.

besides a few larger offset faults at Tokai, Fish Hoek and Smitswinkelbaai (see Figure 3.1). The cross-cutting relation between the dyke swarm and Cape Fold Belt structures is shown by two dykes at Sir Lowry's Pass, 60 km east of Cape Town, where the dykes still conform to the regional trend and cut vertically through the tilted sandstone beds. The block diagram in Figure 3.2 shows the field relations of the dykes to the local basement and although outcrops of dykes in the TMG are limited in the field, some dykes are clearly seen to propagate upwards though the TMG, for example at Chapman's Peak and Nursery Ravine (Figure 3.1).

The dykes are mostly vertical, with dips ranging between 75° - 90°. The regional trend of the False Bay dyke swarm is NW - SE, as was originally suggested by Walker (1956) and later shown by magnetic maps (Day, 1987). The NW trend is confirmed here by the detailed mapping of strike and dip measurements depicted on a rose diagram in Figure 3.2. Local strike variations of individual dykes have been noted in the literature (Walker, 1956; Reid, 1990) and the rose diagram in Figure 3.2 shows the variation in strike of the dykes to vary from due north to due west with a mean northwesterly orientation. The regional trend of the swarm as measured on the magnetic map by Day (1987) is approximately 300°, which agrees well with the field measurements and an average strike of 301° (Figure 3.3). The orientations of the dykes are closely related to regional structures formed in the country rock. Stereograph plots

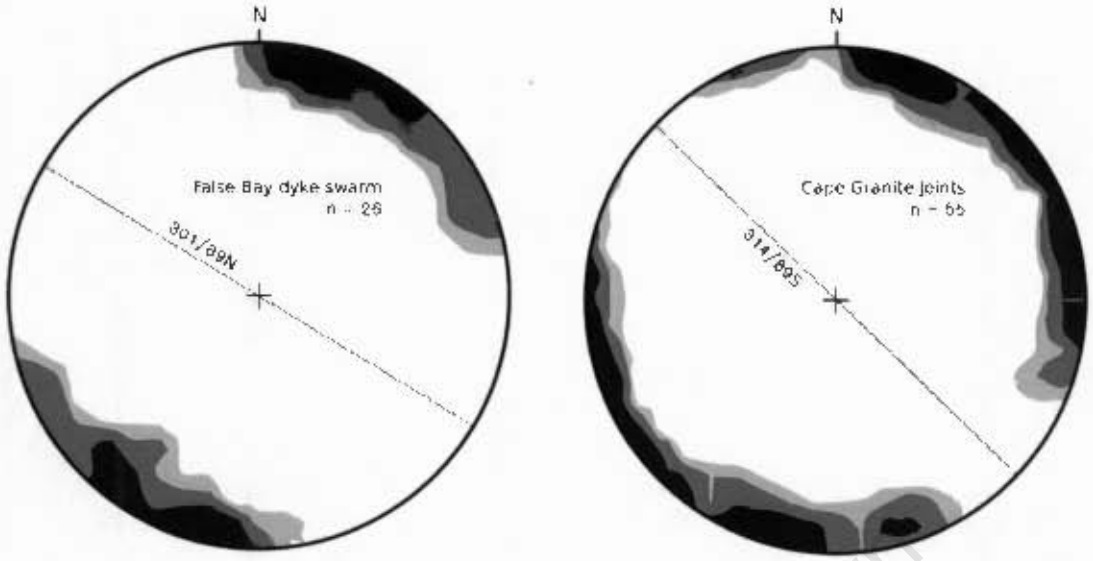

Figure 3.3: Stereonet plots of strike and dip measurements of the False Bay dolerite dyke contacts (left) and jointing in the Cape Granite (right). Shaded contours represent % area of poles to the measured planes with dotted line representing the mean orientation of planes measured.

of the joint system in the Peninsula Granite shows more variation than the dyke orientations; however, the mean orientation of 314° strike for joints in the granite is similar to the 301° trend of the dolerite dykes (Figure 3.3). Variations in strike of individual dykes appear to follow the systematic joint pattern that prevails in the granite country rock. For example at Froggy Pond, the two dominant orientations of the dyke contacts are also expressed in the granite joints (Figure 3.4). A similar northwest prevailing structure is seen across the Cape Peninsula that is emphasised by preferential weathering within the Table Mountain Group, forming ravines and gorges parallel to the regional strike of the dyke swarm and are in some cases accompanied by dolerite dykes, as for example the Kasteelspoort Ravine and at Chapman's Peak (Figure 3.5).

Whether or not the fracture system formed prior to intrusion of the dykes, or simultaneously as a result of dyke emplacement, is speculative. However, it is likely that these structures formed during the same general tectonic event: the breakup of Gondwana. The structures and orientations are consistent across the region and the radiometric dating of the dykes that occupy the joints give a Cretaceous age. Opening of the joints filled by dolerite dykes seems to be mainly dilatational. This is demonstrated by the country rock showing no effective offset across the dykes (Figure 3.4-[2]). The dykes themselves have joints that are approximately perpendicular to the strike orientation (Figure 3.4-[1]) and probably formed during cooling contraction of

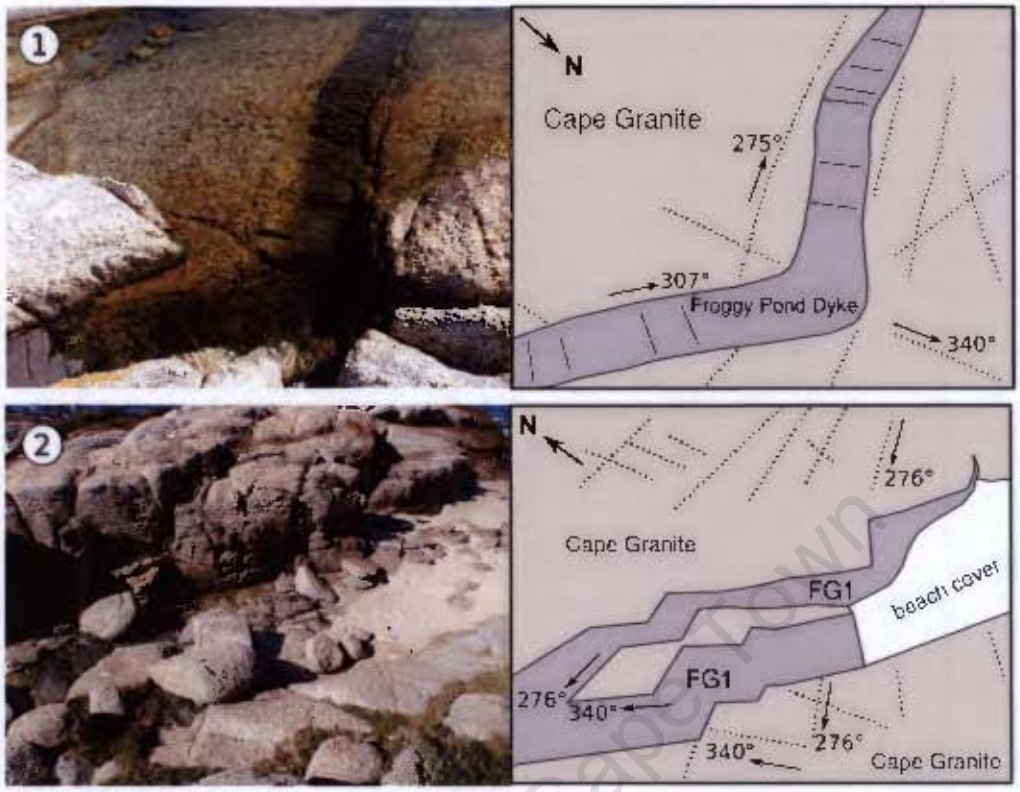

Figure 3.4: Dolerite dyke at Froggy Pond intruding Cape granite with a well defined joint system (dotted lines). [1] dyke with contact perpendicular internal joints highlighted by black solid lines in accompanying sketch; [2] granite xenolith body showing no rotation relative to in situ country rock.

Figure 3.5: Google Earth images of [1] Chapman's Peak and [2] the Twelve Apostles at Camps Bay. Fracture system developed in the Table Mountain Group sandstones highlighted by dotted lines and valleys with dykes are shown by solid line and labelled (see Figure 3.1 for location and abbreviation).

the intruded magma. Examples of strike slip offset across dykes are rarely observed; however, the extent of offset is very minimal.

The sections below describe the location, accessibility, size and outcrop of the individual dykes found on the Cape Peninsula. The order of dyke description is done by the numbering of dykes shown in Figure 3.1 from Sea Point (1) to Smitswinkelbaai (23), which has a north to south order and the Robben Island dyke is added to the list as number 24. The numbering and abbreviations of dyke locations are taken from Reid (1990). Further dyke locations, which are now either covered by development in the city or not identified during this study are shown on the Cape Town geological 1:50,000 maps (Theron, 1984).

3.1 Sea Point (SP)

The Sea Point dyke (SP) is a thin dyke found on the northern end of Queen's Beach in Sea Point (Figure 3.6-[1]) and is the northern-most dolerite outcrop on the Cape Peninsula located during this study, as well as being the narrowest dyke in the suite. With a maximum width of 0.2 m the dyke strikes 290°, is mostly covered by beach sand and its eastern extension is covered by the Sea Point promenade wall (Figure 3.6-[2]). The dyke intrudes the satellite granite within the Sea Point migmatite contact zone (Kolbe, 1966), between the Cape Granite and the Malmesbury Group. The dyke pinches out to the west approximately 6.8 m from the wall. The strike orientation of the dyke is closely related to the major joint direction of the granite country rock, which strike at about 297°.

3.2 Clifton 2 (CL2)

Clifton, which lies south of Sea Point towards Camps Bay, hosts a small network of dykes on its northern-most beach. The dykes are accessed from the south, which lead to the numbering of the Clifton dykes from south to north as Clifton 1 (CL1) and Clifton 2 (CL2) respectively. Not described in previous studies is the presence of a third dyke set, which lies between CL1 and CL2 and is described after CL1 in Section 3.3.1. Clifton 2, being the northern-most dyke is listed here first.

CL2 is made up of one 1.4 to 2 m wide dyke, which can be seen to extend westward from the beach into the ocean, while being covered to the east under urban development (Figure 3.7). The seaward extension of the dyke is not easily accessible, except during spring low tides, when the dyke becomes visible. The dyke strikes at 298° and is mostly covered by extremely large granite boulders, which also make up the country rock. Although the granites at Clifton do show some jointing developed closer to the dolerite dykes, they do not show the development of prominent joints within outcrops.

3.3 Clifton 1 (CL1)

The southern-most dolerite dyke at Clifton (CL1) has 3 parallel smaller dykes within a ~20 m wide area within the granite country rock (Figure 3.8-[1]). The CL1 dyke is 5 m wide and strikes between 298° (Figure 3.8-[3]). Strike variations in the surrounding dyke network seem to be systematic, following joints that are roughly parallel to the larger dyke (CL1) intrusion. Within the area, there are cryptic cross-cutting relations between two dykes (Figure 3.8-[7]). The southern-most smaller dyke close to CL1 is 70 cm wide and strikes close to north at 356° at its most extreme (Figure 3.8-[6]). Figure 3.8-[4] shows a granite xenolith.

3.3.1 Clifton 3 (CL3)

Between CL1 and CL2 is a 2.2 m wide dyke (CL3), which strikes at 348° - 356° and is mostly covered by beach sand (Figure 3.9). Smaller mm-cm wide dykes parallel to CL3 shows an en-echelon intrusion pattern (Figure 3.9-[3]). As CL3 was only mapped during the later parts of the study, the dyke was not sampled.

3.4 Bakoven (BK)

Bakoven lies at the base of Kasteelspoort that runs down off Table Mountain at the southern end of Camps Bay (Figure 3.10-[1]). The area where the geological map indicates an outcrop of dolerite has been developed with new houses on either side of the road leaving no visible

bedrock. Numerous large boulders of dolerite are found on the pebble/boulder beach (Figure 3.10-[2 and 3]), where the stream enters the ocean and this suggests the proximity of a dolerite dyke. However, large boulders of Table Mountain Group sandstones are also present here, therefore the dolerite boulders could have been derived from further up stream.

3.5 Kasteelspoort (KS)

On the southern end of Camps Bay's residential area, the Kasteelspoort stream cuts down from the top of Table Mountain. Most of the stream is densely vegetated with thick reeds, but on the highest residential road access, part of the Kasteelspoort dolerite dyke (KS) is exposed intruding Cape Granite bedrock (Figure 3.11-[1]). The stream seems to follow the dolerite outcrop, which is mostly overgrown (Figure 3.11-[7]). Further up the slope a large granite pavement is visible and can be accessed by small paths through the fynbos vegetation. Here the dyke has more accessible outcrops. At its widest, the dyke is about 7 m and decreases down to 1m further upstream. The strike of the dyke varies between 310° and 342°. Parallel to the main dyke a small network of 1 - 10 cm wide dykes intrude the granite (Figure 3.11-[5]). These, although anastomosing, show strike directions of about 270°, 305° and 340° and utilise the similarly orientated joints developed in the granite.

3.6 Oudekraal 1 (OD1)

Along Victoria Road between Camps Bay and Hout Bay lies the Oudekraal picnic area. South of the Oudekraal picnic area, the Oudekraal dyke (OD1) forms an outcrop at road level in a small cutback into the slope. At sea level the dolerite can be clearly seen intruding the granite (Figure 3.12-[1]). The sea-level outcrop can be accessed by a climb down along the granite on the northern side of the dyke. The strike of the dyke is 286° and is about 13m wide and incorporates large rafts of granite xenolith blocks (Figure 3.12-[2]). These granite blocks have many smaller veins of dolerite intruding them that extend from the main dolerite body (Figure 3.12-[3]).

3.7 Oudekraal 2 (OD2)

A second dolerite dyke (OD2) along Victoria Road is 1.5m wide and has a strike of 300°. The dyke is visible in the road cut just before Llandudno (Figure 3.13-[1]). This outcrop is severely weathered, such that the typical dolerite contrast with granite is not observed and the dyke is easily overlooked. The presence of the OD2 dyke is distinguishable by the straight and vertical contact it forms within the surrounding granite (Figure 3.13-[3 and 4]), typical of other dyke locations. The top part of the outcrop is capped by soil and vegetation, whereas towards the ocean side of the road the slope is also covered and vegetated (Figure 3.13-[2]). No further outcrops were found of this dyke; however, the geological map does show an outcrop at sea level.

3.8 Llandudno Ravine (LR)

The Llandudno Ravine cuts the southern end of the Twelve Apostles mountain range and a dolerite dyke (LR) outcrops within the ravine above Llandudno. The dyke was sampled during the initial work done by Reid (1990), but was not revisited during this study.

3.9 Logies Bay (LB1 & LB2)

Logies Bay, which is situated just north of the beach at Llandudno, hosts the widest dolerite dyke (LB1) outcrop on the Cape Peninsula with a width of ~40 m (Figure 3.14-[1]). The dyke cannot be followed a long way along strike, but a thinner, more weathered dyke, presumably the extension of LB1, is found in a road cut on Suikerbossie Pass. The dyke strikes at 314° and has a very sharp contact with the Cape Granite country rock and dolerite quench textures at the dykes edge are prominent (Figure 3.14-[2]), compared to the coarse grained interior (Figure 3.14-[5]). The interior of LB1 has an average grain size of greater than 2mm and can be classified as gabbroic. A finer grained minor dyke (LB2) that intrudes LB1, was initially described by Walker (1956) and can be seen in Figure 3.14-[4 and 6]. LB2 also shows quench textures at its contact to LB1, supporting its intrusive relation to LB1. On the northern end

of the dyke, a 5 cm thin shear fracture is found 30 cm from the dyke into the granite country rock, and runs parallel to the dyke. In this thin shear fracture one of the granite's alkali-feldspar phenocrysts, shows sinistral offset (Figure 3.14-[3]).

3.10 Sandy Bay (SB)

Sandy Bay lies south of Llandudno and can only be accessed by foot, either from Llandudno or from Hout Bay's Klein Leeukop (Little Lion's Head) area. The presence of a dolerite dyke at Sandy Bay (SB) was documented by Reid (1990, and references therein). No in-situ dolerite outcrops are found at Sandy Bay, but the presence of dolerite boulders suggests the presence of an unexposed dolerite dyke. The slopes of Suther Peak on the southern end of the beach are covered in talus with hardly any in-situ outcrops visible and the local fynbos vegetation covers most of the slopes. Samples of SB were collected from dolerite boulders found on the southern end of Sandy Bay beach.

3.11 Chapman's Peak 1 (CP1)

Chapman's Peak Drive connects Hout Bay and Noordhoek along the western coastline of the Cape Peninsula along the steep cliffs of Chapman's Peak. Five dykes are documented along this traverse and are labelled north to south from 1-5. The northern-most dolerite dyke (CP1) is found close to one of the parking areas on the way towards the viewpoint. As samples of these dykes were collected in previous studies, the dykes were only visited during the later course of this study. A dyke that was thought to be CP1 can also be seen from the sea and intrudes the local granite country rock (Figure 3.15-[1] and [2]). The outcrop shows a fresh 2 m wide dyke that can be accessed close to the top of the granite cliff that strikes at 280° (Figure 3.15-[3]).

Archived photographs marked CP1 found on the Geological Sciences departmental website, show a dolerite dyke cutting the granite basement (Figure 3.15-[4 and 5]). This outcrop is however distinctively different to that identified above and personal communication with D L Reid, confirmed that the samples labelled CP1 were indeed collected from the dyke shown in Figure 3.15-[4 and 5], which is located approximately 320 m south along the shoreline from the

dyke described in the previous paragraph and their relative positions are shown on the Google Earth image in Figure 3.15-[6]. Therefore the dyke visited during this study represents an additional dyke along Chapman's Peak drive (CP0) and was unfortunately not included in the data set. As the new dyke was only identified as coming from "new" location later during the course of the study, it was neither sampled nor analysed. References to CP1 in this thesis refer to the original dyke sampled by D L Reid and seen in Figure 3.15-[4 and 5].

3.12 Chapman's Peak 2 (CP2)

The CP2 dolerite dyke is located just south of the main view point at the highest elevation along Chapman's Peak Drive (Figure 3.16-[1]). This spectacular outcrop is best seen from the sea and the 7 m wide dyke cuts up through the Cape Granite into the Table Mountain Group sandstones and strikes at approximately 290° (Figure 3.16-[2]). The best access to the dyke is along the road, where the dyke is in contact with the Graafwater Formation. The edges of the Graafwater Formation sandstones that are in contact with the dyke show a zone of alteration (Figure 3.16-[3 and 4]). The contrast between the dolerite and granite can be clearly seen in Figure 3.16-[4], which also shows the knife-sharp contact.

3.13 Chapman's Peak 3 (CP3)

Chapman's Peak 3 dyke (CP3) occupies a prominent gully above the Chapman's Peak Drive in the Table Mountain Group (Figure 3.17) and is highly weathered in road cuts, and has been covered in shot-crete obscuring much of the outcrop. The dyke can be accessed behind the rock-fall netting next to the road, by a climb up into the gully. Here the dyke has intruded into the Table Mountain Group sandstones. The strike of the dyke changes across the granite - sandstone boundary, striking at 260° in the granite and 310° in the sandstone (Figure 3.17-[3]).

3.14 Chapman's Peak 4 (CP4)

The fourth dyke (CP4) along Chapman's Peak Drive has a spectacular outcrop below the road, which is best seen from a boat (Figure 3.18-[1]). The valley occupied by the dyke is much more vegetated compared to CP3 (Figure 3.18-[2]) and is less accessible. Dolerite outcrops can be seen from the road and the dyke was previously sampled after fires had cleared out the vegetation (personal communication with D L Reid, 2010). The dip of the 10 m wide dyke changes from a dip of ~85° south to ~85° north at the transition from Cape Granite to Table Mountain Group sandstones along a common strike of 302° (Figure 3.18-[1]).

3.15 Chapman's Peak 5 (CP5)

The southern-most dyke on Chapman's Peak (CP5) is found closer to Noordhoek and Figure 3.19-[1] shows the relative positions of CP2, CP3, CP4 and CP5 along Chapman's Peak drive. This outcrop is very limited and outcrops of the same dyke are not found below the road towards the sea. The dolerite dyke is approximately 5 m wide and freshly split hand samples confirm the mafic mineralogy (Figure 3.19-[2]). The dyke cuts the contact between the Cape Granite (Figure 3.19-[3]) and the Graafwater Formation at 295° strike; however, it terminates within 1-2 m of intruding the sandstone along an irregular contact (Figure 3.19-[4]). Figure 3.19-[5] is a photograph courtesy of D L Reid of the dyke before the road cuts were reinforced by shot-crete.

3.16 Oukaapseweg (OK)

The 1 : 50000 geological map of the Cape Peninsula (3418 AB & AD Kaapse Skiereiland) shows an extensive outcrop of the Oukaapseweg dyke (OK) and D L Reid (personal communication, 2011) indicated that the dyke was exposed after fires and during excavations (Figure 3.20-[1]). Today, the outcrop of this dolerite dyke is restricted to the road cuts in the bend of the M64 road, and extremely weathered outcrops occur on either side of the road adjacent to bedded Peninsula sandstones showing well preserved cross-bedding (Figure 3.20-[2]). Samples of fresh dolerite were collected during previous studies, where the dyke was exposed during

excavations. Only the southern contact of the dyke is exposed in the road cut (Figure 3.20-[3 and 4]). The current outcrop suggests a minimum dyke width of 15m at a strike of 314°.

3.17 Nursery Ravine (NS)

The Nursery Ravine dyke (NS) is seen at a dolerite outcrop that is significantly weathered to a brown colour that only shows the typical dolerite appearance when split open (Figure 3.21-[4]). It is located on the eastern slopes of Reserve Peak above Kirstenbosch Botanical Gardens in Nursery Ravine and intrudes the Table Mountain Group sandstones (Figure 3.21-[1]). The dyke is roughly 10 m wide and strikes at 320°. The outcrop can be found along the contour path where it crosses the Nursery Ravine trail. Further up the trail, more fresh dolerite dyke samples can be found in contact with Table Mountain Group sandstones (Figure 3.21-[6]). The contacts of the dyke show finer grained textures than those found in the core of the dyke.

3.18 Tokai 1 (TK1)

The eastern slopes of Constantiaberg host two dolerite dykes in Tokai forest (Reid, 1990), which split from one single dyke. The first dyke (TK1), was not found during this study. A map of the Tokai dyke area is shown in Figure 3.22-[1] and shows the relation of the dyke outcrop and trend compared to that originally mapped for the geological map of Cape Town (Theron, 1984).

3.19 Tokai 2 (TK2)

The wide dolerite dyke in Tokai (TK2) has been correlated with the Logies Bay dyke (Reid, 1990), due to the large width of the dyke (~30 m) and the coarse grained gabbroic nature of the rock (Figure 3.22-[2]). The kloof that hosts the dyke trends at around 290°, which is estimated from the steep vertical Peninsula Formation cliff, assumed to be roughly parallel to the contact to the dyke. The TK2 dyke has joints that strike at 295°, suggesting contact-parallel joints, which is in contrast to the typical contact-perpendicular joints observed at other dyke outcrops.

The dyke is highly weathered and fresh samples are found when boulders are split open (Figure 3.22-[4]). South of the dyke one of the larger faults mapped at the Cape Peninsula is exposed (Figure 3.22-[3]) and the fault surface has a northwesterly strike, similar to the trend of the False Bay dyke swarm.

3.20 Froggy Pond (FG1)

At Froggy Pond, just south of Boulders Beach, there are a set of dykes in close proximity to one another (Figure 3.23-[1]). These dykes are thin, 0.3 to 2 m wide, and show quench textures of the dyke at the granite contact. Samples were collected from the larger dyke (FG1, see Figure 3.23-[1]). The dykes follow a very distinctive set of orientations, repeated at this locality and these clearly follow the local joint pattern in the granite (Figure 3.23-[5]). The two dominant orientations measured for both joints and dykes are 290° and 335° in strike. This locality shows the lateral pinching out nature of the dykes (Figure 3.23-[2]). Also, blocks of granite have been dislodged from the country rock and are found as xenoliths in the dolerite (Figure 3.23-[3]). The larger block of granite situated in between two ~1.3 m wide dolerite dykes does not show any sense of rotation or shear across the intruding dyke. Most of the outcrop is covered by beach sand, and two adjacent outcrops are found along strike, where the northern outcrop pinches out and the southern outcrop extends beyond the low tide line (Figure 3.23-[1]).

3.21 Oatland Point (FG2)

Oatland point is about 500 m south of Froggy Pond, and the 4 m wide dolerite dyke (FG2) does not show much variation in strike along its limited outcrop length (about 10 m) (Figure 3.24-[1]). The dyke at Oatland Point has a strike of 330°. The Cape Granite country rock at Oatland Point differs from that at other locations with prominent fine grained apalite dykes cutting the granite (Figure 3.24-[2]). The FG2 dolerite clearly cuts these apalite dykes (Figure 3.24-[2]). Figure 3.24-[3] shows the close proximity of FG1 and FG2.

3.22 Millers Point (MP)

The Millers Point dolerite dyke (MP) can only be accessed during spring low tide (Figure 3.25-[1] and [2]). The 6 m wide MP dyke shows interesting outcrop patterns in the granite with many small offshoots including one large piece of broken off granite in its centre, nearly the entire width of the dyke (Figure 3.25-[1]). Smaller individual xenoliths are also common here (Figure 3.25-[5]). Quench textures of the dyke are identified at the contact with granite outcrops by their much smoother weathered surface (Figure 3.25-[4]). To the northwest the dyke extends beneath the sand striking at 310° and is not seen further along strike in road cuts. However, there is a very distinctive vegetated gap in the TMG of the Swartkopberge some 250m above sea level, which falls along strike of the MP dyke. This was not investigated but could possibly be related to the to the preferential weathering of the dolerite adjacent to the Table Mountain Group sandstones.

3.23 Smitswinkelbaai (SM)

The Smitswinkelbaai dyke (SM) is the most southerly exposed dyke and can be accessed by a short hike down from a parking lot close to the Cape Granite - Peninsula Formation contact on the northern side of the Smitswinkelbaai fault (Figure 3.26-[1]). The dyke strikes at 300° and is the only dyke that has a felsic vein cutting through it. After the Logies Bay and Tokai Forrest dykes, the SM dyke is the next widest at 18 m. The outcrop only extends for 15-20 m along strike and covered by vegetation on the mountain slope. The dyke is not observed along the road within the TMG sandstones further up the slope. Xenocrysts and xenoliths are common (Figure 3.26-[4]) and this location shows interesting xenoliths of a very coarse grained granitoid unlike the Cape Granite, described below. Contact of the dyke to the granite country rock is quenched and offshoots of the dyke into the granite are shown in Figure 3.26-[5].

3.23.1 Smitswinkelbaai Xenoliths

The SM dyke shows unusual xenoliths that at first sight appear to be felsic (Figure 3.27-[1]). Not enough material from the xenolith was collected for a complete analysis. The xenolith

is very coarse-grained with up to cm size grains of plagioclase feldspar and pink quartz (Figure 3.27-[7]). Also evident in the rock is a green mineral (Figure 3.27-[3]) that was identified as apatite. No alkali-feldspars were identified by the restricted amount of samples. Unlike the Cape Granite xenoliths in the field area, which are still fresh and unaltered, this xenolith shows significant resorption textures and reaction rims between individual mineral grains (Figure 3.27-[5]) as well as progressive disaggregation and isolation of individual minerals into the dolerite dyke (Figure 3.27-[2]).

3.24 Robben Island (RI)

The geological map of Cape Town (Theron, 1984) shows only one outcrop of a dolerite dyke (RI) on Robben Island. Field work by Rowe et al. (2010) confirmed the western shore dyke outcrop (Figure 3.28-[1]) and they observed a further outcrop of a dolerite dyke on the southern shore of the island, presumably the eastern extension of the dyke (Figure 3.28-[2]). The dolerite is not found as in situ outcrops, as the dyke has been eroded to below sea level and produces a 20m wide and continuous low in the exposed rocks at the shoreline. However, the beaches adjacent to the dyke are littered with dolerite pebbles and larger boulders of dolerite are also found along the assumed dyke path. The Robben Island dykes are likely part of a single dyke on Robben Island (Figure 3.28-[3]) and is the only location in this study, where the country rock consists of the Malmesbury Group. The dyke clearly cuts across the Proterozoic Saldania Belt structures and conforms to the regional trend of the rest of the dyke swarm, which is clearly seen by the photograph imagery in Figure 3.28-[4] from (National GeoSpatial Information Imagery, 2008).

3.25 Other Samples used in study

Besides the 24 dyke localities described above a few extra samples were included in the study to expand the data set. These include two dykes from Sir Lowry's Pass and dolerite samples collected from the Waterfront and along the Silvermine hiking trail.

3.25.1 Sir Lowry's Pass (SL)

Two dykes (SL1 and SL2) were sampled by Creighton-Jones (1982) ~40 km east of Cape Town on Sir Lowry's Pass on the N2 national road. Regionally, these dykes form part of the False Bay dyke swarm as evident from the magnetic data provided by Day (1987) and they have the same regional strike direction. These dykes outcrop within the Table Mountain Group sandstones. The sandstones at Sir Lowry's Pass are tilted and the dykes intrude vertically. Therefore, the dykes are seemingly unaffected by the Cape Orogeny and post-date the Cape Fold Belt deformation event.

3.25.2 Waterfront Breakwater sample

At the Waterfront, Cape Town, dolerite boulders were found in parts of the Breakwater. A sample was collected in order to determine the origin of the dolerite, i.e. if one of the known dolerite outcrops was sampled to provide for the breakwater. Or alternatively, if the dolerite is from a dyke not identified as part of this studies.

3.25.3 Silvermine Pathway sample

The final sample included in the FBDS data set analysed in this study was a loose dolerite rock found along a pathway in the Silvermine National Park. As the case of the Waterfront Breakwater sample the intention was to determine the provenance of this sample by comparison to the available data set.

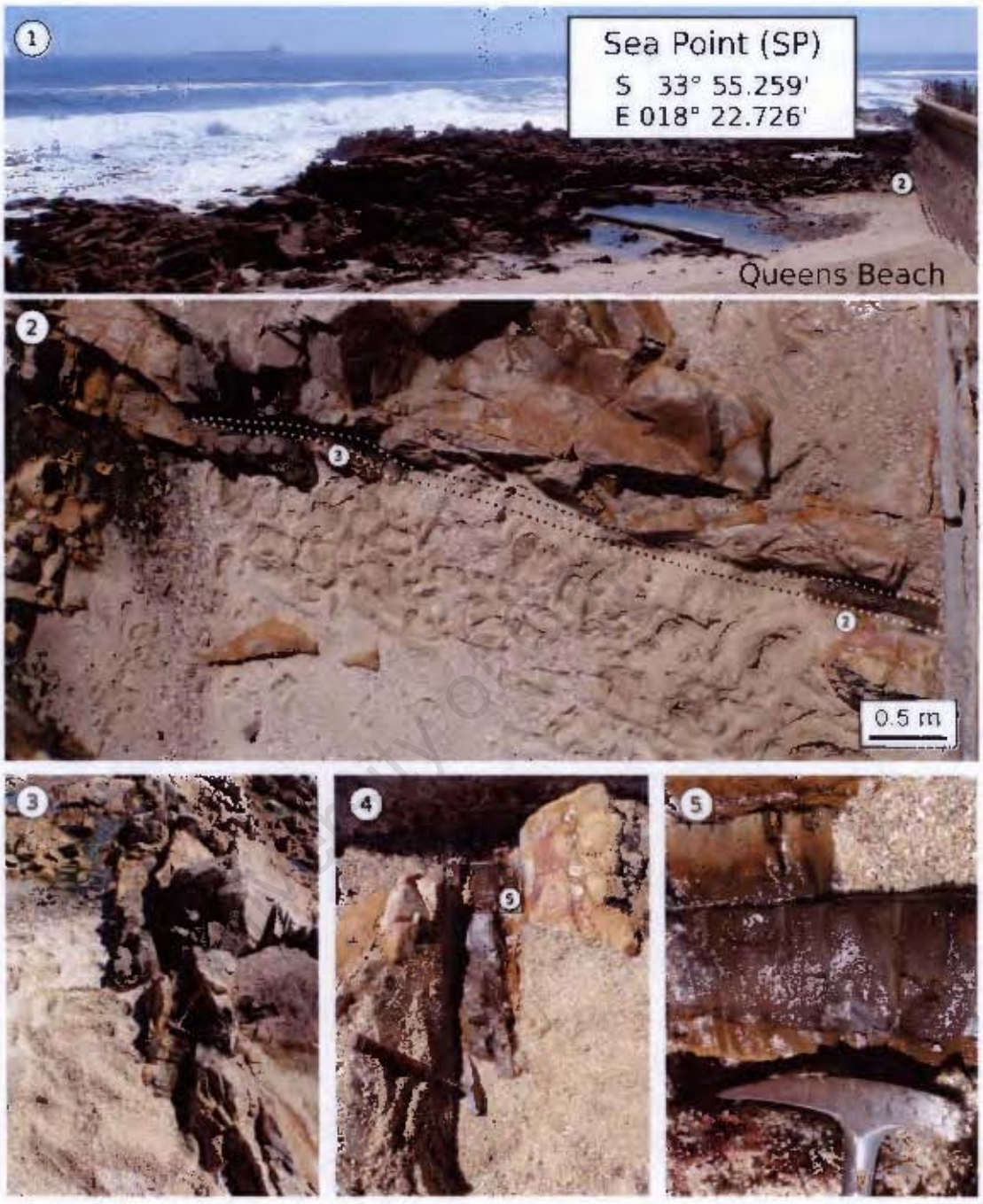

Figure 3.6: Sea Point dyke. [1] Looking north into Table Bay at Queen's Beach, Sea Point; [2] plan view of dyke highlighted by dotted line; [3] western extension and pinching out of dyke in granite; [4] eastern extension of dyke exposed next to the wall of the promenade; [5] dolerite dyke with light coloured edges (probably due to alteration).

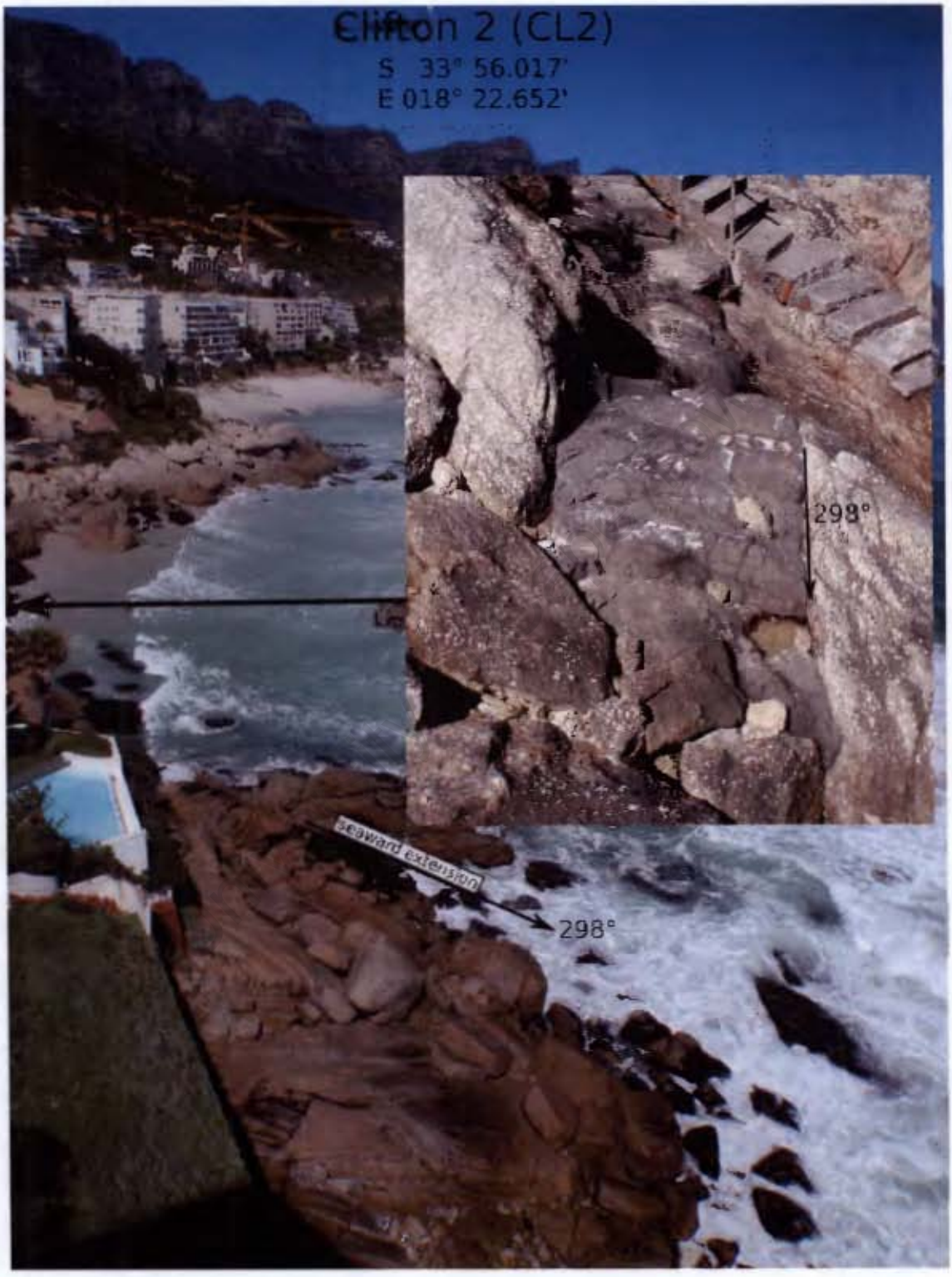

Figure 3.7: Clifton 2 dyke cutting through Cape Granite and extending seaward.

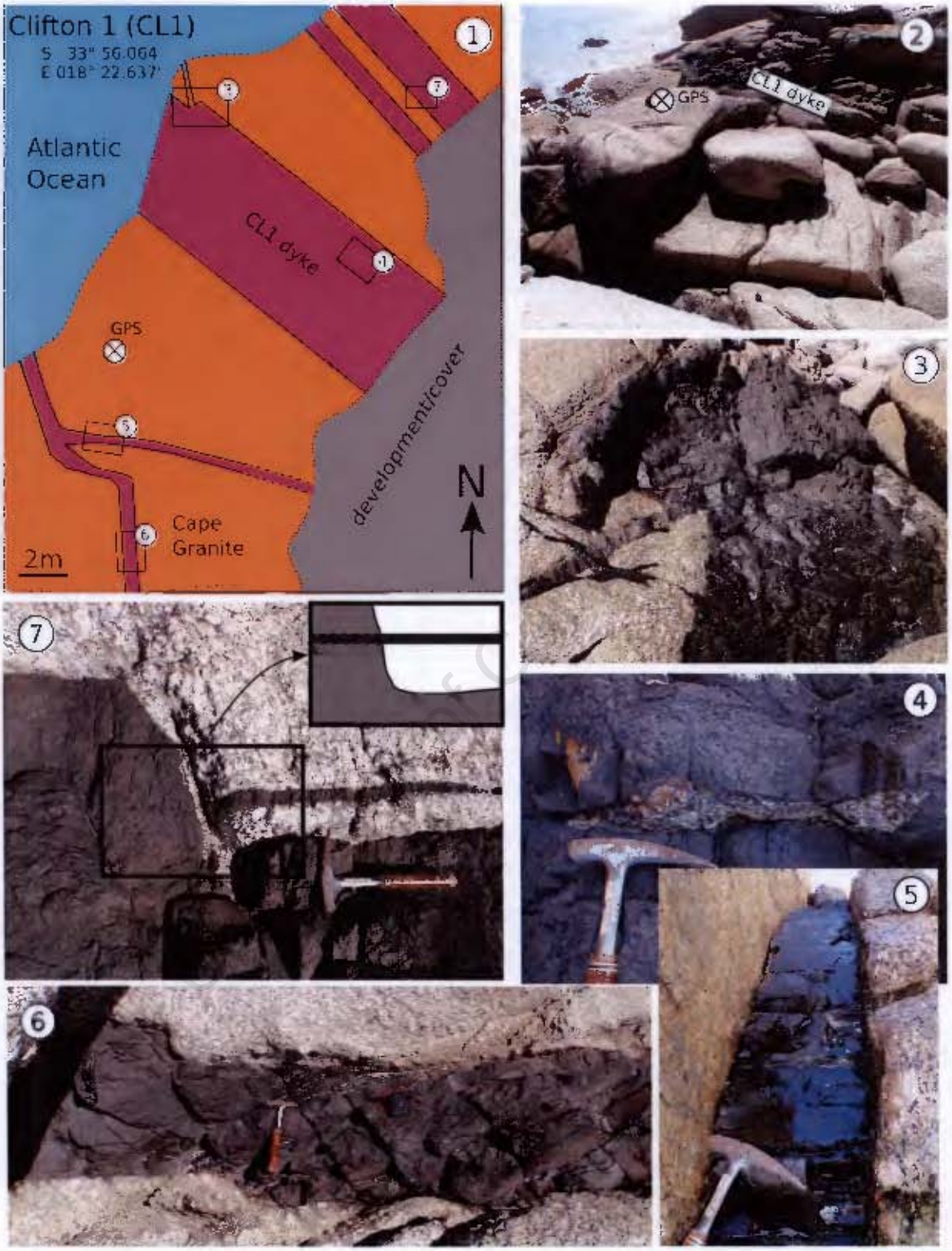

Figure 3.8: Clifton 1 dyke. [1] Sketch of outcrop area showing dyke network around CL1 dyke; [2] picture of CL1 taken from [6] and showing position of GPS co-ordinates; [3] minor dyke off-shoot; [4] granite xenolith; [5] sharp contact and negative profile of dyke cutting Cape Granite; [6] north-south striking minor dyke south of CL1 with non-perpendicular joints in dyke; [7] stringer dyke parallel to larger dyke with cryptic intrusive relation to the other dyke.

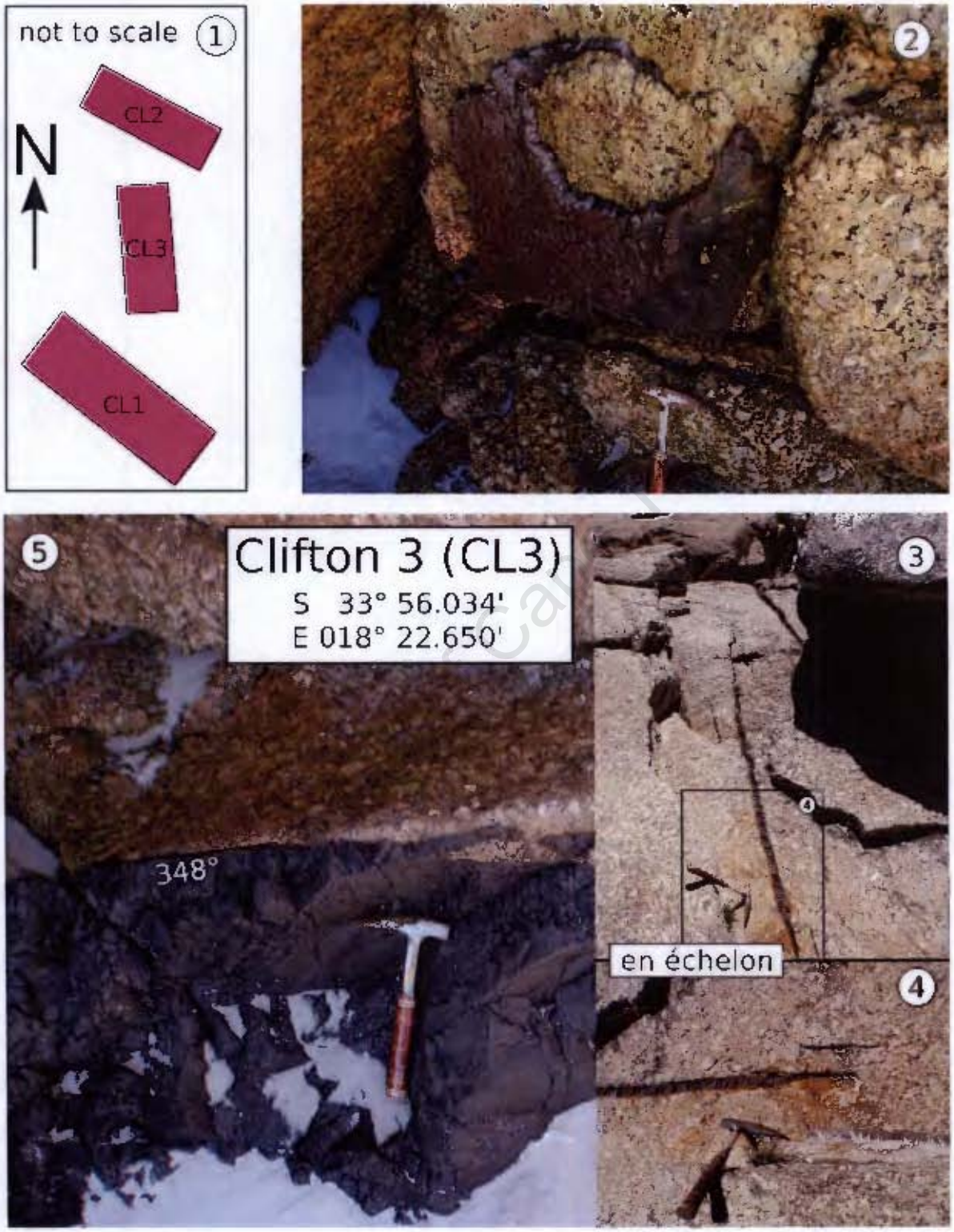

Figure 3.9: Clifton 3 dyke. [1] Sketch of Clifton area showing the relative orientations of the dykes, map is not drawn to scale; [2] anastomozing dyke incorporating granite slabs; [3 - 4] en-echelon pattern of smaller dykes; [4] main CL3 dyke outcrop, mostly covered by beach sand.

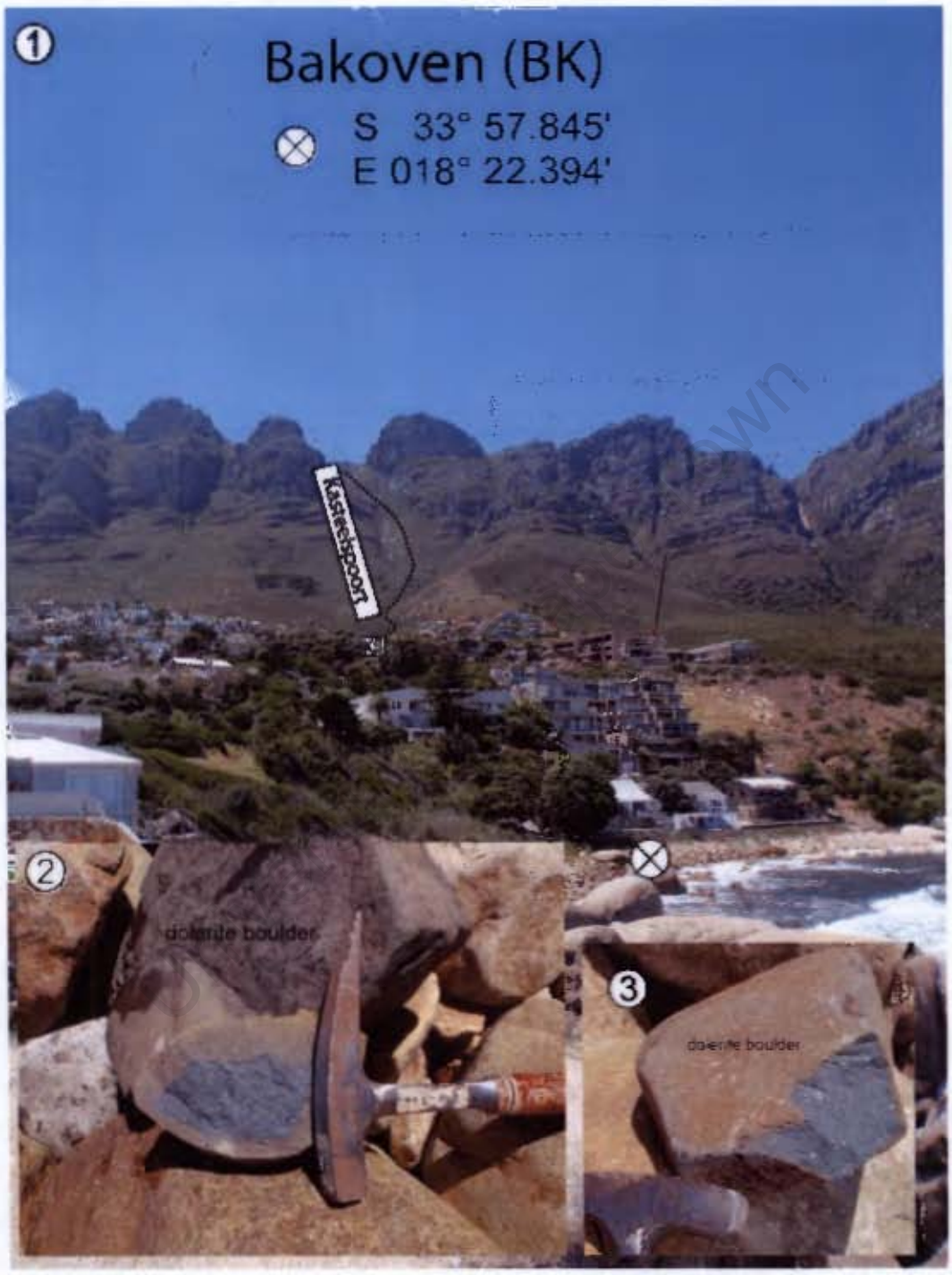

Figure 3.10: Bakoven dyke. [1] View of Bakoven Beach and the Kasteelspoort Ravine with the KS dyke outcrop indicated (Figure 3.11); [2 and 3] Dolerite boulders found on the pebble-boulder beach.

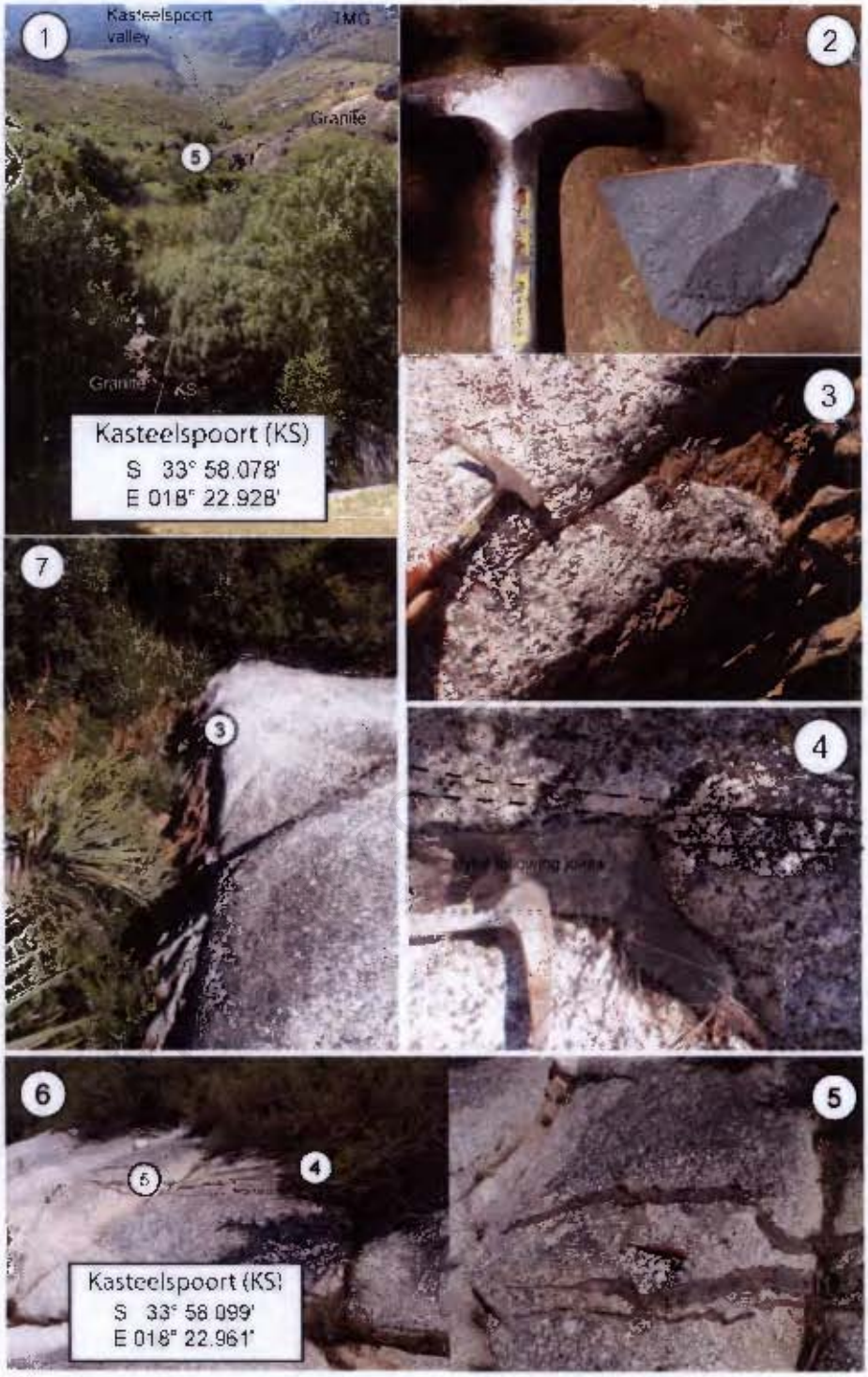

Figure 3.11: Kasteelspoort dyke. [1] Roadside outcrop of dyke in a ravine with the Kasteelspoort Valley shown in the background; [2] dark fresh dolerite sample; [3] small offshoot and [4] minor dyke intruding along joints and deviating into conjugate joint; [5] anastamozing minor dyke network parallel to main dyke; [6] granite pavement hosting dolerite dyke with GPS co-ordinates given; [7] Outcrop and northern contact of main 7 m wide Kasteelspoort dyke.

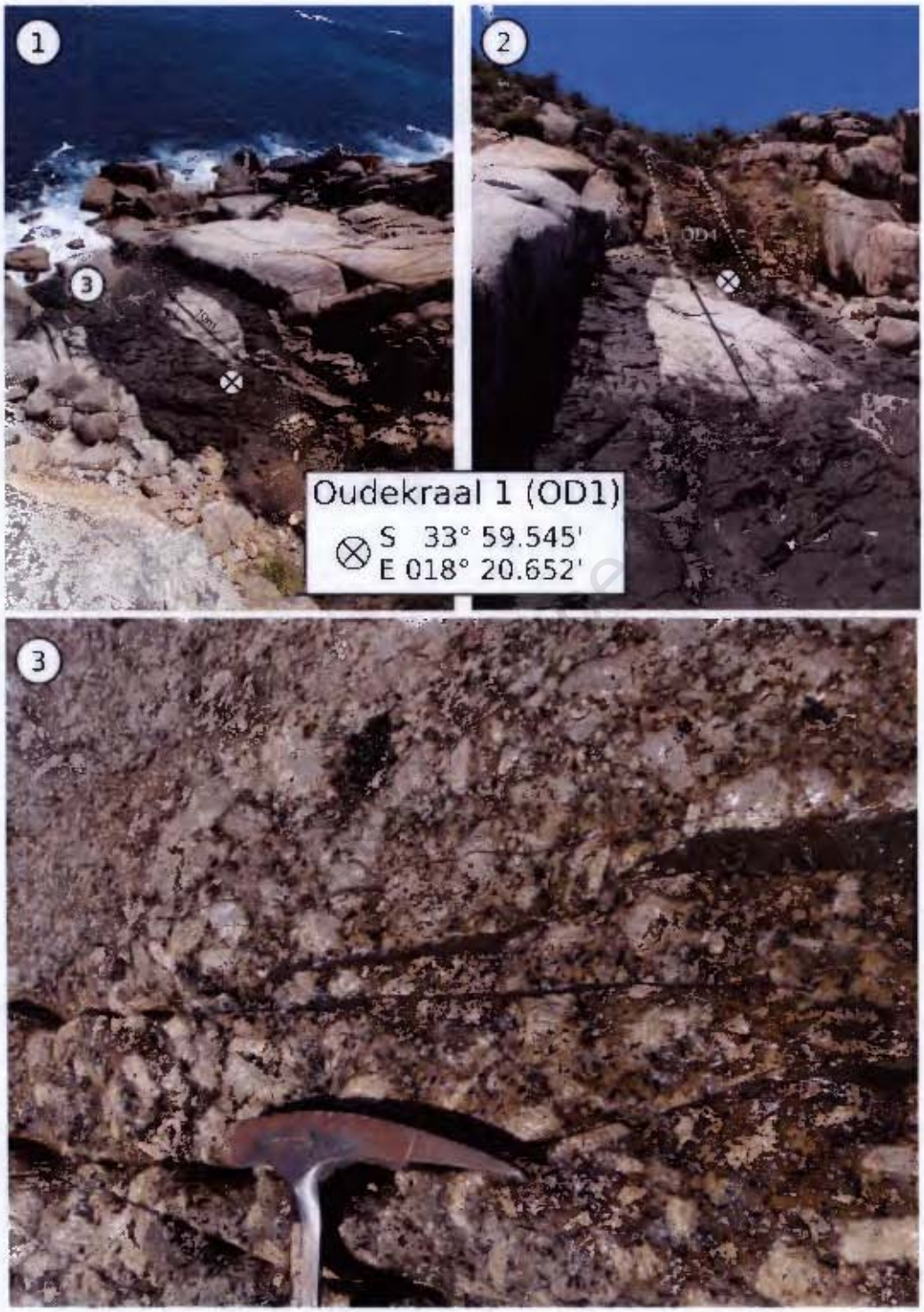

Figure 3.12: Oudekraal 1 dyke. [1] Looking northwest towards seashore outcrop down from granite cliff along Victoria Road; [2] looking up (east) towards road showing large granite 10 m xenolith and vertical extension of dyke indicated by dotted white line; [3] minor dykes following joints in lower granite xenolith.

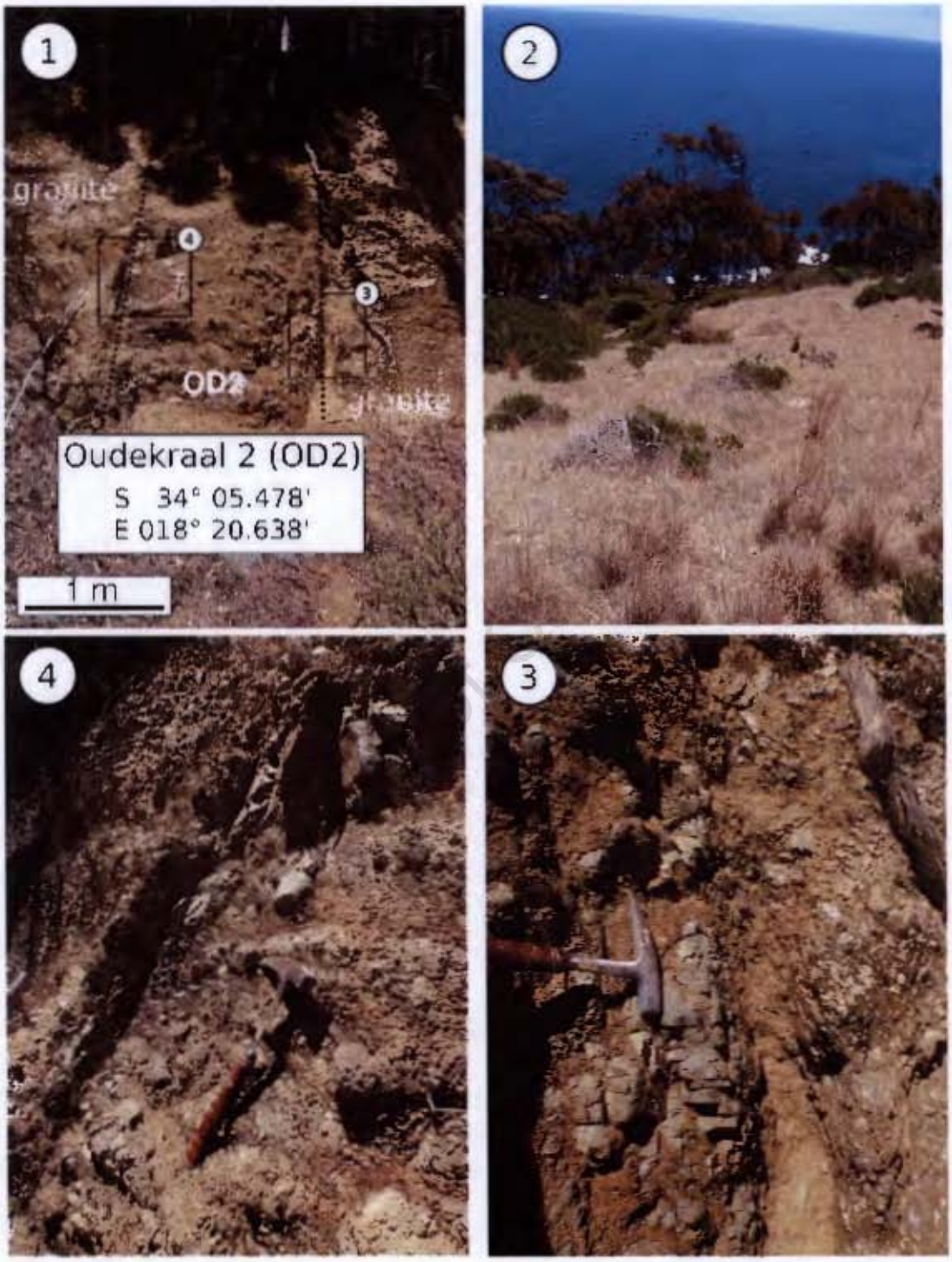

Figure 3.13: Oudekraal 2 dyke. [1] Weathered road-side outcrop in weathered Peninsula Granite; [2] looking west along strike down scree slope towards Atlantic Ocean, where no outcrops of the dyke are found; [3] southern contact with granite; [4] northern contact with granite.

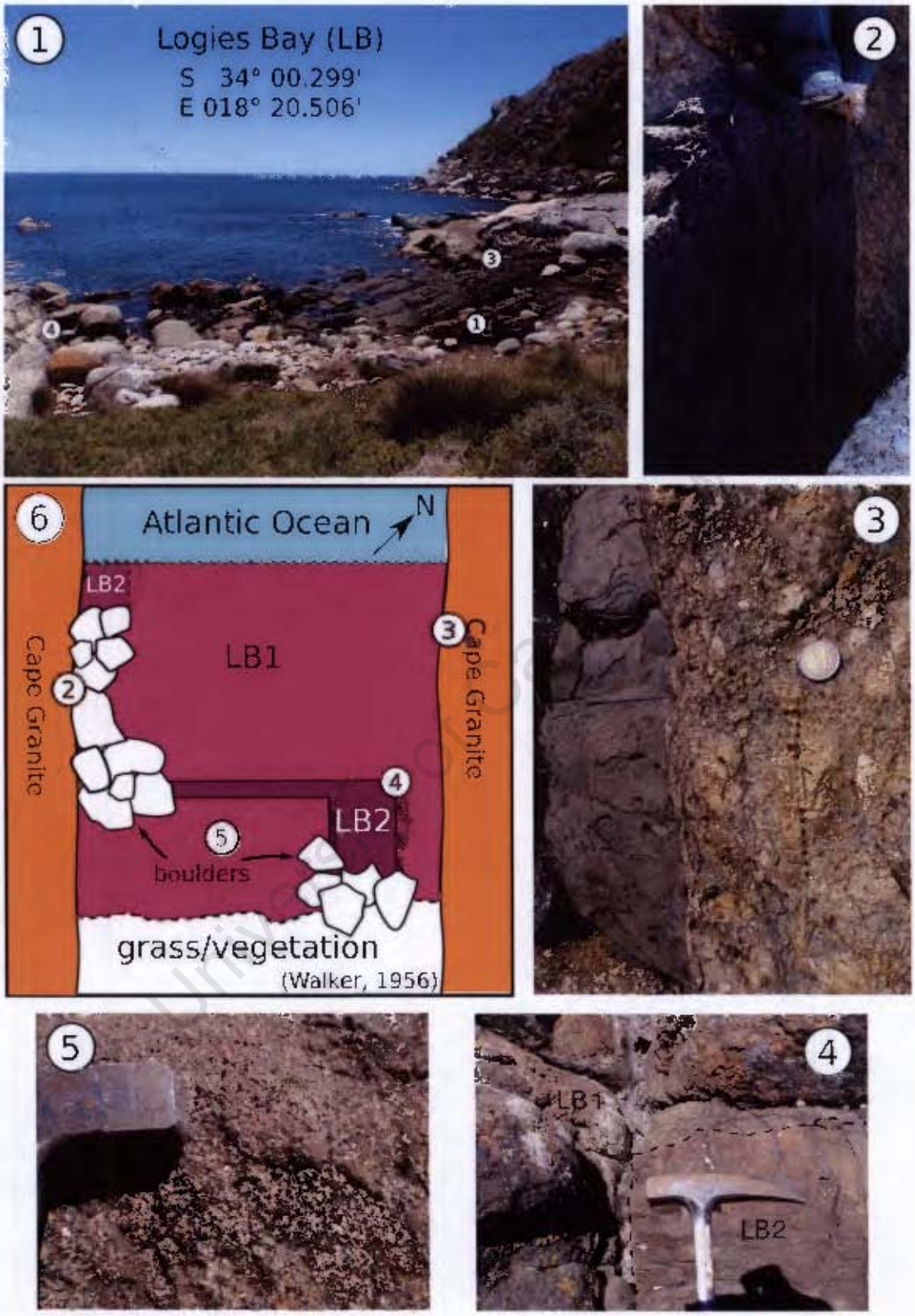

Figure 3.14: Logies Bay 1 & 2 dykes. [1] Logies Bay dyke outcrop north of Llandudno Beach; [2] chilled margin on southern dyke edge; [3] northern contact with granite showing sinistral strike slip shear fracture with fracturing of alkali-feldspar phenocryst; [4] LB1 and LB2 contact; [5] coarse grained nature of LB1; [6] Map of Logies Bay adapted from Walker (1956) with the addition of a further LB2 outcrop (marked with a dotted line) in western corner of the LB1 outcrop.

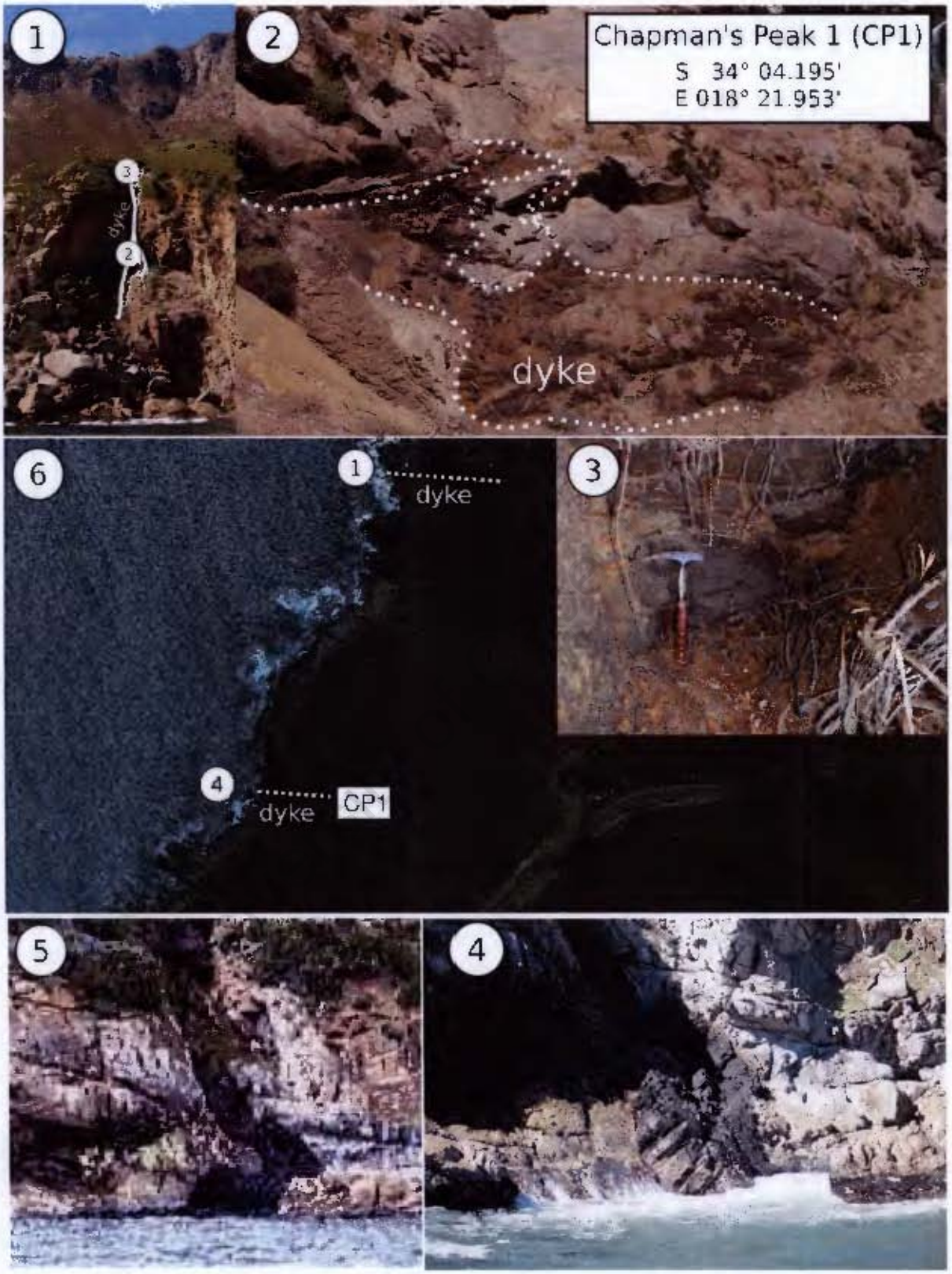

Figure 3.15: Chapman's Peak. [1] View of a dyke from boat in Hout Bay; [2] looking down from northern cliff alongside dyke showing bifurcation; [3] sharp contact of dyke with Peninsula Granite ; [4 and 5] original photographs by D L Reid and J Rogers showing the CP1 dyke outcrop from a the sea. Note: photographs show two different dykes - 1,2,3 and 4,5; [6] Google Earth image showing relative position of CP1 [4] dyke and additional dyke shown in [1].

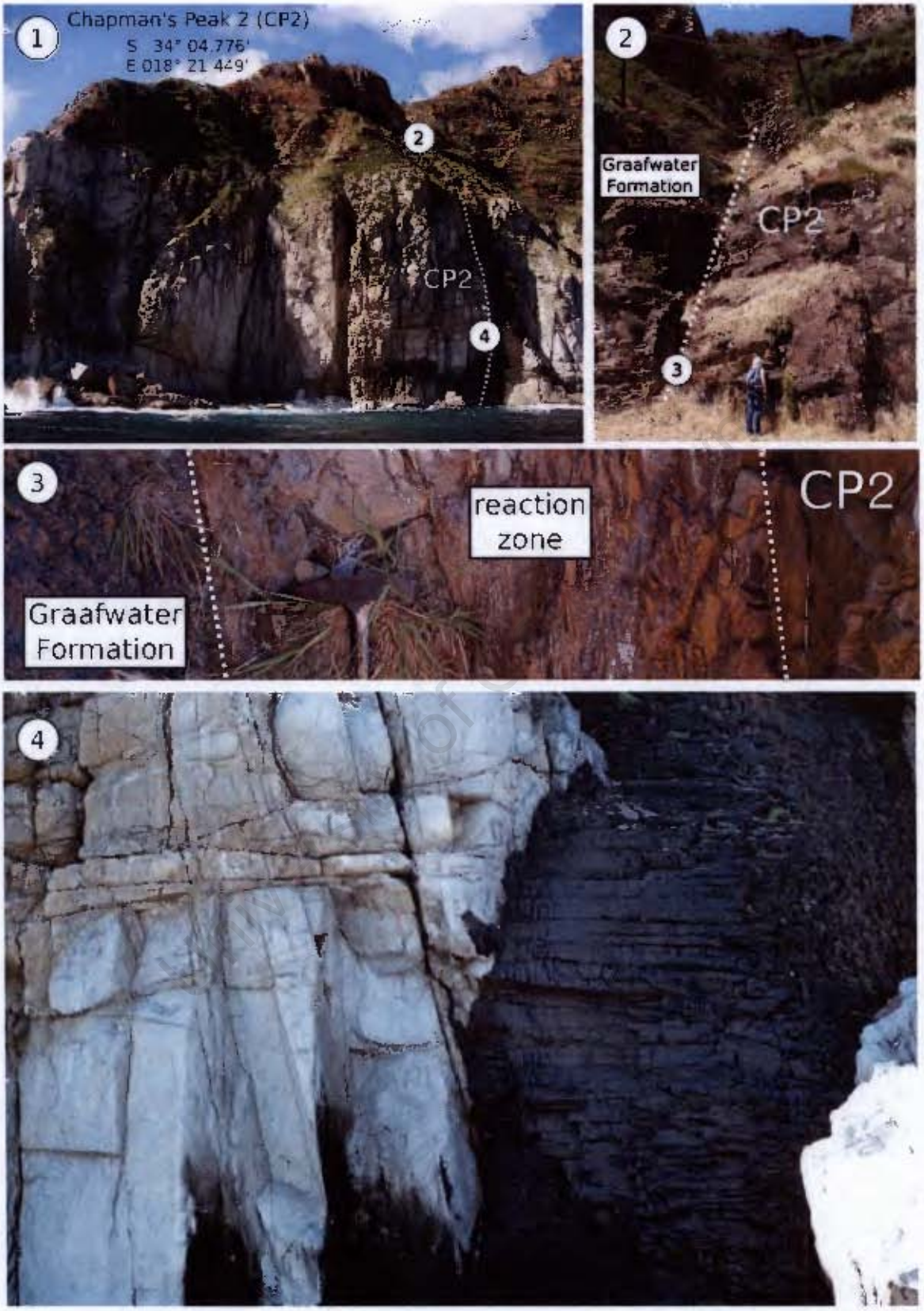

Figure 3.16: Chapman's Peak 2 dyke. [1] View of the dyke from a boat below the main view point on Chapman's Peak Drive; [2] road-side dyke outcrop in Graafwater Formation country rock; [3] northern contact of dyke with alteration zone in adjacent Graafwater Formation; [4] photo of dyke outcrop in the Peninsula Granites, courtesy of D I. Reid (2001, link: http://web.uct.ac.za/depts/geolsci/dlr/106s_01/index.html).

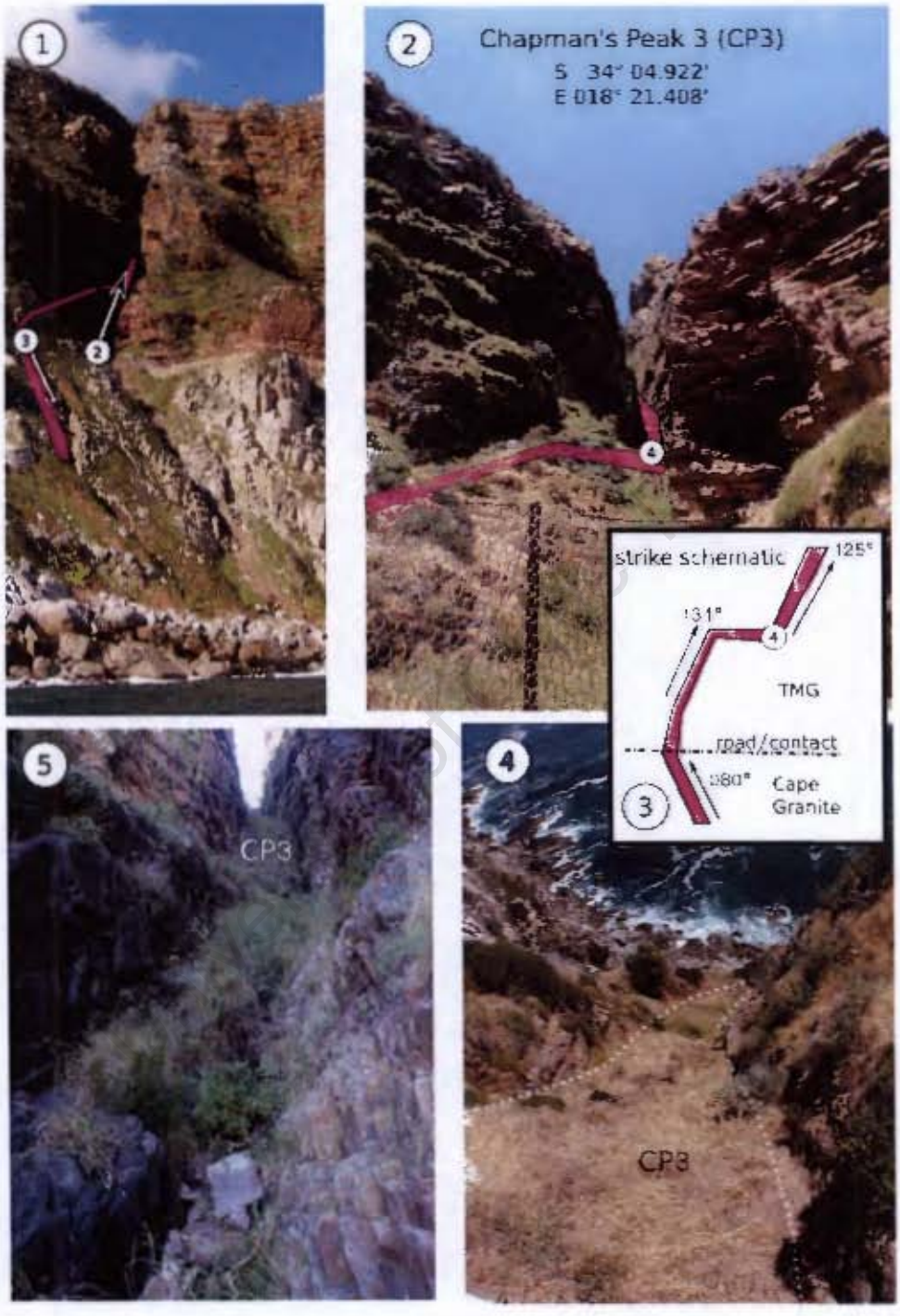

Figure 3.17: Chapman's Peak 3 dyke. [1] View of dyke from boat below Chapman's Peak Drive; [2] view of dyke cutting through the Graafwater Formation into the Peninsula Formation; [3] schematic figure of dyke outcrop pattern showing strike variations; [4] looking down to ocean from road at dyke extension; [5] dyke outcrop in kloof.

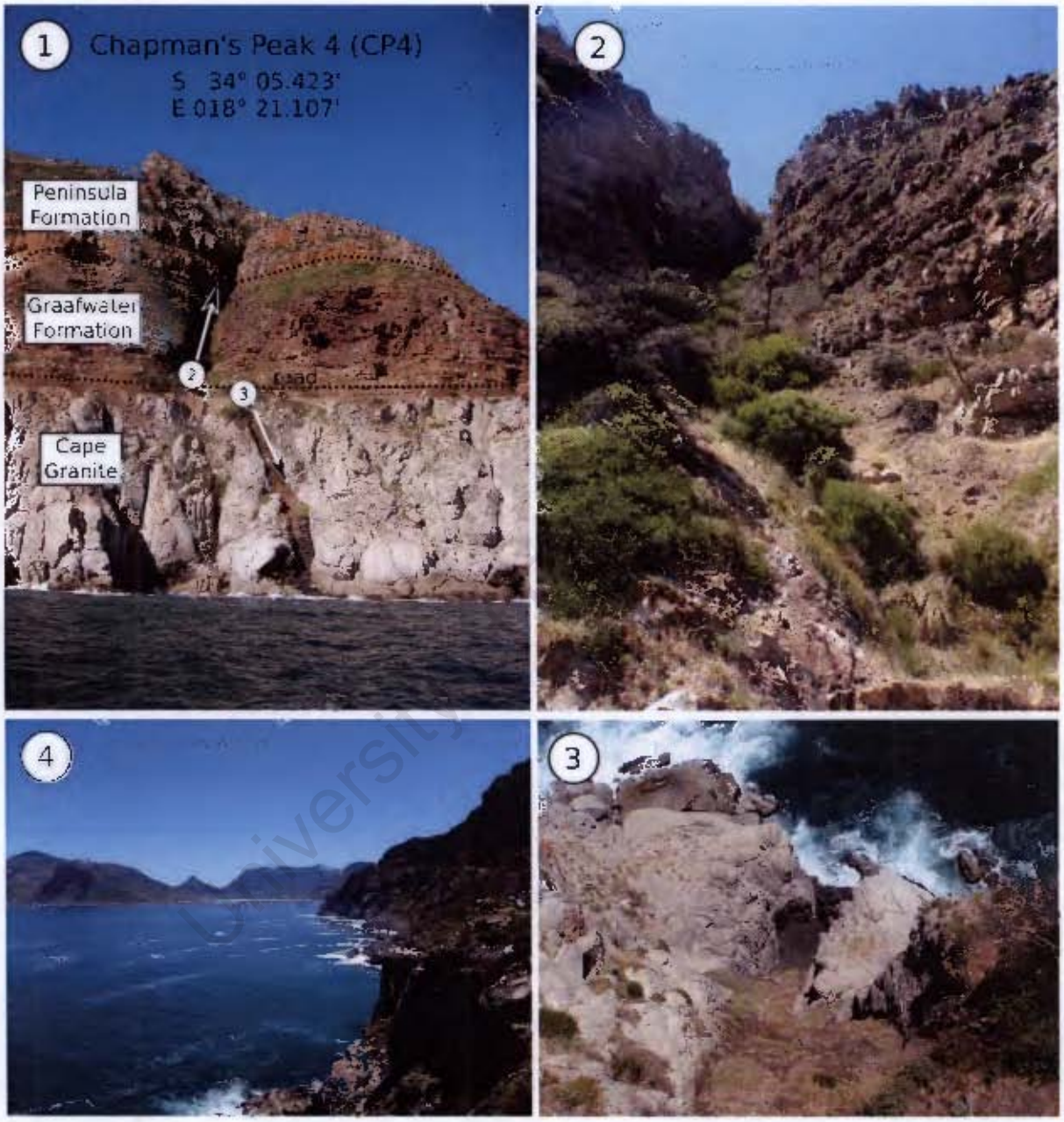

Figure 3.18: Chapman's Peak 4 dyke. [1] View of dyke from boat below Chapman's Peak Drive; [2] densely vegetated kloof occupied by the dyke cutting through the Table Mountain Group sandstones; [3] view down from road of dyke intruding the Peninsula Granite; [4] view of Hout Bay and Chapman's Peak Drive from the CP4 locality.

Figure 3.19: Chapman's Peak 5 dyke. [1] View of Chapman's Peak Drive from the Sentinel Mountain showing location of dykes CP2 through CP5; [2] fresh dolerite sample; [3] contact of dolerite with granite; [4] road cut outcrop of CP5 cutting both Cape Granite and Graafwater Formation with the southern end covered in shock-crete; [5] photo of pre-shock-crete covered dyke with person for scale, courtesy of D L Reid.

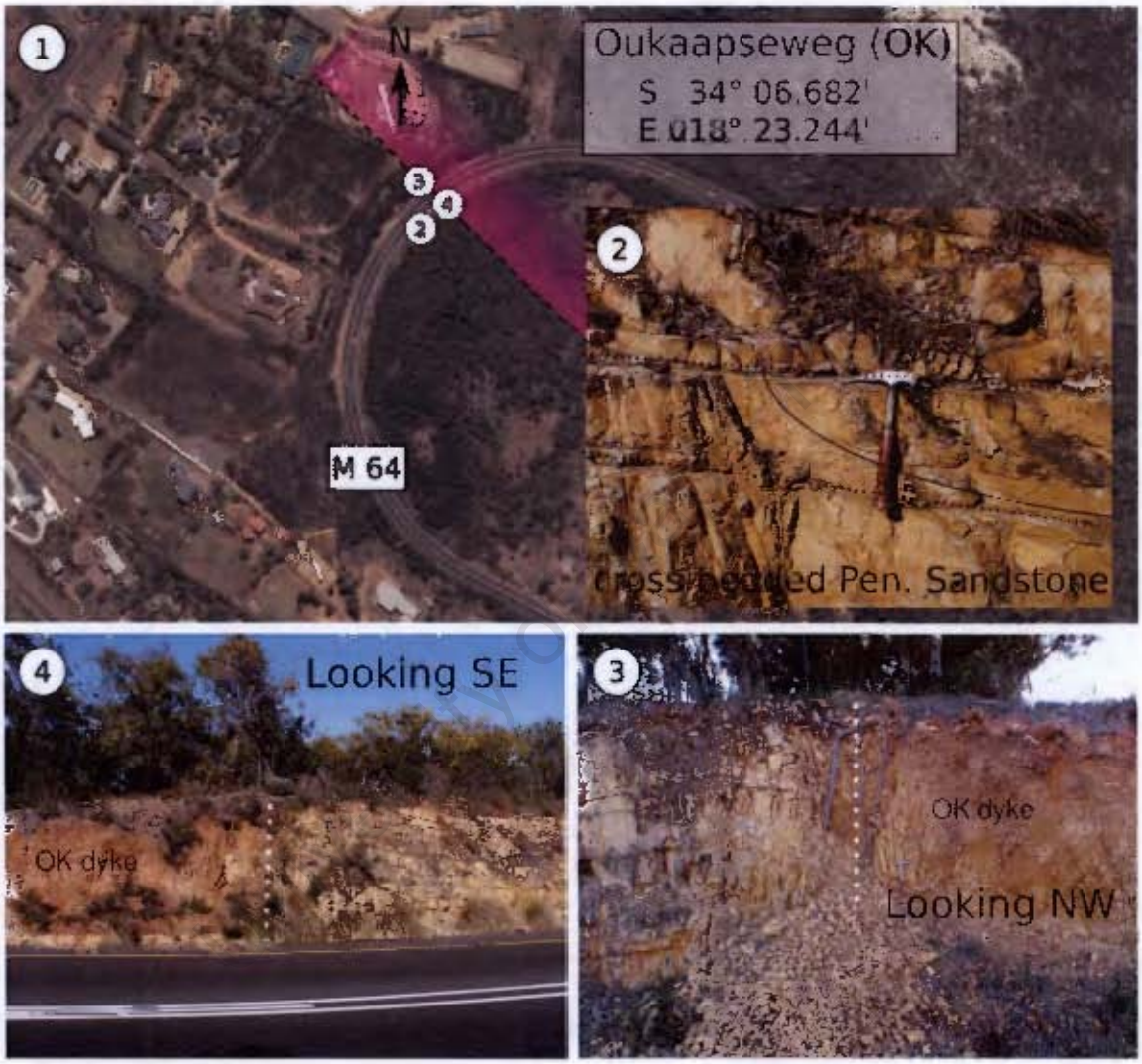

Figure 3.20: Oukaapseweg dyke. [1] Google Earth image of the OK outcrop area and the development northwest of the M64 road where the dyke samples were collected; [2] Peninsula Formation country rock with cross-bedding; [3 and 4] road cuts showing southern dyke contact and highly weathered nature of the dolerite.

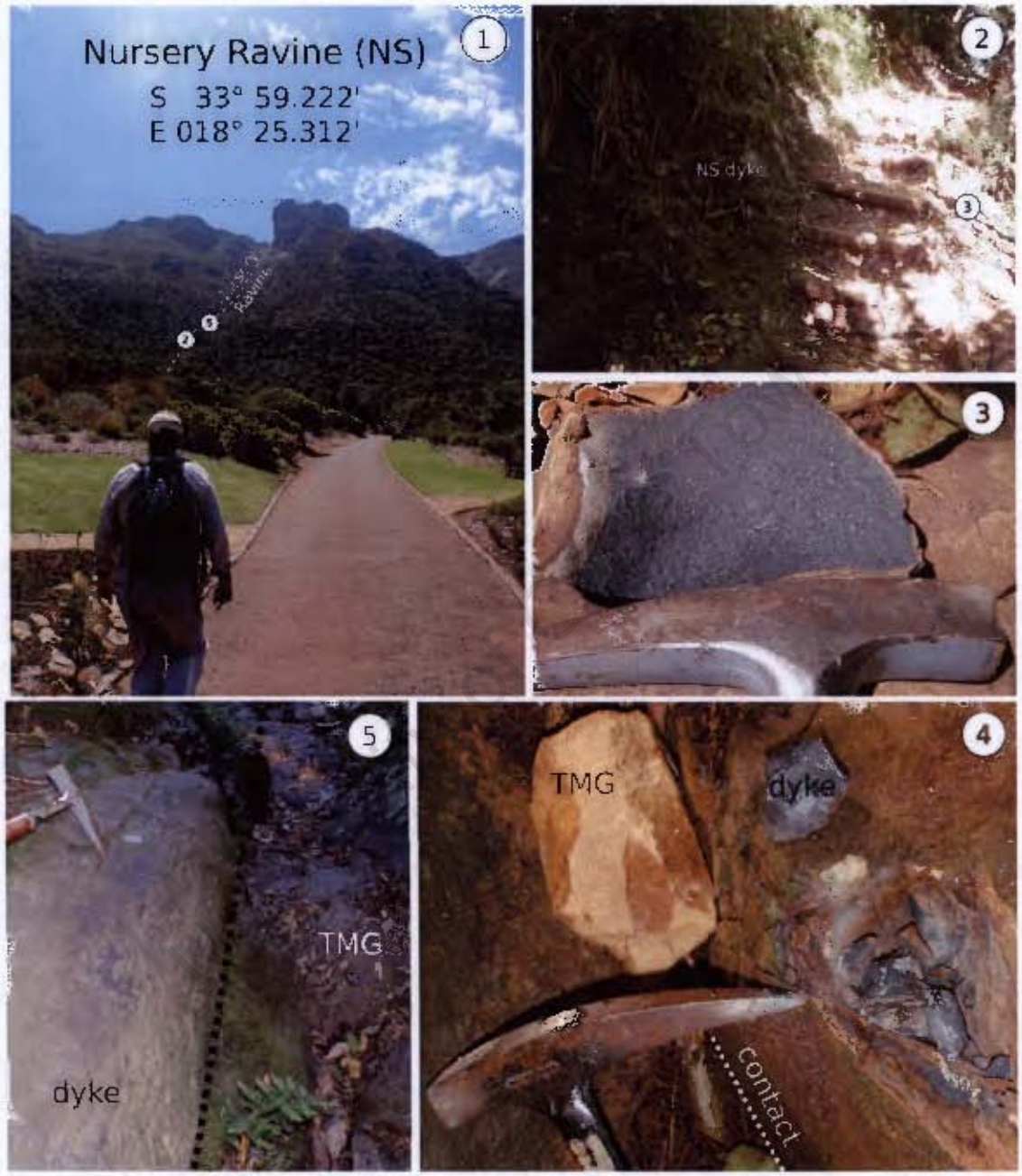

Figure 3.21: Nursery Ravine dyke. [1] Picture taken looking west towards Nursery Ravine from Kirstenbosch Gardens; [2] weathered dyke outcrop alongside contour path; [3] fresh dolerite sample; [4] contrast between dolerite and sandstone when weathered rocks are split to fresh surfaces; [5] contact with Peninsula Formation of the Table Mountain Group (TMG)

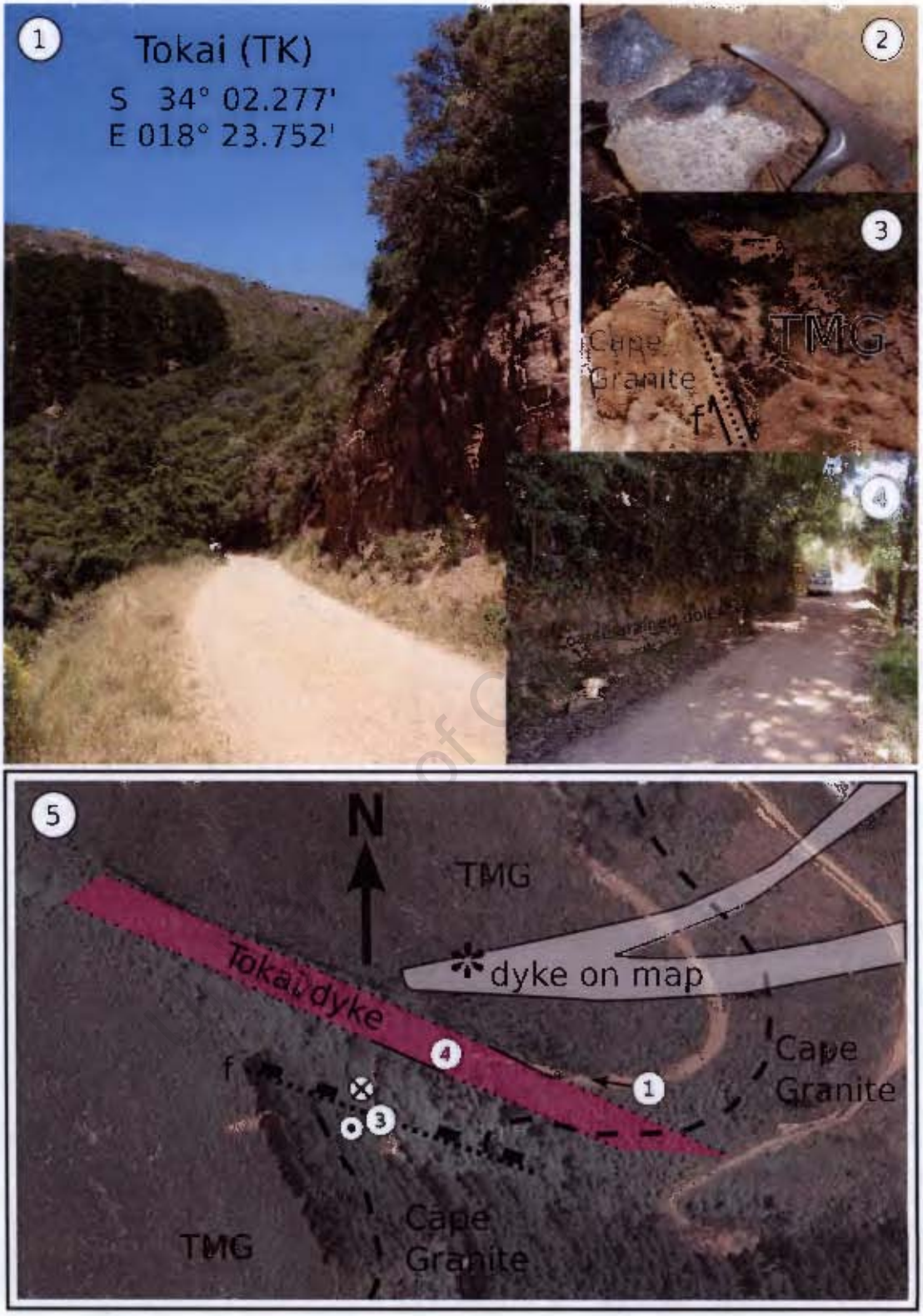

Figure 3.22: Tokai dyke. [1] Picture taken looking west back towards dyke outcrop on path up Constantiaberg; [2] fresh coarse grained dolerite dyke sample; [3] normal fault and estimation of fault orientation is shown in [5] by normal fault symbol; [4] weathered dyke outcrop adjacent to road; [5] Google Earth image showing location of dyke as mapped in this study (pink); * white highlighted area is the dyke outcrop as depicted on the geological map of Cape Town (Theron, 1984).

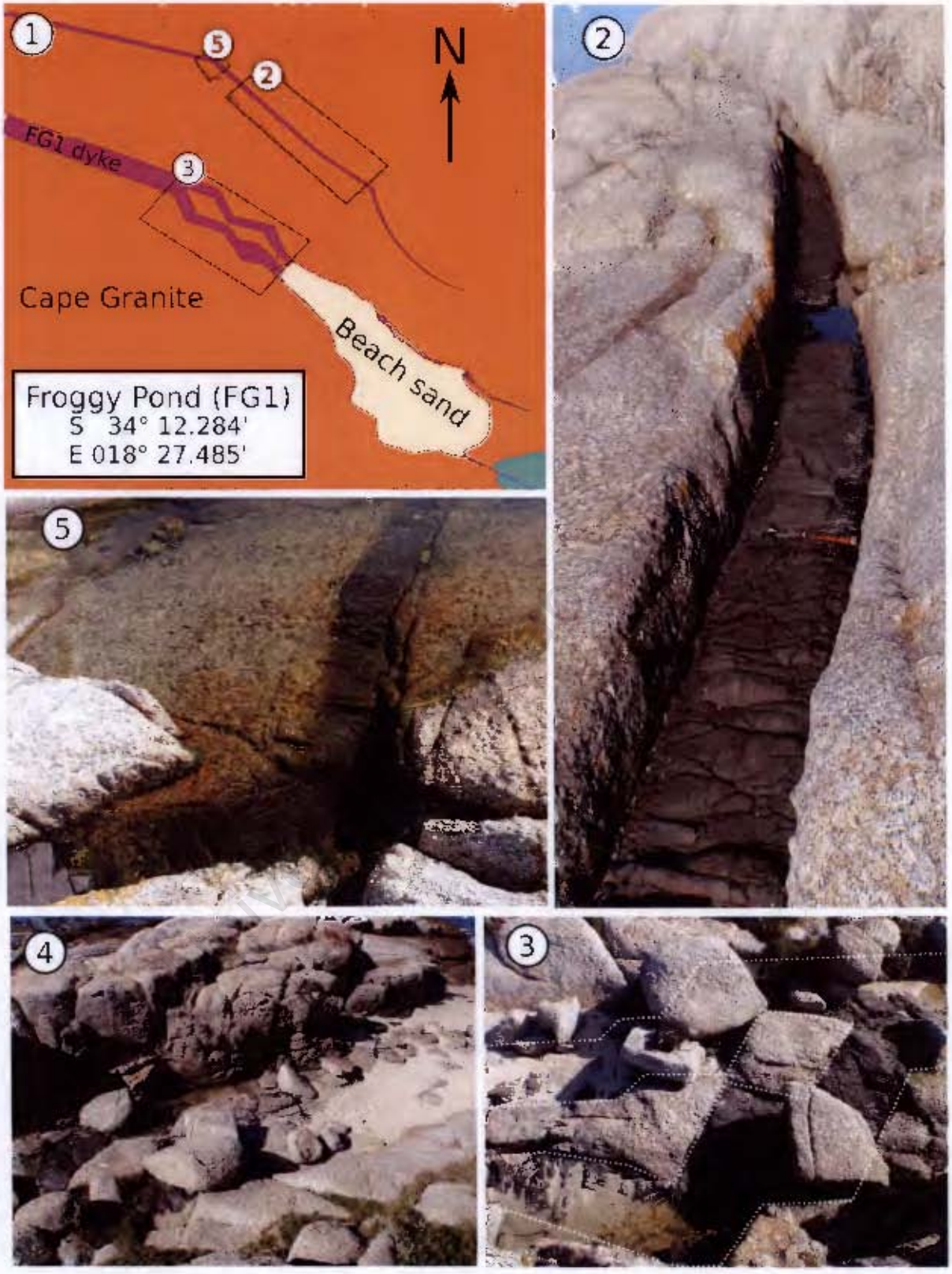

Figure 3.23: Froggy Pond dyke. [1] Sketch map of dykes at Froggy Pond, showing the dyke that was sampled (FG1); [2] minor parallel dyke pinching out in Peninsula Granite country rock; [3] looking southwest at main FG1 dyke with granite xenolith; [4] view opposite to [3], i.e. picture orientated northeast, showing joint pattern in granite country rock; [5] bend/kink of dolerite dyke and parallel joints in granite.

Figure 3.24: Outland Point dyke. [1] Picture of the dyke outcrop in the Peninsula Granite at sea level; [2] felsic veining in granite, which is also cut by the dolerite dyke; [3] Google Earth image showing location of FG1 and FG2 and relative orientations of dykes.

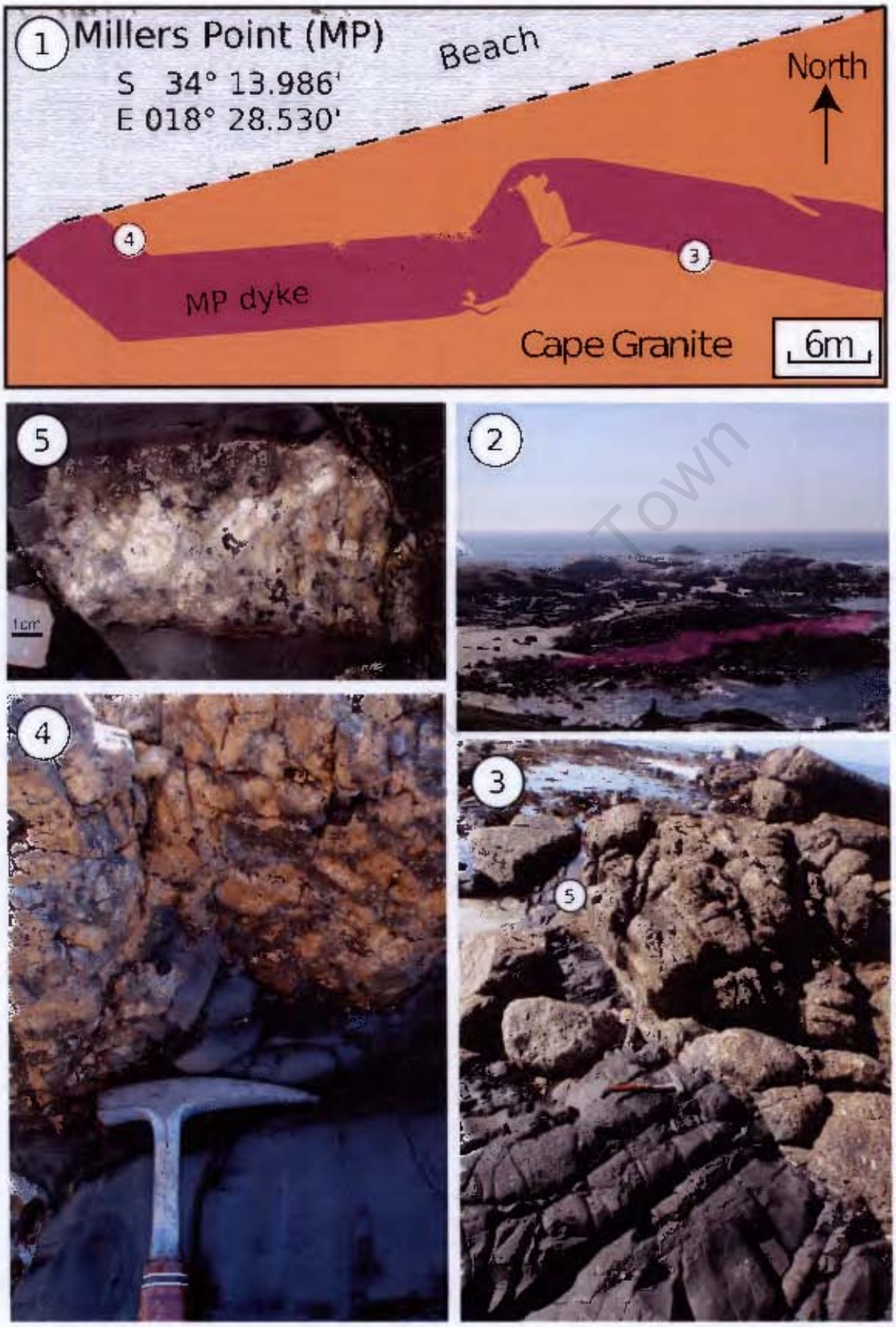

Figure 3.25: Millers Point dyke. [1] Sketch map of the MP dyke; [2] photo view of dyke from parking area highlighting the dyke outcrop below the high tide level; [3] southern contact of dyke with granite country rock, looking east out towards False Bay; [4] quench texture of dolerite at dyke margin; [5] fresh and unaltered granite xenolith block in dolerite.

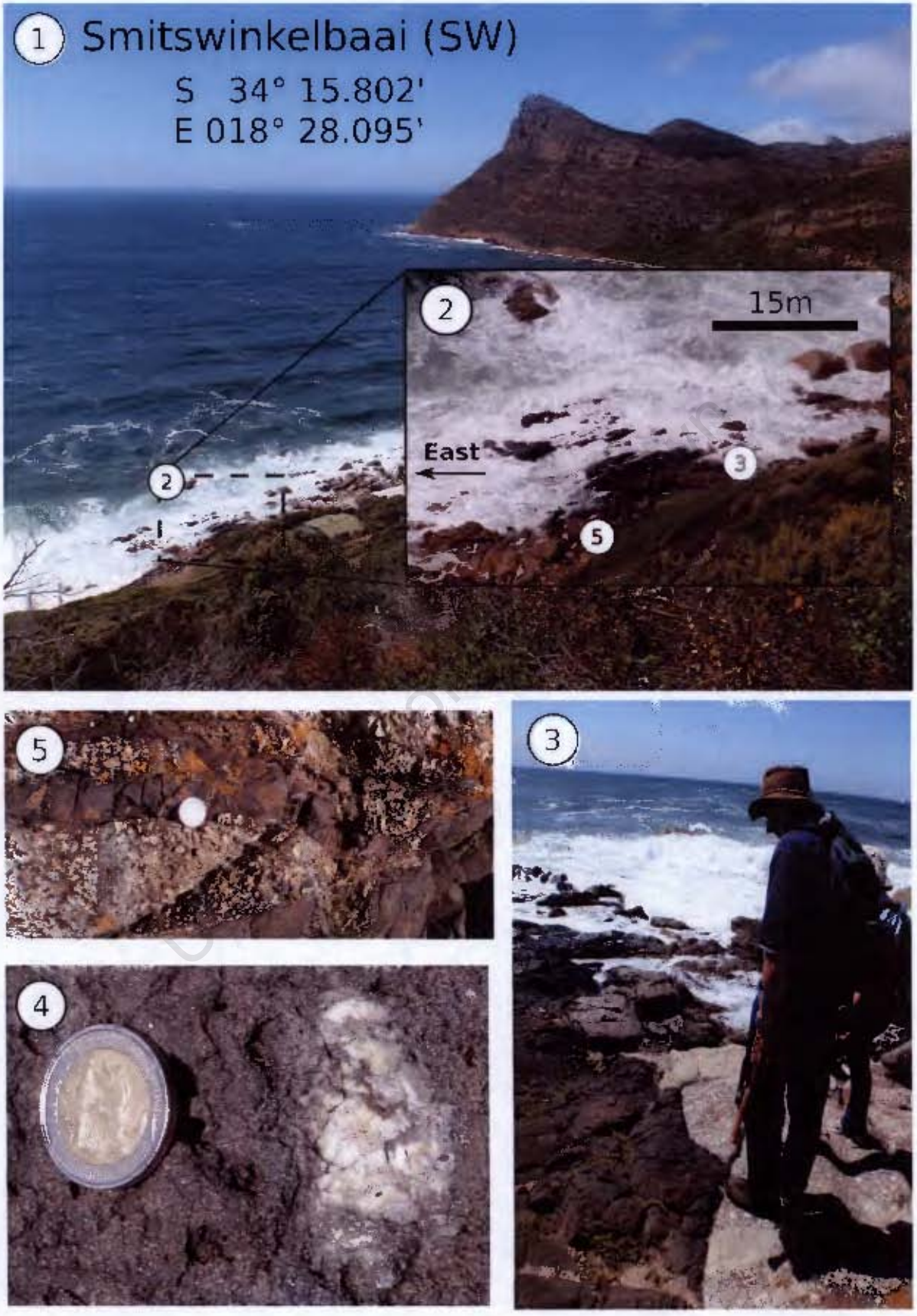

Figure 3.26: Smitswinkelbaai dyke. [1] View of Smitswinkelbaai and False Bay from road leading to Cape Point; [2] approximately 18 m wide Smitswinkelbaai dyke; [3] southern contact with granite country rock; [4] example of a xenolith at Smitswinkelbaai (details shown in Figure 3.27); [5] small dyke off-shoots on northern contact - R5 coin for scale (*diameter* = 26*mm*).

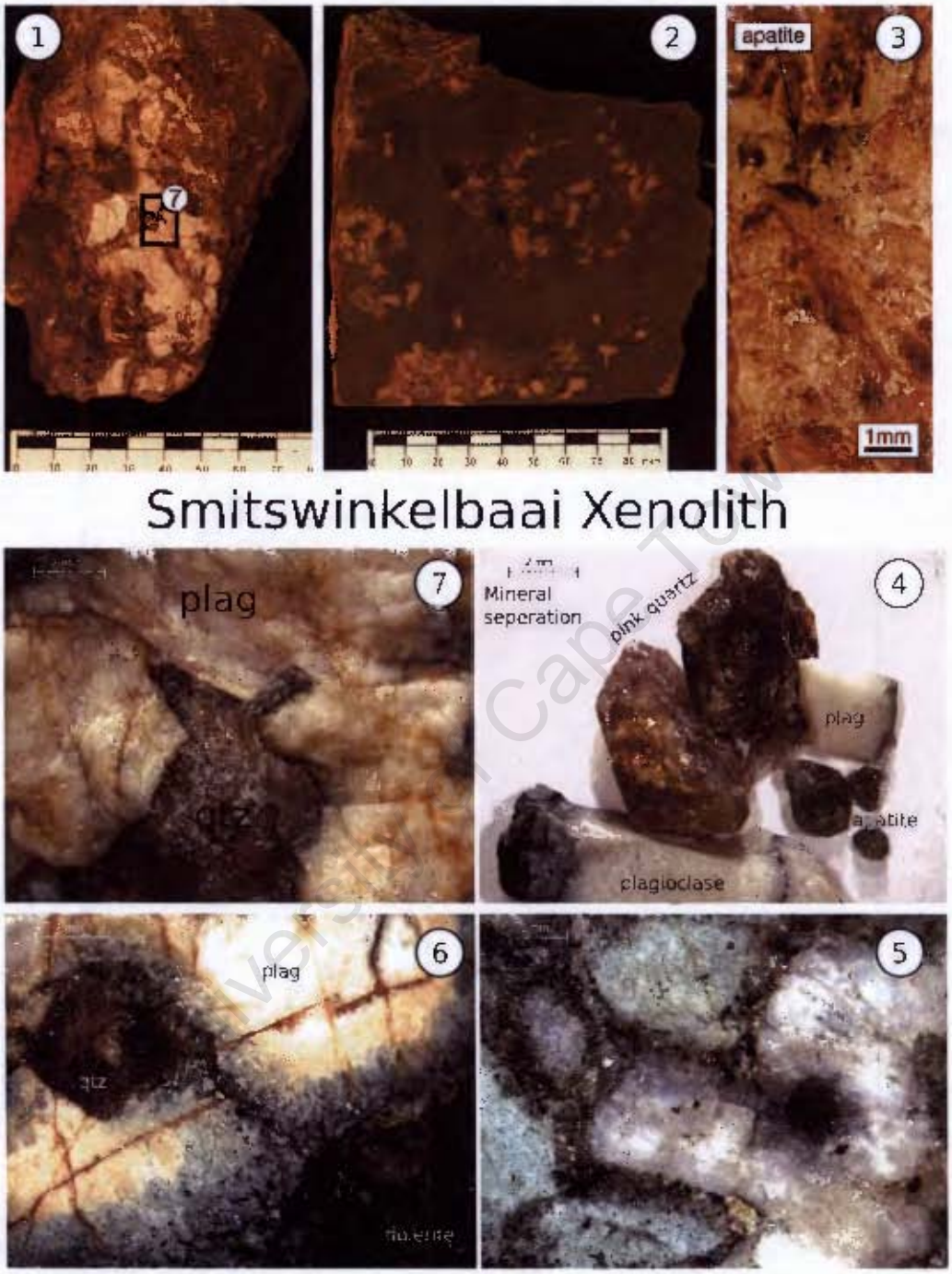

Figure 3.27: Coarse grained tonalite xenolith in Smitswinkelbaai dyke. [1] Xenolith with reaction rims developed between individual grains; [2] disaggregation of xenolith and isolation of individual minerals as xenocrysts; [3] pink quartz with green apatite grain; [4] mineral separates of pink quartz (qtz), plagioclase (plag) and green apatite; [5] binocular microscope view of mineral contact highlighting rounded nature (scale bar = 1mm); [6] granitoid-dolerite contact; [7] reaction rim between quartz and plagioclase producing rounded shape of grains - (scale bar for [4], [6] and [7] = 2mm).

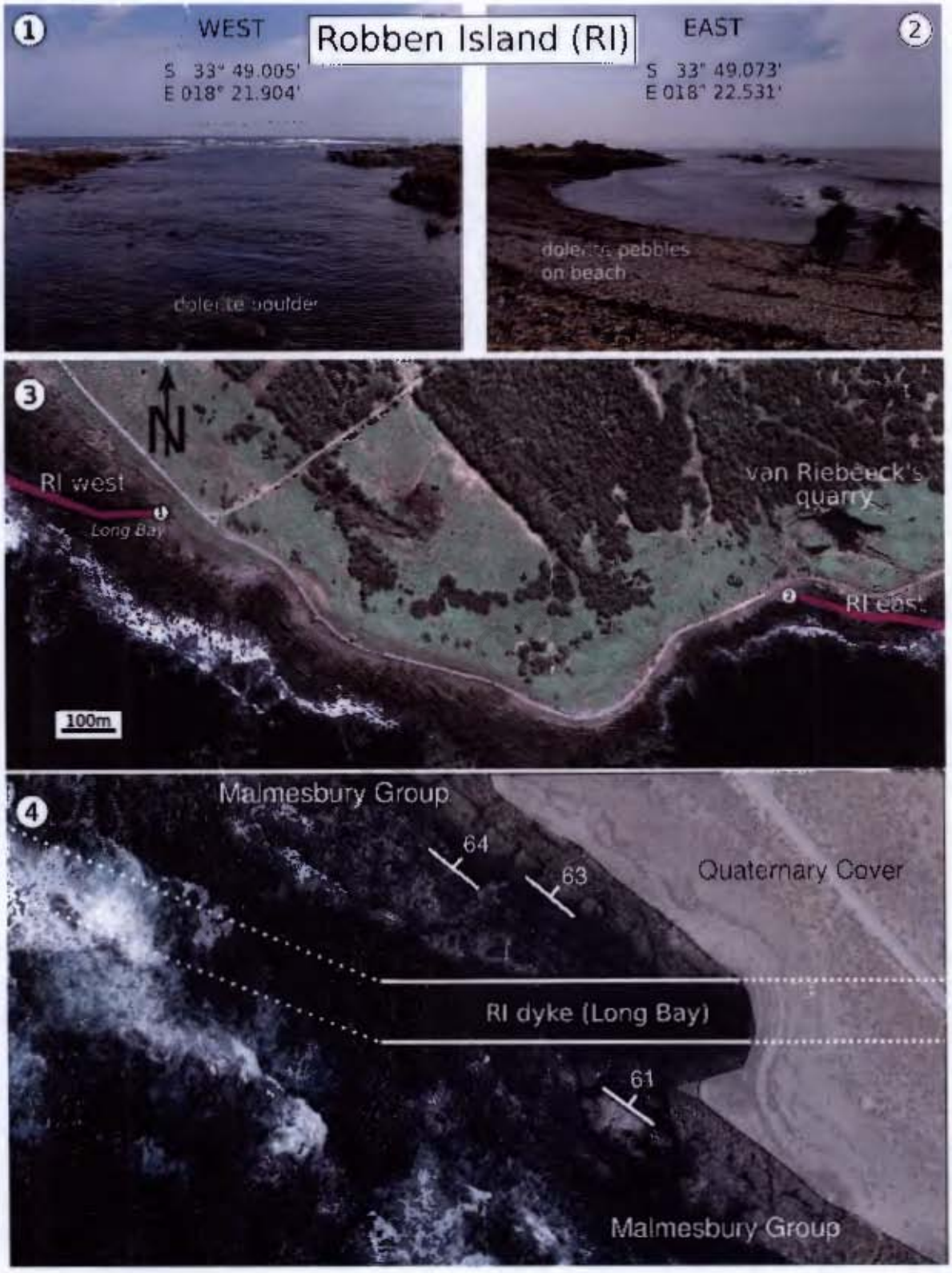

Figure 3.28: Robben Island dyke. [1] Western extension of dyke; [2] eastern extension of dyke; [3] Google Earth image of the southern coast of Robben Island with dyke outcrops indicated; [4] image of Long Bay (National GeoSpatial Information Imagery, 2008), showing western dyke cutting Malmesbury Group structure (structural data from Rowe et al., 2010).

Chapter 4

Petrography and Mineralogy

The petrography and mineralogy of the False Bay dykes were initially investigated by Butt (1989), Hirschel (1989) and Wulfse (1989) (Honours projects at UCT). This work was summarised and published by Reid (1990). The existing thin section collection was examined during this work with the addition of new samples from the Robben Island dolerite dyke (RI) and a summary of the petrography is presented in Table 4.1. The mineralogy of the dykes is typical of dolerites, consisting of fine to medium grained subophitic plagioclase (Figure 4.1-A) and clinopyroxene (Figure 4.1-B), with late stage skeletal octahedra of opaque Fe-Ti oxides (Figure 4.1-E), often as an anhedral interstitial matrix (Figure 4.1-F). Olivine is found in only the two widest dykes (Logies Bay and Tokai) in the coarse-grained interior (Figure 4.1-C) and is often highly altered (Figure 4.1-D).

The quenched margins contain few, if any, phenocrysts. Samples of the Oudekraal dyke (OD2) have a bimodal grain size distribution of equal proportions and contain phenocrysts of plagioclase (1.5 mm) and clinopyroxene (1 mm) set in a still identifiable matrix of plagioclase (0.25 mm) and clinopyroxene (0.1 mm). The phenocrysts in the quenched margins of dykes are commonly of similar grain size to the minerals developed in the interior. Coarser phenocryst phases are observed in a few dyke interiors (see Table 4.1) and these are predominantly plagioclase, with few examples of clinopyroxene phenocrysts and one dyke (LB2) showing olivine phenocrysts. Often the phenocrysts form glomeroporphyritic textures (occur in aggregates) and plagioclase phenocrysts are commonly zoned.

Figure 4.1: Photomicrographs of dyke mineralogy: A - plagioclase (plag); B - clinopyroxene (cpx); C - olivine (ol); D - partially altered olivine; E - Fe-Ti oxides with skeletal texture; F - interstitial Fe-Ti oxides; G - subophitic plagioclase and clinopyroxene inter-growth. A to D shown in PPL (top) and XPL (bottom) for same photomicrographs.

A distinct feature in the dykes is the presence of sub-rounded varioles, identified as amygdales. The presence of vesicles and amygdales in the False Bay dyke suite was reported by Walker (1956) and Reid (1990), which they interpreted to be indicative of a relatively shallow intrusion depth. Amygdales in the False Bay dolerites are clearly identified in specific samples, where the interior has preserved mineral phases of calcite and quartz (Figure 4.2). The quartz grains tend to be nucleated on the circumference of the varioles showing a growth pattern inward into the variole (Figure 4.2-C). This is best seen in a sample that was split into a fresh

Table 4.1: Summary of the False Bay dyke petrography, showing average grain size of mineral phases and extra notes for samples. nf = not found

#	Location	plagioclase	clinopyroxene	olivine	phenocrysts	phenocryst size	amygdales	amygale density	notes
1	SP	——	——	——	——	——	——	——	no thin section
2	CL2	0.5mm	0.25mm	nf	plag	2 - 4mm	0.5mm	very low	Elongated cpx grains and glomeroporpheritic
3	CL1	0.4mm	0.25mm	nf	plag & cpx	1mm	0.5mm	very low	interstitial quench texture
4	BK	0.6mm	0.6mm	nf	plag	1.5mm	1.5mm	low-med	interstitial quench texture
5	KS	0.6mm	0.6mm	nf	nf	——	1mm	med	——
6	OD1	0.3mm	0.2mm	nf	nf	——	1mm	med	——
7	OD2	1.5 & 0.25mm	1 & 0.1mm	nf	nf	——	0.4mm	med	bimodal grain size
8	LR	0.25mm	0.1mm	nf	plag & cpx	1.3mm	no	——	octahedral and hexagonal opaqued
9	LB1	3 4mm	2mm	1mm	nf	——	0.5mm	very low	low frequency, coarse grained opaques
9	LB2	1mm	0.4mm	nf	olivine	1.5mm	1mm	high	——
10	SB	1.5mm	0.5mm	nf	plag	3mm	0.5mm	med	green pleochroic amphiboles
11	CP1	1mm	0.5mm	nf	nf	——	1mm	high	interstitial quench texture
12	CP2	1mm	0.25mm	nf	plag & cpx	1 - 1.5mm	0.5mm	low-med	——
13	CP3	1.5mm	0.7mm	nf	nf	——	0.8mm	med	——
14	CP4	0.4mm	0.5mm	nf	nf	——	0.6mm	low	——
15	CP5	0.4mm	0.25mm	nf	cpx	2mm	1.5mm	very high	up to 2mm long cpx needles
16	OK	0.88mm	0.3mm	nf	plag	2 - 4mm	0.8mm	low	quartzite xenolith
17	NS	1mm	0.5mm	nf	nf	——	0.4mm	med	devitrified glassy matrix
18	TK1	1mm	0.4mm	nf	plag	1.5mm	0.8mm	med-high	relatively opaque poor
19	TK2	3.5mm	1.5mm	0.5mm	nf	——	nf	——	gabbroic grain sizes
20	FG1	0.8mm	0.13	nf	plag	1.5mm	0.5mm	low	strongly bimodal plag texture
21	FG2	1mm	0.4mm	nf	nf	——	nf	——	interstitial quench texture
22	MP	1.5mm	0.2mm	nf	nf	——	1.5mm	med	quartz xenocryst
23	SW	1mm	0.8mm	nf	nf	——	1mm	low	tonalite xenoliths
24	RI	3mm	1.5mm	nf	nf	——	0.4mm	low	coarse cpx grains with elongated habit

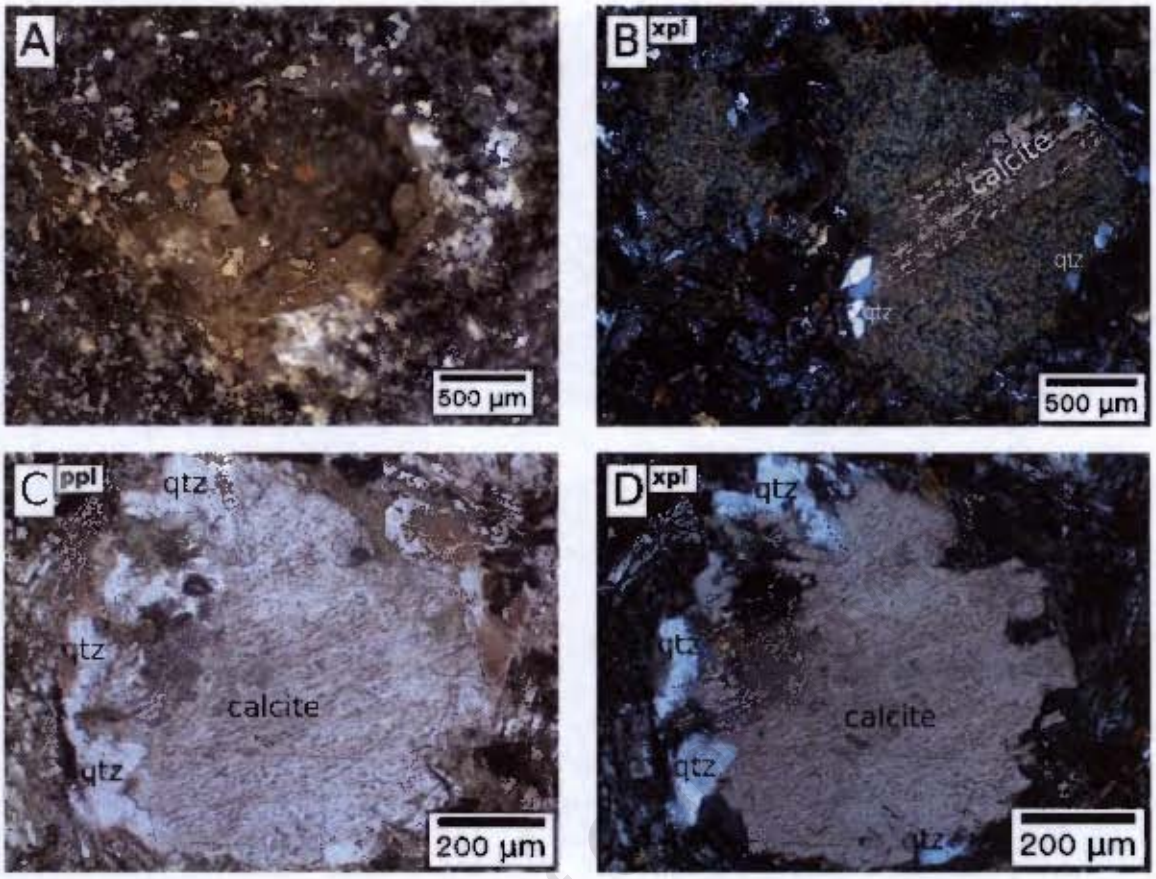

Figure 4.2: Photomicrographs of quartz and calcite filled amygdales found in the dolerites dykes: A - hollow vesicle with quartz crystals growing inward from the circumference; B - altered amygdale with calcite and few quartz grains; C - plain polarised light (PPL) photomicrograph of amygdale; D: cross-polarised light (XPL) of C.

surface and showed an open central void with quartz grains around the circumference (Figure 4.2-A). In field exposures, many amygdales are seen as preferentially eroded features. This is more commonly seen in the finer grained samples, where the amygdales are larger than the average grain size of the dolerite minerals. In thin section most amygdales appear as dark sub-rounded structures that are highly altered and the frequency of their occurrence in the dykes varies (see Table 4.1). One of the Chapman's Peak dykes (CP5) has a very high density of amygdales, while other dykes (e.g. CL1 or FG2) have few or none.

Xenoliths are are commonly observed in the dykes (see Chapter 3). Most xenoliths appear to be fragments of the Cape Granite and do not show extensive alteration or melting associated with the intruding dolerite magma. The sharp edges of the xenoliths are typically parallel to the dyke-granite intrusion contact and show no evidence of rotation. This is consistent with

Table 4.2: Microprobe mineral analyses for selected dykes: Logies Bay (LB1), Tokai (TK2), Chapman's Peak (CP3), Millers Point (MP), Oukaapseweg (OK) and Nursery Ravine (NS). The composition of feldspar, pyroxene and olivine shown is the averaged value of mineral core analyses. Complete data set shown in Appendix D. Data from Butt (1989); Hirschel (1989) and Wulfse (1989).

Sample	Dyke	Feldspar			Pyroxene			Olivine	
		An	Ab	Or	En	Fs	Wo	Fo	Fa
GCH89-47	LB1	76.6	22.8	0.7	48.0	12.8	39.1	62.7	37.3
GCH89-22	TK2	76.1	22.9	1.0	49.4	19.3	31.3	62.7	37.3
GCH89-14	CP3	75.0	24.0	0.9	45.8	21.8	32.5	-	-
GCH89-34	MP	73.1	26.0	1.0	52.0	17.2	30.8	-	-
GCH89-36	OK	51.0	45.7	3.3	42.0	24.6	33.4	-	-
GCH89-24	NS	51.0	46.1	2.8	40.1	31.9	27.9	-	-

wall rock stoping. A quartzite xenolith observed in a thin section cut from the Oukaapseweg dyke shows no alteration associated with it and is likely sourced from the Peninsula Formation, which is also the local country rock at the dyke outcrop. A quartz xenocryst in the Millers Point dyke shows a distinct reaction rim and embayed texture. Xenoliths found at Smitswinkelbaai are distinctively different to the xenoliths of Cape Granite, as they shows resorbed and embayed grain edges (Figure 3.27, Chapter 3).

Mineral compositions of the False Bay dykes were not obtained in this study. A summary of the dolerite mineral compositions from previous studies is presented below along with the original microprobe data, which was produced by Butt (1989); Hirschel (1989) and Wulfse (1989), and later published by Reid (1990). Six samples across the compositional range of the dyke suite were analysed by microprobe and the complete microprobe data is presented in Appendix D. Table 4.2 shows the average plagioclase, clinopyroxene and olivine (if present) compositions for the six samples that were analysed. The average mineral compositions shown in Table 4.2 are calculated excluding analyses taken from the rim of mineral grains.

Compositions of plagioclase are mainly labradoritic with a compositional range of An_{51-76} (Table 4.2), but do show a significant variation in their calcium content as low as An_{23} (Figure 4.3). The lower calcium plagioclase is typically groundmass plagioclase and phenocryst rims, and even the Logies Bay dyke, which has plagioclase with the highest anorthite content (An_{76}), has rim compositions of An_{40}. Although the range in plagioclase compositions of each dyke largely overlaps, the average mineral compositions of plagioclase decreases in calcium content from An_{76} (dyke LB1) to An_{51} (dyke NS) (Table 4.2). The Nursery Ravine and Oukaapseweg dykes have a lower Ca composition of An_{50-60}, compared to the dykes at

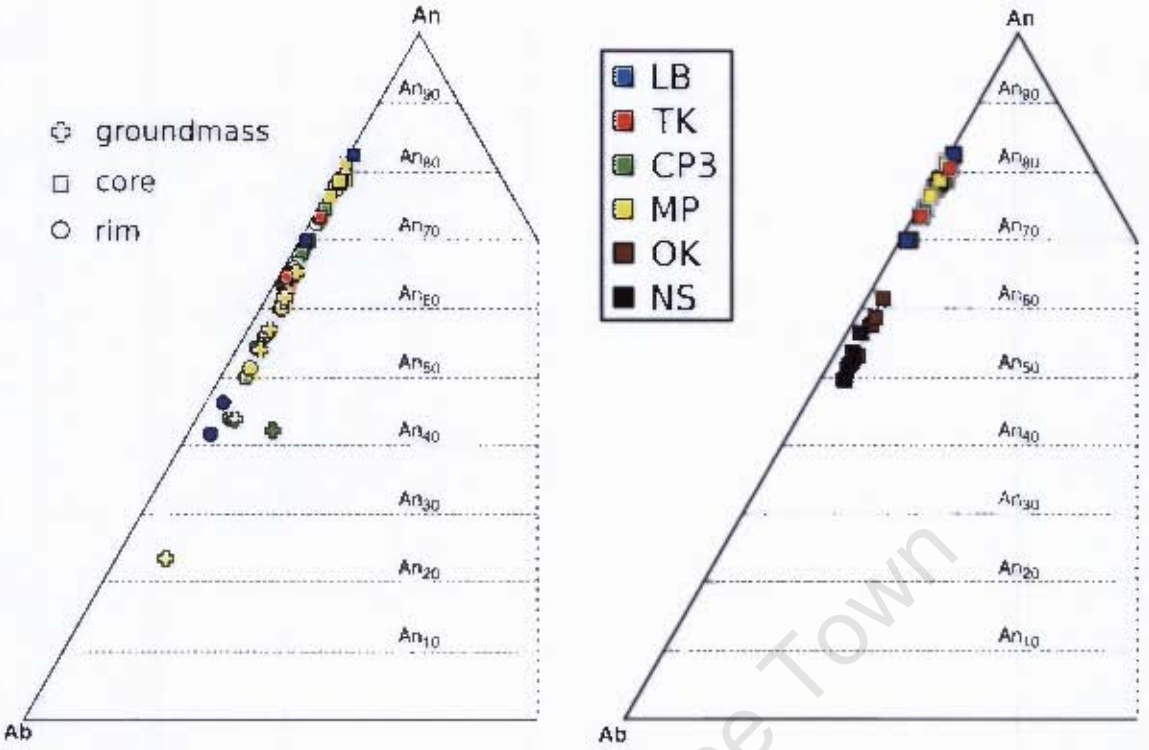

Figure 4.3: Feldspar ternary diagram, with the dyke feldspar compositions plotted. Left diagram compares core, rim and groundmass analyses for each dyke, while the right diagram only plots core compositions.

Logies Bay, Tokai (TK), Chapman's Peak (CP3) and Millers Point (MP), which show a range in plagioclase composition of An_{70-80} (Figure 4.3). Reid (1990) correlated the decrease in An content to differentiation from a more primitive dyke (e.g. LB1) to a more evolved dyke (e.g. NS).

Pyroxene is the dominant mafic mineral in the dykes. Walker (1956) noted the presence of few orthopyroxene grains rimmed with clinopyroxene and Figure 4.4 two analyses of orthopyroxene and one of pigeonite, whereas the majority of the pyroxenes are augite in composition. Figure 4.4 also highlights the trend from more magnesium-rich augite in Logies Bay and Tokai dykes to a more iron-rich augite in the Nursery Ravine dyke. The trend of pyroxene compositions in the False Bay dykes is compared to a know differentiation trend to iron-rich tholeiites as seen in the Birds River complex (Figure 4.4), which shows a similar iron enrichment, interpreted to be related to magmatic differentiation (Eales and Booth, 1974; Eales and Robey, 1976).

Olivine has only been identified in the Logies Bay and Tokai dykes. The composition of

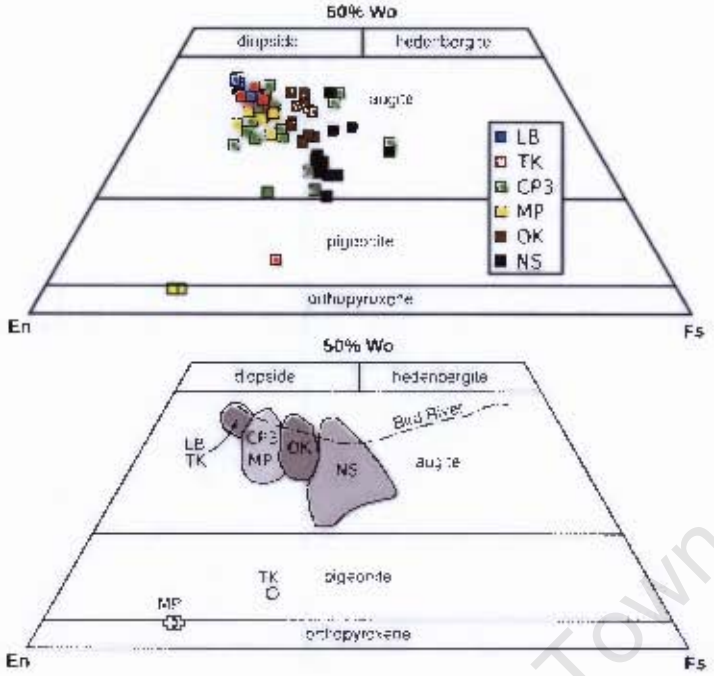

Figure 4.4: Pyroxene quadrilateral showing the compositional range of the six analysed dykes (top figure): Logies Bay (LB), Tokai (TK), Chapman's Peak (CP3), Millers Point (MP), Oukaapseweg (OK) and Nursery Ravine (NS). The lower Figure highlights the trend to more iron-rich augite and is compared compared to the Birds River gabbros of the Karoo, in the Dordrecht District of the Eastern Cape, South Africa(Eales and Booth, 1974; Eales and Robey, 1976).

olivine is predominantly forsterite with a compositional range from Fo_{56-72} and an average of Fo_{63}. Reid (1990) determined this to be out of equilibrium with the predicted Fo_{83} composition given the whole rock composition of the Logies Bay dyke. Reid (1990) also argued that the Fe-rich olivine evolved as a result of re-equilibration during the longer crystallisation period of the interior of the dykes, where the olivine grains are more commonly found.

Chapter 5

Analytical Methods

The False Bay dyke swarm samples used in this study were collected during a combination of past geochemical studies at the University of Cape Town (UCT). New samples collected from Robben Island (RI) and Chapman's Peak (CP4) dykes during this study are included. The samples were analysed using various instruments at both UCT and the GeoForschungsZentrum in Potsdam, Germany (GFZ), which allowed for data comparison across different instruments as well as different laboratories. Some of the dykes were sampled at shoreline outcrop locations (e.g. Sea Point, Clifton, Froggy Pond and Millers Point). Therefore care was taken to avoid alteration by seawater, by splitting the outer weathered surface and washing the sample in distilled or de-ionised water in an ultrasonic bath. Samples were all crushed at UCT using a hydraulic splitter and Sturtevant Laboratory Jaw Crusher (Carbon Steel Ribbed Jaws) and the crushed material was further powdered using a Seibtechnik Swingmill with Carbon-Steel vessels.

5.1 X-ray Fluorescence

Most of the samples for this study were previously analysed by X-ray Fluorescence (XRF) and selected results were published by Reid (1990). Newly sampled dykes (RI and CP4) were added to the data set in this new study. The new samples were analysed for major elements and selected trace elements with the X'Unique XRF spectrometer using fusion disks (prepared with a LiT-LiM flux in the proportion 57:43 and LiBr as the releasing agent) for major elements and

powder briquettes for trace elements.

5.2 Inductively coupled plasma mass spectrometry (ICP-MS)

A subset of the samples (n=27) wes chosen for selected trace element analysis in this new study. The subset covers the entire range of major element compositions and at least one sample per dyke found on the Cape Peninsula (and on Robben Island) was analysed. Samples were analysed using a Thermo Fisher Xseries2 quadrupole ICP-MS at UCT. Trumbull et al. (2007) had previously analysed selected False Bay dyke swarm samples (n=12) for trace elements at the GFZ, using an ICP-MS, whereas rare earth elements (La - Lu) measured at GFZ were determined using an Inductively Coupled Plasma - Optical Emissions Spectrometer (ICP-OES). The internal standard check used in the ICP-MS lab at UCT is BHVO-2 (results shown in Appendix B), which produced values within the range of the published values (Wilson, 1997; Ila and Frey, 2000).

The procedure at UCT for sample preparation follows that described by Le Roex et al. (2001), where 50 mg of sample powder was put into a Teflon beaker and 4ml of a hydrofluoric - nitric acid mixture was added (HF : HNO_3 ratio of 4:1) and placed on a hot plate for 48 hours. Next the beakers were opened and the samples dried to leave a silicate-free precipitate. The precipitate was then further diluted with concentrated HNO_3 and dried on the hot plate. This step was repeated to prepare the precipitate for the ICP-MS. Before insertion into the ICP-MS, the sample precipitates were mixed with 4 ml of an internal standard solution of 5% HNO_3 with 10 ppb indium (In), rhenium (Re), rhodium (Rh) and bismuth (Bi); then left in an ultrasonic bath for 1 hour and afterwards further diluted with the standard solution to 5000:1.

5.3 Multi-collector ICP-MS (MC-ICP-MS)

A further subset of selected samples (n=16), covering the MgO and SiO_2 range of the False Bay dyke swarm, also including five samples of Cape Granite and Malmesbury Group, were analysed for Nd and Sr isotope ratios using the Nuplasma MC-ICP-MS. Samples were prepared by following the Miková and Denková (2007) technique for Sr and Nd separation. Internal long-

term standard BHVO-2 produced $^{87}Sr/^{86}Sr$ values of 0.703468 ± 0.000013 and $^{143}Nd/^{144}Nd$ values of 0.512994 ± 0.000005, compared to recommended values of 0.703479 ± 0.000020 and 0.512984 ± 0.000011 respectively (Weis et al., 2006). Sample powders of the Cape Granites and Malmesbury Group where also analysed for whole-rock Sr and Nd isotopes on a Triton and a Finnigan MAT262 mass spectrometer at the GFZ, following the technique described by Romer et al. (2005). Present day $^{87}Rb/^{86}Sr$ and $^{147}Sm/^{144}Nd$ isotope ratios have been calculated from ICP-MS elemental data and the measured $^{87}Sr/^{86}Sr$ and $^{143}Nd/^{144}Nd$ isotope ratios using GEODATE (Eglington and Harmer, 1999), for use in regression calculations presented later. Initial $^{87}Sr/^{86}Sr$ and $^{143}Nd/^{144}Nd$ isotope ratios were recalculated to 130 Ma (Reid et al., 1991) using GEODATE.

Isotope analyses for the False Bay dolerites include one duplicate measurement of a dyke from Tokai (sample GCH89-22), which was initially published by Trumbull et al. (2007). The results of both studies are highlighted in Table 5.1 and show good correlation and reproducibility for both Sr and Nd systems, where differences are found in the 5th decimal place.

Table 5.1: Isotope analysis comparison of sample GCH89-22 from the Tokai locality.

GCH89-22 (TK2)	this study	Trumbull et al. (2007)
$^{87}Sr/^{86}Sr$	0.706849(13)	0.706878(7)
$^{87}Sr/^{86}Sr$ (130Ma)	0.70644	0.70644
$^{143}Nd/^{144}Nd$	0.512516(6)	0.512502(5)
$^{143}Nd/^{144}Nd$ (130 Ma)	0.51239	0.51237

5.4 Malmesbury Group and Cape Granite Suite Analysis

The country rock intruded by the False Bay dyke swarm in the Cape Peninsula and False Bay region include the Neoproterozoic Malmesbury Group meta-sedimentary rocks and the Peninsula Granite batholith of the Cape Granite suite. Previous studies suggested crustal contamination affected the False Bay magma and that an assimilation model is required to model the observed trends seen in the compositional range of the dyke suite (Trumbull et al., 2007). The petrogenetic models are discussed later in Chapter 7; however, it was necessary to analyse samples of the local basement, as this data is not complete in the available literature. Malmesbury Group meta-sediments were analysed for major and trace element data by Mbangula (2004)

and Mbeje (2005). Two samples of Cape Granite (sample CJ-08 and CJ-12; Appendix C) are analysed for trace elements, Sr and Nd isotopes. The granite samples were originally collected by Creighton-Jones (1982) and the major element data is shown in Appendix C. One new sample of Cape Granite was collected from the Higgovale Quarry in Cape Town below the Cable Way and was analysed for major elements, trace elements, Sr and Nd isotopes (sample CG-A1; Appendix C). Known problems that were encountered during analysis of the Cape Granites are the dissolution of zircons. Different analytical techniques produce Zr concentrations of ~160 ppm in XRF and ~40 ppm in ICP-MS, clearly showing an under evaluation of the Zr content by ICP-MS. Therefore, the concentration for Zr presented in the data tables is that determined by the XRF technique from Creighton-Jones (1982). Zircons are known to be a reservoir for the heavy rare earth elements (Gd - Lu), this should however not affect the light rare earth elements such as Sm and Nd concentration adversely; however, the issue of zircon dissolution needs to be kept in mind.

5.5 Graphs and Data Plots

Results were compiled into spread sheets using the newly collected data and those from Reid (1990). The data were imported into Petrograph (Petrelli et al., 2005), a plotting program that includes discrimination diagrams, ternary diagrams and normalisation values. All plots were created in Petrograph and further edited in Inkscape, a graphics program, for presentation purposes.

Chapter 6

Geochemistry

Major and trace element analyses of all samples determined by XRF techniques are presented in Appendix A. Prior to interpretation the geochemical data set was processed and screened for the purposes of identifying altered or weathered samples (see Chapter 5), rejecting suspect analyses and applying a suitable normalisation. With respect to alteration, field and petrographic observations were the first screen applied to the samples. Inspection of Loss on Ignition (LOI) values with respect to dolerite dykes indicate limited alteration, with only one of the 74 analyses reporting an LOI of > 2% (Table 6.1). Normalisation of major oxides was to 100% on an LOI-free basis, with total Fe as FeO. Table 6.1 lists a subset of the geochemical database, containing a representative sample from each dyke that was selected for ICP-MS traces and radiogenic isotopes. The Mg# value (molecular MgO/(MgO+FeO)) shown in Table 6.1 has been calculated using an assumed Fe_2O_3/FeO wt % ratio of 0.15 (Frey et al., 1974; Brooks, 1976; Langmuir et al., 1977).

6.1 Major Element Variations

To investigate the use of a single sample as representative of the dyke's composition, the widest dyke (LB1) was sampled across its entire width to observe geochemical variations (Figure 6.1). Figure 6.1 shows the limited chemical variations of samples taken across the 40m wide Logies Bay dyke with a range of 0.8 wt.% in SiO_2 and 0.6 wt.% in $Na_2O + K_2O$ and the error bars showing a lot of overlap. Immobile element oxide TiO_2 has a range from 1.22 to 1.59 wt. % in

Table 6.1: Major oxide data (volatile free, total Fe as FeO, recalculated to 100%) from Reid (1990) with new trace element for the False Bay dyke swarm. Measured LOI (Appendix A) is listed below major oxides and dykes are listed in order of decreasing MgO content.

Sample	GCH89-20	LB-07	GCH89-22	GCH89-11	LB-11	GCH89-14	GCH89-03	GCH89-33
Dyke Location	TK1	LB1	TK2	CP1	LB2	CP3	SB	MP
Major element oxides (wt. %)								
SiO_2	50.55	50.13	50.04	50.29	50.51	52.59	50.65	51.16
TiO_2	1.51	1.22	1.42	1.48	1.63	0.99	2.02	2.10
Al_2O_3	14.98	16.92	15.96	15.63	15.02	15.78	14.46	14.54
FeO	11.19	9.63	10.60	10.50	11.48	10.45	13.24	12.26
MnO	0.35	0.17	0.19	0.19	0.20	0.21	0.24	0.23
MgO	7.45	7.42	7.29	7.27	7.03	6.32	6.12	5.81
CaO	11.30	11.63	11.28	11.17	10.81	10.32	9.41	9.36
Na_2O	2.04	2.20	2.35	2.55	2.40	2.14	2.59	2.80
K_2O	0.38	0.50	0.67	0.70	0.66	1.05	0.96	1.27
P_2O_5	0.25	0.18	0.21	0.23	0.27	0.16	0.32	0.47
LOI	1.81	1.19	0.40	1.40	0.82	0.40	1.08	0.91
ICPMS trace elements (ppm)								
Sc	42	38	39	42	44	36	39	42
V	293	254	276	298	319	299	368	348
Cr	270	336	285	194	139	144	36	77
Co	45	44	44	44	46	41	51.3	42.8
Ni	67	89	79	63	63	69	50.6	32.5
Cu	84	80	71	83	83	112	85	40
Zn	96	86	93	101	111	89	141	118
Rb	14.9	11.9	16.4	16.1	14.4	33.1	22.3	31.1
Sr	326	209	214	204	212	163	355	300
Y	25	20	23	27	29	24	26	37
Zr	96	80	84	127	134	98	128	171
Nb	9.5	7.7	9.0	12.0	12.2	7.4	11.8	24.2
Ba	400	137	164	181	180	218	251	323
La	11.2	9.5	11.0	14.5	14.6	12.7	15.7	24.6
Ce	24.8	20.9	24.1	31.7	32.4	27.4	35.3	52.2
Pr	3.28	2.76	3.16	4.10	4.25	3.47	4.67	6.40
Nd	14.9	12.3	14.2	18.2	18.9	14.7	20.8	27.4
Sm	3.84	3.14	3.60	4.49	4.68	3.63	4.93	6.10
Eu	1.29	1.08	1.21	1.41	1.49	1.08	1.68	1.94
Gd	4.36	3.62	4.09	4.98	5.33	4.12	5.35	6.98
Tb	0.70	0.58	0.65	0.77	0.85	0.67	0.80	1.06
Dy	4.64	3.78	4.37	5.12	5.49	4.47	4.99	6.68
Ho	0.95	0.77	0.87	1.04	1.11	0.91	0.99	1.33
Er	2.80	2.30	2.61	3.10	3.30	2.72	2.83	3.85
Tm	0.40	0.33	0.36	0.43	0.46	0.38	0.39	0.52
Yb	2.65	2.15	2.44	2.93	3.12	2.55	2.53	3.41
Lu	0.40	0.32	0.36	0.44	0.46	0.38	0.39	0.50
Hf	2.56	2.14	2.31	3.25	3.45	2.62	3.32	4.28
Ta	0.52	0.46	0.48	0.65	0.70	0.41	0.70	1.23
Pb	3.1	3.7	3.3	4.0	4.4	5.4	4.1	5.6
Th	1.2	1.3	1.4	1.7	1.5	3.2	2.4	3.2
U	0.3	0.4	0.4	0.4	0.4	0.8	0.5	0.8
Mg#	57	60	58	58	55	55	48	48

Table 6.1 continued...

Sample	GCH89-28	GCH89-45	FBD-601	FBD-611	GCH89-31	GCH89-40	GCH89-39	LB-50
Dyke Location	FG1	OD2	RI	RI	FG2	SP	SL	SW
Major element oxides (wt. %)								
SiO_2	52.22	53.74	50.43	48.92	52.73	50.63	51.43	53.12
TiO_2	2.12	1.85	2.53	3.06	2.22	2.97	3.04	1.83
Al_2O_3	14.82	17.24	12.24	12.41	14.36	13.07	13.47	13.46
FeO	11.47	7.73	17.36	17.62	11.84	15.40	14.18	14.23
MnO	0.21	0.12	0.26	0.26	0.19	0.26	0.69	0.23
MgO	5.29	5.16	5.05	5.04	5.01	4.87	4.73	4.63
CaO	8.83	10.67	9.18	9.53	8.52	8.77	7.93	8.14
Na_2O	2.90	2.27	1.80	1.94	2.87	2.32	2.28	2.96
K_2O	1.64	0.92	0.84	0.81	1.72	1.15	1.71	1.16
P_2O_5	0.50	0.31	0.31	0.41	0.54	0.56	0.54	0.24
LOI	0.87	1.38	0.52	0.27	0.89	2.61	1.57	0.52
ICPMS trace elements (ppm)								
Sc	35	44	48	48	36	45	40	44
V	300	290	634	612	329	484	433	535
Cr	69	270	61	81	49	37	29	43
Co	39	43	51	48	39	51	63	47
Ni	37	63	51	55	20	38	21	42
Cu	27	57	420	569	12	41	47	198
Zn	119	129	179	188	121	167	140	136
Rb	46.2	21.7	27.8	26.8	49.3	37.1	51.0	31.8
Sr	302	252	116	116	288	326	207	143
Y	37	35	56	67	38	49	58	40
Zr	220	146	201	244	218	237	283	154
Nb	28.8	15.3	12.3	15.0	28.5	24.0	28.0	11.3
Ba	378	240	195	196	390	396	408	251
La	30.1	18.9	16.5	19.1	30.9	28.2	33.0	18.4
Ce	64.2	35.4	38.3	44.9	66.1	61.2	71.0	40.0
Pr	7.91	5.12	5.17	6.15	8.17	7.64	8.80	5.05
Nd	32.9	22.4	24.2	29.0	33.9	33.6	38.0	21.7
Sm	7.25	5.25	6.72	8.08	7.39	7.81	8.30	5.36
Eu	2.00	1.70	2.02	2.33	1.99	2.42	2.20	1.61
Gd	7.39	6.16	8.82	10.7	7.48	9.22	9.60	6.47
Tb	1.12	0.97	1.46	1.77	1.13	1.43	1.50	1.06
Dy	7.06	6.16	9.97	12.1	7.07	9.28	9.60	7.14
Ho	1.39	1.25	2.07	2.51	1.40	1.88	2.00	1.50
Er	4.09	3.59	6.30	7.65	4.08	5.58	5.70	4.53
Tm	0.57	0.50	0.90	1.07	0.57	0.79	0.80	0.64
Yb	3.76	3.29	6.03	7.18	3.73	5.24	5.30	4.33
Lu	0.56	0.49	0.89	1.08	0.55	0.78	0.80	0.65
Hf	5.36	3.74	5.37	6.42	5.39	5.95	5.30	4.14
Ta	1.55	0.82	0.69	0.84	1.54	1.29	1.40	0.73
Pb	8.0	5.8	4.1	6.4	8.7	7.2	11.1	7.8
Th	4.8	2.6	2.8	3.0	5.4	3.9	7.7	5.2
U	1.3	1.0	0.5	0.6	1.4	1.0	2.1	1.3
Mg#	48	57	37	37	46	38	40	39

Table 6.1 continued...

Sample	LB-40	LB-60	LB-43	GCH89-17	GCH89-36	GCH89-43	PD-2	GCH89-41	LB-33	GCH89-24	GCH89-07
Dyke Location	CL1	WF	CL2	CP5	OK	BK	LR	KS	OD1	NS	CP2
Major element oxides (wt. %)											
SiO_2	53.03	55.59	53.59	54.50	55.42	52.91	55.79	54.01	56.01	54.64	55.22
TiO_2	2.24	1.57	2.17	2.36	2.24	2.91	2.53	2.67	2.57	2.55	2.65
Al_2O_3	14.63	13.99	14.32	13.69	13.72	12.65	13.46	12.44	13.27	12.33	12.60
FeO	13.00	12.05	12.79	12.62	12.59	15.39	13.08	15.86	12.68	15.38	14.90
MnO	0.23	0.20	0.21	0.28	0.20	0.24	0.42	0.24	0.20	0.24	0.27
MgO	4.34	4.24	4.23	4.13	3.89	3.55	3.28	3.13	3.01	2.90	2.74
CaO	6.51	7.61	8.09	7.32	6.86	7.43	6.20	7.11	5.95	7.42	6.26
Na_2O	3.09	2.28	2.48	2.36	2.44	2.32	1.73	2.18	2.95	2.04	2.09
K_2O	2.52	2.22	1.70	2.20	2.14	1.83	2.87	1.96	2.68	2.07	2.49
P_2O_5	0.42	0.24	0.41	0.53	0.51	0.77	0.65	0.42	0.67	0.43	0.78
LOI	1.63	1.29	0.92	0.77	1.13	1.43	1.45	1.25	1.69	0.77	1.18
ICPMS trace elements (ppm)											
Sc	39	35	39	35	39	41	38	42	37	39	37
V	444	333	440	410	349	375	421	401	404	343	286
Cr	42	73	46	23	65	15	13	3	8	3	11
Co	41	39	40	39	35	43	39	45	35	40	32
Ni	30	46	32	25	29	16	16	4	12	3	9
Cu	47	100	47	26	20	16	12	16	7	13	1
Zn	140	120	140	132	136	169	145	169	146	166	156
Rb	134.1	84.1	67.0	80.3	83.7	62.8	105.3	76.1	133.5	76.3	98.3
Sr	170	155	181	182	187	142	198	138	159	427	161
Y	44	38	44	42	45	55	54	52	48	53	53
Zr	214	189	220	225	195	230	239	220	243	226	239
Nb	19.8	12.7	20.1	21.9	18.3	20.5	23.9	16.8	24.3	17.0	21.6
Ba	372	350	337	413	358	375	961	356	408	845	614
La	26.7	25.1	27.3	31.3	27.6	32.3	34.5	26.5	35.2	27.8	35.1
Ce	57.7	54.0	58.4	66.9	58.6	69.0	73.6	57.3	75.4	60.3	76.4
Pr	7.17	6.64	7.24	8.26	7.10	8.42	8.90	7.02	9.23	7.54	9.51
Nd	30.4	27.5	30.7	34.1	29.6	35.8	37.2	30.1	38.1	32.2	39.8
Sm	7.01	6.30	7.04	7.60	6.72	8.18	8.25	7.20	8.36	7.81	9.18
Eu	1.93	1.61	1.92	1.95	1.95	2.32	2.15	2.22	2.12	2.16	2.23
Gd	7.81	6.73	7.84	7.94	7.79	9.76	9.23	8.98	8.86	8.93	9.69
Tb	1.22	1.06	1.25	1.21	1.22	1.53	1.41	1.44	1.37	1.44	1.52
Dy	8.05	6.92	8.16	7.79	8.06	10.12	9.08	9.49	8.75	9.62	9.75
Ho	1.62	1.39	1.65	1.55	1.64	2.06	1.87	1.96	1.76	1.96	1.96
Er	4.89	4.14	4.95	4.57	4.90	6.14	5.46	5.84	5.27	5.91	5.83
Tm	0.69	0.57	0.70	0.64	0.69	0.86	0.75	0.83	0.73	0.85	0.82
Yb	4.64	3.86	4.70	4.26	4.56	5.75	4.87	5.49	4.89	5.64	5.51
Lu	0.69	0.56	0.69	0.63	0.68	0.84	0.72	0.82	0.74	0.84	0.81
Hf	5.50	4.95	5.63	5.78	5.05	5.94	6.11	5.71	6.25	6.01	6.28
Ta	1.20	0.80	1.21	1.36	1.19	1.19	1.53	0.99	1.64	1.04	1.41
Pb	9.4	11.6	10.1	12.4	12.3	11.7	14.3	10.9	14.6	11.5	14.0
Th	6.2	7.3	6.4	8.3	8.3	8.0	10.0	7.3	10.4	7.8	10.2
U	1.6	1.6	1.7	2.3	2.5	2.1	2.8	1.8	2.7	2.0	2.6
Mg#	40	41	40	39	38	31	33	28	32	27	27

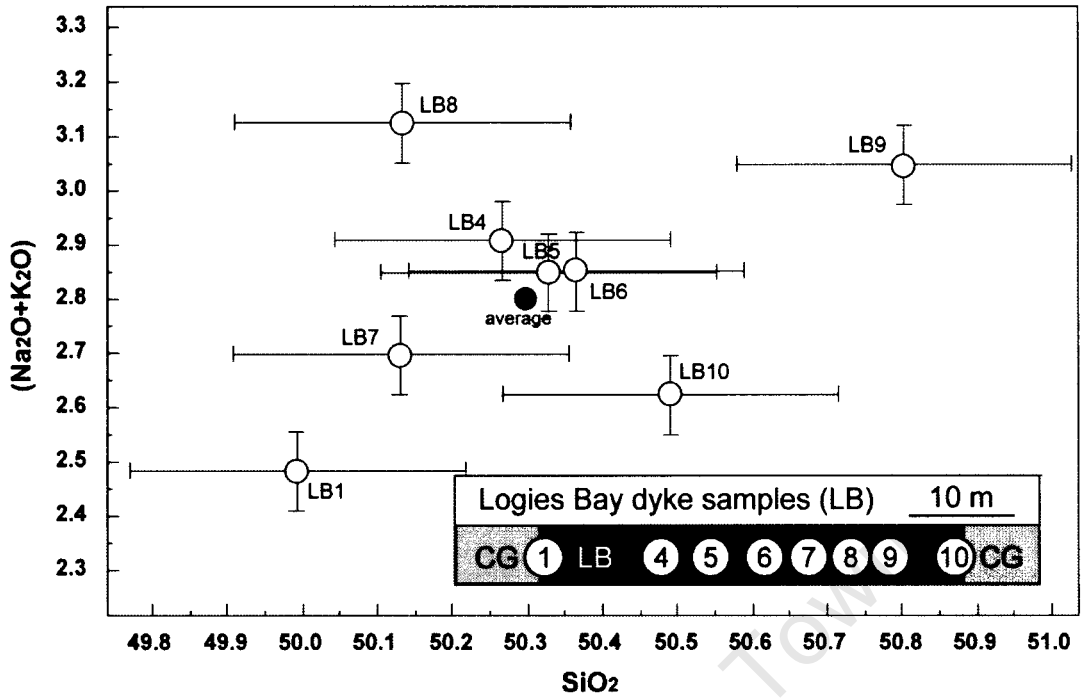

Figure 6.1: Logies Bay (LB) dyke samples (open symbols with error bars) taken across the width of the 40m dyke including the quenched dolerite close to the Cape Granite (CG) contacts. Closed symbol represents the average dyke composition.

the LB1 dyke with a maximum 12% difference from an average TiO_2 of 1.40 wt. %, smaller than the % difference of K_2O (68 %), which is plotted along with Na_2O and SiO_2 in Figure 6.1. Therefore, intra-dyke variations are minimal, even in the widest dykes (e.g. LB1), and a single sample provides a good geochemical representation for the respective dyke.

The compositional range of the False Bay dolerite suite is shown in two conventional classification diagrams (Figure 6.2), where the bulk of the data points plot within the sub-alkaline fields with basalt and basaltic andesite compositions (Figure 6.2a) and show a distinct tholeiitic affinity (Figure 6.2b). For purposes of further description and subsequent discussion the dykes with the lowest and highest SiO_2 (Logies Bay LB1 and Chapman's Peak CP2 respectively) have been labelled. Other major element plots are shown in Figure 6.3, where the degree of differentiation can be monitored by the MgO content, which changes from 8% in dykes with basaltic composition to 2% in dykes with basaltic andesite composition. Relatively smooth correlation between MgO and other high abundance major oxides, such Al_2O_3, FeO and CaO, and minor oxides like K_2O, P_2O_5 and TiO_2 reveal continuous change with no obvious compositional gaps. The behaviour of Na_2O appears to be more complex but perhaps indicative of a

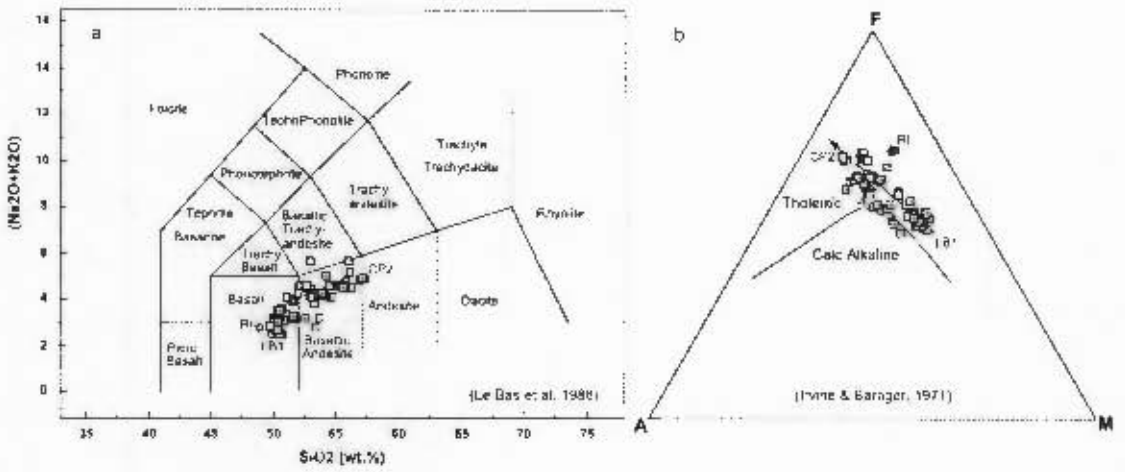

Figure 6.2: (a) Total alkali-silica diagram and (b) AFM diagram for the False Bay dyke swarm, where A = Na_2O+K_2O, F = Total Fe as FeO, M = MgO. Logies Bay (LB1), Chapman's Peak 2 (CP2) and Robben Island (RI) dykes are labelled.

maximum at intermediate MgO. Samples from the Robben Island dyke (RI) and one from the Oudekraal locality (OD2) reveal notable departures in composition away from the trend defined by the dyke suite's end-member compositions (LB1 and CP2).

The relationship between Mg# (Table 6.1) and geographical distribution of the dykes is examined to observe if any spacial control on dyke locations is related to the degree of differentiation (Figure 6.4). Bearing in the mind the general NW-SE orientation of the dykes and their restricted outcrops that essentially span a N-S tract down the Cape Peninsula, the dykes with highest Mg# are exposed around Hout Bay, whereas the other dykes do not show spatial restrictions in terms of their Mg#. However, the Chapman's Peak location contains adjacent dykes separated by only a few 10s of metres that encompass the entire range in Mg#. Therefore, there is no apparent spatial variation in MgO.

6.2 Trace Elements Variations

Variation of compatible trace elements such as Cr and Ni show progressive depletion with decreasing MgO and follow curved trends, with continuous depletion during early stages of differentiation (high-MgO dykes) followed by a more subdued behaviour in the low-MgO dykes of basaltic andesite compositions (Figure 6.5). Other compatible traces, like V, have a maximum defined at intermediate MgO, while Sr shows significant scatter, but appears to define a

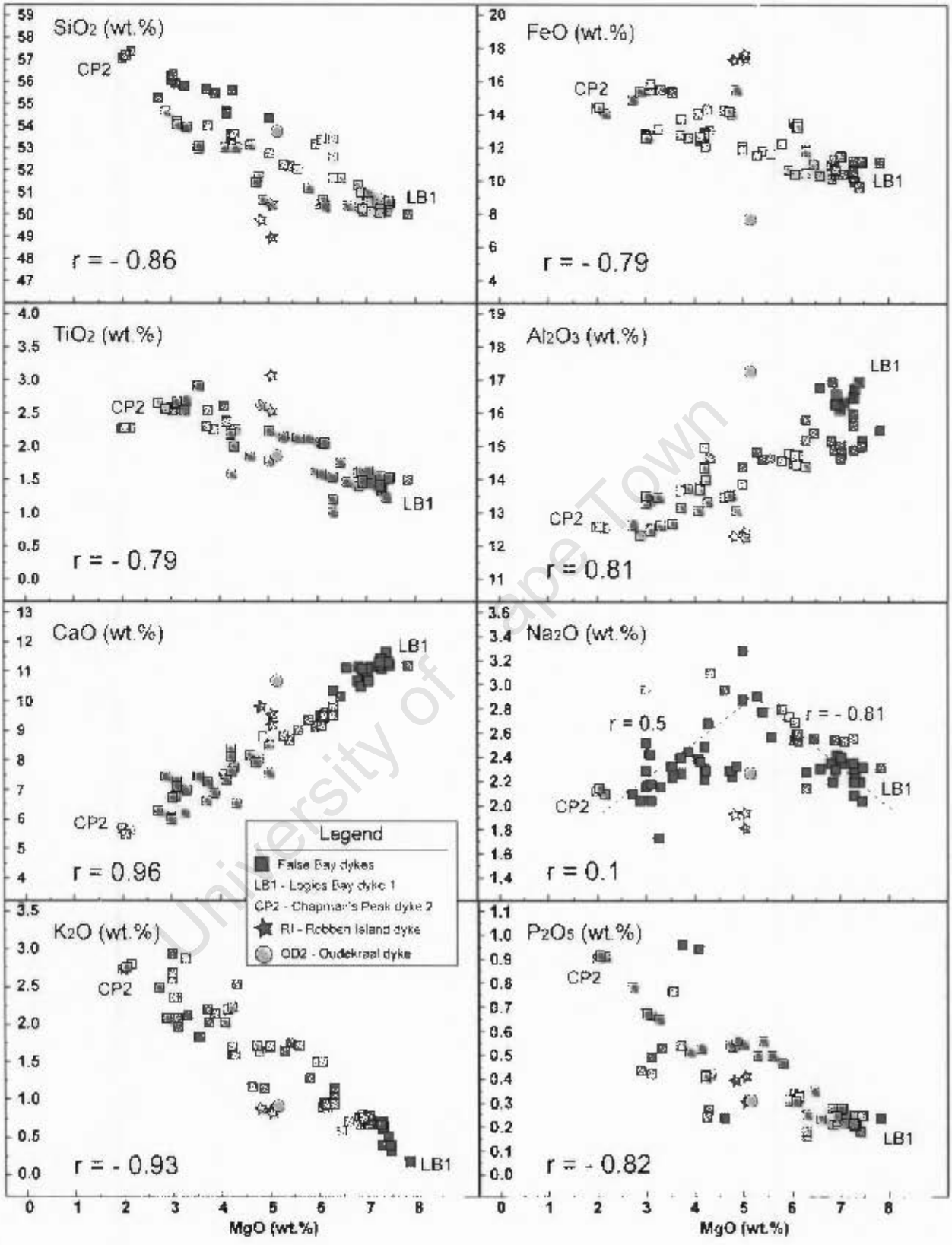

Figure 6.3: Major element oxides of the False Bay dyke swarm. End-member dykes (LB1 and CP2) are labelled and star symbol used for Robben Island dyke and circle symbol used for Oudekraal dyke (see Legend). Correlation coefficient (r) indicated for each plot in lower left corner. The dotted line in MgO versus Na_2O plot represents a bimodal trend of the sample set with a positive correlation from 2 - 5 wt.% MgO and a negative correlation from 5 - 8 wt.% MgO, with respective r values shown.

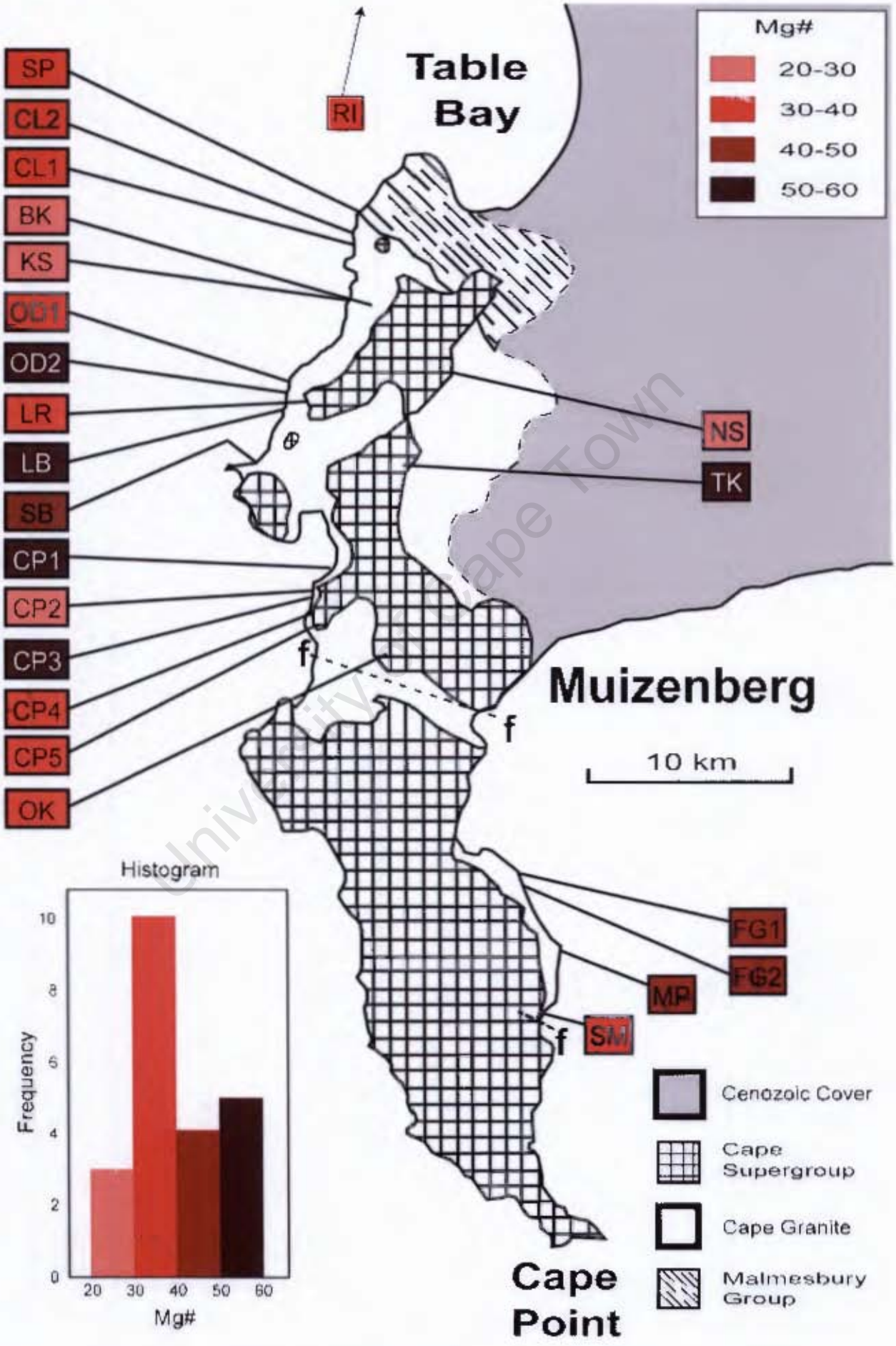

Figure 6.4: Frequency and outcrop distribution of Mg# in the dyke swarm.

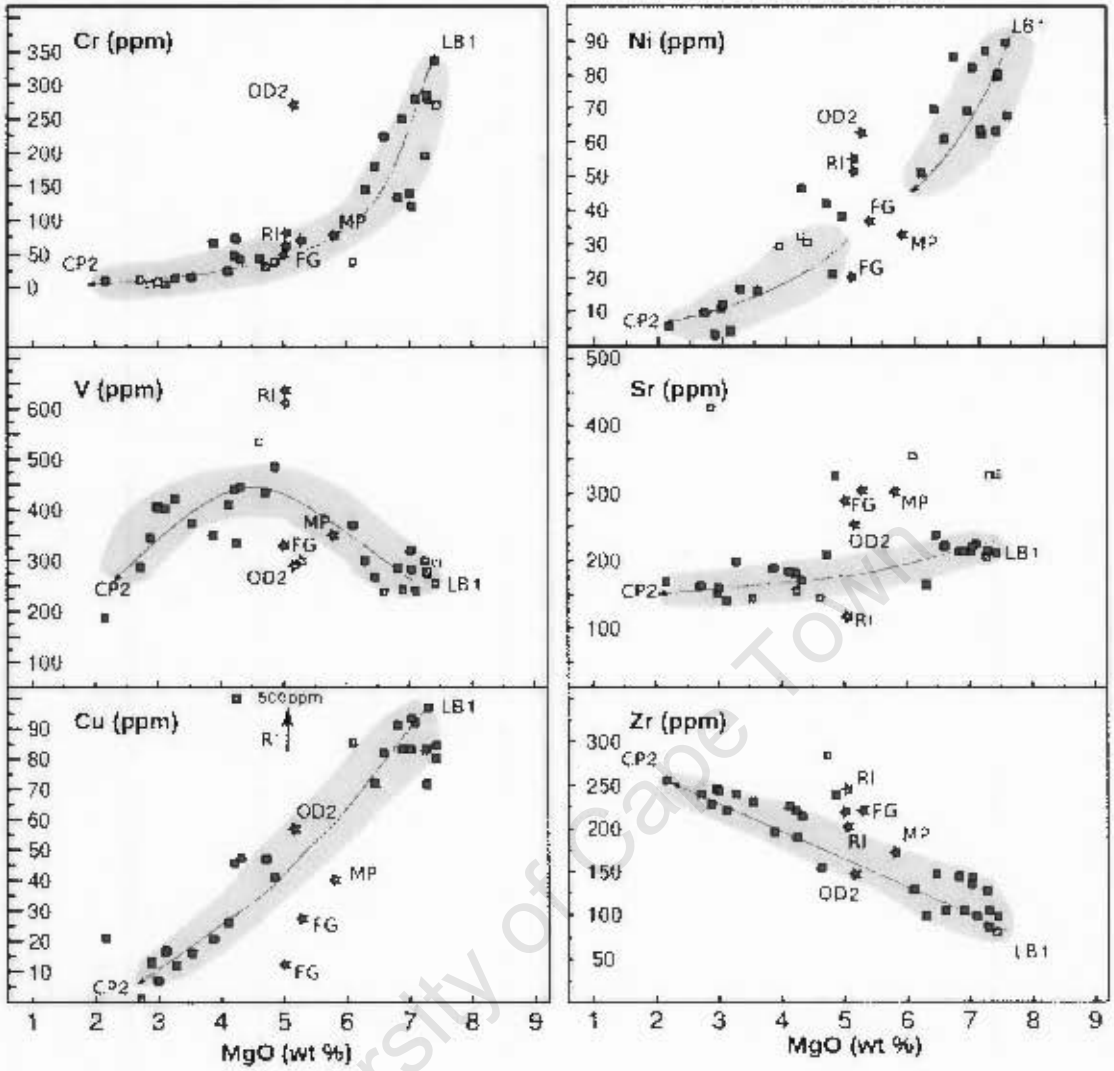

Figure 6.5: Trace elements of Cr, Ni, V, Sr and Cu plotted against MgO. Bottom right shows variation of Zr with MgO.

trend of slight depletion with decreasing MgO. The behaviour of Cu displays a clear positive correlation with MgO. Some dykes (labelled on the diagrams) have anomalous compositions and the same samples are identified repeatedly in Figures 6.5 and 6.6. The anomalous dykes include the Millers Point (MP), Froggy Pond (FG1), Oatland Point (FG2), Oudekraal 2 (OD2) and Robben Island (RI) dykes, all of which fall within a narrow range of 5 to 6 wt. % MgO.

The variation of an immobile incompatible trace element such as Zr shows a steady progressive enrichment with decrease in MgO content (Figure 6.5), ranging from about 80 ppm and increasing by a factor of three in the most differentiated dykes with basaltic andesite compositions. In order to highlight the correlation of changes in trace element contents with differenti-

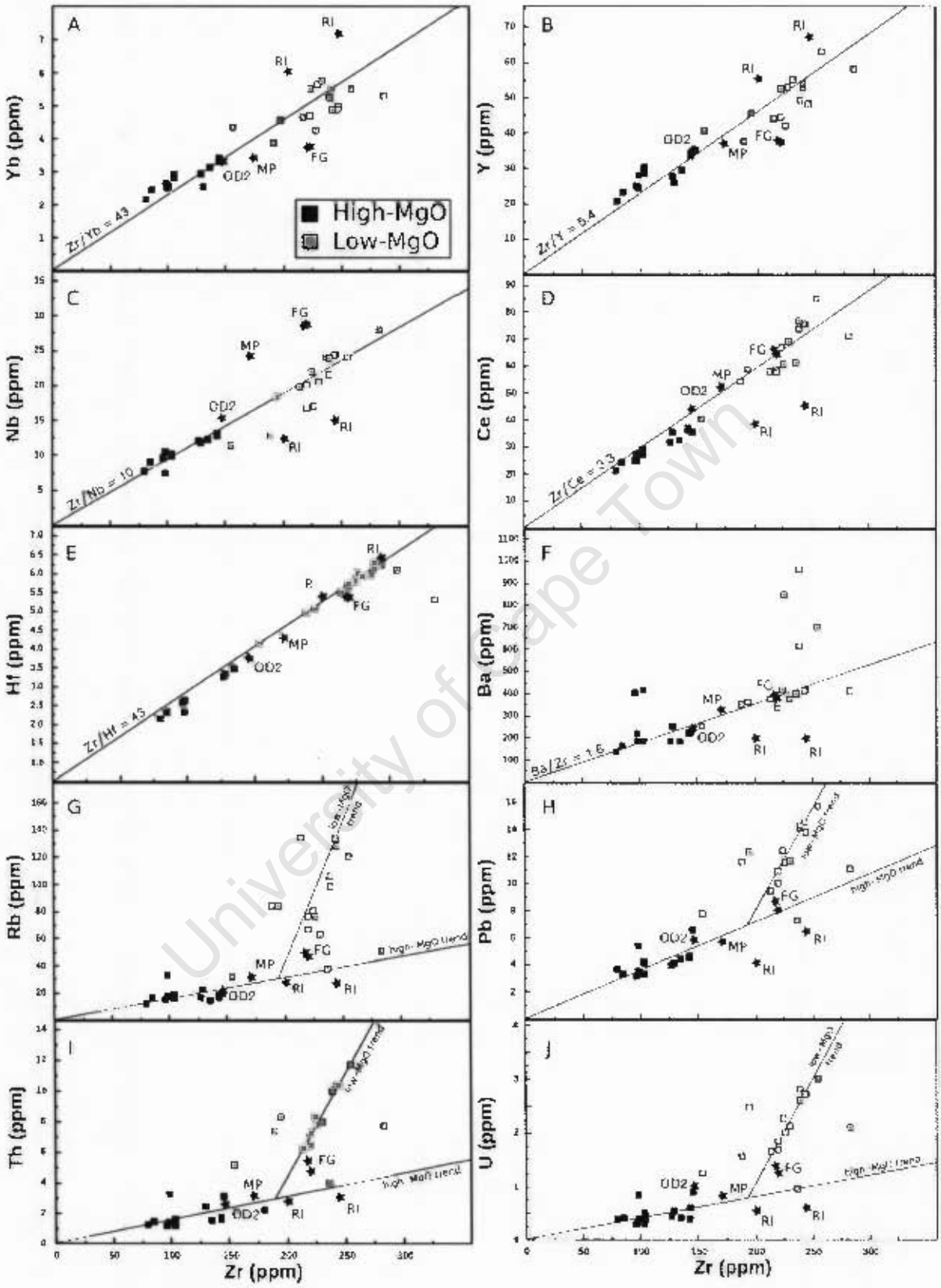

Figure 6.6: Incompatible trace elements plotted against Zr. Samples are grouped into high- and low-MgO groups (see text for details). Star symbols represent dykes (labelled) that have MgO compositions of approximately 5 wt%.

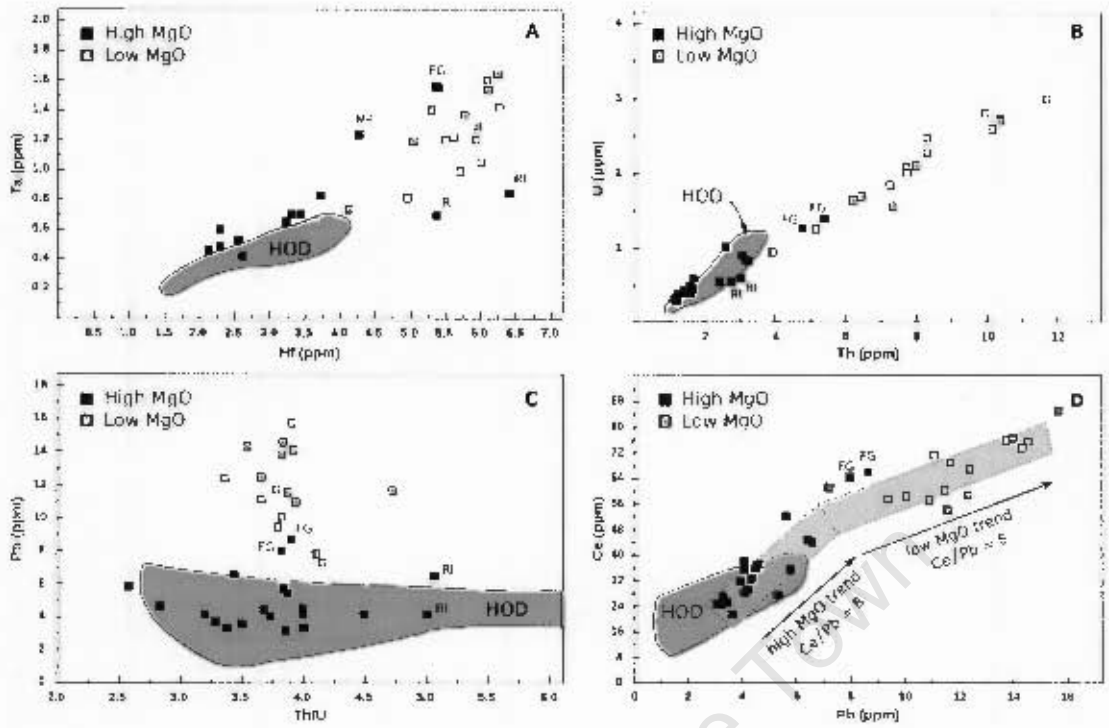

Figure 6.7: New trace element data of Hf, Ta, Pb, Th and U. Samples are divided into high- and low-MgO groups (see text for details) and shaded area represents the HOD for comparison (Trumbull et al., 2007). The average relative standard deviation (%RSD) for the elements are: Ta = 1.04; Hf = 0.81; U = 1.82; Th = 0.92; Pb = 0.77; and Ce = 0.25. Error bars are excluded from graph to maintain a clearer overview.

ation, the graphs utilise different symbols to distinguish between samples with > 5 wt.% MgO (high-MgO range) and < 5 wt.% MgO (low-MgO range). Variations of other incompatible trace elements analysed in the present study are plotted against Zr in Figure 6.6. Well-defined positive correlations of Yb and Y (representing the heavy REE), Ce (light REE), Nb and Hf (high field strength elements or HFSE), Ba (large ion lithophile element or LILE) are noteworthy. The previously identified anomalous dykes also appear anomalous in the trace element graphs, where these dykes are grouped as part of the high-MgO group, but overlap with both high- and low-MgO dyke groups in Zr and other incompatible trace element concentrations (Figures 6.6 and 6.7). Departures from simple linear relationships are evident in the behaviour of Rb and Pb (LILE), as well as U and Th (HFSE), with the more differentiated low-MgO dykes defining a completely different trend to that observed for the higher-MgO dykes (Figure 6.7).

Selected inter-element plots are presented in Figure 6.7, where the False Bay dyke swarm is compared with Etendeka-age dykes in Namibia. The higher degrees of differentiation of

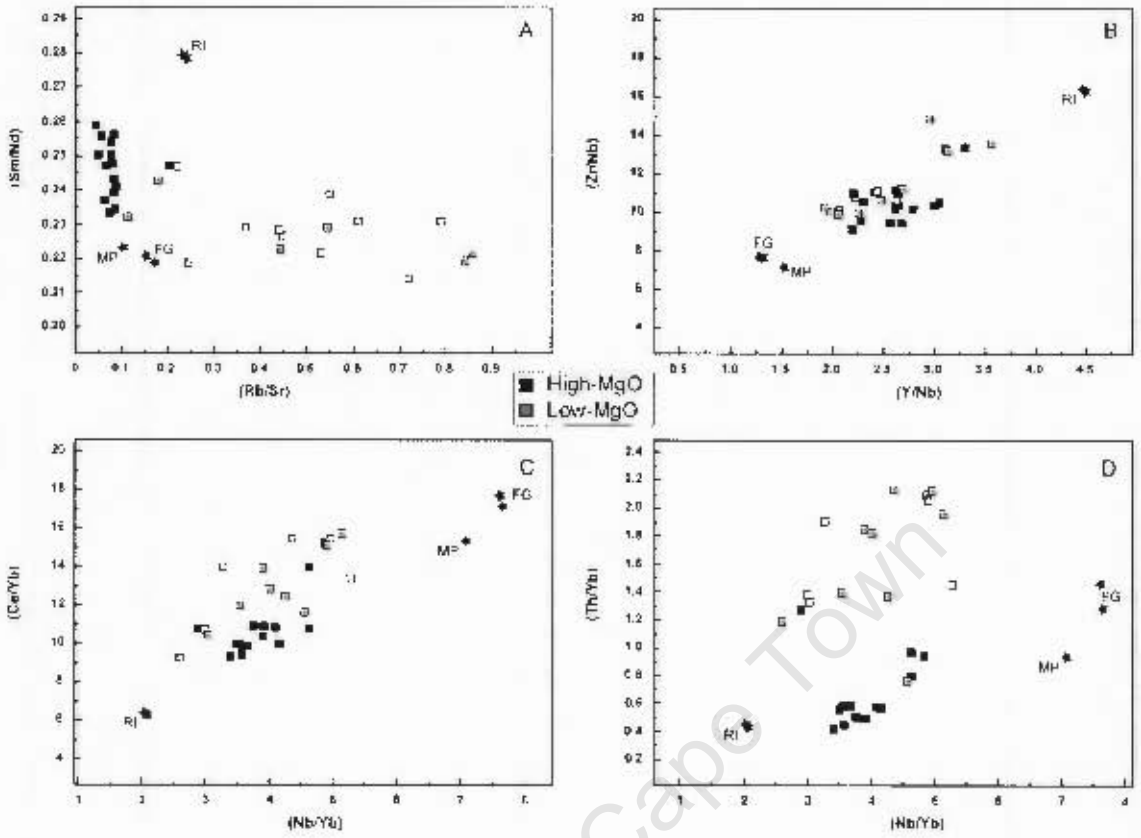

Figure 6.8: Trace element ratio plots. Samples divided into high- and low-MgO groups (see text for details).

the low-MgO dykes associated with high Ta, Hf, U and Th contents, is emphasised in the comparison with the more primitive dykes from the HOD mega-swarm in Namibia, which overlap with the high-MgO group of the False Bay dyke swarm. The near constant Th/U ratio in both the high- and low-MgO dykes provides a useful reference when tracking the behaviour of Pb. The more differentiated low-MgO dykes show anomalous Pb enrichment patterns. A similar pattern is observed when plotting Ce vs Pb, which shows the trend to high enrichment in the False Bay dykes, but with a gentle change in slope at the passage from the high- to low-MgO dykes, suggesting a changes in the processes that control the behaviour of these elements. Inter-element ratios pertinent to the radiogenic isotope system presented later are plotted in Figure 6.8, where the high-MgO members of the False Bay dyke swarm show restricted variation in Sm/Nd and Rb/Sr, but the more differentiated low-MgO dykes show variations to much higher Rb/Sr ratios. Other inter-element ratios plotted in Figure 6.8 are normalized to Nb or Yb. These plots highlight a clustered range in Zr, Y and Nb for all the dykes from False Bay, when

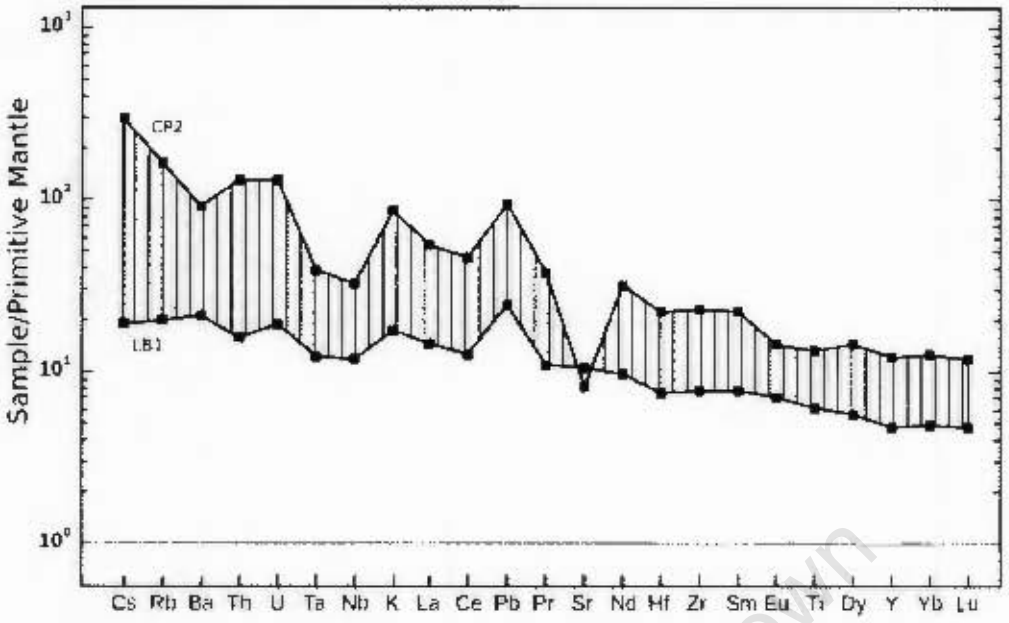

Figure 6.9: Incompatible trace elements normalised to primitive mantle (McDonough and Sun, 1995). Samples LB1 and CP2 represent least- and most differentiated dykes of the False Bay dyke swarm respectively.

excluding the anomalous dykes identified above. Plots of Ce/Yb and more-so Th/Yb vs Nb/Yb seem to indicate a more complex behaviour, dominated by higher Ce/Yb and Th/Yb ratios in the low-MgO basaltic andesites (Figure 6.8c and d).

Another popular approach adopted in geochemical characterisation of basaltic rocks is the mantle-normalised spider-grams where perturbations in the behaviour of trace elements may indicate source region control during the formation of parental magmas. Figure 6.9 shows the range in mantle-normalised composition of the False Bay dyke suite, with the Logies Bay dyke (LB1) representing the least differentiated composition and Chapman's Peak 2 (CP2) being the most differentiated composition. Of particular significance is the development of a positive Th-U anomaly, the Ta-Nb negative anomaly, as well as the presence of a positive Pb anomaly. Also evident is the large negative Sr- and Eu anomalies, although the latter is better illustrated in the REE plots.

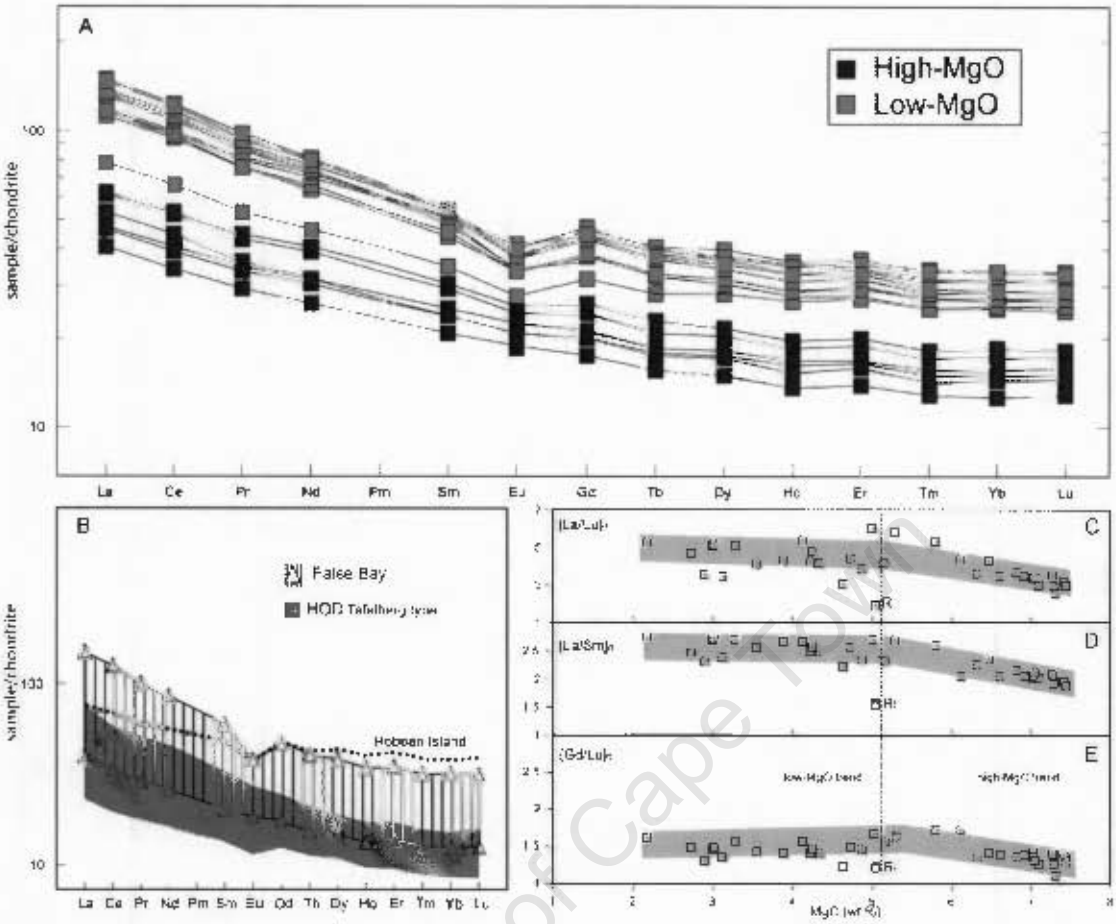

Figure 6.10: (A) Chondrite normalised REE data of the False Bay dyke swarm. Chondrite values taken from McDonough and Sun (1995). (B) False Bay dyke swarm range from least to most evolved samples and is compared to the range of compositions of the Tafelberg type of the HOD (Trumbull et al., 2007). (C) total REE ratio (La/Lu); (D) light REE ratio (La/Sm); (E) heavy REE ratio (Gd/Lu).

Variation of the REE as a separate group is displayed in Fig 6.10, where the analysed compositions are normalized to chondrite. Large changes in normalised REE concentration values are observed across the range of the dyke suite, although limited changes in the slope of overall REE profiles are evident in Figure 6.10a, which shows approximately parallel profiles. The detail of REE profile slopes can be observed in the ratio plots as a function of MgO (Figures 6.10c, d, and e). Although the normalised REE concentrations show approximately parallel profiles, subtle changes in slope are observed. The relative fractionation of the LREE is gradual and progressive in the passage from least to most differentiated dykes, while the HREE show even less perceptible changes, but again are gradual. However, the ratio plots all show a subtle but distinctive change at intermediate MgO concentrations of close to 5 wt.% MgO. The development

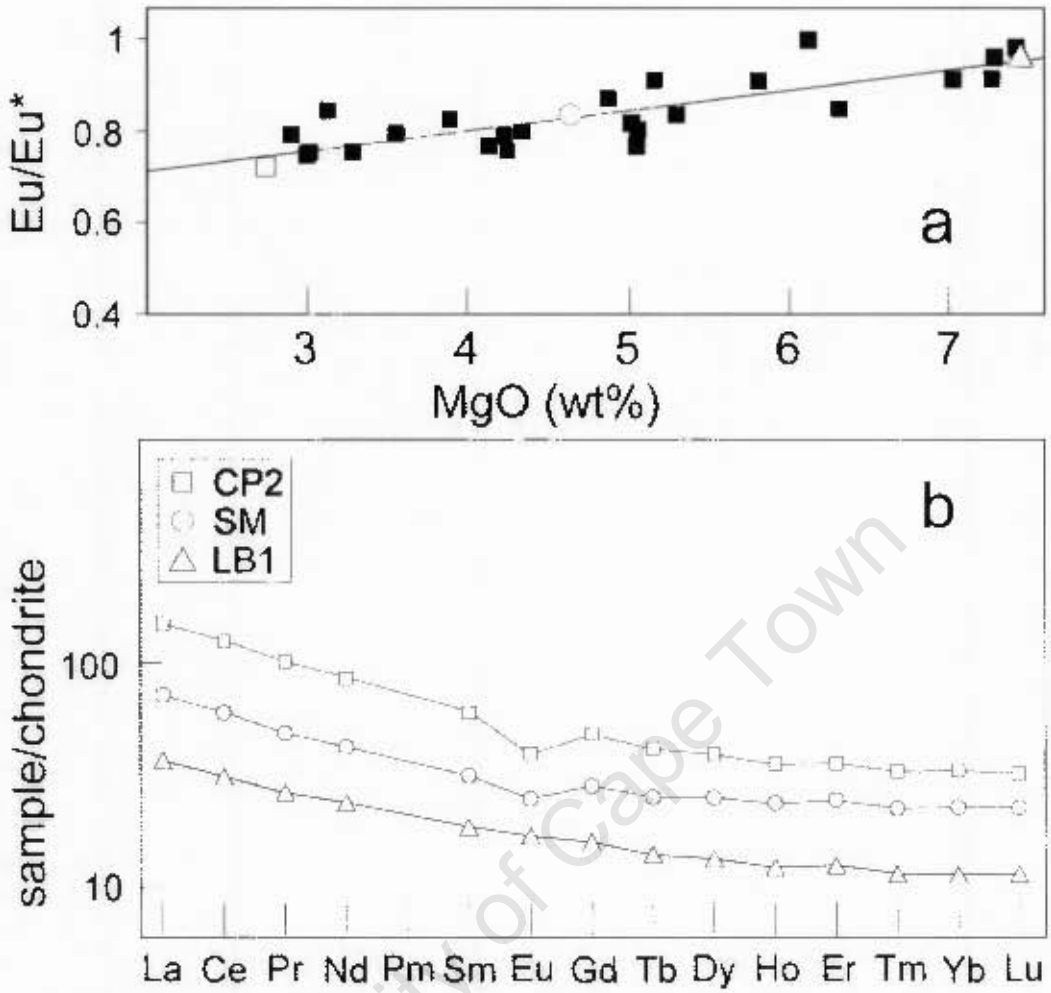

Figure 6.11: Eu-anomalies of the False Bay dykes, where $Eu* = \sqrt{Sm * Gd}$. Logies Bay (LB1), Smitswinkel (SM) and Chapman's Peak (CP2) dykes are highlighted by triangle, circle and square symbols respectively. (a) Variation of the Eu anomaly with MgO. (b) Comparative REE trends of selected dykes (LB1, SM and CP2) with varying degrees of the Eu anomaly, highlighting the change in the Eu-anomaly with increasing REE abundances.

of a negative Eu anomaly as a function of decreasing MgO is shown in Figure 6.11.

6.3 Sr and Nd Isotope Variations

6.3.1 False Bay Dykes

Further augmentation of the False Bay dyke swarm geochemical database involved the analysis of $^{87}Sr/^{86}Sr$ and $^{143}Nd/^{144}Nd$ isotope ratios (Table 6.2) in selected samples covering the compositional range described above. On a Rb-Sr isochron diagram (Figure 6.12a) the data

points show a rough correlation that produces a regression age of 563 ± 85 Ma with a MSWD error of 1.85. When the high-MgO basaltic samples are regressed separately the age produced is slightly younger at 313 ± 86 Ma and a lower MSWD error of 0.596. A similar approach has been taken in the Sm-Nd isochron diagram (Figure 6.12b) where the high-MgO basaltic samples follow a rough trend equivalent to an age of 279 ± 122 Ma (MSWD error of 34.1). Regression of the entire Sm-Nd dataset produces an age of 680 ± 428 Ma (MSWD error of 516.4). None of the regression ages are consistent with the Ar-Ar age of 130 Ma, which is interpreted as the intrusion-age of the dykes, but the older values calculated here probably reflect an open system behaviour discussed in later chapters.

Initial Sr and Nd isotope ratios, assuming a 130 Ma emplacement age, are plotted against MgO in Figure 6.13, where it is clear that the more differentiated dykes have higher initial $^{87}Sr/^{86}Sr$ and lower initial $^{143}Nd/^{144}Nd$ respectively. The data points and presence of some scatter does not differentiate between changes in isotope ratios as either a step-wise function at about 5 wt.% MgO, or as a curvilinear change. However, either case shows a relative progression in isotope ratios with change in MgO concentration. The high-MgO dykes have an initial $^{87}Sr/^{86}Sr$ ratio of 0.706 at the time of emplacement, whereas the low-MgO dykes have higher values up to 0.720. The corresponding values for initial $^{143}Nd/^{144}Nd$ are 0.51237 and 0.51213 respectively, equivalent to an εNd range of -1.6 to -6.6 (Table 6.2). The negative correlation of initial Sr and Nd isotopes is presented in Figure 6.14, where the array forms a well-defined linear trend from near bulk Earth to higher Sr-isotope and lower Nd-isotope ratios with progressive changes. Also pertinent in Figure 6.14 is the cluster of the high-MgO dykes (dark symbols) relative to the linear trend of the low-MgO dykes (light symbols).

6.3.2 Country Rock

The country rocks into which the False Bay dykes are intruded include the Malmesbury Group, Cape Granite Suite and Table Mountain Group. In this study and the discussion that follows, reference to the Cape Granite is restricted to samples of the S-type Peninsula Granites exposed at the Cape Peninsula. Samples from the Peninsula Granite and the Malmesbury Group were also analysed during this study for Sr- and Nd-isotopes with the view that the results described

Table 6.2: $^{87}Sr/^{86}Sr$ and $^{143}Nd/^{144}Nd$ isotope ratios of the False Bay dyke swarm with initial values recalculated to 130 Ma. Present day $^{87}Rb/^{86}Sr$ and $^{147}Sm/^{144}Nd$ calculated using GEODATE. Data given in order of decreasing MgO concentration.

Sample	LB-07	GCH89-22	GCH89-11	LB-11
Dyke Location	LB1	TK2	CP1	LB2
MgO (wt %)	7.42	7.29	7.27	7.03
Isotope ratios				
$^{87}Sr/^{86}Sr \pm 2\sigma$ measured	0.706671 ± 12	0.706850 ± 13	0.707372 ± 12	0.706703 ± 11
$^{87}Sr/^{86}Sr$ (130Ma)	0.706368	0.706441	0.706950	0.706341
$^{87}Rb/^{86}Sr$ (present day)	0.1641	0.2210	0.2284	0.1956
$^{143}Nd/^{144}Nd \pm 2\sigma$ measured	0.512509 ± 9	0.512516 ± 6	0.512498 ± 8	0.512497 ± 9
$^{143}Nd/^{144}Nd$ (130Ma)	0.512378	0.512386	0.512371	0.512370
εNd (130 Ma)	-1.81	-1.66	-1.94	-1.97
$^{147}Sm/^{144}Nd$ (present day)	0.1545	0.1535	0.1496	0.1494
Sample	GCH89-03	GCH89-33	GCH89-28	GCH89-45
Dyke Location	SB	MP	FG1	OD2
MgO (wt %)	6.12	5.81	5.29	5.16
Isotope ratios				
$^{87}Sr/^{86}Sr \pm 2\sigma$ measured	0.707569 ± 16	0.707304 ± 11	0.707628 ± 10	0.707854 ± 14
$^{87}Sr/^{86}Sr$ (130Ma)	0.707233	0.706751	0.706810	0.707395
$^{87}Rb/^{86}Sr$ (present day)	0.1816	0.2994	0.4421	0.2483
$^{143}Nd/^{144}Nd \pm 2\sigma$ measured	0.512473 ± 6	0.512511 ± 6	0.512498 ± 7	0.512469 ± 7
$^{143}Nd/^{144}Nd$ (130Ma)	0.512351	0.512396	0.512383	0.512349
εNd (130 Ma)	-2.33	-1.46	-1.72	-2.36
$^{147}Sm/^{144}Nd$ (present day)	0.1432	0.1348	0.1332	0.1416
Sample	FBD-601	GCH89-31	GCH89-39	LB-50
Dyke Location	RI	FG2	SL	SW
MgO (wt. %)	5.05	5.01	4.73	4.63
Isotope ratios				
$^{87}Sr/^{86}Sr \pm 2\sigma$ measured	0.709223 ± 10	0.708965 ± 15	0.717372 ± 12	0.713931 ± 17
$^{87}Sr/^{86}Sr$ (130Ma)	0.707939	0.708050	0.716053	0.712746
$^{87}Rb/^{86}Sr$ (present day)	0.6942	0.4949	0.7135	0.6414
$^{143}Nd/^{144}Nd \pm 2\sigma$ measured	0.512559 ± 7	0.512466 ± 7	0.512362 ± 6	0.512405 ± 5
$^{143}Nd/^{144}Nd$ (130Ma)	0.512416	0.512354	0.512250	0.512278
εNd (130 Ma)	-1.06	-2.28	-4.3	-3.76
$^{147}Sm/^{144}Nd$ (present day)	0.1681	0.1320	0.1320	0.1491
Sample	LB-40	GCH89-17	LB-33	GCH89-07
Dyke Location	CL1	CP5	OD1	CP2
MgO (wt %)	4.34	4.13	3.01	2.74
Isotope ratios				
$^{87}Sr/^{86}Sr \pm 2\sigma$ measured	0.721096 ± 18	0.717324 ± 17	0.724626 ± 16	0.723599 ± 10
$^{87}Sr/^{86}Sr$ (130Ma)	0.716861	0.714957	0.720114	0.720323
$^{87}Rb/^{86}Sr$ (present day)	2.2906	1.2805	2.4409	1.7718
$^{143}Nd/^{144}Nd \pm 2\sigma$ measured	0.512341 ± 7	0.512371 ± 6	0.512337 ± 6	0.512253 ± 7
$^{143}Nd/^{144}Nd$ (130Ma)	0.512222	0.512257	0.512224	0.512134
εNd (130 Ma)	-4.85	-4.17	-4.81	-6.57
$^{147}Sm/^{144}Nd$ (present day)	0.1395	0.1346	0.1327	0.1396

Table 6.3: $^{87}Sr/^{86}Sr$ and $^{143}Nd/^{144}Nd$ isotope analysis of three Cape Granite Suite and two Malmesbury Group samples. Error in measured value (m) is given by 2sigma and values are recalculated to 130 Ma for comparison with the False Bay dyke swarm.

Rock Type	Cape Granite Suite			Malmesbury Group	
Sample	CG-A1	CJ-08	CJ-12	MM-001	NM-012
Location	Cable Way Quarry	Sea Point	Sea Point	Grotto Bay	Robben Island
$^{87}Sr/^{86}Sr \pm 2\sigma$ (m)	0.782517 ± 12	0.780039 ± 17	0.779631 ± 10	0.731160 ± 12	0.778917 ± 14
$^{87}Sr/^{86}Sr$ (130Ma)	0.76472	0.76305	0.76291	0.72717	0.76451
$^{143}Nd/^{144}Nd \pm 2\sigma$ (m)	0.512177 ± 7	0.512174 ± 7	0.512213 ± 9	0.512149 ± 5	0.512054 ± 5
$^{143}Nd/^{144}Nd$ (130Ma)	0.51209	0.51207	0.51210	0.51205	0.51195
εNd (130 Ma)	-7.5	-7.9	-7.2	-8.2	-10.1

previously for the False Bay dykes might have been influenced by interaction with country rock during intrusion. Previously published Sr-isotope data are available for the Cape Granite (Allsopp and Kolbe, 1965), while for the Malmesbury Group both Sr-isotope (Allsopp and Kolbe, 1965) and Nd-isotope data (Buggisch et al., 2010) exist and have been incorporated in the graphs that follow. However, both isotope systems have never before been analysed in combination on common samples for either the Cape Granite suite or the Malmesbury Group. Therefore, four samples (two Malmesbury and two granite) were analysed at both UCT and GFZ for $^{87}Sr/^{86}Sr$ and $^{143}Nd/^{144}Nd$ and one further granite sample from the Higgovale Quarry, was also analysed at UCT. The complete geochemical data set, including major and trace elements by XRF, as well as ICP-MS traces are listed in Appendix C, whereas Sr-Nd isotopic data corrected to the same False Bay dyke swarm age of 130 Ma for comparison are given in Table 6.3. The Malmesbury Group samples give $^{87}Sr/^{86}Sr_{130Ma}$ of 0.7645 and 0.7272 for the Robben Island sample (NM-012) and Grotto Bay sample (MM-001), respectively. The $^{143}Nd/^{144}Nd_{130Ma}$ ratio for the same samples is 0.5121 and 0.5120, respectively. The three samples of Cape Granite show relatively limited variation in isotopic ratios and give an average of 0.7636 for $^{87}Sr/^{86}Sr_{130Ma}$ and 0.5121 for $^{143}Nd/^{144}Nd_{130Ma}$.

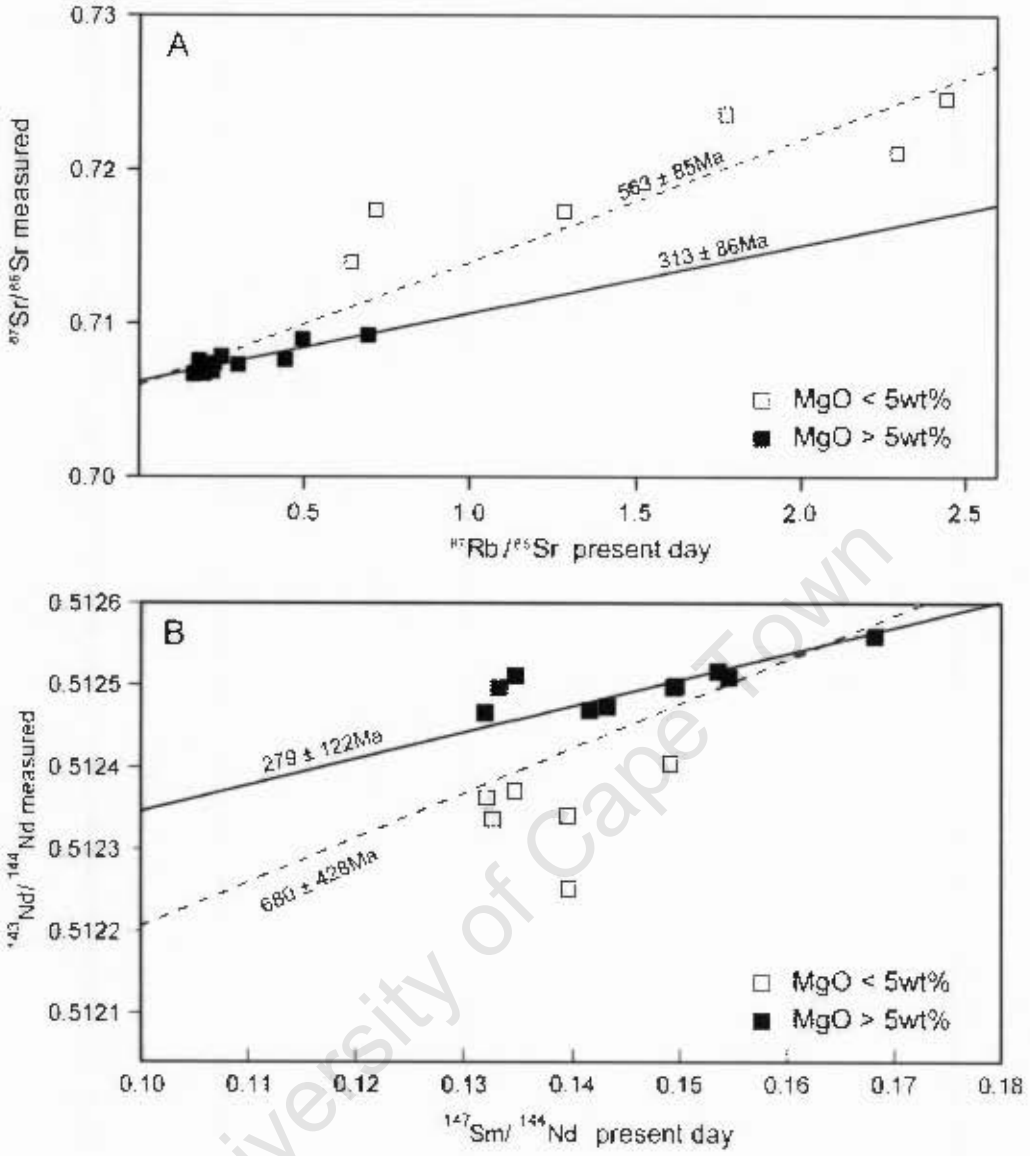

Figure 6.12: Plot of Rb-Sr (A) and Sm-Nd (B) regression calculations. Solid line represents high-MgO trend and dashed line represents the high- and low-MgO trend with samples represented by closed and open symbols respectively.

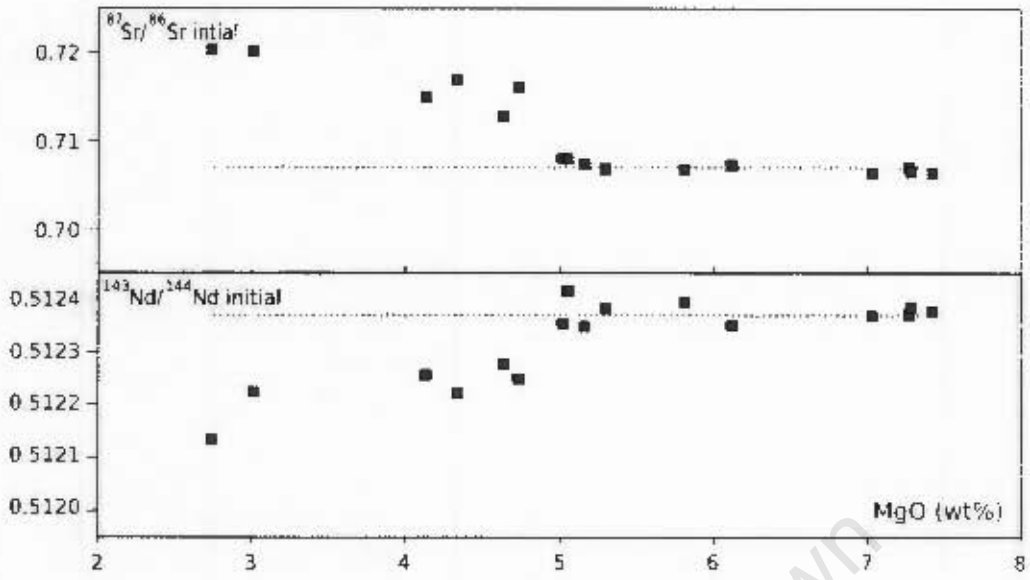

Figure 6.13: Plots of Sr- and Nd-isotope ratios vs MgO.

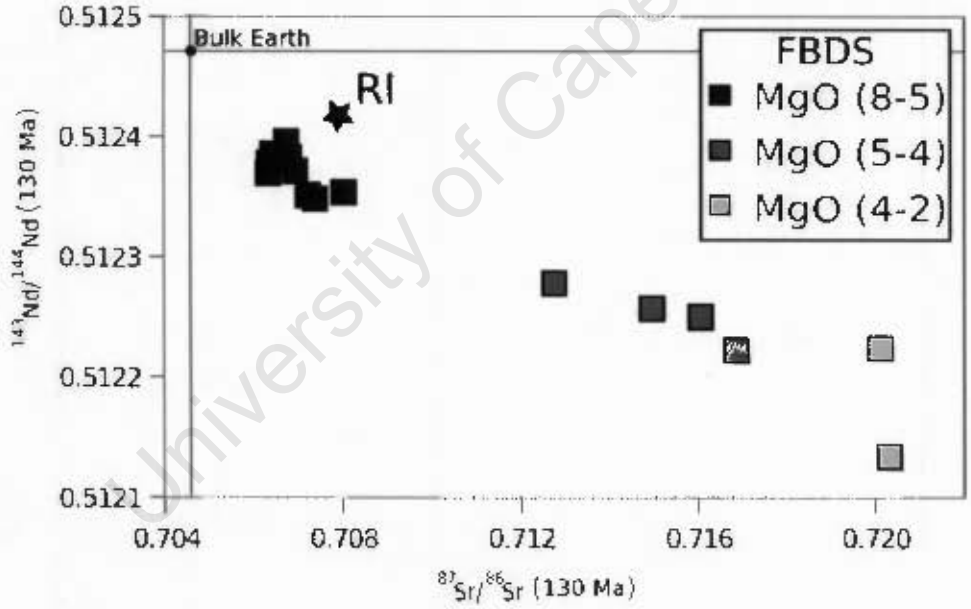

Figure 6.14: Sr- vs Nd-initial isotope ratio recalculated to 130 Ma. The Robben Island dyke (RI) is highlighted and the dyke swarm is subdivided into MgO groups (See legend).

6.4 Correlating dykes exposed along strike

Limited exposure away from shoreline outcrops around the Cape Peninsula make it difficult to track individual dykes along their strike and separate dolerite outcrops that lie approximately along strike have been tentatively assumed to be the same dyke. Day (1987) provided one means of correlation based on magnetic anomalies interpreted as lineaments and another based on dyke petrology and geochemistry, specifically the degree of differentiation, is explored here. It is permissible to relate dykes based on their composition, having established that limited chemical variations exist within dykes. Further, blocks of dolerite have been noted in some building operations around Cape Town and their compositions have been determined for purposes of establishing possible sources. This was included in order to establish if the samples represent dykes not mapped in this study (see Chapter 3), or if they belong to known outcrops.

6.4.1 Logies Bay and Tokai Dykes

The two dykes most likely to be grouped together are the largest dolerite dykes from Logies Bay and Tokai, which line up along strike (Chapter 3, Figure 3.1). From field and petrographic evidence this assumption can already be drawn, as both are greater than 30 m wide (not seen in any other location) and have coarse grained (> 2 mm) interiors. These are the only olivine-phyric dykes found in the dyke swarm and thin sections from both localities are essentially identical. A lower estimate for dyke thickness:length ratios is approximately 1:100 with more common aspect ratios of 1 to 2 orders of magnitude smaller (Rubin, 1995), which for a 30 m wide dyke results in a > 30 km length along strike. Before the development of residential areas in the northern parts of Hout Bay, Nell and Brink (1944) mapped a considerable length of the Logies Bay dyke across into Hout Bay, and magnetic maps by Day (1987) also show a continuous linear anomaly for over 20 km (see Chapter 2, Figure 2.6).

Two samples were taken from the Tokai dyke locality (TK1 and TK2) and show slight differences in thin section, in that TK2 is coarser grained than TK1. The geological maps of the Cape Peninsula show a dyke splitting into two splays at Tokai, a feature not observed during

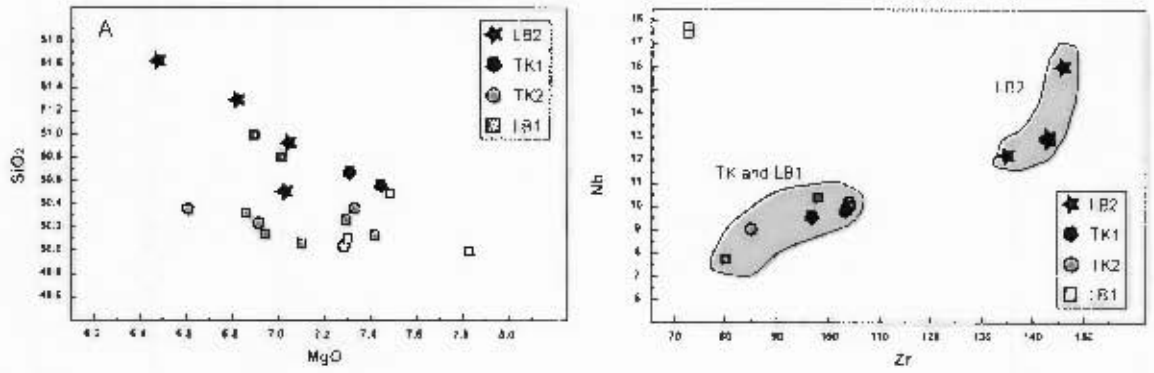

Figure 6.15: (A) Major element and (B) trace element comparison of Logies Bay (LB) and Tokai (TK) dykes.

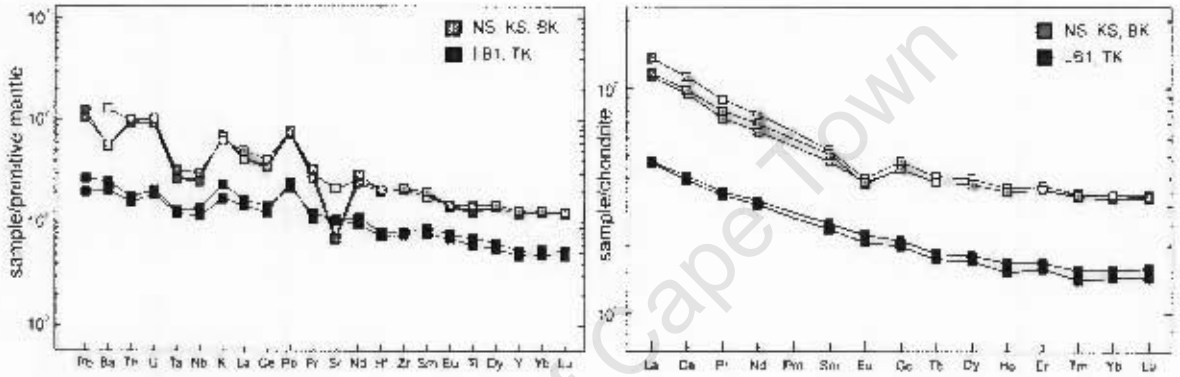

Figure 6.16: Trace element plots of the Logies Bay (LB1), Tokai (TK), Nursery Ravine (NS), Kasteelspoort (KS) and Bakoven (BK) dykes: normalisation values from McDonough and Sun (1995) for primitive mantle (left) and chondrite (right). Open square symbols highlight the enriched Ba and Sr concentrations in the samples from NS relative to samples from KS and BK.

this study; however, the magnetic data does suggest a split in the Tokai area (Day, 1987) and thus was probably used to draw in the contacts. At Logies Bay there are definitely two dykes, with LB1 representing the widest and coarsest intruded by LB2, which is a much smaller, very finer grained intrusive vein (Walker, 1956). Geochemically all the TK and LB dyke samples have compositions which plot at the most MgO-rich end of the SiO_2 vs MgO plot (Figure 6.15A). The Zr and Nb abundances (Figure 6.15B) separate the more enriched LB2 dyke from LB1 and TK. Normalised trace element plots (Figure 6.16) confirm the compositional overlap of the TK and LB1 dykes and would be consistent with them being correlated across the 6 km stretch between the two locations. Therefore, from field, petrographic and geochemical observations, it is plausible to suggest that dolerite outcrops at Logies Bay and Tokai are of the same dyke.

6.4.2 Bakoven, Kasteelspoort and Nursery Ravine

On the western shore of the Peninsula, just south of Camps Bay, there are two dyke outcrops that fall along strike of one another within the Kasteelspoort ravine that cuts down from Table Mountain, namely the Kasteelspoort and Bakoven dykes (Figure 3.11 and 3.10). Field outcrops are no longer possible to compare, as the Bakoven residential area has been developed and the dyke is only seen as individual boulders on the beach. It is possible that the boulders have been transported to the beach along the Kasteelspoort valley, but previous studies and geological maps indicate an outcrop of dolerite existed here (Nell and Brink, 1944; Walker, 1956; Theron, 1984).

Following the regional trend of the dyke swarm across Table Mountain and the Twelve Apostles from the Kasteelspoort ravine lies the Nursery Ravine dyke outcrops. Although the country rock is different on each side of the mountain where the dyke outcrops, with Cape Granite at Kasteelspoort and Table Mountain Group at Nursery Ravine, the geometry and petrography of the dykes are very similar. Normalised trace element concentration are shown in Figure 6.16, which groups samples from the three dykes together: Bakoven (BK) - Kasteelspoort (KS) - Nursery Ravine (NS). Small variations exist in the Nursery Ravine dyke, which shows less pronounced negative Sr and Ba anomalies. However, overall the dykes have the same trace element concentrations and show the same degree of enrichment relative to the Logies Bay dyke.

6.4.3 Robben Island

The southern coast of Robben Island has two dyke outcrops that are present in the field as topographic lows in the reef around the island, which have been preferentially eroded and flooded by the sea, compared to the folded greywacke and siltstone beds of the Malmesbury Group. Recent sediments cover the interior of the island. The composition and petrography of samples collected from both outcrops are identical and the dyke is presumed to extend under the Quaternary cover present on Robben Island suggesting a minimum strike length of approximately 2 km, well within the range of a typical aspect ratio for a 15m wide dyke (Rubin, 1995). Both dyke samples plot as clustered outliers in many geochemical plots (e.g. higher Cu content, Fig-

ure 6.5) and the most noticeable common geochemical difference of the Robben Island dykes is the shallower slope of REE chondrite normalised profile compared to the rest of the swarm (Figure 6.10B).

6.4.4 Waterfront Breakwater sample

The dolerite that was sampled from the old Waterfront Breakwater does not show compositions that are common with any dyke currently exposed, which have been sampled for this study. The dyke with the composition that most closely matches the Waterfront sample is from Clifton, which has similar MgO concentration; however, the Cr and Ni concentrations of the Waterfront sample are significantly higher and there are other distinct chemical differences shown in Table 6.1. The geological map of Cape Town (Theron, 1984) shows two dykes located within the city centre close to the Cape Town railway station. These no longer outcrop due to urbanisation, but could have been a possible source for the boulders found at the Waterfront Breakwater.

6.4.5 Silvermine Pathway sample

The dolerite boulder collected from the Silvermine pathway shows a composition, which is similar to one of the Chapman's Peak dykes, namely CP3. The Silvermine Nature Reserve from where the loose sample was collected is roughly along the regional dyke swarm trend from Chapman's Peak, supporting that a possible CP3 strike parallel outcrop could exist here. As field evidence from many localities shows that the dykes intrude the Table Mountain Group sandstones (e.g. Nursery Ravine, Oukaapseweg, Sir Lowry's Pass and Chapman's Peak), it is likely that dykes could exist in the Silvermine Nature Reserve. Certainly the CP3 dyke also clearly shows extension from the Cape Granite up into the overlying sandstone strata, yet no outcrops of dolerite have been found or mapped in the Silvermine Nature Reserve. Alternatively dolerite from the CP3 dyke could have been exposed during the construction of the new Chapman's Peak Drive, where the road was cut back into the mountain and sampling of the loose rock could have been used for pathway demarcation in national parks.

The methodology of comparing the degree of differentiation of the different dykes is appropriate to compare and relate dyke outcrops that are exposed along strike of one another.

Correlating different outcrops to one another means that a smaller number of dykes have been sampled than suggested by the 24 listed dykes locations (Figure 3.1) and therefore less variety of the False Bay dyke swarm composition is recorded. The sample set collected and analysed is, however, the largest sample set available given the limited outcrop of the dyke swarm and the differentiation process that produced the observed geochemical variations is discussed in the following Chapters.

Chapter 7

Petrogenetic Modelling

It was shown in Chapter 6 that the False Bay dyke swarm ranges in composition from basalt to basaltic andesite. The relatively continuous variation from 8% MgO to at 2 wt.% MgO is accompanied by progressive depletion in compatible trace elements such as Ni, Cr and Sr, concomitant enrichments in the immobile incompatible trace elements Zr, Nb and the LREE. Other elements like V also define continuous trends, but these involve maxima at intermediate MgO. All the geochemical variations are broadly consistent with the progressive removal of a typical gabbroic mineral assemblage including olivine, pyroxenes, plagioclase and Fe-Ti oxides. In this chapter the possible role of fractional crystallisation processes on producing the observed chemical variation will be investigated quantitatively.

Closed-system fractional crystallisation appears to be ruled out for the entire magmatic suite since the radiogenic isotope data reported in Chapter 6 show significant variation. Progressive changes in isotope ratios in the lower MgO basaltic andesites with differentiation suggest assimilation of an isotopically distinct material. Thus the quantitative petrogenetic modelling needs to explore combined assimilation and fractional crystallisation.

7.1 Fractional Crystallisation and High-MgO Dykes

Limited variation in initial Sr- and Nd-isotope ratios permit the basaltic dyke compositions with > 5 wt.% MgO to be modelled as products of closed system fractional crystallisation (FC) with no or little crustal contamination. Phenocrysts of olivine, clinopyroxene and plagioclase are

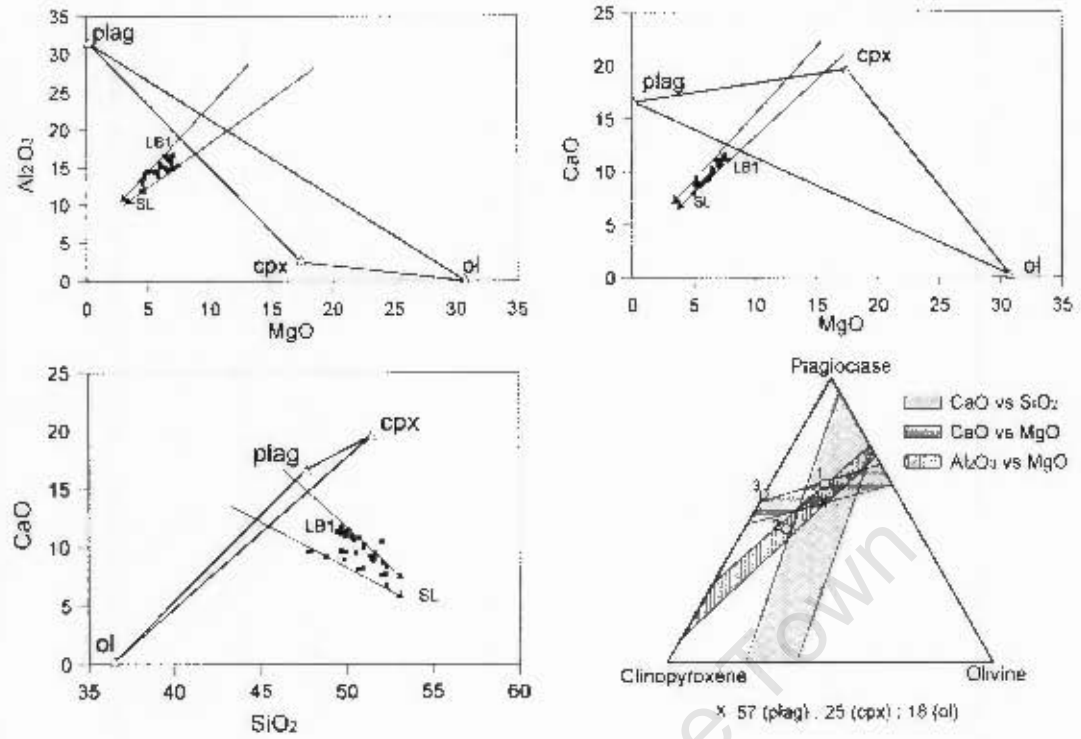

Figure 7.1: Mineral control lines using plagioclase, clinopyroxene and olivine as dominant fractionating phases. The data cloud includes only the high-MgO samples from highest MgO contents (Logies Bay dyke LB1) to approximately 5 wt% MgO (Sir Lowry's Pass dyke SL). Composition of minerals determined by microprobe analysis (Reid, 1990). Bottom right triangle combines all three plots to produce a range of modal proportions, represented by the overlap of mineral control fields. Best fit regression lines through data produce mineral control lines with mineral fractionation mode represented by "x" on the figure. Labelled open symbols (1, 2 and 3) represent mineral modes determined by MIXER (Table 7.2).

commonly observed at the chilled margins of dykes, where these are identified. Binary plots of the more abundant major oxides have been utilised to relate the compositional trend lines followed by the dykes to combinations of the three major phenocryst phases (Figure 7.1). Although the near linear cloud of data points represent a fan of projections through the range (solid arrows in Figure 7.1), the best estimate for the relative proportions of olivine : clinopyroxene : plagioclase is 18 : 25 : 57. The overlap of the fields from the three binary plots predicts a range of mineral proportions that are broadly similar to mineral modes predicted by Mixer (open circles 1 and 2 in Figure 7.1). The third mineral mode predicted by Mixer (open symbol number 3) plots outside of the field defined in Figure 7.1, because olivine is no longer a fractionating phase (see discussion on Mixer results below). Application of crystallisation models using the MELTS program (Ghiorso and Sack, 1995), adopting an Fe^{3+}/Fe^{2+} ratio of 0.15,

Table 7.1: Partition coefficients of selected trace elements in plagioclase and clinopyroxene taken from McKenzie and O'Nions (1991), Jenner et al. (1993), Bindeman et al. (1998), Paster et al. (1974) and Villemant et al. (1981). The values listed here lie within the range of published values for low pressure tholeiitic basalts as available from the online GERM partition coefficient database (http://earthref.org/GERM/).

Element	Clinopyroxene	Plagioclase	Element	Clinopyroxene	Plagioclase
Rb	0.01	0.1	Gd	0.3	0.066
Sr	0.067	2.00	Tb	0.31	0.06
Y	0.72	0.03	Dy	0.33	0.055
Zr	0.128	0.01	Ho	0.31	0.048
Ba	0.01	0.3	Er	0.3	0.041
La	0.054	0.27	Tm	0.29	0.036
Ce	0.098	0.20	Yb	0.28	0.031
Pr	0.15	0.17	Lu	0.28	0.025
Nd	0.21	0.14	Hf	0.233	0.01
Sm	0.26	0.11	Ta	0.04	0.06
Eu	0.31	0.73			

predicted olivine, plagioclase and clinopyroxene phases as liquidus minerals, when applied to samples from the least evolved dyke with the highest MgO content (e.g. sample LB-07 from Logies Bay 1 dyke with 7.4 wt.% MgO) at relatively low pressures (1 kbar). Olivine compositions estimated by the MELTS program range from Fo_{69} down to Fo_{50-40}, which is broadly consistent with the observed range (Fo_{72-56}) (Reid, 1990). According to MELTS, olivine disappears from the liquidus assemblage at about 6% MgO (Millers Point dyke, MP) and this is consistent with the absence of this mineral in the more differentiated dykes.

Least squares mixing models for major elements were calculated using the program Mixer (based on the methodology of Bryan et al., 1969). Computation of least squares mixing as one interval for the range 7.4 to 4.7 wt.% MgO, spanning the high-MgO dyke group, did not produce satisfactory results. Therefore, the compositional suite was sub-divided into three intervals at 7.4 to 7.0, 7.0 to 5.8 and 5.8 to 4.7 wt.% MgO, to model fractional crystallisation of the separate intervals individually in order to allow for changes in crystallising assemblages. A summary of the results is shown in Table 7.2. Agreement between computed and observed compositions is measured by the sum of the squares of residuals, with values of 0.05 - 0.32, indicating a satisfactory to reasonable match, respectively, for the results shown in Table 7.2. Intervals two and three were calculated using the observed compositions of the dykes and not

Table 7.2: Least squares mixing results, of selected intervals (1-3) covering the high-MgO compositional range. Samples used in calculations are LB-07 for Logies Bay 1 (LB1), LB-11 for Logies Bay 2 (LB2), GCH89-33 for Millers Point (MP) and GCH89-39 for Sir Lowry's (SL) (see Table 6.1). Average olivine, clinopyroxene and plagioclase compositions from sample GCH89-47 (Appendix D), listed at the top of the table, were used in least squares calculations and are taken from microprobe results from sample GCH89-47, which is from the Logies Bay dyke (see Table 4.2). Relative mineral modes during a fractional crystallisation process are presented below the results. The percent of fractionation is given by the value for $(1-F)*100$, where F is the proportion of residual melt remaining after each fractionation interval. n.d. = not determined.

	SiO2	TiO2	Al2O3	FeO	MnO	MgO	CaO	Na2O	K2O	
Mineral compositions (input)										
Olivine	36.48	0.00	0.00	32.67	0.51	30.83	0.24	n.d.	n.d.	
Plagioclase	49.74	n.d.	30.40	0.63	n.d.	0.12	15.02	2.84	0.14	
Clinopyroxene	52.17	0.65	2.55	8.16	0.20	17.13	19.43	0.25	n.d.	
Interval 1 (LB1 - LB2): 7.4 to 7.0 wt% MgO										
Obs.	50.13	1.22	16.92	9.63	0.17	7.42	11.63	2.20	0.50	
Calc.	50.10	1.14	16.91	9.69	0.18	7.39	11.71	2.38	0.45	
Diff.	-0.03	-0.08	-0.01	0.06	0.01	-0.03	0.08	0.18	-0.05	$\sum R^2 = 0.05$
melt portion (F) = 0.67 (33% fractionation)										
Interval 2 (LB2 - MP): 7.0 to 5.8 wt% MgO										
Obs.	50.51	1.63	15.02	11.48	0.20	7.03	10.01	2.40	0.66	
Calc.	50.51	1.72	15.05	11.41	0.22	7.11	10.77	2.38	1.01	
Diff.	0.00	0.09	0.03	-0.07	0.02	0.08	0.76	-0.02	0.35	$\sum R^2 = 0.14$
melt portion (F) = 0.79 (21% fractionation)										
cumulative melt portion (F) = 0.53 (47% fractionation)										
Interval 3 (MP - SL): 5.8 to 4.7 wt% MgO										
Obs.	51.16	2.1	14.54	12.26	0.23	5.81	9.36	2.8	1.27	
Calc.	51.22	2.03	14.36	12.26	0.47	5.43	9.57	2.76	1.1	
Diff.	0.06	-0.07	-0.18	0.00	0.24	-0.38	0.21	-0.04	-0.17	$\sum R^2 = 0.32$
melt portion (F) = 0.64 (36% fractionation)										
cumulative melt portion (F) = 0.34 (66% fractionation)										

Mineral mode results					Plagioclase proportions
Interval	Olivine	Plagioclase	Clinopyrox.	Magnetite	plag/(plag + cpx)
1	13	64	23	0	0.74
2	10	46	44	0	0.51
3	0	56	38	6	0.60

Table 7.3: Comparison of measured analysis and modelled values of selected trace element compositions across the high-MgO group with sample LB-07 as the starting composition. Values were calculated using the Raleigh fractional crystallisation (see text). Partition coefficients (D) for trace elements are shown in Table 7.1. Melt portions (f) and mineral modes used to calculate bulk D for each interval is taken from major element models (Table 7.2). Olivine and magnetite is taken as D = 0.000 for the element list (see text).

Sample	LB-07	LB-11				GCH89-33				GCH89-39			
Dyke	LB1	LB2				MP				SI			
MgO content (wt%)	7.4	7.0				5.8				4.7			
interval melt portion (f)	1.00	0.87				0.79				0.64			
Element	start	analysis	calculated	difference	absolute %diff	analysis	calculated	difference	absolute %diff	analysis	calculated	difference	absolute %diff
Rb	11.9	14.40	17.53	3.13	21.73	37.10	16.12	-12.98	41.74	51.00	47.96	-3.04	5.97
Sr	209	213	186	-26.76	12.58	301	215	-85.56	28.47	207	282	74.61	36.04
Y	21	30	28	-1.02	3.46	37	34	-3.24	8.75	58	51	-7.09	12.23
Zr	80	135	118	-17.10	12.67	171	168	-3.68	2.15	289	261	-21.59	7.63
Ba	138	181	159	9.06	5.01	324	221	-102.40	31.65	408	468	60.45	14.82
La	9.5	14.6	13.2	-1.39	9.55	24.8	17.8	-6.81	27.63	33.0	35.7	2.66	8.06
Ce	20.9	32.4	29.4	-3.02	9.31	52.2	39.7	-12.52	23.99	71.0	76.3	5.28	7.41
Pr	2.76	4.25	3.89	-0.36	8.41	6.40	5.18	-1.23	19.15	8.80	9.35	0.55	6.24
Nd	12.3	18.9	17.4	-1.55	8.18	27.4	22.9	-4.42	16.17	38.0	39.9	1.85	4.87
Sm	3.14	4.68	4.45	-0.22	4.72	6.10	5.65	-0.45	7.39	8.30	8.87	0.57	6.92
Eu	1.08	1.49	1.30	-0.19	12.62	1.94	1.67	-0.27	13.68	2.20	2.40	0.20	8.8?
Gd	3.62	5.33	4.43	-0.90	16.84	5.58	6.04	-0.94	13.60	9.60	8.79	-0.81	8.47
Tb	0.58	0.85	0.83	-0.02	2.07	1.06	1.02	-0.03	3.20	1.50	1.54	0.04	2.72
Dy	3.78	5.49	5.39	-0.10	1.75	6.68	6.61	-0.07	1.01	9.60	9.74	0.14	1.43
Ho	0.77	1.11	1.10	-0.01	0.88	1.33	1.35	0.02	1.23	2.00	1.95	-0.05	2.66
Er	2.30	3.30	3.31	0.01	0.29	3.85	4.00	0.15	3.83	5.70	5.66	-0.04	0.67
Tm	0.33	0.46	0.47	0.00	1.07	0.52	0.56	0.04	7.84	0.80	0.77	-0.03	3.99
Yb	2.15	3.12	3.11	-0.01	0.44	3.41	3.79	0.39	11.37	5.30	5.03	-0.27	5.01
Lu	0.32	0.46	0.47	0.01	1.35	0.50	0.56	0.06	12.19	0.80	0.74	-0.06	7.27
Hf	2.14	3.45	3.12	-0.33	9.68	4.28	4.24	-0.05	1.09	5.10	6.42	1.32	21.04
Ta	0.48	0.70	0.67	-0.03	4.41	1.23	0.87	-0.36	28.94	1.40	1.88	0.48	33.99
Average % difference					7.00				14.52				9.82
Range					22 to 0				42 to 1				36 to 1

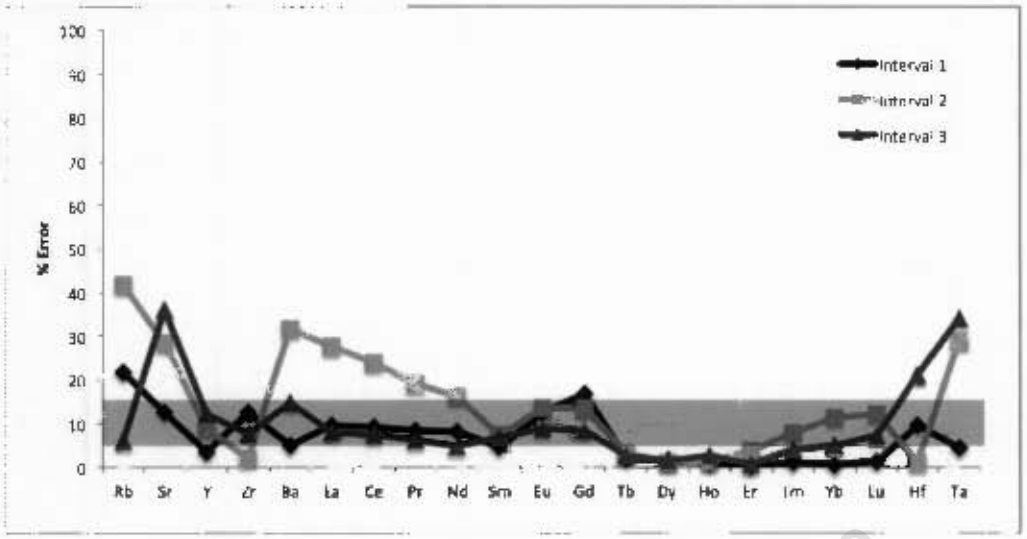

Figure 7.2: Percent difference of trace element modelling for the 3 intervals defined for the high-MgO dykes. Shaded block indicates the average percent difference from 7 - 15%.

the resultant calculated composition from the preceding interval, therefore the error measurements refer to calculations of its respective interval only and not a cumulative error. Various combinations of mineral compositions were computed using Mixer. Combining end-member fayalite and forsterite compositions as an input file into the Mixer program, resulted in a range of olivine compositions, but typically the most agreeable results produced olivine compositions of Fo_{75-60}. For plagioclase, least square calculations computing end-member anorthite and albite compositions produced plagioclase compositions of An_{75-79} for the most agreeable computations in the first and second interval. The third interval was considerably lower (An_{50-40}), which is inconsistent with microprobe analyses for the high-MgO dykes shown in Chapter 4 (An_{80-70}, Figure 4.3). The most agreeable results for all three intervals are shown in Table 7.2 and were calculated using the average mineral compositions from microprobe analyses on mineral grain cores from the Logies Bay dyke sample GCH89-47 (see Table 4.2). The compositions are olivine at Fo_{63}, plagioclase at An_{77} and clinopyroxene at En_{48}. Predicted mineral proportions from least squares mixing models show olivine featuring early, but disappearing in later differentiates (see also open circles in Figure 7.1). Fe-Ti oxides as magnetite has been invoked in the end stages of differentiation (third interval) in order to compute agreeable results.

Changes in trace element concentrations during fractional crystallisation can be modelled

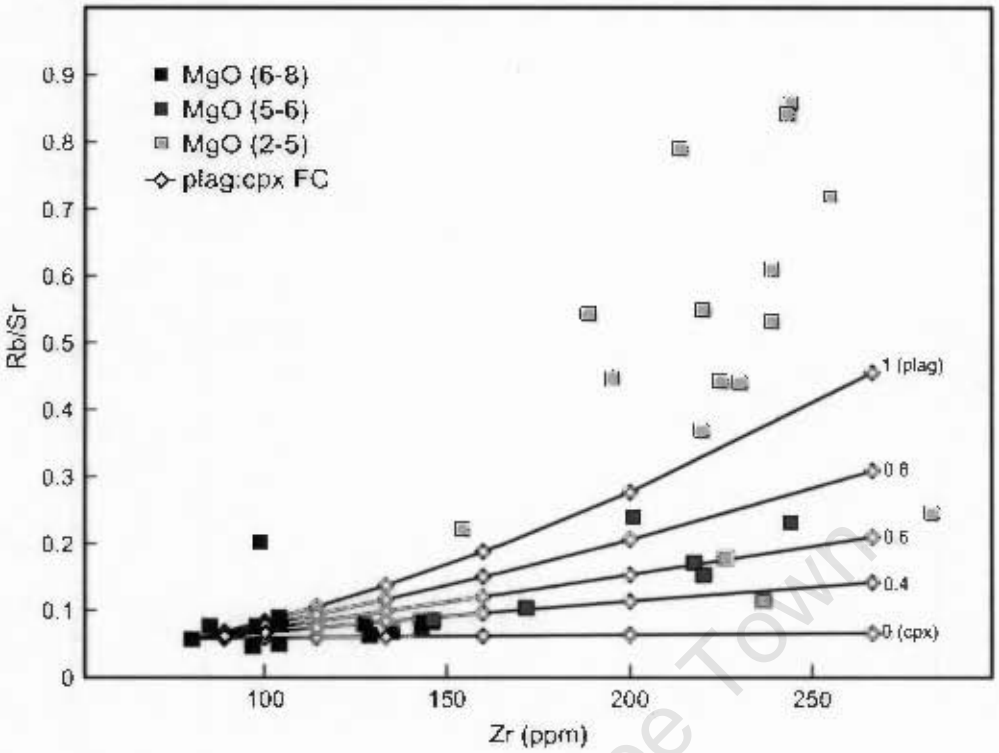

Figure 7.3: Plot of Rb/Sr vs Zr showing different dyke groups based on MgO content (2-5, 5-6 and 6-8 wt%). Also plotted are curves representing up to 70 % Rayleigh fractional crystallisation of a magma having the composition of the from the dyke sample with the lowest Zr content. Intervals of 10% F are indicated along the curves for varying plagioclase and clinopyroxene proportions, where the value shown next to each line represents the total proportion of plagioclase as a fractionating phase (plagioclase/(plagioclase+clinopyroxene)) . Element partition coefficients are shown in Table 7.1.

using the Rayleigh fractionation equation (Gast, 1968), where C^l = residual element concentration in the daughter rock, C^o = original element concentration in the parent rock, F = residual melt portion (taken from major element least squares modelling, Table 7.2) and D = bulk partition coefficient of the modelled elements (partition coefficients shown in Table 7.1) and the equation is given by:

$$C^l \quad C^0 * F^{(D-1)} \tag{1}$$

Results for trace element calculations are show in Table 7.3 and, in general, show a good agreement between the calculated and observed values with an average percent difference of 7 - 15% (Figure 7.2). The percent difference is acceptable given the range in published partition coefficient values for the elements that were calculated (http://earthref.org/GERM/). The low proportion of magnetite in the fractionating assemblage (Table 7.2) with typically low partition

coefficient values does not introduce unacceptable errors (see Figure 7.2). Olivine and magnetite partition coefficients are set equal to 0.000, mostly acceptable for the elements listed in Table 7.1. Models of fractional crystallisation trends for Rb/Sr and Zr are shown for varying plagioclase proportions (Figure 7.3). The Rb/Sr ratio is one that may be affected by contamination or alteration. Alteration was assessed to be negligible in the fresh dolerite samples with LOI of < 2 wt.%. Table 7.3 shows a large misfit between calculated and observed Rb and Sr concentrations for the second interval (sample GCH89-33). The misfit and highest average percent difference of 15% for the second interval can be explained by the anomalous dykes identified within the range of 5 to 6 wt. % MgO (Millers Point (MP), Froggy Pond (FG1), Oatland Point (FG2), Oudekraal 2 (OD2) and Robben Island (RI)), plotting away from the general trend defined by the end-member samples from the dyke suite (see Chapter 6, Figures 6.5 and 6.6). Although these dykes show anomalies in various elements, their Sr and Nd isotope ratios are within the range of the high-MgO group, which suggests that they are less affected by assimilation and are modelled here as part or end of the FC process. Variations in the Rb/Sr ratio can typically be used to test for fractional crystallisation throughout the differentiation process, comparing observed chemical variations with modelled curves for different modes of mineral fractionates, but considering the larger compositional range (e.g. variations in Rb and Sr) of some of the dykes mentioned above, care needs to be taken when interpreting Figure 7.3. Individual curves do not explain the total variation of the high-MgO dykes and some samples plot on or below the 100% clinopyroxene curve. The Rb/Sr vs Zr plot suggests a broad range in fractionation of mineral modes of approximately 40 to 80% plagioclase and 60 - 20% clinopyroxene. Although these results define a broad range, the mineral modes are in reasonable agreement with least squares mixing models (Table 7.2). Most notably however, Figure 7.3 shows the clear departure of the low-MgO group from the high-MgO group, in having much higher Rb/Sr ratios.

The geochemical variations of the False Bay dolerite magma for dyke samples with > 5 wt.% MgO are broadly consistent with closed-system fractional crystallisation (Tables 7.2 and 7.3). Most dykes with lower MgO concentrations (< 5 wt.%) are not consistent with a fractional crystallisation model involving any ratio of plagioclase and clinopyroxene proportions (Figure

7.3). Obvious changes in $^{87}Sr/^{86}Sr$ and $^{143}Nd/^{144}Nd$ isotope ratios in the low-MgO group further suggest an alternative model needs to be established to explain the chemical variation of these more evolved dykes.

7.2 Crustal Assimilation in Low-MgO Dykes

Certain incompatible trace element abundances, trace element ratios and initial Sr- and Nd-isotope ratios in the more differentiated members of the False Bay dykes (< 5 wt.% MgO) show distinct departures from those expected of closed system fractional crystallisation. The salient feature of these is the progressive change in initial $^{87}Sr/^{86}Sr$ and $^{143}Nd/^{144}Nd$ isotope ratios with decreasing MgO concentrations (Figure 6.13 and 6.14), providing the best evidence for assimilation during magma evolution. The change towards higher Sr- and lower Nd-isotope ratios in the more evolved dykes, suggests that the material assimilated was continental crust. Although the high-MgO group does not appear to be affected by a progressive crustal contamination with decreasing MgO content from 8 to 5 wt.%, it is important to note that even the high-MgO dykes have higher initial Sr- and lower initial Nd-isotope ratios than Bulk Earth and could already represent a contaminated parental magma prior to their intrusion. Fields for various crustal provinces in south-western Africa have been added to Figure 7.4 for purposes of identifying the most suitable source of contaminant. The variation for the Malmesbury Group and Peninsula Granites of the Cape Granite Suite were determined from samples analysed in the present study together with published Sr-isotope data from Allsopp and Kolbe (1965) and Nd-isotope data from Buggisch et al., (2010). The Malmesbury Formation and the Cape Granites are the most obvious candidates for crustal contaminants, as the False Bay dykes intrude these rocks, and xenoliths of granite are found hosted in the dolerite dykes. As only the Peninsula Granite of the Cape Granite suite is exposed at the Cape Peninsula and was sampled, reference to Cape Granites in the discussion that follows is restricted to the S-type Peninsula Granites of the Cape Granite Suite. Da Silva et al. (2000) showed similar εNd for both S- and I-type granites, therefore parts of the discussion could be pertinent to the entire Cape Granite suite, but the details require further studies. In keeping with their Neoproterozoic - Cambrian age, the fields

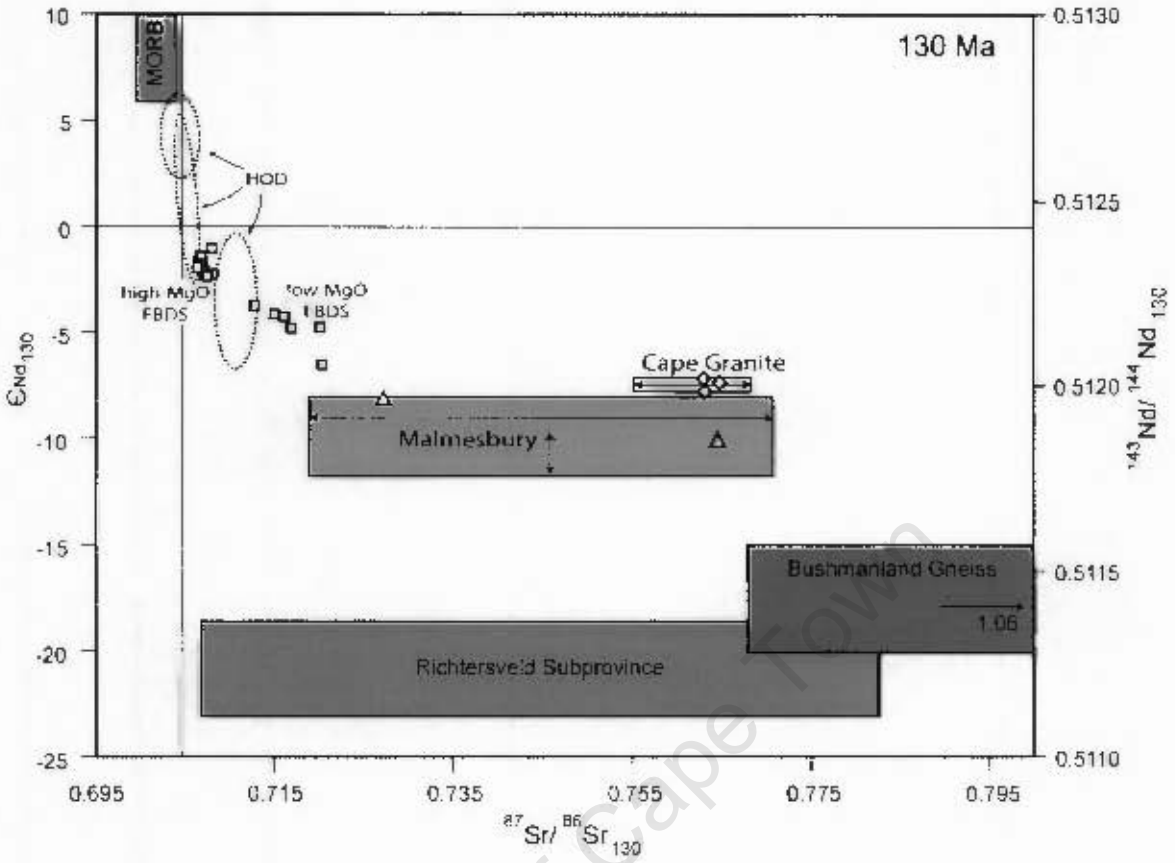

Figure 7.4: Initial Sr isotope and εNd plot for the False Bay dyke swarm samples (FBDS) (all data fields at 130 Ma). Open symbols from data collected from this study for the False Bay dykes (squares), Malmesbury Group (triangles) and Cape Granites (diamonds). The Sr range (solid double-headed arrows) for the Malmesbury Group and Cape Granite fields is defined by data from Allsopp and Kolbe (1965). Range in εNd (dotted double-headed arrow) for the Malmesbury Group field is from data published by Buggisch et al. (2010). Fields for the Bushmanland Terrane (Reid et al., 1997), Richtersveld Subprovince (Reid et al., 1987; Reid, 1997), Namibian Henties Bay Outjo dyke swarm - HOD (Trumbull et al., 2007) and MORB (Hofmann, 1997) have been included for comparison.

for Malmesbury Group and Cape Granite plot at an intermediate εNd, compared to that occupied by older terranes such the Palaeo- to Mesoproterozoic Namaqua Province, represented by the Richtersveld Subprovince (1.9 Ga) and Bushmanland Terrane (1.2 - 1.0 Ga).

The fields of Namaqua-Natal Belt terranes cover a large range (Figure 7.4) and a sample of the Bushmanland Terrane (Reid et al., 1997) was chosen to compare assimilation models between Mesoproterozoic basement (with significantly lower Nd-isotope ratios) and that of Neoproterozoic Malmesbury Group and Cape Granite basement. Although it is clear from the compositional range of existing Namaqua-Natal Terrane data that various different mixing

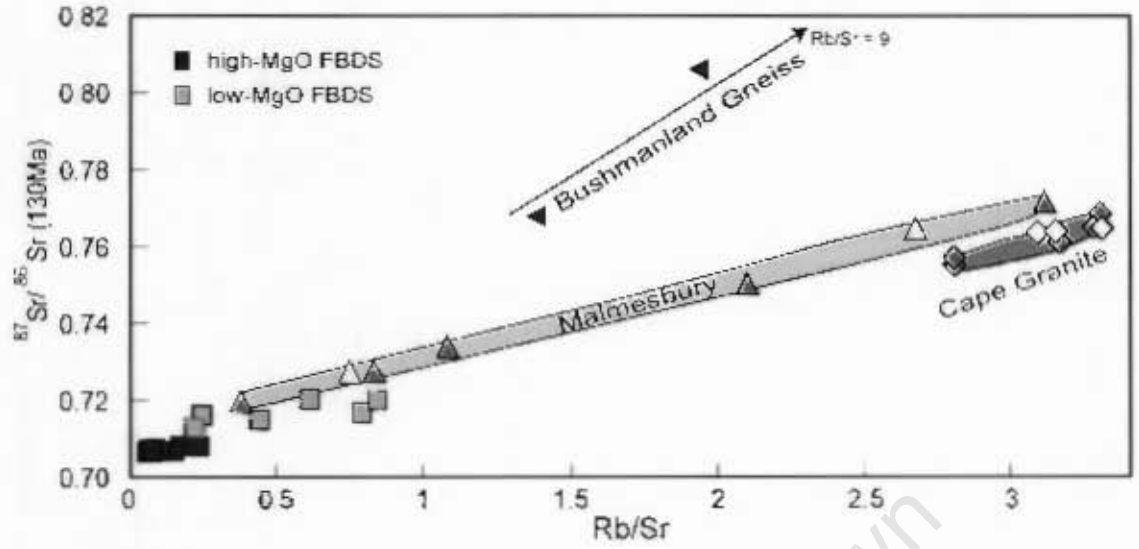

Figure 7.5: Plot of $^{87}Sr/^{86}Sr$ vs Rb/Sr showing compositional fields of Cape Granite (diamonds) and Malmesbury Group (upright triangles) samples and the Bushmanland Terrane (Reid et al., 1997). Open symbols for Malmesbury Group and Cape Granite from this study, whereas filled symbols are from Allsopp and Kolbe (1965). The False Bay dyke swarm is divided into high- and low-MgO groups (see legend).

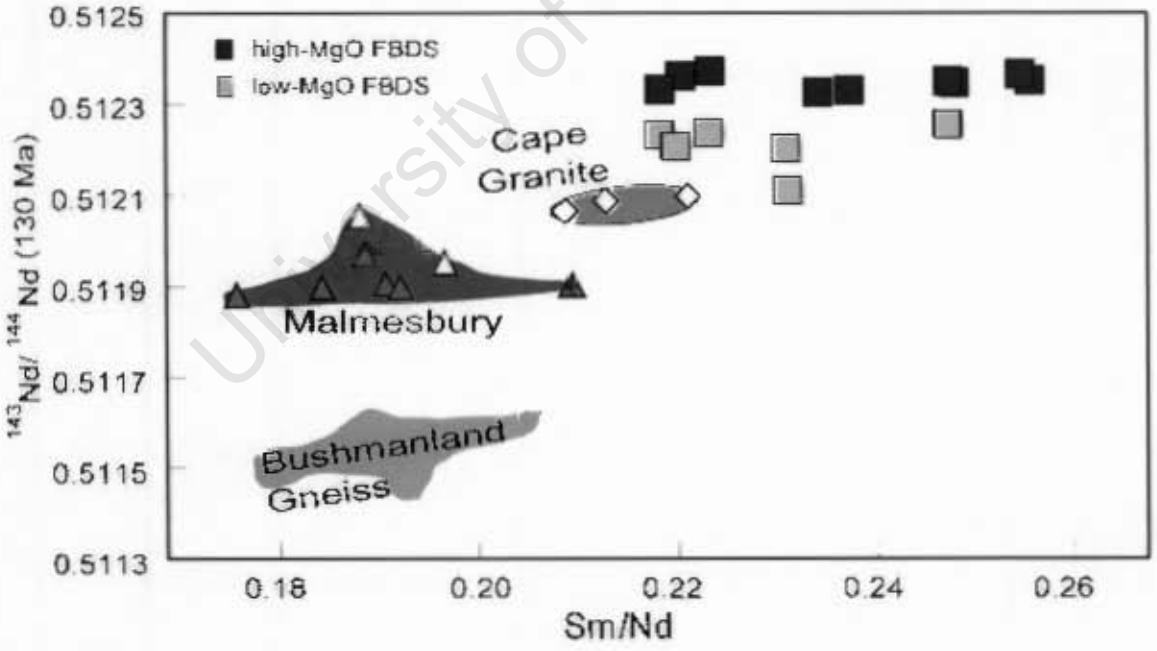

Figure 7.6: Plot of $^{143}Nd/^{144}Nd$ vs Sm/Nd showing compositional fields of Cape Granite (diamonds) and Malmesbury Group (upright triangles) samples and the compositional field of the Bushmanland Terrane (Reid et al., 1997). Open symbols for Malmesbury Group and Cape Granite from this study, whereas filled symbols (Malmesbury Group only) are from Buggisch et al. (2010). The False Bay dyke swarm is divided into high- and low-MgO groups (see legend).

curves would result, the generally higher Sr-isotope ratios and *particularly* the much lower Nd-isotope ratios consistent for the older basement allow for comparison of modelled mixing and assimilation curves for isotopically distinct older Bushmanland Terrane and younger Malmesbury Group and Cape Granite. The $^{87}Sr/^{86}Sr$ and $^{143}Nd/^{144}Nd$ isotope ratios of the dyke swarm are compared with crustal compositions of Cape Granite, Malmesbury and Bushmanland Gneiss in Figure 7.5 (for Rb-Sr) and Figure 7.6 (for Sm-Nd). In the Rb-Sr system the dykes trend towards the Cape Granite Suite and the Malmesbury Group and are consistent with a mixing line. The Malmesbury Group forms a trend parallel to that of the dykes, where the higher $^{87}Sr/^{86}Sr$ ratios generally belong to shales and siltstones (e.g. sample NM-012) and the lower $^{87}Sr/^{86}Sr$ ratios correspond to greywacke (e.g. MM-001). Mixing of the magma with pure greywacke suggests that the most differentiated dykes, which overlap with $^{87}Sr/^{86}Sr$ isotope and Rb/Sr ratios of greywacke, to be 100% greywacke, while increasing proportions of shale/siltstone would decrease the required amount of assimilation - a more likely model. Bushmanland Terrane gneisses form an array with a much steeper slope with higher ratios of Rb/Sr and $^{87}Sr/^{86}Sr$. It is likely that the Namaqua-Natal Province as a whole has a much broader spread in trace element composition and radiogenic isotope ratio than represented solely by the Bushmanland Gneisses, and the models should be taken only as an indication of the different effects of Meso- to Neoproterozoic assimilation. A plot of $^{143}Nd/^{144}Nd$ vs Sm/Nd ratios shows a less well defined trend compared to that of the $^{87}Sr/^{86}Sr$ vs Rb/Sr plot (Figure 7.5), but similarly the low-MgO group plots towards crustal compositions (Figure 7.6). All three crustal compositions fall within the array of mixing lines that could account for the compositional change from high- to low-MgO dykes.

Simple mixing curves calculated using the equations by Langmuir et al. (1978) for both trace elements and radiogenic isotopes are shown in Figure 7.7. As the high-MgO dykes are shown to be consistent with essentially closed-system fractional crystallisation, mixing curves are calculated using a dyke with intermediate MgO content (OD2 with 5.2 wt.% MgO). In Figure 7.7 the low-MgO dykes, which were analysed for Sr- and Nd-isotope ratios are also plotted and the most evolved dyke (CP2 with 2.7 wt.% MgO) is labelled along with OD2 to show the least and most evolved of the low-MgO dykes. The most evolved dyke, CP2, also

Table 7.4: Concentration data used for simple mixing models in Figure 7.7. Data for Bushmanland sample NF-66 from Reid et al. (1997). Composition of low-MgO dykes plotted in Figure 7.7 are also shown in order of decreasing MgO.

	OD2 dyke	SL dyke	CL1 dyke	CP5 dyke	OD1 dyke	CP2 dyke	Cape Granite		Malmesbury Group		Bushmanland
Sample	GCH89-45	GCH89-39	LB-40	GHH89-17	LB-33	GCH89-07	CG-08	CG-A1	MM001	MM012	NF-66
Rb	21.7	51	134.1	80.25	133.5	98.3	238	109	101	153	302.5
Ba	240	408	372	413	408	614	364	247	499	491	n.d.
Sr	252.4	207.0	169.6	181.5	158.5	160.8	75.4	33	136	57.2	105.2
Y	34.8	58.0	44.0	42.0	47.9	52.8	21	14	30	19	n.d
Nd	22.4	39.0	30.4	34.1	38.1	37.8	23.9	20.3	38.2	25.3	40.3
Sm	22.41	8.30	7.01	7.60	8.36	9.18	4.99	4.32	7.18	4.97	7.72
Rb/Y	0.62	0.88	3.05	1.91	2.78	1.86	11.33	7.79	3.37	8.05	n.d
Ba/Sr	0.95	1.97	2.19	2.28	2.58	3.82	4.83	7.48	3.67	8.58	n.d
Sm/Nd	1.00	0.22	0.23	0.22	0.22	0.24	0.21	0.21	0.19	0.20	0.19
Rb/Sr	0.09	0.25	0.79	0.44	0.84	0.61	3.16	3.30	0.74	2.67	2.87
87Sr/86Sr (130Ma)	0.7079	0.7161	0.7169	0.7150	0.7201	0.7203	0.7629	0.7647	0.7272	0.7640	0.9020
143Nd/144Nd (130Ma)	0.51235	0.51225	0.51222	0.51226	0.51222	0.51213	0.51207	0.51209	0.51205	0.51177	0.51157

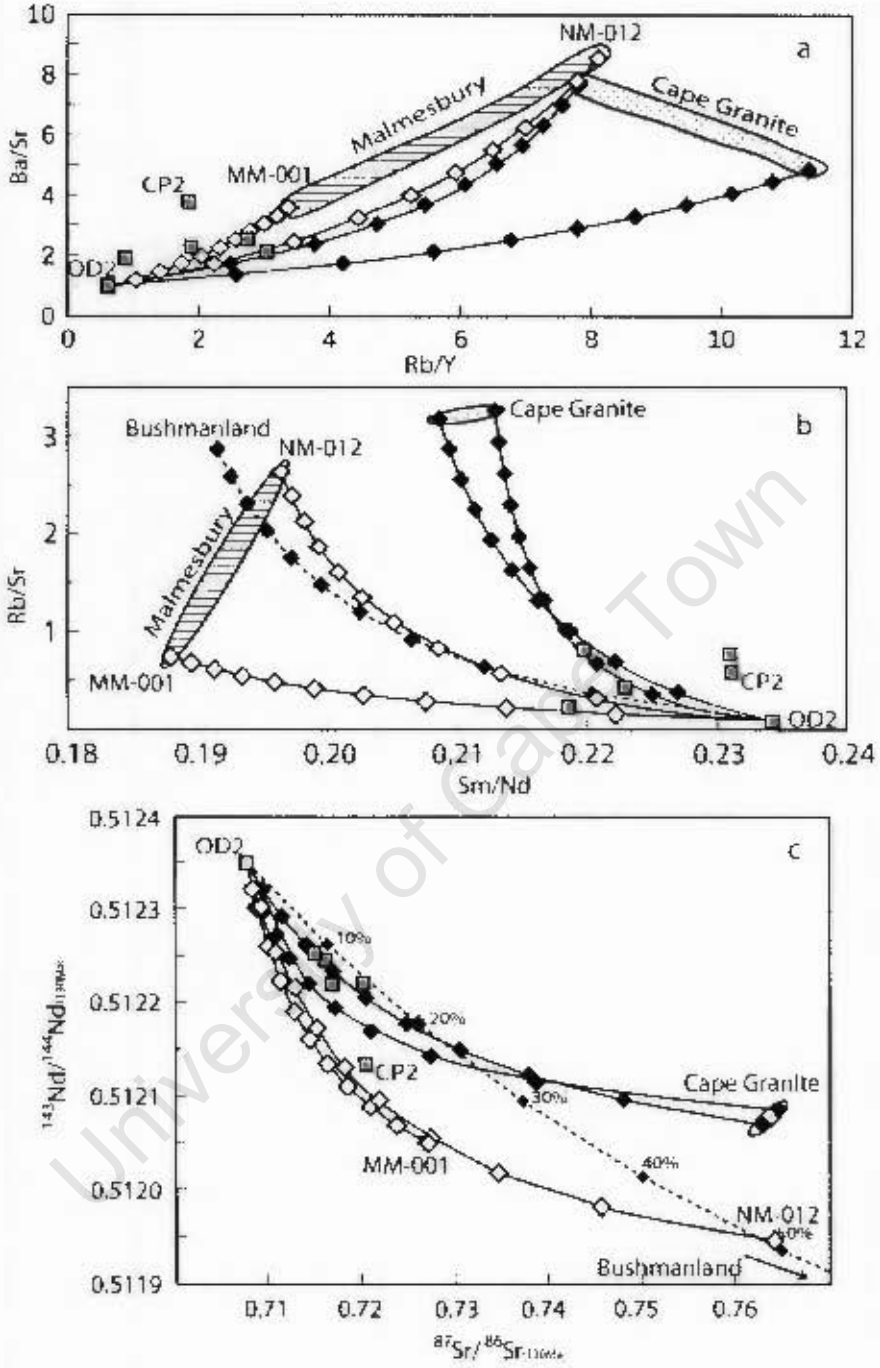

Figure 7.7: Selected trace element ratio (a, b) and Sr- and Nd-isotope ratio (c) simple mixing curves (Langmuir et al., 1978). Mixing was calculated using a dyke with intermediate MgO concentration (OD2 with 5.2 wt% MgO) and mixing with Malmesbury (samples MM-001 and NM-012, open diamonds), Cape Granite (samples CJ-08 and CG-A1, filled diamonds) and Bushmanland Terrane gneiss (sample NF-66 (Reid et al., 1997), dashed line, solid diamonds). Ticks on curves are shown at 10% mixing increments (diamond symbol). Low-MgO dyke samples shown in grey squares and sample GCH89-07 (CP2) indicates the most evolved dyke composition.

shows the most extreme Sr- and Nd-isotope ratios of the dyke suite (Figure 7.7c), however in Figure 7.7a and b, CP2 does not show the most evolved Rb/Y, Rb/Sr and Sm/Nd element ratios. Although it is clear that not a single mixing curve can account for all of the variation in the low-MgO dykes, individual samples could be explained by a combination of mixing curves involving both Malmesbury and Cape Granite. The plot of Ba/Sr vs Rb/Yb shows the best agreement with the sample MM-001 from the Malmesbury group of up to 70 % mixing, whereas a smaller 10 to 20 % of mixing is shown with samples NM-012 from the Malmesbury Group and/or Cape Granite (Figure 7.7a). Element ratios of Rb/Sr and Sm/Nd show mixing proportions of 10 to 30 % Cape Granite and Malmesbury to account for the variation seen in the dyke suite (Figure 7.7b). Observed variations of the Sr- and Nd-isotope ratios in the low-MgO dykes correlate to about 50 to 60% mixing with Cape Granite and sample NM-012 (Figure 7.7c). Although some samples can be adequately explained in one plot, overall the mixing patterns are inconsistent for trace elements and isotope ratios, in that the degrees of mixing vary considerably between the different modelled curves: for example 20% for trace element ratios and 50% for isotope ratios. Compositional heterogeneity of the country rocks, which is not covered in the simple mixing models above, or mixing of multiple components could overcome this lack of fit. Nevertheless, mixing with either Cape Granite and/or Malmesbury Group to an extent of 60%, which is required to explain the isotope ratio variations, is unlikely to be consistent with the observed range in trace element ratios that relate better to smaller amounts of mixing (Figure 7.7a and b) and dyke magmas would be unlikely to maintain a less evolved basaltic andesite composition of the low-MgO dykes with respect to their major element compositions.

It is accepted that assimilation of crustal material (specifically at larger quantities of assimilation) is achieved by melting and therefore is an endothermic process resulting in cooling and therefore crystallisation of the magma (e.g. Thirlwall and Jones, 1983). Contamination of hot basaltic magma is likely to be accompanied by cooling and resulting fractionation when assimilating crustal rocks, making a simple mixing model unrealistic. Rather, combined assimilation and fractional crystallisation (AFC) modelling is applied here to assess the amount of assimilation and the nature of the crustal component involved. DePaolo (1981) presented a model

that describes both assimilation and fractional crystallisation. The concentration of a selected element during assimilation and fractional crystallisation is governed by the equations below, where C_m = concentration in melt, C_l = concentration in residual melt, dC_m = change in element concentration during AFC, F = residual melt portion, C_a = concentration in assimilant, r = mass assimilation/mass fractionation, and D = bulk partition coefficient:

$$dC_m/d(lnF) = \frac{r}{r-1}C_a - zC_m \quad (2)$$

where:

$$z = \frac{r+D-1}{r-1} \quad (3)$$

and:

$$C_l = C_m + dC_m \quad (4)$$

Similarly for isotope ratios DePaolo (1981) defined the equation below, where E_m = original isotope ratio of magma, E_l = isotope ratio in residual magma, dE_m = change in isotope ratio during AFC:

$$dE_m/d(lnF) = \frac{r}{r-1}C_a/C_m * (E_a - E_m) \quad (5)$$

and:

$$E_l = E_m + dE_m \quad (6)$$

Equations (4) and (6) are then used to calculate element concentration and isotope ratio variations at 10 % intervals of differentiation, which are defined by the residual melt portion (F). Figure 7.8 shows the effects of AFC observed from modelled curves with a starting composition of a dyke with an intermediate composition of 5.2 wt.% MgO (OD2, sample GCH89-45), which has equal trace element ratios and isotope ratios to the high-MgO group (i.e. mostly unaffected by assimilation). Resulting curves for AFC involving contaminants of Cape Granite, Malmesbury Group and Bushmanland Gneiss are shown in Figure 7.8. Simple mixing lines for Cape Granite and Malmesbury Group are also shown. Bulk partition coefficients are calculated for fractional crystallisation of 60% plagioclase and 40% clinopyroxene (Table 7.5), based on the assumption that the FC portion of differentiation in the low-MgO dyke group is broadly similar

Table 7.5: Input data for AFC model (Figure 7.8). Bulk partition coefficients for trace elements calculated for 60% plagioclase and 40% clinopyroxene fractionating modes. This ratio is based on the FC portion of the model being broadly similar to the results for high-MgO group of dyke compositions (see text, Figure 7.1 and Table 7.2 for details).

Input data	Sample	Source	Rb	Sr	Nd	Sm	$^{87}Sr/^{86}Sr_{130}$	$^{143}Nd/^{144}Nd_{130}$
False Bay dyke	GCH89-45	this study	21.7	252	5.3	22.4	0.70729	0.51235
Cape Granite	CJ-12	this study	247	79.5	24.2	5.4	0.76291	0.51164
Malmesbury Group	NM-012	this study	153	57.2	25.3	5.0	0.76451	0.51195
Bushman and T.	NF-66	Reid et al. (1997)	301	81	42.9	7.8	0.88344	0.51155
Partition Coefficients (D)			Rb	Sr	Nd	Sm		mode
Plagioclase			0.07	2.00	0.14	0.11		0.6
Clinopyroxene			0.00	0.07	0.21	0.28		0.4
Bulk D			**0.04**	**1.23**	**0.17**	**0.17**		

to what has been used in the high-MgO FC models. The calculations are done at 10% crystallisation increments used to construct the curves. A critical variable in AFC models is the mass assimilation / mass crystallisation ratio (r) and curves are labelled according to their respective r-value. Given the same r-value, assimilation of granite results in a higher $^{87}Sr/^{86}Sr$ for a given F compared to the Malmesbury Group, whereas the opposite is true for $^{143}Nd/^{144}Nd$. Even the high mass assimilation to crystallisation ratio ($r = 0.4$) used to calculate AFC curves involving these assimilants does not reproduce the most extreme isotope ratios of the low-MgO dykes, which at 70% crystallisation implies that 28% of the differentiation is attributed to assimilation. The alternative source suggested here, the Mesoproterozoic Namaqua-Natal Province (using the Bushmanland Gneiss as an example), produces a more satisfactory fit to the models for both $^{87}Sr/^{86}Sr$ and $^{143}Nd/^{144}Nd$ isotopes. Using a Mesoproterozoic basement sample as the contaminant, results in a model with a lower mass assimilation to crystallisation ratio (r = 0.1 to 0.2), requiring less than half the amount of assimilation at a given stage of fractionation compared to assimilation of Neoproterozoic Malmesbury Group or Cape Granite. Although neither model exactly reproduces all of the observed values of the low-MgO dykes, Figure 7.8 highlights the more reasonable fit of the model using a Mesoproterozoic contaminant.

The above model was calculated from one sample (GCH89-45 from dyke OD2) and it is likely that this dyke does not represent the parent magma for all of the low-MgO dykes and from the model it is clear that not one single curve will be able to explain every evolved sample. Possibly the Sm/Nd ratio (and also the Rb/Sr ratio) of the assimilant (or assimilants) is variable and defines rather a field, which encompasses the actual contaminant. Further, the modelling is based only on the Rb-Sr and Sm-Nd isotope systems. Although not all trace element variations

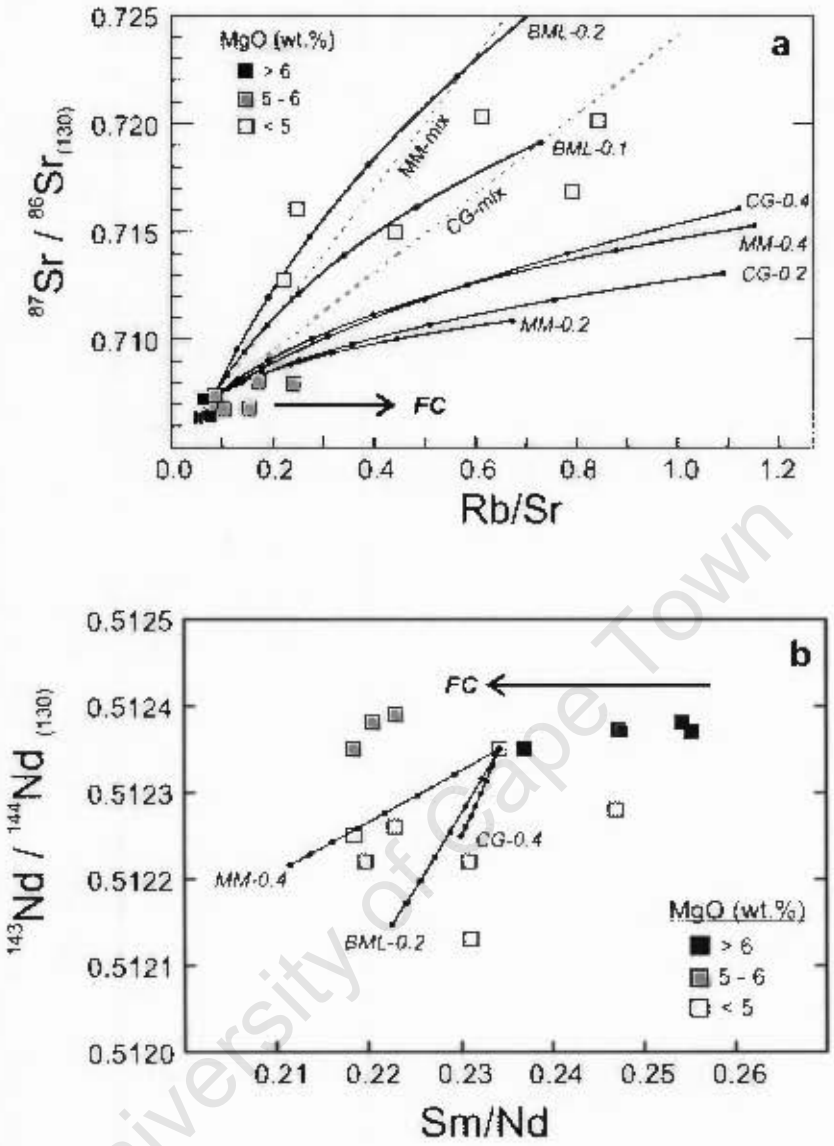

Figure 7.8: Assimilation and fractional crystallisation models of magma evolution in the False Bay dyke swarm. Model AFC curves start from sample GCH89-45 with 5.2 wt.% MgO (dyke OD2), and represent a range of f = 1 to 0.3 (30% melt remaining), with tic marks at intervals of 10%. Labels indicate the crustal component and r-value used for each curve (CG-Cape Granite, MM-Malmesbury metasediments, BML-Bushmanland gneiss). The arrows labeled FC show trends for fractional crystallisation only. (a) The Rb-Sr model results are not consistent with assimilation of Cape Granite and Malmesbury Formation, but are consistent with assimilation of Bushmanland Gneiss. Binary mixing of Cape Granite and Malmesbury are shown (dashed lines). (b) The Sm-Nd data plots with a first stage magma evolution of no change in Nd isotopic composition (high-MgO samples), after which crustal assimilation progressively lowers $^{143}Nd/^{144}Nd$ ratios. AFC models starting from sample GCH89-45 (labeled curves with tic marks) show that Bushmanland gneiss can produce the observed Nd- isotopic range at moderate r-value of 0.2, whereas the Cape Granite and Malmesbury curves do not reach the most evolved isotope ratios, even for $r = 0.4$. Bulk partition coefficients used in the calculations are given in Table 7.5. Compositional data are from Cape Granite (sample CJ12) and Malmesbury Group (sample NM-012), and for Bushmanland Gneiss (Reid et al., 1997) (Table 7.5).

show the same distinction between Meso- and Neoproterozoic assimilants, many incompatible trace elements and trace element ratios show distinct variations in samples with < 5 wt.% MgO. The departures of trace element ratios in the low-MgO group from the high-MgO group are also indicative of contamination and are included here for completion. One example is the Ce/Pb ratio (Figure 6.7D), which decreases from 8 in the high-MgO samples to 5 in the low-MgO samples. The lower Ce/Pb ratio can be explained by a greater increase of Pb compared to the increase of Ce, by assimilating an enriched crustal source, which would have had lower Ce/Pb ratios (Hofmann, 1989). Figure 7.9 highlights the Nb-Yb-Th relationships, with the high-MgO group plotting at the upper limit of the mantle array, whereas the low-MgO group plots between the mantle array and the continental crust on a sub-vertical trend away from the less evolved dykes. Element ratios of Th/Yb and Nb/Yb show a narrow range in the least evolved dykes (6 to 8 wt.% MgO), whereas the dykes with 5 to 6 wt. % MgO composition (dykes RI, MP, FG1 an FG2) define a linear trend nearly parallel to the mantle array with the 6 to 8 wt.% MgO cluster at its centre. The dykes that occupy the range from 5 to 6 wt. % MgO were identified in earlier element plots (Figures 6.5 and 6.6) in having anomalous compositions and these same dykes are identified and labelled in Figure 7.9. The low-MgO dykes show a broader compositional range compared to the 6 to 8 wt. % MgO dykes. The field defined by the low-MgO dykes defines a migration of the magma composition towards crustal components from the cluster of the high-MgO group (see arrow in Figure 7.9). Pearce (1982) used a similar plot (Ta-Yb-Th) to discuss crustal contamination and differentiation vectors, but Nb instead of Ta (Figure 7.9) is preferred here, because of the greater availability of Nb data for some of the crustal sources. Substituting Nb for Ta is suitable for these samples as Nb and Ta both show similar incompatible behaviours across the compositional range, even in the anomalous dyke samples: see plot of Nb vs Zr (Figure 6.6c) and Ta vs Hf (Figure 6.7a), where Hf and Zr show a strong positive correlation (Figure 6.6e).

A possible explanation for the misfit between modelled and observed isotope ratio variations is that the AFC model, as used above, represents a bulk assimilation process. Mixing with *partial* melts from, inter alia, Malmesbury Group, Cape Granite and Bushmanland Gneiss could be a more realistic contamination processes that would account for higher incompatible

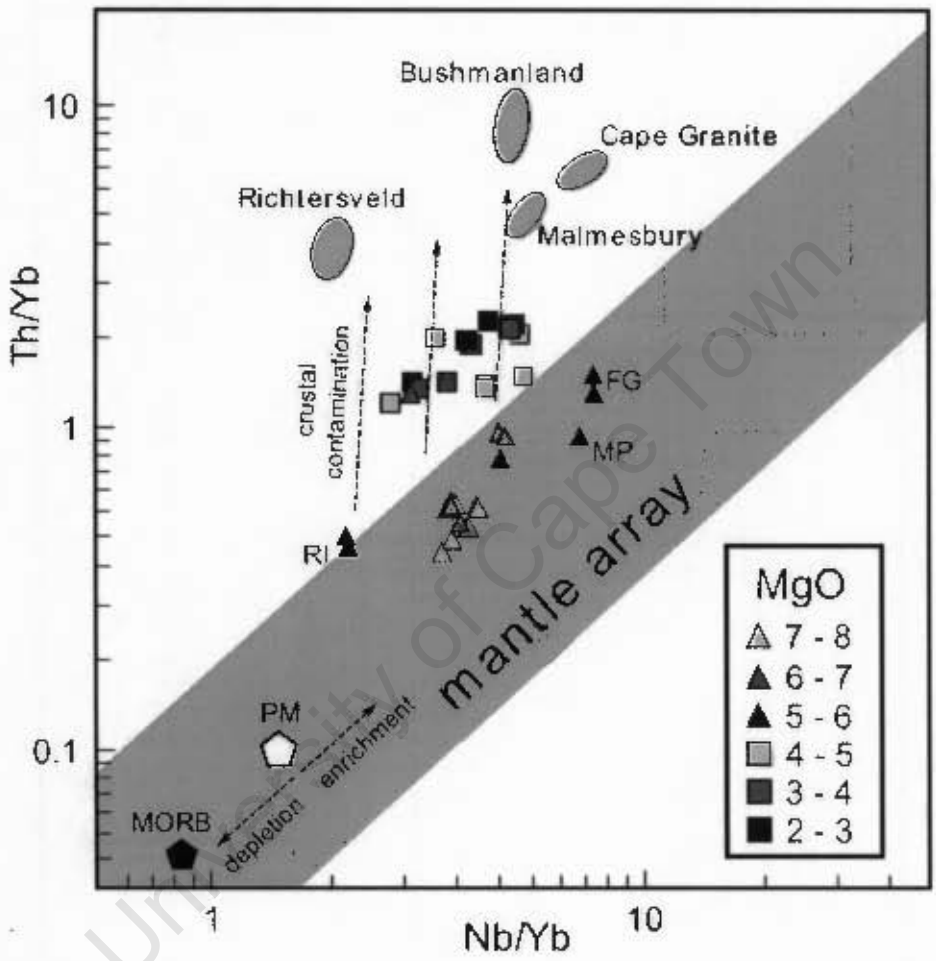

Figure 7.9: Plot of Th/Yb vs Nb/Yb Pearce (adapted from 1982). Symbols show different MgO groups (triangles = high MgO samples; squares = low MgO samples) with various possible contamination fields shown. Cape Granite and Malmesbury Formation (this study), Richtersveld Subprovince (Reid, 1997) and Bushmanland Gneiss (Reid et al., 1997). Mantle array, MORB (Hofmann, 1997) and Primitive Mantle (PM) (Pearce, 1982) are included for comparison. Robben Island (RI), Millers Point (MP), Froggy Pond (FG) and Oatland Point (FG) dykes are labelled.

trace element input for smaller amounts of assimilation. Partial melting is well documented in the literature (Zeng et al., 2005; Vásquez et al., 2009), where partial melts from the wall-rock or engulfed wall-rock material are mixed into the magma, leaving a restitic wall-rock material that is not mixed into the magma. Different elements are concentrated into specific minerals (Sr for example is preferentially concentrated into feldspar), but of particular significance is the fact that other trace elements such as Sm and Nd are bound into accessory phases (zircon or xenotime). For example, partial melting of feldspar into an intruding magma would have profound affects on Sr concentrations, whereas Sm and Nd concentrations would not change by assimilation of many major phases such as feldspar. Therefore, addition of many trace elements into the magma is restricted to the melting behaviour of their respective minerals in a particular rock (Zeng et al., 2005). This means that for certain refractory minerals (like zircon) disequilibrium melting can result in the partial melt having a lower Zr (and other trace elements) content than application of batch melting equations would suggest. Assimilation is a far more complex process than modelled here and in order to produce a more comprehensive model, more information about the crustal sources is required than is currently available.

However, the mixing and AFC models (Figures 7.7 and 7.8) do show an important difference involving contaminants of Malmesbury Group and Cape Granite compared to an older Namaqua-Natal Province rock, such as the Bushmanland Gneiss. Mixing curves incorporating Malmesbury Group and Cape Granite (Neoproterozoic) contaminants show that a much higher proportion of the assimilant is required to achieve the observed change in isotope ratios (50-60%) compared to mixing with melts of the Mesoproterozoic Bushmanland Terrane (10-20%). Similarly, the AFC models show that a lower assimilation/fractional crystallisation ratio (r) incorporating a Bushmanland Terrane contaminant (r = 0.1 to 0.2) achieves a better fit to the data compared to contamination of the Malmesbury or Cape Granite (r = 0.4). Within the scope of this study it is only possible to speculate on how partial melts from these different rocks could differ. But, based on the relatively narrow range of Nd-isotope ratios for each Neo- and Mesoproterozoic terranes and the large difference between them, assimilation or mixing of a partial melt of Cape Granite would probably require a higher assimilation/fractional crystallisation ratio relative to assimilation of a partial melt from the Namaqua-Natal Belt (e.g. of the Bush-

manland Gneiss). Hence, for the purpose of this study the models sufficiently illustrates the assimilation restrictions between Meso- and Neoproterozoic basement, as well as support an assimilation model for the low-MgO False Bay dykes. Whereas studies of mixing, assimilation and/or fractional crystallisation have been much reported on in the literature (e.g. Langmuir et al., 1978; DePaolo, 1981; Pearce, 1982; Thirlwall and Jones, 1983) with variable degrees of success, it must be noted that this thesis lacks a comprehensive geochemical database both in terms of parameters (e.g. additional isotope measurements such as oxygen, lead, hafnium, osmium), as well as limited samples that were analysed due to limited dyke exposure, although the magnetic signature suggests more dyke occurrences (Day, 1987). In addition, the presence of seemingly anomalous outliers in many geochemical plots (the Robben Island dyke is probably the most notable) shows a more complicated transition from high- to low-MgO dykes in the transition from FC to AFC processes. Therefore, this work provides possible causes for the general trends only and the detail will have to await a more in-depth study.

Chapter 8

Discussion

8.1 Tectonic Setting and Intrusion Dynamics

The Cretaceous age of the False Bay dyke swarm (ca 130 Ma Reid et al., 1991) indicated that it is not related to the Karoo igneous province (Duncan et al., 1984, 1990) and thus appears to be related to the 138 - 128 Ma Etendeka - Parana igneous episode (e.g. Renne et al., 1996a,b; Jerram et al., 1999; Kirstein et al., 2001; Trumbull et al., 2004b,a) that preceded the breakup of western Gondwana (e.g. Nürnerg and Müller, 1991). The general NW-SE trend of the dyke outcrops is consistent with the regional magnetic anomaly pattern of the dyke swarm established by Day (1987). The orientation of the dykes also follows the regional development of tensional joints and faults developed in the Table Mountain Group (Figure 3.5). Few dykes have been noted to deviate from the regional trend at the outcrop scale and intrude along older Cape Orogeny structures (Walker, 1956). The older structures developed in the Malmesbury Group, related to the Saldania Belt, are cut by the dyke on Robben Island (Rowe et al., 2010) parallel to the regional trend of the dyke swarm (Figure 3.28-[4]). Therefore, crosscutting relations and most specifically the 130 Ma intrusion age (Reid et al., 1991) are consistent with the formation of the False Bay magmatism being related to the Cretaceous palaeo-rift and breakup of western Gondwana.

Two deep seismic profiles from the region provide insight into the structures and composition of the deeper crust that are relevant to this discussion. One profile oriented ENE-WSW

crosses the continental margin near Springbok, about 700 km north of Cape Town (Hirsch et al., 2009), and 400 km east of Cape Town the other profile trends north-south across the southern margin (Stankiewicz et al., 2007; Lindeque et al., 2011). Both profiles indicate a high velocity layer at the base of the 35-45 km thick crust, which was suggested by Trumbull et al. (2007) and Stankiewicz et al. (2007) to indicate under-plating of breakup-related gabbroic intrusions. The under-plated mafic intrusions are a possible equivalent of the parental magma that gave rise to the intruding dolerite dykes. Basaltic liquidus temperatures are well known from experimental data to be around 1300°C at 15 kbar (e.g. Kogiso et al., 1998). Trumbull et al. (2007) highlighted the contrasting thermal characteristics along the Atlantic margin using petrogeophysical modelling and contrasting MgO concentrations, where the temperature of the False Bay magma was approximately 1300°C, compared to the hotter (1560°C) inferred temperatures for the Namibian HOD dyke swarm. The hotter magma and higher MgO contents in the north is postulated to be associated with the presence of the Tristan Plume (Ernesto et al., 2002), possibly the initial driving force of the breakup of western Gondwana (Morgan, 1981). The plume, however, had no or minimal influence on the dyke swarms and associated gabbroic intrusions further south (Trumbull et al., 2007), which they interpret as being the major influence on the less voluminous magmatism south of the HOD towards False Bay. The contrast in magmatism between north and south is also shown in a deep-seismic profile directly related to the Henties Bay Outjo dyke swarm area in Namibia (Bauer et al., 2000), which shows the same high velocity anomaly at nearly twice the thickness than that farther south.

8.2 Magmatic affinity

The geochemical patterns established for the False Bay dyke swarm indicate parental magmas that were sub-alkaline basaltic with relatively high Fe/Mg ratios typical of tholeiites. Variation in elements such as TiO_2, Zr, Y and Nb in basalts have been used to define separate magma types (Reid, 1990; Trumbull et al., 2007), perhaps produced from different source regions or by degrees of partial melting (Pearce and Norry, 1979). Limited variation in the abundances of these elements at 5-8% MgO, together with relatively homogeneous initial Sr and Nd isotope

ratios restrict the range in possible magma types present in the False Bay swarm. Comparison to other major dyke swarms shows similarities in trace element ratios and normalised element ratios with the Lesotho type (defined by Duncan et al., 1984) of the Karoo dyke swarms (Reid, 1990) and the Tafelberg type (defined by Marsh et al., 2001) of the Henties Bay Outjo dyke swarms (HOD) (Trumbull et al., 2007). These authors and others have suggested that these basaltic magmas were sourced from the sub-continental lithospheric mantle that was heated by the uprise of sub-lithospheric plumes and/or the convecting mantle during passive rifting (Reid, 1990). The False Bay dyke swarm is set apart by limited element ratio variations in the high-MgO group, whereas both the Karoo and the HOD define various fields of element and isotope ratios (e.g. three defined groups of the HOD are circled in and Figure 7.4). An age gap of approximately 50 Ma (Reid et al., 1991) precludes any magmatic relation between the False Bay and Karoo dykes, but Trumbull et al. (2007) argued that similar mantle regions produced both the Tafelberg type and False Bay dykes, the same could be suggested for the Lesotho type of the Karoo.

From field and petrographic observations there is no compelling reason to separate the high-MgO (basalts) from the low-MgO (basaltic andesite) dykes in the FBDS. They show no systematic crosscutting relationships, possess common mineral assemblages and share amygdaloidal textures that preclude any major difference in emplacement depth. It is therefore argued that the FBDS represents a single magma type similar to the HOD Tafelberg or the Karoo central types, but displays distinctive chemical characteristics due to its petrogenetic history discussed below.

8.3 Petrogenesis

The False Bay dyke swarm includes relatively differentiated tholeiitic basaltic andesites, which require derivation from a basalt parent by combined assimilation and fractional crystallisation (AFC). Trumbull et al. (2007) eluded that AFC was a likely process involved in more evolved differentiates and this study shows the different petrogenetic processes that predominately governed two groups of the False Bay dykes. Assimilation of crustal material is best explains

the radiogenic isotope patterns while fractional crystallisation is required to produce the very low Mg# values of < 30, depletion in compatible trace elements (Ni, Cr, Sr, Eu), as well as enrichment in immobile incompatible trace elements (Zr, Nb, Y, LREE). Geochemical variations in the dyke suite form a well defined and continuous differentiation trend from high- to low-MgO dykes as shown in the previous chapters. One unique pair of dykes (LB1 and LB2, Figure 3.14) is in agreement in relative age between geochemical variations and cross-cutting relations, in that LB2 is the younger (intrudes LB1 and shows a quenched margin) and more evolved dyke (lower MgO content). Clifton is the only other location where crosscutting dykes are observed (Figure 3.10-[7]). Unfortunately crosscutting dykes at Clifton were not sampled, and the samples that were collected from Clifton (LB-40 and LB-43) are of dykes that do not intersect (see Chapter 3, dykes CL1 and CL2). Therefore, the comparing relative emplacement timing with degrees of differentiation cannot be further assessed here.

The False Bay dyke swarm has a range in compositions that require a two-stage evolution based on the geochemical variations with decreasing MgO. The high-MgO dykes (5-8%) have constant isotope ratios and can be explained by closed-system FC. The low-MgO dykes (< 5 %) require an open system process such as AFC to account for an increase in Sr- and a decrease in Nd-isotope ratios. Initial differentiation of the False Bay dolerite magma, recorded in the high-MgO dykes, evolved via closed-system fractional crystallisation of mainly plagioclase and clinopyroxene with diminishing contribution of olivine. Fractionation of abundant plagioclase within the parent magma suggests a relatively low-pressure regime of less than 40km depth (~13 kbar). Seismic profiles show under-plated gabbros at depths of 10 to 30km (Bauer et al., 2000; Hirsch et al., 2009), which are thought to be the host magmas of the Cretaceous dyke swarms (Trumbull et al., 2007) and are in good agreement with the depth (pressure) range for plagioclase fractionation. The observed changes in Sr- and Nd-isotopes in the low-MgO dykes are related to assimilation of crustal material (Figure 7.4). The relatively smooth and continuous pattern of geochemical variations, specifically the progressive near linear trend of Sr- and Nd-isotopes towards crustal values (Figure 6.14), as well as spatial relations and common petrographical features of both high- and low-MgO dyke groups are consistent with a genetic link between the two, although the differentiation process for each group differs.

The marked geochemical variations in the low-MgO dykes are compared with AFC models of magma with similar geochemical characteristics to a dyke with intermediate MgO content (e.g. OD2 with 5.2 wt.% MgO) that progressively assimilates crustal materials during further fractional crystallisation. Although the petrogenetic modelling in Chapter 7 does not account for all of the variation seen in the low-MgO dykes, the model curves do show that chemical variations in the low-MgO dykes are consistent with assimilation of crustal material. Assimilation of various crustal materials and speculation on deeper crustal sources are discussed below.

8.3.1 Assimilation of Mesoproterozoic Crust

The most differentiated dykes of the False Bay magma (< 5 wt.% MgO) show evidence for crustal assimilation, which is discussed in this section. Although the high-MgO dykes can be modelled by closed-system fractional crystallisation, it is possible that the parental magma was already contaminated, giving rise to the increased Sr- and decreased Nd-isotope ratios of the high-MgO group relative to Bulk Earth. The low-MgO dykes plot at lower Nd- and higher Sr-isotope ratios than the high-MgO dykes (Figure 7.4) and the change in isotope ratios is correlated with a progressive decrease in MgO (Figure 6.13). Changes in trace element ratios and isotope ratios from the high-MgO group to the low-MgO group define a trend towards compositional fields of crustal materials (Figures 7.9 and 7.4). The results presented in this study are consistent with models involving assimilation of Mesoproterozoic crust (with lower Nd-isotope ratios) as opposed to models involving assimilation of the younger rocks of the Cape Granite or Malmesbury Group. Nevertheless, the dykes in the field occasionally contain certain country rock xenoliths, mostly in the form of Cape Granite (e.g. Oudekraal 1, Millers Point and Froggy Pond). These xenoliths are fresh and competent in exposures and show no clear evidence of melting or mixing into the dolerite magmas, rather the xenoliths have sharp, unaltered edges, which are parallel to the dyke walls, therefore consistent with brittle side wall stoping.

Compositional variations in the Namaqua-Natal Belt are very diverse, even within individual terranes (Figure 2.2), and assimilation of other and/or multiple sources could likely define AFC models with a better fit to the dyke compositions of the low-MgO group. The

models of assimilation of melts derived from Mesoproterozoic terranes better explain the compositional variations of the low-MgO dykes than models involving the assimilation of melt from Neoproterozoic terranes.

Assimilation of a Namaqua-Natal equivalent basement into the intruding magma that fed the False Bay dyke swarm, would imply that there is a likely deeper crustal unit below the Malmesbury Group and Cape Granite, which is of similar geochemical and isotopic composition to that of the Bushmanland Terrane and/or other Namaqua-Natal Province terranes. Even though the Malmesbury Group and Cape Granite likely exist to depths of at least a few to 10s km (the exact depth-extent is not known), the Mesoproterozoic isotopic signatures are a better candidate to model the more evolved dykes, mainly due to smaller volumes of the required contaminant. A study of the deep seismic profile to the east of Cape Town is consistent with the extension and presence of the Namaqua-Natal belt rocks at depths as far south as the Agulhas Fracture Zone (Lindeque et al., 2007, 2011), which south of False Bay traces west across the Atlantic Ocean to the Falkland Islands (Ben-Avraham et al., 1997).

Melting of granitic country rock along the path of the intruding FBDS magma is a distinct possibility. Deep seismic profiles show the presence of high-velocity zones at approximately 30 km depth along the Atlantic continental margin (Bauer et al., 2000; Hirsch et al., 2009), suggesting the presence of significant basaltic material within the rifted crustal profile. The melting curve of granites are such that at about 10 kbar melting will begin at temperatures around 650°C (if water saturated), and is not influenced by small pressure variations (Boettcher and Wyllie, 1968). Solidus - liquidus temperatures of water under saturated granites at 10kbar are 760°C - 1160°C respectively (Huang and Wyllie, 1973).

It can be argued that the temperatures of basaltic magmas would provide sufficient heat to raise the crustal units above their solidus, thereby producing partial melts that could be assimilated. For the incorporation of crustal material into the FBDS magma to be restricted to the more differentiated basaltic andesites, could be explained by a progressive build up of heat during the magmatic event. Only after the establishment of a significant magma chamber (perhaps accompanied by significant closed system crystal fractionation) could the country rock be rendered reactive by partial melting and gain access to the system.

Chapter 9

Conclusions

A series of dyke suites along the Cretaceous western Gondwana palaeo-rift that separated South America from Africa provide evidence for compositionally and volumetrically variable magma generation along the Atlantic continental margin. The False Bay dyke swarm is the southernmost exposed dyke suite and represents a tholeiitic low-Ti-Zr basaltic magma type similar in composition to the Etendeka HOD Tafelberg magma type (Trumbull et al., 2007) and the Karoo Central type (Duncan et al., 1984). At False Bay a restricted range in magma types represents the Etendeka large igneous province and relatively low volumes of dykes are preserved, unlike the polygenetic voluminous magmatic system developed further north in Namibia (Trumbull et al., 2007).

The False Bay dykes have compositions that show a continuous range from basalt to basaltic andesite, which can be explained by a magmatic differentiation model that involves evolution from a fractional crystallisation dominated system (high-MgO dyke group, 8 - 5 wt. % MgO) to that of a differentiation process involving both fractional crystallisation and assimilation (low-MgO dyke group, < 5 wt. % MgO). The high-MgO dykes were produced from a parental magma that experienced closed-system fractional crystallisation of a gabbroic mineral assemblage dominated by plagioclase and clinopyroxene, accompanied by olivine in the early stages and by magnetite in the later stages. Build up of magma in the crust is assumed to result in a temperature rise that increased the chances of assimilation of the intruded country rock, possibly assisted by partial melting. Evidence for assimilation is shown in trace element ratios

and Sr- and Nd-isotope ratios, in that the low-MgO dykes plot towards crustal compositions, relative to the high-MgO dykes. The effects of crustal contamination are not observed in the less evolved dykes, although it is possible for the magma to have been already contaminated.

Despite field and petrographic evidence indicating the mechanical incorporation of local country-rock into the intruding dykes, in particular the S-type Peninsula Granite of the Cape Granite Suite, the compositional characteristics of the low-MgO dykes are not consistent with the granite being the prime contaminant. Mixing curves incorporating Neoproterozoic Cape Granite and/or Malmesbury as contaminants indicated higher amounts of contamination was required (50-60%) to replicate the Sr- and Nd-isotope ratios, compared to approximately 20% contamination that is required for most of the trace element variations. In order to restrict the amount of contaminant to ~ 20% and in keeping with the observed major and trace element variations, it was necessary to invoke an older crustal source as the contaminant, such as the Bushmanland Terrane gneisses. The Mesoproterozoic Namaqua-Natal Bushmanland Terrane displays higher Sr-isotope ratios and more specifically lower Nd-isotope ratios compared to the Malmesbury Group and Cape Granite. Contamination of the False Bay magma by a melt of the Bushmanland Terrane does not account for the all of the chemical variations seen in each of the low-MgO dykes, but mixing curves for the incorporation of an older Mesoproterozoic basement do sufficiently demonstrate that a smaller portion of the contaminant is required to replicate the Sr- and Nd-isotope ratios of the most evolved dykes (e.g. Chapman's Peak 2 dyke). While this older source is not exposed in the Cape Peninsula, there is ample evidence that Mesoproterozoic gneisses of the Namaqua-Natal crustal Province underlie the Neoproterozoic rocks in the area. Unconformities between sequences of similar age of the Malmesbury Group and Namaqua-Natal basement are documented in southern Namaqualand (e.g. Gresse and Scheepers, 1993) and their presence has been detected in geophysical surveys of the southern Cape region (Lindeque et al., 2011). Therefore, it is likely the host magma of the False Bay dyke swarm interacted at depth with crustal units that are compositionally (and isotopically) similar to the Bushmanland Terrane, or other Namaqua-Natal Province terranes, to produce the compositional variation that is observed in the more differentiated low-MgO dykes.

9.1 Future Complementary Research

Variations in element ratios of Ce/Pb as well as high U and Th trace element abundances associated with the low-MgO group (Figure 6.7), suggest that the U-Th-Pb isotope system similarly reflects the genetic change in the differentiation process of the False Bay dyke swarm from fractional crystallisation to one where assimilation becomes more inherent. To compliment the research presented in this study, future work should focus on the U-Th-Pb isotope system to complete the isotopic data set, which was unable to be accomplished during this study due to unforeseen circumstances that delayed analytical procedures. Trumbull et al. (2007) published Pb isotope data for selected False Bay dykes, but these did not cover the more evolved low-MgO samples, thus do not help refine the contamination model presented here.

Bibliography

Allsopp, H. L. and Kolbe, P. (1965). Isotopic age determinations on the Cape Granite and intruded Malmesbury sediments, Cape Peninsula, South Africa. *Geochimica et Cosmochimica Acta*, 29:1115–1130.

Armstrong, R., de Wit, M. J., Reid, D., York, D., and Zartman, R. (1998). Cape Town's Table Mountain reveals rapid Pan-African uplift of its basement rocks. *Journal of African Earth Sciences*, 27(1A):10–11.

Backeberg, N. R. and Rowe, C. D. (2009). Mega-scale (~50m) Ordovician load casts at de Balie, South Africa: Sediment fluidization by thermal destablization. *South African Journal of Geology*, 112(2):187–196.

Bauer, K., Neben, S., Schreckenberger, B., Emmermann, R., Hinz, K., Fechner, N., Gohl, K., Schulze, A., Trumbull, R. B., and Weber, K. (2000). Deep structure of the Namibia continental margin as derived from integrated geophysical studies. *Journal of Geophysical Research*, 105:25829–25853.

Bauer, K., Trumbell, R. B., and Vietor, T. (2003). Geophysical images and a crustal model of intrusive structures beneath the Messum ring complex, Namibia. *Earth and Planetary Science Letters*, 216:65–80.

Ben-Avraham, Z., Hartnady, C. J. H., and Kitchin, K. A. (1997). Structure and tectonics of the Agulhas-Falkland fracture zone. *Tectonophysics*, 282:83–98.

Bindeman, I. N., Davis, A. M., and Drake, M. J. (1998). Ion microprobe study of plagioclase-basalt partition experiments at natural concentration level of trace elements. *Geochimica et Cosmochimica Acta*, 62:1175–1193.

Boettcher, A. L. and Wyllie, P. J. (1968). Melting of granite with excess water to 30 kilobars pressure. *The Journal of Geology*, 76(2):235–244.

Brooks, C. K. (1976). The Fe2O3/FeO ratio of basalt analyses: an appeal for a standardized procedure. *Bulletin of the geological Society of Denmak*, 25:117–120.

Bryan, W. B., Finger, L. W., and Chayes, F. (1969). Estimating proportions in the petrographic mixing equations by least squares approximation. *Science*, 163:926–927.

Buggisch, W., Kleinschmidt, G., and Krumm, S. (2010). Sedimentology, geochemistry and tectonic setting of the Neoproterozoic Malmesbury Group (Tygerberg Terrane) and its relation to neighbouring terranes, Saldania Fold Belt, South Africs. *Neues Jahrbuch für Geologie und Paläontologie - Abhandlungen*, 257(1):85–114.

Butt, G. J. (1989). The geology and geochemistry of the Cape Peninsula dolerites. unpublished Honours Thesis at the University of Cape Town.

Chevallier, L. and Woodford, A. (1999). Morpho-tectonics and mechanism of emplacement of the dolerite rings and sills of the western Karoo, South Africa. *South African Journal of Geology*, 102:43–54.

Cornell, D. H., Thomas, R. J., Moen, H. F. G., Reid, D. L., Moore, J. M., and Gibson, R. L. (2006). The Namaqua-Natal Province. *in: the Geology of South Afica*, pages 325–379.

Creighton-Jones, D. J. (1982). Some aspects of the geochemistry of the Sea Point granite-hornfels contact area. unpublished Honours Thesis at the University of Cape Town.

Curtis, C. (2009). Stable isotope and whole rock geochemical study of the Cretaceous Koegel Fontein Complex: magma characterisation, evidence for fluid-rock interaction and source constraints for low-d18O magmas. Master's thesis.

Da Silva, L. C., Gresse, P. G., Scheepers, R., McNaughton, N. J., Hartmann, L. A., and Fletcher, I. (2000). U-Pb SHRIMP and Sm-Nd age constraints on the timing and sources of the Pan-African Cape Granite Suite, South Africa. *Journal of African Earth Sciences*, 30:795–815.

Day, R. W. (1987). False Bay dolerites. *Annals Geological Survey of South Africa*, 21:1–7.

De Beer, C. H. and Armstrong, R. A. (1998). Age and tectonic setting of Mesozoic anorogenic complex west of Bitterfontein, Namaqualand, South Africa. *IAVCEI International Volcanological Congress, Cape Tow*, 15. in: Abstract volume.

De Beer, C. H., Gresse, P. G., Theron, J. N., and Almond, J. E. (2002). The geology of the Calvinia area. *The Councilfor Geoscience South Africa*. Explanation of 1:250,000 scale Sheet 3118 Calvinia.

De Villiers, J. and Söhnge, P. G. (1959). The geology of the Richtersverd. *Memoirs of the Geological Survey, South Africa*, 48:295 pp.

DePaolo, D. J. (1981). Trace element and isotopic effects of combined wallrock assimilation and fractional crystallization. *Earth and Planetary Science Letters*, 53:189–202.

Duncan, A. R., Armstrong, R. A., Erlank, A. J., Marsh, J. S., and Watkins, R. T. (1990). MORB-related dolerites associated with the final stages of Karoo flood basalt volcanism in southern Africa. *Mafic Dykes and Emplacement Mechanisms*, pages 119–129. A. A. Balkema, Rotterdam, The Netherlands.

Duncan, A. R., Erlank, A. J., and Marsh, J. S. (1984). Regional geochemistry of the KAroo igneous province. *Special Publication of the Geological Society of South Africa*, 13:355–387.

Eales, H. V. and Booth, P. W. K. (1974). The Birds River gabbro complex, Dordrecht district. *Transactions Geological Society South Africa*, 77:1–15.

Eales, H. V. and Robey, J. V. (1976). Differentiation of tholeiitic Karoo magma at Birds River. *Contributions to Mineralogy and Petrology*, 56:101–117.

Eglington, B. M. (2006). Evolution of the Namaqua-Natal Belt, southern Africa - A geochronological and isotope geochemical review. *Journal of African Earth Sciences*, 46:93–111.

Eglington, B. M. and Harmer, R. E. (1999). GEODATE for Windows version 1.3: Isotope regression and modelling software. Council for Geoscience Open File Report, 1999-0206-O, pp. 1 -51.

Elburg, M. and Goldberg, A. (2000). Age and geochemistry of Karoo dolerite dykes from northeast Botswana. *Journal of African Earth Sciences*, 31(3/4):539–554.

Erlank, A. J., Marsh, J. S., Duncan, A. R., Miller, R. M., Hawkesworth, C., Betton, P. J., and Rex, D. C. (1984). Geochemistry and petrogenesis of the Etendeka volcanic rocks from SWA/Namibia. *Special Publication of the Geological Society of South Africa*, 13:195–245. in: Petrogenesis of Volcanic Rocks of the Karoo Province.

Ernesto, M., Marques, L. S., Piccirillo, E. M., Molina, E. C., Ussami, N., Comin-Chiaramonti, P., and Bellieni, G. (2002). Paraná Magmatic Province - Tristan da Cunha plume system: fixed versus mobile plume, petrogenetic considerations and alternative heat sources. *Journal of Volcanology and Geothermal Research*, 118(1-2):15–36.

Ewart, A., Marsh, J. S., Milner, S. C., Duncan, A. R., Kamber, B. S., and Armstrong, R. (2004). Petrology and geochemistry of Early Cretaceous bimodal continental flood volcanism of the northwest Etendeka, Namibia. Part 1: Introduction, mafic lavas and re-evaluation of mantle source components. *Journal of Petrology*, 45:59–105.

Ewart, A., Milner, S. C., Armstrong, R., and Duncan, A. R. (1998). Etendeka volcanism of the Goboboseb Mountains and Messum Igneous Complex, Namibia. Part 1: Geochemical evidence of early Cretaceous Tristan plume melts and the role of crustal contamination in the Parana-Etendeka CFB. *Journal of Petrology*, 39:191–225.

Frey, F. A., Bryan, W. B., and Thompson, G. (1974). Atlantic ocean floor: geochemistry and petrology of basalts from legs 2 and 3 of the Deep Sea Drilling Project. *Journal of Geophysical Research*, 79:5507–5527.

Frimmel, H. E. and Frank, W. (1998). Neoproterozoic tectono-thermal evolution of the Gariep Belt and its basement, Namibia/South Africa. *Precambrian Research*, 90:1–28.

Frimmel, H. E. and Frölling, P. G. (2004). Late Vendian closure of the Adamaster Ocean: Timing of tectonic inversion and syn-orogenic sedimentation in the Gariep Basin. *Gondwana Research*, 7:685–699.

Gast, P. W. (1968). Trace element fractionation and the origin of tholeiitic and alkaline magma types. *Geochimica et Cosmochimica Acta*, 32(10):1057–1086.

Ghiorso, M. S. and Sack, R. O. (1995). A Revised and Internally Consistent Thermodynamic Model for the Interpolation and Extrapolation of Liquid-Solid Equilibria in Magmatic Systems at elevated temperatures and pressures. *Contributions to Mineralogy and Petrology*, 119(2/3):197–212. in: Chemical Mass Transfer in Magmatic processes IV.

Gibson, S. A., Thompson, R. N., Day, J. A., Humphris, S. E., and Dickin, A. P. (2005). Melt-generation processes associated with the Tristan mantle plume: Constraints on the origin of EM-1. *Earth and Planetary Science Letters*, 237(3-4):744–767.

Gladczenko, T. P., Hinz, K., Eldholm, O., Meyer, H., Neben, S., and Skogseid, J. (1997). South Atlantic volcanic margins. *Journal Geological Society London*, 154:465–470.

Goscombe, B. and Gray, D. R. (2007). The Coastal Terrane of the Kaoko Belt, Namibia: Outboard arc-terrane and tectonic significance. *Precambrian Research*, 155:139–158.

Goscombe, B., Hand, M., and Gray, D. R. (2003). Structure of the Kaoko Belt, Namibia: progressive evolution of a classic transpressional orogen. *Journal of Structural Geology*, 25:1049–1081.

Gresse, P. G. and Scheepers, R. (1993). Neoproterozoic to Cambrian (Namibian) rocks or South Africa: a geochronological and geotectonic review. *Journal of African Earth Sciences*, 16(4):375–393.

Hälbich, I. W. (1983). A tectogenesis of the Cape Fold Belt (CFB). *The Geological Society of South Africa Special Publication*, 12:165–175.

Hartnady, C. J. H., Newton, A. R., and Theron, J. N. (1974). Stratigraphy and structure of the Malmesbury Group in the southwestern Cape. *Bulletin of the Precambrian Research Unit, University of Cape Town, South Africa*, 15:193–213.

Hirsch, K., Bauer, K., and Scheck-Wenderoth, M. (2009). Deep Structure of the western South African passive margin - Results of a combined approach of seismic, gravity and isostatic investigations. *Tectonophysics*, 470:57–70.

Hirschel, P. (1989). Cape Peninsula dolerites. unpublished Honours Thesis at the University of Cape Town.

Hofmann, A. W. (1989). Geochemistry and Models of Mantle Circulation. *Philosophical Transactions of the Royal Society of London*, 328:425–439.

Hofmann, A. W. (1997). Mantle geochemistry: the message from oceanic volcanism. *Nature*, 385(16):219–229.

Huang, W. L. and Wyllie, P. J. (1973). Melting relations of Muscovite-Granite to 35 kbar as a model for fusion of metamorphosed subducted oceanic sediments. *Contributions to Mineralogy and Petrology*, 42:1–14.

Hunter, D. R. and Reid, D. L. (1987). Mafic dyke swarms in southern Africa. In Halls, H. and Fahrig, W., editors, *Mafic Dyke Swarms*, volume 34, pages 445–456. Geological Association of Canada, Special Paper. in: Mafic dyke swarms.

Ila, P. and Frey, F. A. (2000). Trace element analysis of USGS standards ASV2, BCR2, BHVO2, DTS2 and GSP2 by INAA. *Journal of Radioanalytical and Nuclear Chemistry*, 244(3):599–602.

Jenner, G. A., Foley, S. F., Jackson, S. E., Green, T. H., Fryer, B. J., and Longerich, H. P. (1993). Determination of partition coefficients for trace elements in high pressure-temperature experimental run products by laser ablation microprobe-inductively coupled plasma-mass spectrometry (LAM-ICP-MS). *Geochimica et Cosmochica Acta*, 57:5099–5103.

Jerram, D., Mountney, N., Holzförster, F., and Stollhofen, H. (1999). Internal stratigraphic relationships in the Etendeka Group in the Huab Basin, north west Namibia: understanding the onset of flood volcanism. *Journal of Geodynamics*, 28:393–418.

Jordaan, L. J., Scheepers, R., and Barton, E. S. (1995). The geochemistry and isotopic composition of the mafic and intermediate igneous components of the Cape Granite Suite, South Africa. *Journal of African Earth Sciences*, 21(1):59–70.

Kirstein, L. A., Kelley, S., Hawkesworth, C., Turner, S., Mantovani, M., and Wijbrans, J. (2001). Protracted felsic magmatic activity associated with the opening of the South Atlantic. *Journal of the Geological Society, London*, 158:583–592.

Kogiso, T., Hirose, K., and Takahashi, E. (1998). Melting experiments on homogeneous mixtures of peridotite and basalt: application to the genesis of ocean island basalts. *Earth and Planetary Science Letters*, 162:45–61.

Kolbe, P. (1966). Geochemical investigation of the Cape Granite, South-Western Cape Province, South Africa. *Transactions Geological Society South Africa*, 69:161–199.

Langmuir, C. H., Bender, J. B., Bence, A. E., Hanson, G. N., and Taylor, S. R. (1977). Petrogenesis of basalts from the Famous area: Mid-Atlantic Ridge. *Earth and Planetary Science Letters*, 36:133–156.

Langmuir, C. H., Vocke, R. D. J., Hanson, G. N., and Hart, S. (1978). A general mixing equation with applications to Icelandic basalts. *Earth and Planetary Science Letters*, 37:380–392.

Le Roex, A. P., Späth, A., and Zartman, R. E. (2001). Lithospheric thickness beneath the southern Kenya Rift: implications from basalt geochemistry. *Contributions to Mineralogy and Petrology*, 142:89–106.

Lindeque, A. S., de Wit, M. J., Ryberg, T., Weber, M. H., and Chevallier, L. (2011). Deep crustal profile across the southern Karoo Basin and Beattie Anomaly, South Africa: an integrated interpretation with tectonic implications. *South African Journal of Geology*, in press.

Lindeque, A. S., Ryberg, T., Stankiewicz, J., Weber, M. H., and de Wit, M. J. (2007). Deep crustal seismic reflection experiment across the southern Karoo Basin, South Africs. *South African Journal of Geology*, 110(2/3):419–438.

Mahanyele, P. J., Bauer, K., Franke, D., Schulze, A., Ryberg, T., De Beer, C. H., Neben, S., Schreckenberger, B., and Stettler, E. H. (2004). How far to the south does the volcanic margin of Southwest Africa extend? An initial velocity model for the ocean-continent transition in the southern Cape Basin. *64. Jahrestagung der Deutschen Geophysikalischen Gesellschaft, Berlin*, abstract volume:443–444.

Marsh, J. S., Ewart, A., Milner, S. C., Duncan, R. A., and Miller, R. M. (2001). The Etendeka Igneous Province: magma types and their stratigraphic distribution with implications for the evolution of the Paraná-Etendeka flood basalt province. *Bulletin of Volcanology*, 62:464–486.

Mbangula, N. (2004). Characterisation of provenance and tectonic setting of source rock for the Tygerberg Formation, on Robben Island. unpublished Honours Thesis at the University of Cape Town.

Mbeje, M. J. (2005). Geochemistry and tectonic setting of the Bloubergstrand volcanic rocks and later Grotto Bay dykes within the Malmesbury Group. unpublished Honours Thesis at the University of Cape Town.

McDonough, W. F. and Sun, S. (1995). The Composition of the Earth. *Chemical Geology*, 120:223–253.

McKenzie, D. and O'Nions, R. K. (1991). Partial Melt distributions from inversion of rare earth element concentrations. *Journal of Petrology*, 32:1021–1091.

Miková, J. and Denková, P. (2007). Modified chromatographic separation scheme for Sr and Nd isotope analysis in geological silicate samples. *Journal of Geosciences*, 52:221–226.

Moore, J. M., Watkeys, M. K., and Reid, D. L. (1990). The regional setting of the Aggenys/Gamsberg base metal deposits, Namaqualand, South Africa. *Regional Metamorphism of Ore Deposits*, pages 77–95.

Morgan, W. J. (1981). Hotspot tracks and the opening of the Atlantic and Indian Oceans. *in: The Sea*, 7:443–487. John Wiley, New York.

National GeoSpatial Information Imagery (2008). Robben Island. Job 3318C_2008_127, strip 2, image 13, 0.15mGSD.

Nell, G. and Brink, W. C. (1944). The Petrology of the Western Province dolerites. *Annals University of Stellenbosch*, 22:27–62.

Nürnerg, D. and Müller, R. D. (1991). The tectonic evolution of the South Atlantic from Late Jurassic to present. *Tectonophysics*, 191:27–53.

Paster, T. P., Schauwecker, D. S., and Haskin, L. A. (1974). The behavior of some trace elements during solidification of the Skaergaard layered series. *Geochimica et Cosmochimica Acta*, 38:1549–1577.

Pearce, J. A. (1982). Trace element characteristics of lavas from destructive plate boundaries. *in: Andesites: Orogenic Andesites and Related Rocks*, pages 525–548.

Pearce, J. A. and Norry, M. J. (1979). Petrogenetic implications of Ti, Zr, Y and Nb variations in volcanic rocks. *Contributions to Mineralogy and Petrology*, 69:33–47.

Peate, D. W., Hawkesworth, C., Mantovani, M. S. M., Rogers, N. W., and Turner, S. P. (1999). Petrogenesis and stratigraphy of the high Ti/Y Urubici magama type in the Paraná flood basalt province and implications for the nature of "Dupal"-type mantle in the South Atlantic region. *Journal of Petrology*, 40:451–473.

Petrelli, M., Poli, G., Perugini, D., and Peccerillo, A. (2005). PetroGraph: A new software to visualize, model and present geochemical data in igneous petrology. *Geochemistry Geophysics Geosystems*, 6(7):1–15.

Petzer, G. (2006). An investigation into the chemical composition of dolerite dykes in the Van Rhynsdorp area, in the Western Cape of Southern Africa and their regional significance. unpublished Honours Thesis at the University of Cape Town.

Powell, C. M., Roots, S. R., and Veevers, J. J. (1988). Pre-breakup continental extension in East Gondwanaland and the early opening of the eastern Indian Ocean. *Tectonophysics*, 155:261–283.

Rao, M. . J. (2002). Petrology and geochemistry of dolerite dykes, West Garo Hills, Meghalaya: a preliminary study. *Gondwana Research*, 5(4):884–888.

Reeves, C. V. (2000). The geophysical mapping of Mesozoic dike swarms in southern Africa and their origin in the disruption of Gondwana. *Journal of African Earth Sciences*, 30:499–513.

Reid, D. L. (1990). The Cape Peninsula dolerite dyke swarm, South Africa. *Mafic Dykes and Emplacement Mechanisms*, pages 325–334. A. A. Balkema, Rotterdam, The Netherlands.

Reid, D. L. (1997). Sm-Nd age and REE geochemistry of Proterozoic arc-related igneous rocks in the Richtersveld Subprovince, Namaqua Mobile Belt, Southern Africa. *Journal of African Earth Sciences*, 24(4):621–633.

Reid, D. L., Erlank, A. J., and Rex, D. C. (1991). Age and correlation of the False Bay dolerite dyke swarm, south-western Cape, Cape Province. *South African Journal of Geology*, 94(2-3):155–158.

Reid, D. L. and Rex, D. C. (1994). Cretaceous dykes associated with the opening of the South Atlantic: the Mehlberg dyke, northern Richtersveld. *South African Journal of Geology*, 97(2):135–145.

Reid, D. L., Smith, C. B., Watkeys, M. K., Welke, H. J., and Betton, P. J. (1997). Whole-rock radiometric age patterns in the Aggeneys-Gamsberg ore district, central Bushmanland, South Africa. *South African Journal of Geology*, 100(1):11–22.

Reid, D. L., Welke, H. J., Erlank, A. J., and Moyes, A. (1987). The Orange River Group: a major Proterozoic calcalkaline volcanic belt in the western Namaqua Province, southern Africa. *Geological Society Special Publication*, (33):327–346. in: Geochemistry and Mineralization of Proterozoic Volcanic Suites.

Renne, P. R., Deckart, K., Ernesto, M., Féraud, G., and Piccirillo, E. M. (1996a). Age of Ponta Grossa Dike Swarm (Brazil), and implications to Paraná flood volcanism. *Earth and Planetary Science Letters*, 144:199–211.

Renne, P. R., Glen, J. M., Milner, S. C., and Duncan, A. R. (1996b). Age of Etendeka flood volcanism and associated intrusions in southwestern Africa. *Geology*, 24:659–662.

Romer, R. L., Heinrich, W., Schröder-Smeibidl, B., Meixner, A., Fischer, C.-O., and Schulz, C. (2005). Elemental dispersion and stable isotope fractionation during reactive fluid-flow and fluid immiscibility in the Bufa del Diente aureole, NE-Mexico: Evidence from readiographies and Li, B, Sr, Nd, and Pb isotope systematics. *Contributions to Mineralogy and Petrology*, 149:400–429.

Rowe, C. D., Backeberg, N. R., van Rensburg, T., MacLennan, S. A., Faber, C., Curtis, C., and Viglietti, P. A. (2010). Structural geology of Robben Island: implications for the tectonic environment of Saldanian deformation. *South African Journal of Geology*, 113(1):1–15.

Rubin, A. M. (1995). Propoagation of magma-filled cracks. *Annual Reviews in Earth and Planetary Sciences*, 23:287–336.

Rust, I. C. (1967). *On the sedimentation of the Table Mountain Group in the Western Cape Province*. PhD thesis. Geology Department, University of Stellenbosch, South Africa.

Rust, I. C. (1981). Early Paleozoic Pakhuis Tillite, South Africa. In Hambrey, M. J. and Harland, W. B., editors, *Earth's pre-Pleistocene glacial record*, pages 113–117. Cambridge University Press.

Scheepers, R. (1995). Geology, geochemistry and petrogenesis of Late Precambrian S-, I- and A- typ granitoids in the Saldania belt, Western Cape Province, South Africa. *Journal of African Earth Sciences*, 21(1):35–58.

Scheepers, R. and Armstrong, R. (2002). New U-Pb SHRIMP zircon ages of the Cape Granite Suite: implications for the magmatic evolution of the Saldania Belt. *South African Journal of Geology*, 105(3):241–256.

Stankiewicz, J., Ryberg, T., Schulze, A., Lindeque, A., Weber, M. H., and de Wit, M. J. (2007). Initial results from wide-angle seismic refraction lines in the southern Cape. *South African Journal of Geology*, 2-3:407–418.

Stewart, K., Turner, S., Kelley, S., Hawkesworth, C., Kirstein, L., and Mantovani, M. (1996). 3-D, Ar-Ar geochronology in the Paraná continental flood basalt province. *Earth and Planetary Science Letters*, 143:95–109.

Thamm, A. G. and Johnson, M. R. (2006). The Cape Supergroup. In Johnson, M. R., Anhaeusser, C. R., and Thomas, R. J., editors, *The Geology of South Africa*, pages 443–460. Geological Society of South Africa and the Coucil for Geoscience.

Theron, J. N. (1972). *The stratigraphy and sedimentation of the Bokkeveld Group (Series)*. PhD thesis, University of Stellenbosch.

Theron, J. N. (1984). The geology of Cape Town and environs: Sheet Expl. 3318CD and DC, and 3418AB, AD and BA. Scale 1:50 000. *Geological Survey South Africa*, page 77.

Thirlwall, M. F. and Jones, N. W. (1983). Isotope geochemistry and contamination mechanisms of Tertiary lavas from Skye, northwest Scotland. In Hawkesworth, C. J. and Norry, M. J., editors, *Continental Basalts and Mantle Xenoliths*, pages 186–208. Shiva.

Thompson, R. N., Gibson, S. A., Dickin, A. P., and Smith, P. M. (2001). Early Cretaceous Basalt and Picrite Dykes of the Southern Etendeka Region, NW Namibia: Windows into the Role of the Tristan Mantle Plume in Paraná-Etendeka Magmatism. *Journal of Petrology*, 42(11):2049–2081.

Trumbull, R. B., Harris, C., Frindt, S., and Wigand, M. (2004a). Oxygen and neodymium isotope evidence for source diversity in Cretaceous anorogenic granites from Namibia and implications for A-type granite genesis. *Lithos*, 73:21–40.

Trumbull, R. B., Reid, D. L., De Beer, C., van Acken, D., and Romer, R. L. (2007). Magmatism and continental breakup at the west margin of southern Africa: A geochemical comparison of dolerite dikes from northwestern Namibia and the Western Cape. *South African Journal of Geology*, 110(2-3):477–502.

Trumbull, R. B., Vietor, T., Hahne, K., Wackerle, R., and Ledru, P. (2004b). Aeromagnetic mapping and reconnaissance geochemistry of the Early Cretaceous Henties Bay-Outjo dike swarm, Etendeka Igneous Province, Namibia. *Journal of African Earth Sciences*, 40:17–29.

Turcotte, D. L. and Emerman, S. H. (1983). Mechanisms of Active and Passive Rifting. *Tectonophysics*, 94:39–50.

Ussami, N., Kolisnyk, A., Raposo, M. I. B., Ferreira, F. J. F., Molina, E. C., and Ernesto, M. (1991). Detectabilidade magnética de diques do Arco de Ponta Grossa: Um estudo integrado de magnetometria aérea e magnetismo de rocha. *Rev. Brasil Geociências*, 21:317–327.

Vásquez, P., Glodny, J., Franz, G., Romer, R. L., and Gerdes, A. (2009). Origin of fayalite granitoids: New insights from the Cobquecura Pluton, Chile, and its metapelitic xenoliths. *Lithos*, 110(1-4):181–198.

Villemant, B., Jaffrezic, H., Joron, J. L., and Treuil, M. (1981). Distribution coefficients of major and trace elements: Fractional crystallization in the alkali basalt series of Chaine de Puys. *Geochimica et Cosmochimica Acta*, 45:1997–2016.

Walker, F. (1956). The Dolerites of the Cape Peninsula. *Transactions Geological Society South Africa*, 77:77–92.

Weis, D., Kieffer, B., Maerschalk, C., Barling, J., de Jong, J., Williams, G. A., Hanano, D., Pretorious, W., Mattielli, N., Scoates, J. S., Goolaerts, A., Friedman, R. M., and Mahoney, J. B. (2006). High-precision isotopic characterization of USGS reference materials by TIMS and MC-ICP-MS. *Geochemistry Geophysics Geosystems*, 7:Q08006.

Wilson, S. A. (1997). Data compilation for USGS reference material BHVO-2, Hawaiian Basalt. *U.S. Geological Survey Open-File Report*.

Wulfse, A. D. (1989). Geochemistry and petrology of the Cape Peninsula dolerites. unpublished Honours Thesis at the University of Cape Town.

Zeng, L., Asimov, P. D., and Saleeby, J. B. (2005). Coupling of anatectic reactions and dissolution of accessory phases and the Sr and Nd isotope systematics of anatectic melts from a metasedimentary source. *Geochimica et Cosmochimica Acta*, 69:3671–3682.

APPENDICES

Appendix A

XRF data of complete sample set

The complete False Bay dyke swarm XRF data set. The trace elements reported here are also measured by XRF and were used for comparison to the new ICP-MS data collected for this study (shown in Chapter 6).

Sample	LB-01	LB-02	LB-03	LB-04	LB-05	LB-06	LB-07	LB-08	LB-09	LB-10	GCH89-46	GCH89-47
Location	LB1	LB2	LB2	LB1	LB1	LB1	LB1	LB1	LB1	LB1	LB2	LB1
XRF Major elements (wt%)												
SiO2	48.6	50.2	50.5	49.7	49.8	49.8	49.2	49.4	49.8	49.2	49.3	48.7
TiO2	1.45	1.55	1.70	1.33	1.37	1.31	1.20	1.42	1.41	1.49	1.56	1.34
Al2O3	15.1	14.8	15.1	16.3	16.7	16.5	16.6	16.3	15.8	14.8	14.4	16.0
Fe2O3	12.0	11.8	12.0	11.2	11.1	11.0	10.5	11.3	11.3	12.0	12.1	11.0
MnO	0.19	0.19	0.19	0.18	0.17	0.17	0.16	0.18	0.18	0.20	0.22	0.17
MgO	7.62	6.68	6.34	7.22	6.79	7.25	7.28	6.84	6.88	7.30	6.67	7.10
CaO	10.9	10.4	9.91	11.0	11.0	10.9	11.4	10.9	10.6	10.9	10.1	11.0
Na2O	2.25	2.30	2.49	2.27	2.16	2.19	2.15	2.38	2.33	2.25	2.46	2.13
K2O	0.16	0.75	0.56	0.61	0.65	0.63	0.49	0.70	0.66	0.31	0.76	0.65
P2O5	0.23	0.27	0.34	0.20	0.21	0.21	0.18	0.22	0.25	0.24	0.27	0.20
H2O-	0.94	0.93	0.90	0.46	0.39	0.37	0.53	0.54	0.62	0.80	1.02	0.35
LOI	1.47	1.10	0.93	0.72	0.90	0.80	1.19	0.87	0.95	1.29	0.91	0.98
Total	100.86	101.09	100.89	101.20	101.28	101.15	100.87	101.04	100.75	100.75	99.87	99.67
XRF trace elements (ppm)												
Nb	10.8	13.6	15.9	9.4	9.2	9.7	8.5	10.6	10.7	10.6	13.1	9.6
Zr	102.4	142.8	146.4	91.9	93.3	93.0	80.4	97.8	108.9	102.9	143.8	93.0
Y	30.0	33.5	35.1	26.3	27.3	26.6	23.6	27.6	29.9	30.2	34.2	26.4
Sr	180.9	211.8	236.1	209.5	217.1	209.6	208.0	219.9	211.9	190.8	207.2	212.3
Ba	82.1	222.0	228.6	185.0	179.0	171.1	142.1	186.3	198.6	127.0	212.9	161.9
Sc	40.0	38.3	34.8	34.1	32.1	33.6	34.2	34.8	36.2	39.7	39.6	36.8
Co	57.1	55.1	49.6	50.4	50.5	49.6	49.6	49.5	51.2	56.8	52.4	52.7
Cr	292.9	132.6	177.0	285.6	239.0	291.1	316.2	256.0	277.3	281.5	139.7	321.7
V	271.2	283.5	266.5	222.3	232.5	222.8	220.0	242.6	236.7	273.8	277.2	233.6
Zn	97.9	96.6	85.7	77.0	76.6	76.9	71.7	78.8	85.4	94.5	89.1	78.7
Cu	99.1	91.4	71.7	88.1	82.9	80.2	89.4	85.4	91.3	103.1	92.8	82.4
Ni	83.8	68.9	61.2	92.2	90.0	95.3	99.9	85.4	89.4	76.2	68.8	95.6
S	1251	2017	1095	1593	1619	1015	757	1010	1526	1099	1265	1467.8

Sample	GCH89-48	LB-11	LB-12	LB-30	LB-31	LB-32	LB-33	LB-34	GCH89-45	LB-40	LB-41	LB-42
Location	LB1	LB2	LB2	OD1	OD1	OD1	OD1	OD1	OD2	CL1	CL1	CL1
XRF Major elements (wt%)												
SiO2	48.2	49.2	49.7	54.3	54.2	54.3	54.0	54.3	51.3	51.0	52.0	51.8
TiO2	1.37	1.59	1.59	2.47	2.47	2.48	2.47	2.44	1.77	2.16	2.14	2.10
Al2O3	15.7	14.6	14.4	12.9	13.0	13.0	12.8	13.0	16.5	14.1	14.0	14.5
Fe2O3	11.1	12.4	12.4	13.8	13.7	13.7	13.6	13.5	8.2	13.9	14.0	13.6
MnO	0.18	0.20	0.20	0.21	0.20	0.19	0.19	0.20	0.11	0.22	0.21	0.22
MgO	6.84	6.84	6.87	2.90	2.91	3.01	2.90	2.92	4.93	4.17	4.10	4.10
CaO	10.7	10.5	10.4	5.88	5.80	6.57	5.74	6.48	10.2	6.27	8.08	8.13
Na2O	2.44	2.33	2.29	2.43	2.20	2.35	2.85	2.08	2.16	2.97	2.24	2.15
K2O	0.64	0.64	0.71	2.50	2.82	2.29	2.59	2.28	0.88	2.43	1.56	1.55
P2O5	0.21	0.27	0.27	0.65	0.65	0.65	0.65	0.65	0.30	0.40	0.41	0.39
H2O-	0.75	1.35	0.96	0.37	0.44	0.44	0.48	0.41	1.52	0.72	0.61	0.66
LOI	0.60	0.82	1.01	1.70	1.91	1.29	1.69	1.83	1.38	1.63	1.28	1.32
Total	98.81	100.74	100.71	100.13	100.26	100.20	99.94	100.04	99.22	99.97	100.59	100.56
XRF trace elements (ppm)												
Nb	10.4	13.7	13.5	26.6	26.7	26.2	27.1	26.6	17.0	22.7	21.9	21.2
Zr	97.7	140.5	142.7	253.1	256.1	251.9	255.4	256.4	159.1	228.8	226.0	220.3
Y	27.9	34.2	34.3	54.6	55.5	54.3	54.8	55.5	41.6	50.7	51.3	50.0
Sr	224.0	209.7	220.0	148.8	163.8	142.1	158.7	131.8	252.4	170.1	176.1	178.9
Ba	178.7	182.1	218.0	421.9	452.6	405.0	411.4	397.7	244.8	372.8	341.0	324.5
Sc	34.0	40.1	37.8	37.2	37.4	35.9	36.6	38.4	45.0	39.4	35.4	39.1
Co	49.1	55.6	53.1	42.1	39.9	41.7	42.4	42.9	50.9	44.2	46.8	45.8
Cr	278.9	133.0	120.0	11.5	12.2	11.2	9.2	12.9	272.5	47.9	51.2	62.7
V	238.2	279.8	280.9	379.7	378.2	364.3	372.8	380.3	274.3	423.6	412.7	406.5
Zn	80.1	99.0	94.2	132.3	131.8	120.1	132.9	128.5	120.5	129.7	118.4	116.3
Cu	91.6	95.3	92.6	29.3	30.4	31.3	29.9	30.2	72.6	65.8	64.2	66.2
Ni	87.5	70.1	62.4	10.6	10.6	10.5	8.7	10.3	70.1	32.4	31.0	38.4
S	1197	1227	1423	874	592	911	977	774	44	1434	1004	927

Sample	LB-43	LB-50	LB-51	LB-52	SL-01	GCH89-39	SL-02	GCH89-38	GCH89-1	GCH89-2	GCH89-3	GCH89-4
Location	CL2	SW	SW	SW	SL1	SL1	SL2	SL2	SB	SB	SB	SB
XRF Major elements (wt%)												
SiO2	52.5	52.4	53.8	52.8	50.5	49.1	53.0	51.2	48.7	48.9	49.1	48.0
TiO2	2.13	1.81	1.76	1.96	2.87	2.89	2.48	2.52	1.99	1.99	1.95	1.94
Al2O3	14.0	13.3	13.7	13.1	13.2	12.8	12.9	12.6	13.9	14.0	14.0	14.0
Fe2O3	13.9	15.6	13.3	15.6	15.2	15.0	15.0	15.0	14.5	14.5	14.3	14.1
MnO	0.20	0.23	0.20	0.24	0.55	0.66	0.38	0.33	0.23	0.22	0.23	0.23
MgO	4.14	4.57	4.97	4.23	4.67	4.51	3.67	3.94	5.86	5.98	5.93	5.87
CaO	7.93	8.03	7.47	7.60	7.85	7.56	7.12	7.23	9.16	9.30	9.12	9.00
Na2O	2.43	2.91	3.25	2.64	2.18	2.18	2.22	2.31	2.45	2.46	2.51	2.46
K2O	1.67	1.14	1.69	1.56	1.61	1.63	1.99	1.95	0.87	0.86	0.93	0.88
P2O5	0.40	0.23	0.29	0.27	0.52	0.52	0.94	0.91	0.33	0.32	0.31	0.31
H2O-	0.40	0.59	0.61	0.48	0.71	0.62	0.34	0.98	1.21	1.22	0.94	1.15
LOI	0.92	0.52	0.47	0.54	1.18	1.57	0.69	0.90	1.00	0.70	1.08	1.33
Total	100.69	101.26	101.56	101.04	101.08	99.05	100.69	99.83	100.19	100.44	100.33	99.25
XRF trace elements (ppm)												
Nb	21.9	11.5	16.1	13.6	27.9	28.2	24.9	23.3	12.8	12.9	13.1	12.2
Zr	226.4	160.1	183.3	177.7	274.4	282.8	248.3	231.5	133.2	131.2	136.6	128.8
Y	50.6	46.2	43.3	50.9	57.6	58.3	63.6	62.2	29.8	29.1	30.9	30.2
Sr	179.8	144.1	178.2	148.3	204.6	207.0	164.5	163.5	355.9	354.8	352.6	372.3
Ba	348.8	270.5	331.9	320.0	407.2	408.5	392.6	385.0	257.5	264.2	264.7	246.3
Sc	34.2	38.8	33.4	38.1	36.0	39.5	34.4	37.4	36.9	38.0	38.8	37.1
Co	44.6	51.4	43.8	48.7	70.8	63.5	38.6	40.7	61.0	62.3	57.7	64.1
Cr	52.0	45.9	55.4	35.8	33.5	36.2	20.5	27.8	30.5	33.7	33.9	31.6
V	396.9	465.0	303.9	465.8	417.1	432.8	220.8	250.5	343.3	339.5	341.4	341.2
Zn	117.1	119.4	102.2	114.0	132.0	139.5	137.3	145.6	99.2	98.3	124.9	96.3
Cu	65.2	220.6	100.9	170.3	45.2	47.4	28.4	32.4	121.8	120.0	108.3	115.0
Ni	31.7	42.7	42.1	38.0	34.7	36.6	11.2	15.1	60.2	61.5	54.6	69.0
S	1431	1036	935	1099	1983	2045	1663	1763	2435	2256	2430	2302

Sample	GCH89-6	GCH89-7	GCH89-8	GCH89-9	GCH89-11	GCH89-12	GCH89-14	GCH89-15	Chappies	GCH89-16	GCH89-17	GCH89-18
Location	CP2	CP2	CP2	CP2	CP1	CP1	CP3	CP3	CP4	CP5	CP5	TK1
XRF Major elements (wt%)												
SiO2	55.1	53.5	55.4	54.8	47.7	48.9	51.8	50.0	52.9	52.5	52.5	49.3
TiO2	2.19	2.57	2.20	2.18	1.40	1.57	0.98	1.48	2.17	2.29	2.28	1.50
Al2O3	12.2	12.2	12.1	12.1	14.8	14.2	15.6	14.7	13.3	13.2	13.2	14.5
Fe2O3	15.4	16.0	15.1	15.4	11.1	12.3	11.4	12.8	13.5	13.3	13.5	12.0
MnO	0.35	0.26	0.23	0.22	0.18	0.20	0.21	0.22	0.33	0.27	0.28	0.34
MgO	1.93	2.65	2.10	1.96	6.89	6.80	6.23	6.12	3.79	3.97	3.98	7.11
CaO	5.49	6.07	5.39	5.23	10.6	10.7	10.2	9.46	6.38	7.02	7.06	11.1
Na2O	2.04	2.03	2.02	2.05	2.42	2.32	2.11	2.21	1.93	2.27	2.27	2.02
K2O	2.63	2.41	2.69	2.63	0.66	0.76	1.04	0.91	2.35	2.10	2.12	0.37
P2O5	0.87	0.76	0.88	0.88	0.22	0.27	0.16	0.24	0.45	0.50	0.51	0.24
H2O-	0.48	0.49	0.63	0.59	4.37	0.76	0.43	0.87	0.59	1.65	1.50	0.49
LOI	1.01	1.18	1.14	1.01	0.40	1.48	0.40	0.89	1.71	0.85	0.77	1.42
Total	99.73	100.17	99.78	99.02	100.69	100.31	100.55	99.96	99.38	99.93	100.01	100.35
XRF trace elements (ppm)												
Nb	24.6	24.1	23.9	24.9	13.8	14.2	8.5	11.0	23.0	24.6	24.8	10.9
Zr	256.1	248.3	254.8	259.0	138.3	142.8	103.3	119.9	235.2	237.9	239.0	103.6
Y	64.4	61.2	62.7	60.7	33.7	34.4	27.5	29.3	46.1	51.2	48.8	30.2
Sr	171.4	160.6	167.9	171.4	208.3	210.0	158.4	271.8	161.6	183.4	182.3	323.5
Ba	591.3	637.8	701.4	608.4	192.1	205.0	219.5	236.9	514.1	425.9	432.2	415.7
Sc	34.9	35.3	35.4	35.5	40.7	44.2	35.8	36.2	37.5	35.1	34.4	40.4
Co	29.4	34.1	29.7	26.8	52.4	50.7	48.0	56.4		46.0	43.9	51.9
Cr	10.5	12.0	10.5	8.6	196.9	212.7	146.6	85.4		24.8	23.2	277.6
V	185.0	264.7	187.5	189.0	288.8	291.7	277.9	311.5		405.7	391.5	270.6
Zn	139.5	144.6	141.8	144.0	93.5	99.7	80.6	89.9	98.5	112.8	116.7	87.1
Cu	22.3	24.5	21.0	21.4	96.3	95.2	119.4	118.9	58.4	48.4	47.8	97.3
Ni	<2.392	6.3	<2.377	<2.402	72.3	71.5	76.5	69.1	28.2	32.5	25.7	80.4
S	1295	1515	1043	1281	3044	1957	574	1490		1676	1831	1605

Sample	GCH89-20	GCH89-21	GCH89-22	GCH89-23	GCH89-24	GCH89-26	GCH89-27	GCH89-28	GCH89-29	GCH89-31	GCH89-32	GCH89-33
Location	TK1	TK2	TK2	TK2	NS	NS	FG1	FG1	FG1	FG2	MP	MP
XRF Major elements (wt%)												
SiO2	48.7	49.4	49.0	49.1	52.6	51.9	50.7	50.2	50.5	51.5	52.0	49.5
TiO2	1.46	1.45	1.38	1.43	2.46	2.52	2.11	2.04	2.04	2.17	1.59	2.04
Al2O3	14.4	16.0	15.6	16.3	11.9	12.0	14.2	14.3	14.2	14.0	14.5	14.1
Fe2O3	12.0	11.6	11.5	11.2	16.4	16.4	12.8	12.3	12.6	12.8	11.6	13.2
MnO	0.34	0.18	0.18	0.17	0.23	0.27	0.19	0.20	0.20	0.19	0.18	0.22
MgO	7.18	6.80	7.13	6.44	2.79	2.99	5.26	5.09	5.43	4.89	5.83	5.62
CaO	10.9	10.9	11.0	10.8	7.14	6.97	8.44	8.49	8.76	8.31	8.93	9.06
Na2O	1.96	2.26	2.30	2.24	1.96	1.95	2.69	2.79	2.50	2.80	2.67	2.71
K2O	0.37	0.73	0.65	0.68	1.99	2.00	1.69	1.57	1.66	1.67	1.46	1.23
P2O5	0.24	0.24	0.21	0.23	0.42	0.47	0.54	0.48	0.48	0.53	0.30	0.45
H2O-	0.61	0.48	0.28	0.78	1.29	1.47	0.86	1.45	0.66	0.37	0.59	0.94
LOI	1.81	0.57	0.40	0.59	0.77	1.08	0.98	0.87	1.07	0.89	0.58	0.91
Total	99.97	100.46	99.65	99.90	99.94	100.06	100.41	99.73	100.07	100.13	100.16	99.99
XRF trace elements (ppm)												
Nb	10.8	10.3	9.8	9.8	19.2	19.3	32.7	32.8	32.0	32.0	17.8	25.9
Zr	102.7	104.3	96.2	104.5	238.0	236.1	236.2	234.3	227.4	228.5	156.4	179.0
Y	30.0	28.5	26.8	30.1	60.8	61.5	43.6	43.2	43.0	44.6	35.0	43.4
Sr	323.6	212.1	211.5	219.9	415.3	209.2	293.3	303.9	329.5	286.3	227.8	302.1
Ba	419.8	181.2	168.6	179.6	908.7	925.5	426.8	412.9	394.4	411.9	328.9	353.1
Sc	39.6	35.5	36.4	34.5	37.9	36.0	30.9	31.8	33.6	33.3	34.5	36.8
Co	53.9	47.6	50.5	49.8	42.8	44.3	44.6	44.4	44.5	45.3	46.7	48.5
Cr	275.9	248.9	286.0	222.3	3.6	6.2	65.3	68.4	70.1	48.6	157.9	76.0
V	265.5	241.8	244.5	235.7	321.0	364.3	283.9	280.4	280.5	300.5	257.6	310.8
Zn	86.7	81.7	78.6	80.7	146.4	146.9	106.3	104.3	107.5	105.7	90.2	106.0
Cu	98.1	83.3	86.5	82.5	35.1	41.7	50.1	46.6	50.8	32.8	76.5	59.4
Ni	77.0	82.1	89.1	85.2	<2.483	<2.492	37.2	41.7	40.1	21.2	58.2	33.0
S	1638	1328	1324	193	2081	2284	1679	1912	1639	1342	1181	1980

Sample	GCH89-34	GCH89-36	GCH89-37	GCH89-40	GCH89-41	GCH89-42	GCH89-43	GCH89-44	PD-2	LB-100
Location	MP	OK	OK	SP	KS	KS	BK	BK	LR	SM
XRF Major elements (wt%)										
SiO2	51.8	53.5	53.7	48.0	51.7	51.6	50.6	51.0	53.6	51.6
TiO2	1.53	2.16	2.21	2.82	2.55	2.58	2.79	2.78	2.43	1.15
Al2O3	14.3	13.3	13.2	12.4	11.9	12.1	12.1	12.2	12.9	13.9
Fe2O3	11.2	13.5	13.7	16.2	16.9	16.4	16.4	16.3	14.0	12.6
MnO	0.18	0.20	0.18	0.25	0.23	0.23	0.23	0.23	0.40	0.46
MgO	5.89	3.75	3.59	4.62	2.99	3.18	3.39	3.42	3.15	6.10
CaO	8.88	6.62	6.38	8.32	6.80	6.67	7.11	7.15	5.95	9.19
Na2O	2.61	2.35	2.31	2.20	2.08	2.07	2.22	2.14	1.66	1.59
K2O	1.45	2.06	2.12	1.09	1.88	2.02	1.75	1.76	2.75	1.11
P2O5	0.30	0.50	0.52	0.53	0.40	0.51	0.73	0.74	0.62	0.17
H2O-	0.37	0.66	0.74	0.66	0.83	0.87	0.76	0.73	0.81	0.45
LOI	0.74	1.13	1.36	2.61	1.25	1.29	1.43	1.16	1.45	1.71
Total	99.17	99.71	99.94	99.74	99.51	99.48	99.43	99.59	99.64	100.05
XRF trace elements (ppm)										
Nb	17.6	20.0	20.8	27.0	18.1	20.4	22.7	22.0	26.7	10.5
Zr	156.0	205.9	211.1	251.8	228.6	238.3	241.5	241.2	248.5	122.2
Y	36.5	52.4	65.0	57.8	59.7	62.1	63.7	69.9	62.6	26.2
Sr	226.4	190.2	193.3	323.7	138.3	137.5	142.5	144.9	197.2	173.1
Ba	331.1	378.2	410.4	409.7	379.1	388.6	389.0	410.4	114.0	252.6
Sc	34.6	37.7	36.2	44.7	39.1	40.9	40.1	38.3	35.6	33.8
Co	48.5	38.7	38.7	56.7	48.1	45.2	47.3	46.5	40.0	42.7
Cr	165.9	70.2	58.4	37.5	3.8	8.3	15.0	14.5	12.3	88.1
V	252.3	306.3	303.0	445.4	363.6	371.9	345.6	329.9	383.0	324.5
Zn	91.0	112.1	111.1	156.4	142.3	145.8	156.9	149.9	114.0	83.3
Cu	65.0	40.5	37.1	65.4	39.7	47.4	40.5	39.6	32.9	119.9
Ni	54.6	30.8	28.0	41.1	<2.504	4.3	14.2	16.3	16.4	47.8
S	1213	854	823	2189	1440	1560	1411	1523	0	433

Appendix B

BHVO-2 Standard Results

Internal standard results of BHVO-2 run with the new ICP-MS trace element batch for comparison with compiled values (www.georem.mpch-mainz.gwdg.de). Percent error shown.

BHVO 2	UCT 2010	Average Compiled Values	Difference	Absolute % Difference
Sc	30.58	32.15	-1.57	4.9
V	330.8	317	13.8	4.4
Cr	288.8	280	8.8	3.1
Co	45.12	45	0.12	0.3
Ni	119.6	120	-0.4	0.3
Cu	103.7	125	-21.3	17.0
Zn	116.8	102	14.8	14.5
Rb	8.88	9.8	-0.92	9.4
Sr	395.1	392.5	2.6	0.7
Y	23.51	27	-3.49	12.9
Zr	163.8	175	-11.2	6.4
Nb	17.23	18.65	-1.42	7.6
Ba	126.7	130.5	-3.8	2.9
La	14.62	15.1	-0.48	3.2
Ce	36.08	37.75	-1.67	4.4
Pr	5.05	5.31	-0.26	4.9
Nd	23.6	24.7	-1.1	4.5
Sm	5.81	6.14	-0.33	5.3
Eu	2.04	2.07	-0.03	1.4
Tb	0.92	0.92	0.00	0.0
Gd	6.36	6.27	0.09	1.4
Dy	5.27	5.31	-0.04	0.8
Ho	0.97	1.01	-0.03	3.5
Er	2.52	2.54	-0.02	0.8
Tm	0.34	0.36	-0.02	4.2
Yb	1.98	2	-0.02	1.0
Lu	0.29	0.28	0.02	5.5
Hf	4.33	4.19	0.14	3.3
Ta	0.95	1.4	-0.45	32.1
Ob	1.47	1.55	-0.08	5.2
Th	1.19	1.225	-0.04	2.9
U	0.45	0.409	0.04	10.0
			average:	5.6

Appendix C

Cape Granite and Malmesbury Group

Cape Granite Suite and Malmesbury Group major element oxides and trace elements. Unpublished major element oxide data by XRF for Cape Granites (CJ-08 and CJ-12) from Creighton-Jones (1982). Unpublished major element oxide and trace element data for Malmesbury Formation samples MM-001 and NM-012 from Mbeje (2005) and Mbangula (2004) respectively. *Zr concentration of granites is measured XRF.

	Cape Granite			Malmesbury Formation	
	CG-A1	CJ-08	CJ-12	MM-001	NM-012
	Cable Way quarry	Sea Point	Sea Point	Grotto Bay	Robben Island
Major element oxides (wt.%)					
SiO_2	71.8	71.4	71.5	72.9	60.9
TiO_2	0.48	0.38	0.38	0.88	0.91
Al_2O_3	13.7	14.6	14.5	11.8	19.4
FeO	3.02	2.57	2.60	4.89	7.33
MnO	0.07	0.07	0.06	0.08	0.12
MgO	1.11	0.88	0.92	2.34	4.23
CaO	1.3	1.16	1.18	1.29	0.28
Na_2O	2.55	3.00	2.77	2.67	2.04
K_2O	5.14	4.97	4.95	2.92	4.65
P_2O_5	0.21	0.24	0.23	0.23	0.15
LOI	0.55	0.83	0.88	-	-
ICPMS trace elements (ppm)					
Sc	8	4	5	10	16
V	35	30	31	87	123
Cr	23	14	15	68	85
Co	4	5	5	11	16
Ni	10	7	7	30	40
Cu	<0.5	1	7	23	46
Zn	49	49	55	-	-
Rb	109	238	247	101	153
Sr	33	75	80	136	57
Y	14	21	23	30	19
Zr	*135	*147	*155	145	112
Nb	14.8	12.4	13.2	12.2	13.7
Ba	274	364	357	499	491
La	18.6	25.2	25.5	40.1	25.1
Ce	45.8	53.7	54.3	84.8	56.3
Pr	5.18	6.20	6.36	9.72	6.35
Nd	20.3	23.9	24.2	38.2	25.3
Sm	4.32	4.99	5.36	7.18	4.97
Eu	0.49	0.84	0.87	1.41	0.97
Gd	3.78	4.56	5.05	6.53	4.44
Tb	0.56	0.71	0.80	0.96	0.67
Dy	3.52	4.35	4.68	5.64	4.12
Ho	0.64	0.76	0.82	1.12	0.81
Er	1.76	2.15	2.13	3.14	2.39
Tm	0.25	0.30	0.28	0.47	0.36
Yb	1.53	1.89	1.68	2.99	2.49
Lu	0.21	0.27	0.22	0.44	0.36
Hf	2.15	1.59	1.55	3.99	2.94
Ta	1.43	1.55	1.27	0.87	7.28
Pb	22.9	23.9	62.3	16.6	31.9
Th	8.6	11.1	11.5	10.9	12.2
U	5.5	3.1	4.3	3.2	1.5

Appendix D

Microprobe Data

Original microprobe analysis by Butt (1989); Hirschel (1989); Wulfse (1989) of 6 dykes from the Cape Peninsula, with major elements concentrations reported as their respective oxides:

- Logies Bay
- Tokai
- Chapman's Peak 3
- Millers Point
- Oukaapseweg
- Nursery Ravine

Sample: GCH89-47 – Logies Bay

Feldspar

		Weight Percent Oxide								Plagioclase		Ternary Fsp		
		Na	Si	Al	K	Ca	Fe	Mg	Sum	An	Ab	An	Ab	Or
1	Plag 1 – core	1.90	47.64	31.86	0.07	16.60	0.41	0.16	98.64	82.84	17.16	82.50	17.09	0.41
2	Plag 1 – rim	5.59	55.30	25.77	0.39	9.12	1.41	0.27	97.85	47.41	52.59	46.29	51.35	2.36
3	Plag 2 – rim	6.23	56.93	24.82	0.51	8.46	0.57	0.00	97.52	42.87	57.13	41.59	55.42	2.99
4	Plag 2 – core	3.29	50.63	30.13	0.13	14.18	0.67	0.12	99.15	70.43	29.57	69.89	29.34	0.76
5	Plag 3	3.66	51.67	29.02	0.19	13.50	0.75	0.08	98.87	67.09	32.91	66.34	32.55	1.11
6	Plag 4 – rim	2.00	47.69	31.50	0.08	16.50	0.58	0.11	98.46	82.01	17.99	81.62	17.90	0.47
7	Plag 4 – core	2.11	47.79	32.11	0.08	16.14	0.63	0.08	98.94	80.87	19.13	80.48	19.04	0.47
8	Plag 5 A	3.02	50.25	30.24	0.14	14.76	0.78	0.14	99.33	72.98	27.02	72.38	26.80	0.82
9	Plag 5 B	3.43	51.01	28.83	0.18	13.87	0.52	0.15	97.99	69.08	30.92	68.35	30.59	1.06
10	Plag 6	2.25	48.83	31.48	0.10	15.94	0.88	0.09	99.57	79.65	20.35	79.18	20.23	0.59
11	Plag 7 A	4.53	53.37	27.45	0.30	12.06	0.83	0.09	98.63	59.53	40.47	58.50	39.77	1.73
12	Plag 8	2.10	47.98	31.11	0.12	16.54	0.42	0.12	98.39	81.32	18.68	80.75	18.55	0.70
13	Plag 9	2.08	48.22	31.80	0.07	16.58	0.40	0.13	99.28	81.50	18.50	81.17	18.43	0.41

Pyroxene

		Weight Percent Oxide										End-member-percentages		
		Na	Mg	Al	Si	Ca	Ti	Mn	Fe	Cr	Sum	En	Fs	Wo
1	Pyro 1	0.22	17.46	2.14	52.62	19.51	0.58	0.16	7.70	0.34	100.73	48.77	12.06	39.16
2	Pyro 2	0.27	17.12	3.33	51.39	20.00	0.55	0.18	6.63	0.86	100.33	48.62	10.56	40.82
3	Pyro 3	0.25	17.46	2.71	51.44	19.57	0.63	0.19	7.48	0.52	100.25	48.88	11.75	39.37
4	Pyro 4	0.26	16.93	2.35	52.27	18.94	0.78	0.23	9.2	0.1	101.06	47.42	14.45	38.12
5	Pyro 5	0.25	17.21	2.35	52.45	19.07	0.74	0.21	9.08	0.13	101.49	47.80	14.14	38.06
6	Pyro 6	0.26	17.04	2.95	52.33	19.9	0.55	0.19	7.22	0.55	100.99	48.15	11.44	40.41
7	Pyro 7	0.27	16.72	2.05	52.71	18.99	0.72	0.22	9.78	0.08	101.54	46.64	15.30	38.06

Sample: GCH89-47 – Logies Bay

Olivine

		Weight Percent Oxide										End-member-percentages	
		Si	Al	Fe	Mg	Ca	Mn	Ni	Cr	Ti	Sum	Fo	Fa
1	Olivine 1 A	36.15	0.00	37.47	28.08	0.26	0.51	0.00	0.00	0.00	102.47	57.19	42.81
2	Olivine 1 B	35.41	0.00	35.91	28.31	0.29	0.60	0.00	0.00	0.00	100.52	58.43	41.57
3	Olivine 2 A	36.53	0.00	32.41	30.70	0.27	0.51	0.00	0.00	0.00	100.42	62.81	37.19
4	Olivine 2 B	36.92	0.00	29.28	33.14	0.18	0.52	0.12	0.00	0.00	100.16	66.86	33.14
5	Olivine 3 A	35.65	0.00	37.99	26.44	0.24	0.53	0.00	0.00	0.00	100.85	55.37	44.63
6	Olivine 3 B	36.44	0.00	32.91	30.46	0.26	0.54	0.00	0.00	0.00	100.61	62.27	37.73
7	Olivine 4 A	37.63	0.00	28.21	34.55	0.21	0.41	0.00	0.00	0.00	101.01	68.59	31.41
8	Olivine 4 B	37.48	0.00	28.11	35.10	0.20	0.43	0.00	0.00	0.00	101.32	69.00	31.00
9	Olivine 5 A	36.41	0.00	31.77	31.14	0.24	0.49	0.00	0.00	0.00	100.05	63.60	36.40
10	Olivine 5 B	36.60	0.00	32.43	30.45	0.23	0.54	0.00	0.00	0.00	100.25	62.60	37.40
11	Olivine 6 A	36.10	0.00	32.90	30.79	0.27	0.49	0.00	0.00	0.00	100.55	62.53	37.47

Oxide

		Weight Percent Oxide								
		Mg	Al	Si	Ti	Fe	Ca	Mn	Cr	Sum
1	Oxide 2	0.09	2.35	0.00	14.46	76.59	0.00	0.56	0.10	94.15
2	Oxide 4	13.93	1.62	34.87	5.84	27.61	2.37	0.72	0.00	86.96
3	Oxide 5	0.00	0.00	0.00	0.12	78.91	0.00	0.00	0.00	79.03
4	Oxide 6	0.39	0.00	0.00	50.57	46.92	0.00	1.15	0.00	99.03
5	Oxide 7	0.12	1.80	0.11	15.81	76.25	0.00	0.55	0.00	94.64
6	Oxide 8	0.38	1.26	0.18	20.06	73.95	0.00	0.42	0.00	96.25
7	Oxide 8	0.44	0.84	1.00	31.43	61.60	0.06	0.96	0.00	96.33

Sample: GCH89-22 – Tokai GM = groundmass

Feldspar

		Weight Percent Oxide								Plagioclase		Ternary Fsp		
		Na	Si	Al	K	Ca	Fe	Mg	Sum	An	Ab	An	Ab	Or
1	Plag 1	3.97	51.62	28.15	0.29	12.42	0.64	0.11	97.20	63.35	36.65	62.26	36.01	1.73
2	Plag 1	3.70	52.35	29.28	0.21	13.23	0.80	0.12	99.69	66.40	33.60	65.57	33.19	1.24
3	Plag 2 Glom	2.56	49.71	31.31	0.14	15.16	0.49	0.16	99.53	76.59	23.41	75.95	23.21	0.84
4	Plag 3 Glom	4.03	53.35	28.76	0.24	12.69	0.75	0.14	99.96	63.50	36.50	62.61	35.98	1.41
5	Plag 4 G. Rim	3.79	52.60	29.11	0.20	12.93	0.78	0.11	99.52	65.34	34.66	64.56	34.25	1.19
6	Plag 4 G. Core	2.89	50.40	30.63	0.14	14.95	0.48	0.17	99.66	74.08	25.92	73.48	25.70	0.82
7	Plag 5 Glom	2.06	48.29	32.05	0.08	16.03	0.55	0.18	99.24	81.13	18.87	80.74	18.78	0.48
8	Plag 6 Glom	3.19	51.68	29.73	0.15	14.03	0.55	0.21	99.54	70.85	29.15	70.22	28.89	0.89
9	Plag 7 Glom	3.79	53.00	29.27	0.25	12.93	0.91	0.17	100.32	65.34	34.66	64.37	34.15	1.48
10	Plag 8 (Oliv 8)	3.19	51.26	29.94	0.18	14.03	0.58	0.13	99.31	70.85	29.15	70.09	28.84	1.07
11	Plag 9 GM	3.40	51.63	29.72	0.24	13.78	0.71	0.08	99.56	69.13	30.87	68.16	30.43	1.41
12	Plag 11 Glom	2.07	49.06	32.09	0.08	16.17	0.46	0.19	100.12	81.19	18.81	80.80	18.72	0.48
13	Plag 12 Glom	1.97	48.49	32.15	0.07	16.08	0.47	0.16	99.39	81.85	18.15	81.51	18.07	0.42
14	Plag 14 Glom	1.94	47.86	31.97	0.12	16.10	0.71	0.12	98.82	82.10	17.90	81.50	17.77	0.72

Pyroxene

		Weight Percent Oxide										End-member-percentages		
		Na	Mg	Al	Si	Ca	Ti	Mn	Fe	Cr	Sum	En	Fs	Wo
1	Pyroxene 1	0.11	20.92	0.87	53.40	4.70	0.48	0.51	20.75	0.00	101.74	58.21	32.39	9.40
2	Pyroxene 2	0.00	20.60	0.80	52.34	4.70	0.44	0.48	20.49	0.00	99.85	58.08	32.40	9.52
3	Pyroxene 3	0.28	15.76	1.99	51.41	17.29	0.79	0.35	11.70	0.00	99.57	45.36	18.89	35.76
4	Pyroxene 4	0.26	16.04	2.01	50.24	18.14	0.69	0.27	10.13	0.00	97.78	46.15	16.35	37.50
5	Pyroxene 5 GM	0.28	16.02	2.73	49.87	19.09	0.74	0.22	8.62	0.19	97.76	46.34	13.98	39.68
6	Pyroxene 6 GM	0.25	16.97	2.55	50.81	19.58	0.52	0.17	6.74	0.63	98.22	48.74	10.86	40.41
7	Pyroxene 7	0.23	17.17	1.75	50.66	18.57	0.54	0.21	7.96	0.15	97.24	49.09	12.76	38.15
8	Pyroxene 8 GM	0.28	16.71	3.35	49.88	19.19	0.57	0.18	6.77	0.83	97.76	48.72	11.07	40.21
9	Pyroxene 9	0.27	15.16	1.72	49.61	15.00	0.94	0.41	15.79	0.00	98.90	43.57	25.45	30.98

Sample: GCH89-22 – Tokai

Olivine

	Weight Percent Oxide										End-member-percentages	
	Si	Al	Fe	Mg	Ca	Mn	Ni	Cr	Ti	Sum	Fo	Fa
1 Olivine 1	35.84	0.00	33.83	29.98	0.21	0.55	0.00	0.00	0.00	100.41	61.24	38.76
2 Olivine 2	35.21	0.00	36.95	27.24	0.22	0.59	0.00	0.00	0.00	100.21	56.79	43.21
3 Olivine 3	35.33	0.00	34.99	28.60	0.26	0.52	0.00	0.00	0.00	99.70	59.30	40.70
4 Olivine 4	35.52	0.00	33.81	29.55	0.21	0.47	0.00	0.00	0.00	99.56	60.91	39.09
5 Olivine 5	36.59	0.00	27.99	34.06	0.26	0.41	0.00	0.00	0.00	99.31	68.45	31.55
6 Olivine 6	37.02	0.00	25.06	36.61	0.25	0.36	0.00	0.00	0.00	99.30	72.26	27.74
7 Olivine 7	35.54	0.00	34.72	28.83	0.25	0.53	0.00	0.00	0.00	99.87	59.68	40.32
8 Olivine 8	32.27	0.00	32.40	30.94	0.20	0.46	0.00	0.00	0.00	96.27	63.00	37.00

Oxide

	Weight Percent Oxide								
	Mg	Al	Si	Ti	Fe	Ca	Mn	Cr	Sum
1 Oxide 1	0.00	0.00	0.20	0.00	61.90	0.06	0.00	0.00	62.16

Sample: GCH89-14 – Chapmna's Peak 3 (CP3)

Feldspar

		Weight Percent Oxide								Plagioclase		Ternary Fsp		
		Na	Si	Al	K	Ca	Fe	Mg	Sum	An	Ab	An	Ab	Or
1	Plag 1 core	2.42	49.49	30.78	0.10	15.59	0.60	0.24	99.22	78.07	21.93	77.61	21.80	0.59
2	Plag 1 rim	3.34	51.93	28.93	0.19	13.53	0.85	0.23	99.00	69.12	30.88	68.33	30.53	1.14
3	Plag 2 core	2.36	48.69	31.07	0.12	15.47	0.59	0.18	98.48	78.37	21.63	77.80	21.48	0.72
4	Plag 2 rim	3.31	51.58	28.93	0.22	13.72	0.83	0.23	98.82	69.61	30.39	68.70	29.99	1.31
5	Plag 3 rim	5.86	56.89	24.59	0.73	8.98	0.70	0.00	97.75	45.85	54.15	43.90	51.85	4.25
6	Plag 3 rim	5.19	55.94	26.25	0.54	10.02	0.74	0.08	98.76	51.62	48.38	49.96	46.83	3.21
7	Plag 3 core	3.38	51.09	29.31	0.18	13.60	0.68	0.20	98.44	68.98	31.02	68.24	30.69	1.08
8	Plag 3 core	3.21	50.95	29.48	0.20	14.04	0.68	0.23	98.79	70.73	29.27	69.90	28.92	1.19
9	Plag 3 core	3.50	51.82	28.66	0.22	13.27	0.88	0.20	98.55	67.69	32.31	66.80	31.88	1.32
10	plag	3.51	51.70	29.58	0.24	13.67	0.87	0.23	99.80	68.28	31.72	67.31	31.28	1.41
11	Plag 4 core	2.40	48.48	31.14	0.14	15.52	0.68	0.27	98.63	78.13	21.87	77.48	21.68	0.83
12	Plag 4 rim	2.31	48.53	31.71	0.10	15.87	0.59	0.23	99.34	79.15	20.85	78.68	20.73	0.59
13	Plag 4 core	2.32	48.38	31.57	0.13	15.73	0.67	0.23	99.03	78.93	21.07	78.32	20.90	0.77
14	Plag 4 rim	3.84	51.69	28.89	0.25	12.88	0.94	0.21	98.70	64.96	35.04	63.99	34.53	1.48
15	Plag 5 core	2.32	49.06	30.57	0.12	15.82	0.67	0.19	98.75	79.03	20.97	78.47	20.82	0.71
16	Plag 5 rim	2.34	49.19	30.72	0.12	15.66	0.62	0.19	98.84	78.72	21.28	78.15	21.13	0.71
17	plag gm	3.79	52.30	27.81	0.23	12.29	1.75	0.42	98.59	64.18	35.82	63.28	35.31	1.41
18	Plag 6	2.22	49.31	31.63	0.13	15.98	0.60	0.19	100.06	79.91	20.09	79.30	19.94	0.77
19	Plag 6 core	2.23	49.66	31.63	0.15	15.88	0.54	0.20	100.29	79.74	20.26	79.03	20.08	0.89
20	Plag 6 rim	2.98	51.67	30.23	0.17	14.55	0.78	0.26	100.64	72.96	27.04	72.23	26.77	1.00
21	Plag 6 rim	3.67	53.17	29.12	0.24	13.31	1.03	0.21	100.75	66.71	33.29	65.77	32.82	1.41
22	Plag 7	2.20	49.73	31.73	0.11	15.89	0.61	0.20	100.47	79.97	20.03	79.44	19.90	0.65
23	Plag 7	2.61	51.24	30.81	0.15	15.28	0.59	0.23	100.91	76.39	23.61	75.71	23.40	0.88
24	Plag 8	2.70	51.00	30.66	0.15	14.94	0.71	0.23	100.39	75.36	24.64	74.68	24.42	0.89
25	Plag 8 rim	4.60	55.90	27.19	0.45	11.25	0.93	0.13	100.45	57.47	42.53	55.94	41.39	2.66
26	Plag 8 rim	3.69	53.85	28.72	0.30	13.11	1.01	0.17	100.85	66.25	33.75	65.08	33.15	1.77
27	Plag 9	2.18	49.61	31.68	0.14	16.15	0.59	0.20	100.55	80.37	19.63	79.71	19.47	0.82
28	Plag 9 rim	4.81	56.25	26.66	0.42	10.96	0.84	0.10	100.04	55.74	44.26	54.35	43.17	2.48

Sample: GCH89-14 – Chapmna's Peak 3 (CP3)

Feldspar

	Weight Percent Oxide								Plagioclase		Ternary Fsp		
	Na	Si	Al	K	Ca	Fe	Mg	Sum	An	Ab	An	Ab	Or
29 Plag 10	2.16	50.29	30.85	0.21	15.37	0.78	0.39	100.05	79.73	20.27	78.70	20.02	1.28
30 Plag 10 rim	3.75	53.23	29.16	0.23	13.23	1.00	0.21	100.81	66.10	33.90	65.20	33.45	1.35
31 Plag 11	2.29	49.74	31.31	0.13	15.99	0.57	0.20	100.23	79.42	20.58	78.81	20.43	0.76
32 Plag 11 rim	4.66	54.17	27.62	0.46	11.34	0.94	0.09	99.28	57.35	42.65	55.81	41.50	2.70
33 Plag	4.28	54.92	27.87	0.45	11.84	0.99	0.21	100.56	60.45	39.55	58.84	38.49	2.66
34 Plag	3.43	52.95	29.32	0.36	13.54	0.82	0.27	100.69	68.57	31.43	67.11	30.76	2.12
35 Plag gm	3.48	53.00	28.91	0.38	13.42	0.85	0.26	100.30	68.06	31.94	66.53	31.22	2.24
36 Plag gm	3.66	53.44	28.92	0.31	13.12	1.08	0.19	100.72	66.45	33.55	65.23	32.93	1.84
37 Plag gm	4.16	54.57	27.95	0.44	12.07	1.05	0.15	100.39	61.59	38.41	59.98	37.41	2.60
38 Plag gm	4.56	55.38	27.70	0.46	11.31	0.68	0.12	100.21	57.82	42.18	56.24	41.03	2.72
39 Plag gm	5.69	58.05	26.64	0.81	8.81	0.20	0.00	100.20	46.11	53.89	43.89	51.30	4.81
40 Plag gm	4.98	60.19	24.62	1.66	8.04	0.80	0.12	100.41	47.15	52.85	42.25	47.36	10.39

Pyroxene

	Weight Percent Oxide										End-member-percentages		
	Na	Mg	Al	Si	Ca	Ti	Mn	Fe	Cr	Sum	En	Fs	Wo
1 Pyrox int	0.17	18.01	2.81	50.41	15.67	0.50	0.29	10.45	0.13	98.44	51.26	16.68	32.05
2 Pyrox int	0.13	16.46	2.16	51.14	10.82	0.68	0.50	20.66	0.00	102.55	45.95	32.35	21.70
3 Pyrox int	0.25	11.50	2.55	49.04	18.20	1.01	0.33	16.50	0.00	99.38	33.99	27.35	38.66
4 Pyrox	0.30	12.34	2.71	49.73	17.71	1.03	0.45	16.90	0.00	101.17	35.72	27.44	36.84
5 Pyrox int	0.19	16.78	2.84	51.54	17.77	0.63	0.25	10.21	0.00	100.21	47.57	16.23	36.20
6 Pyrox int	0.14	19.35	2.85	52.59	14.61	0.51	0.28	10.22	0.28	100.83	54.38	16.11	29.51
7 Pyrox	0.23	15.67	2.40	51.59	17.76	0.51	0.27	11.73	0.00	100.16	44.76	18.79	36.45
8 Pyrox	0.21	15.39	2.75	51.29	19.42	0.55	0.23	10.13	0.00	99.97	43.94	16.22	39.84
9 Pyrox	0.17	18.01	2.91	51.80	15.60	0.50	0.32	10.48	0.16	99.95	51.31	16.75	31.94
10 Pyrox	0.20	15.74	3.46	50.46	18.55	0.60	0.21	10.10	0.16	99.48	45.31	16.31	38.38
11 Pyrox	0.17	16.60	2.96	51.04	17.50	0.60	0.24	10.09	0.11	99.31	47.65	16.25	36.10

Sample: GCH89-14 – Chapmna's Peak 3 (CP3)

Pyroxene

	Weight Percent Oxide										End-member-percentages		
	Na	Mg	Al	Si	Ca	Ti	Mn	Fe	Cr	Sum	En	Fs	Wo
12 Pyrox	0.19	16.21	2.50	50.64	15.07	0.62	0.29	14.19	0.00	99.71	46.32	22.74	30.94
13 Pyrox	0.24	16.05	3.19	50.75	16.87	0.67	0.23	11.89	0.00	99.89	46.07	19.14	34.79
14 Pyrox	0.15	15.53	2.30	50.04	11.92	0.64	0.37	18.26	0.00	99.21	45.23	29.83	24.95
15 Pyrox	0.12	19.16	1.91	51.96	10.62	0.46	0.41	16.11	0.00	100.75	53.48	25.22	21.30
16 Pyrox	0.19	10.33	1.56	49.39	14.06	0.56	0.62	23.42	0.00	100.13	30.77	39.13	30.10
17 Pyrox	0.18	17.91	2.58	51.64	15.11	0.49	0.27	11.73	0.09	100.00	50.67	18.61	30.72
18 Pyrox	0.22	17.47	3.07	51.26	16.61	0.60	0.24	10.48	0.16	100.11	49.51	16.66	33.83
19 Pyrox	0.20	16.07	2.48	50.93	15.77	0.54	0.26	13.63	0.00	99.88	45.85	21.81	32.33

Oxide

	Weight Percent Oxide								
	Mg	Al	Si	Ti	Fe	Ca	Mn	Cr	Sum
1 Oxide 1	0.00	2.22	0.25	20.37	69.52	0.09	1.74	0.00	94.19
2 Oxide 2	0.00	2.16	0.22	19.53	70.69	0.11	1.44	0.00	94.15
3 Oxide 3	0.00	2.16	0.18	19.22	71.43	0.00	1.31	0.00	94.30
4 Oxide 4	0.00	2.27	0.19	20.17	69.31	0.07	1.80	0.00	93.81
5 Oxide 5	0.00	2.17	0.16	20.93	68.85	0.10	1.64	0.00	93.85
6 Oxide 6	0.00	2.16	0.15	21.03	69.01	0.09	1.65	0.00	94.09
7 Oxide 7	0.00	2.38	0.52	18.68	72.38	0.06	1.52	0.00	95.54
8 Oxide 8	1.57	2.34	5.33	24.42	59.19	0.28	1.11	0.19	94.43
9 Oxide 9	3.54	3.44	15.70	52.10	15.28	1.87	0.23	0.00	92.16
10 Oxide 10	0.46	2.14	1.52	23.14	62.72	0.14	1.72	0.00	91.84
11 Oxide 11	0.29	2.41	1.82	20.26	68.96	0.14	1.94	0.00	95.82

Sample: GCH89-34 – Millers Point

Feldspar

		Weight Percent Oxide								Plagioclase		Ternary Fsp		
		Na	Si	Al	K	Ca	Fe	Mg	Sum	An	Ab	An	Ab	Or
1	Plag 1 – core	2.57	50.13	31.50	0.10	15.40	0.52	0.19	100.41	76.81	23.19	76.35	23.06	0.59
2	Plag 1 – rim	2.54	50.79	31.30	0.13	15.42	0.41	0.19	100.78	77.04	22.96	76.45	22.79	0.77
3	Plag 2 phen core	2.33	49.54	31.90	0.08	16.00	0.54	0.18	100.57	79.14	20.86	78.77	20.76	0.47
4	Plag 3 gm	4.07	52.77	28.72	0.34	12.59	0.76	0.16	99.41	63.09	36.91	61.84	36.17	1.99
5	Plag 4 phen core	4.16	54.37	28.34	0.41	12.14	0.99	0.15	100.56	61.72	38.28	60.23	37.35	2.42
6	Plag 4 phen rim	5.07	56.41	27.09	0.56	10.31	0.69	0.07	100.20	52.91	47.09	51.16	45.53	3.31
7	Plag 5 gm	3.90	53.62	28.99	0.35	12.59	0.70	0.18	100.33	64.08	35.92	62.75	35.17	2.08
8	Plag 6 gm	4.52	55.25	28.01	0.45	11.54	0.71	0.10	100.58	58.52	41.48	56.97	40.38	2.65
9	Plag 7 gm	3.69	53.57	29.23	0.30	13.19	0.83	0.15	100.96	66.39	33.61	65.22	33.02	1.77
10	Plag 8 gm	3.64	53.37	29.25	0.33	13.15	0.71	0.15	100.60	66.63	33.37	65.33	32.72	1.95
11	Plag 10 gm	3.96	53.25	28.43	0.40	12.06	2.09	0.33	100.52	62.73	37.27	61.21	36.37	2.42
12	Plag 11 gm	7.95	62.39	22.78	1.07	4.83	0.30	0.00	99.32	25.13	74.87	23.57	70.21	6.22
13	Plag 13 phen core	2.06	48.94	32.52	0.00	16.23	0.44	0.16	100.35	81.32	18.68	81.32	18.68	0.00
14	Plag 14 gm	3.97	53.60	28.50	0.33	12.30	1.42	0.23	100.35	63.13	36.87	61.88	36.14	1.98
15	Plag 15 gm	4.03	53.81	28.78	0.35	12.42	0.91	0.21	100.51	63.00	37.00	61.70	36.23	2.07
16	Plag 16 phen	3.16	51.24	29.49	0.17	13.39	2.62	0.54	100.61	70.07	29.93	69.34	29.61	1.05
17	Plag 17 phen	2.28	49.88	32.06	0.07	15.96	0.47	0.18	100.90	79.46	20.54	79.13	20.46	0.41
18	Plag 18 phen	3.89	53.74	28.89	0.36	12.61	0.75	0.14	100.38	64.17	35.83	62.80	35.06	2.13
19	Plag 19 phen	5.11	56.57	26.98	0.59	10.35	0.57	0.09	100.26	52.81	47.19	50.99	45.55	3.46
20	plag gm	4.80	54.47	27.25	0.49	10.91	0.61	0.10	98.63	55.67	44.33	54.06	43.04	2.89
21	Plag 20 phen alt.	3.27	51.60	30.47	0.19	14.11	0.54	0.18	100.36	70.45	29.55	69.67	29.22	1.12
22	Plag 21 phen	2.54	48.87	31.18	0.10	15.45	0.56	0.19	98.89	77.07	22.93	76.62	22.79	0.59

Sample: GCH89-34 – Millers Point

	Pyroxene	Weight Percent Oxide										End-member-percentages		
		Na	Mg	Al	Si	Ca	Ti	Mn	Fe	Cr	Sum	En	Fs	Wo
1	Pyrox 1 phen core	0.31	16.65	3.98	51.28	19.96	0.62	0.18	6.62	0.67	100.27	47.97	10.70	41.33
2	Pyrox gm	0.29	17.11	3.27	51.73	19.88	0.46	0.18	6.46	0.46	99.84	48.86	10.35	40.79
3	Pyrox 2 phen core	0.20	17.56	1.83	52.38	17.54	0.56	0.29	9.66	0.14	100.16	49.35	15.23	35.42
4	Pyrox 2 phen rim	0.30	17.03	3.83	51.59	19.41	0.48	0.18	6.48	0.71	100.01	49.20	10.50	40.30
5	Pyrox 3 phen core	0.21	18.62	1.75	52.68	16.52	0.45	0.21	9.28	0.13	99.85	52.16	14.58	33.26
6	Pyrox gm	0.21	14.57	2.29	50.22	15.39	1.11	0.34	15.86	0.00	99.99	42.20	25.77	32.03
7	Pyrox gm	0.06	22.49	0.73	53.65	4.02	0.31	0.48	19.68	0.00	101.42	61.76	30.31	7.93
8	Pyrox gm	0.27	13.89	1.17	50.92	17.23	0.61	0.38	15.28	0.00	99.75	39.87	24.60	35.54
9	Pyrox gm	0.20	16.14	2.12	51.63	17.33	0.81	0.28	12.22	0.00	100.73	45.53	19.34	35.13
10	Pyrox gm	0.21	17.42	1.95	52.40	17.65	0.54	0.31	9.30	0.20	99.98	49.32	14.77	35.91
11	Pyroxene	0.00	28.27	0.96	56.24	2.31	0.24	0.29	13.88	0.09	102.28	74.96	20.64	4.40
12	Pyroxene	0.22	16.58	2.57	52.40	15.13	0.52	0.28	12.66	0.16	100.52	47.98	20.55	31.47
13	Pyroxene	0.05	28.36	1.38	56.09	2.29	0.25	0.28	12.94	0.22	101.86	76.11	19.48	4.42

	Oxide	Weight Percent Oxide								
		Mg	Al	Si	Ti	Fe	Ca	Mn	Cr	Sum
1	Oxide 1	0.48	0.13	0.12	50.71	48.10	0.19	0.49	0.00	100.22
2	Oxide 2	0.71	2.51	0.13	13.06	76.72	0.00	0.31	0.09	93.53
3	Oxide 3 – lamination	1.58	0.08	0.09	51.52	45.85	0.00	0.92	0.00	100.04
4	Oxide 4	0.75	0.09	0.00	51.64	47.07	0.00	0.62	0.00	100.17
5	Oxide 5	0.23	3.74	0.08	13.35	74.72	0.00	1.37	0.13	93.62
6	Oxide 5 – large lam.	2.15	0.11	0.00	51.76	45.31	0.00	0.56	0.00	99.89
7	Oxide 5 – small lam.	2.50	0.64	1.44	45.80	47.58	0.00	0.69	0.00	98.65
8	Oxide 6	0.07	2.86	0.32	18.31	69.60	0.15	1.59	0.00	92.90
9	Oxide 7	0.00	1.85	0.21	22.18	69.12	0.09	0.52	0.00	93.97
10	Oxide 8	0.00	1.53	0.24	20.50	71.92	0.09	0.36	0.00	94.64
11	Oxide 9	0.27	0.15	0.48	49.39	46.63	0.05	0.62	0.00	97.59
12	Oxide 10	0.00	2.17	0.29	22.98	69.51	0.09	0.38	0.00	95.42
13	Oxide 11	0.00	1.88	0.19	23.38	69.17	0.07	0.92	0.00	95.61
14	Oxide 12	0.00	1.80	0.30	22.52	69.93	0.12	0.38	0.00	95.05
15	Oxide 13	0.00	1.70	0.17	24.99	68.65	0.05	0.71	0.00	96.27
16	Oxide 14	0.11	1.98	0.51	20.41	71.39	0.14	0.36	0.00	94.90
17	Oxide 15	0.00	1.90	0.16	20.68	71.77	0.00	1.11	0.00	95.62
18	Oxide 16	0.00	1.18	0.18	20.85	72.78	0.08	0.37	0.00	95.44
19	Oxide 17	0.43	0.09	0.08	50.47	47.36	0.18	0.52	0.00	99.13

Sample: GCH89-36 – Oukaapseweg

Feldspar	Weight Percent Oxide								Plagioclase		Ternary Fsp		
	Na	Si	Al	K	Ca	Fe	Mg	Sum	An	Ab	An	Ab	Or
1 Plag	6.60	60.73	24.64	1.00	7.10	0.59	0.00	100.66	37.28	62.72	35.09	59.03	5.88
2 Plag	6.33	59.17	25.10	0.80	8.08	0.43	0.00	99.91	41.36	58.64	39.44	55.91	4.65
3 Plag	5.65	58.44	25.73	0.63	9.00	0.59	0.06	100.10	46.82	53.18	45.06	51.19	3.76
4 Plag	5.01	55.86	27.15	0.46	10.54	0.60	0.08	99.70	53.76	46.24	52.30	44.98	2.72
5 Plag	4.05	53.21	28.37	0.37	12.32	1.05	0.13	99.50	62.70	37.30	61.33	36.48	2.19
6 Plag	4.44	54.76	27.87	0.42	11.56	0.69	0.07	99.81	59.00	41.00	57.53	39.98	2.49
7 Plag	4.43	54.96	27.75	0.43	11.65	0.77	0.11	100.10	59.24	40.76	57.73	39.73	2.54
8 Plag	5.31	56.99	26.91	0.52	10.09	0.70	0.07	100.59	51.22	48.78	49.66	47.29	3.05
9 Plag	4.82	56.29	27.21	0.51	10.62	0.62	0.07	100.14	54.91	45.09	53.23	43.72	3.04
10 Plag	4.35	54.19	27.85	0.42	11.90	0.79	0.12	99.62	60.19	39.81	58.70	38.83	2.47

Pyroxene	Weight Percent Oxide										End-member-percentages		
	Na	Mg	Al	Si	Ca	Ti	Mn	Fe	Cr	Sum	En	Fs	Wo
1 pyroxene	0.25	13.92	2.48	50.48	17.93	1.09	0.34	14.25	0.00	100.74	40.00	22.97	37.03
2 pyroxene	0.21	15.44	2.04	52.70	14.82	0.88	0.41	16.37	0.00	102.87	43.77	26.03	30.19
3 pyroxene	0.18	14.48	1.98	50.85	15.08	0.95	0.44	17.07	0.00	101.03	41.50	27.44	31.06
4 pyroxene	0.21	14.70	2.15	50.68	15.11	1.02	0.35	16.54	0.00	100.76	42.20	26.63	31.17
5 pyroxene	0.23	14.45	2.38	50.53	18.82	0.96	0.29	12.42	0.12	100.20	41.36	19.94	38.71
6 pyroxene	0.23	14.44	2.34	50.35	17.54	0.90	0.27	13.60	0.00	99.67	41.65	22.00	36.35
7 pyroxene	0.20	15.29	2.08	51.15	16.26	0.87	0.37	14.13	0.00	100.35	43.81	22.71	33.48
8 pyroxene	0.26	13.70	2.40	50.31	18.60	1.11	0.36	13.66	0.00	100.40	39.45	22.06	38.49
9 pyroxene	0.23	15.49	1.68	51.87	16.06	0.75	0.35	14.26	0.00	100.69	44.22	22.83	32.95
10 pyroxene	0.21	15.48	2.26	50.80	14.74	0.99	0.43	16.44	0.00	101.35	43.86	26.13	30.01
11 pyroxene	0.22	13.74	2.39	50.18	17.04	1.16	0.32	15.49	0.00	100.54	39.63	25.06	35.32
12 pyroxene	0.13	14.95	1.14	51.60	12.77	0.68	0.44	19.32	0.00	101.03	42.76	30.99	26.25

Oxide	Weight Percent Oxide								
	Mg	Al	Si	Ti	Fe	Ca	Mn	Cr	Sum
1 Oxide 1	0.00	2.06	0.34	21.53	69.07	0.51	1.42	0.00	94.93

Sample: GCH89-24 – Nursery Ravine

Feldspar

		Weight Percent Oxide								Plagioclase		Ternary Fsp		
		Na	Si	Al	K	Ca	Fe	Mg	Sum	An	Ab	An	Ab	Or
1	plagioclase	4.81	55.50	27.17	0.38	11.15	0.75	0.12	99.88	56.16	43.84	54.91	42.86	2.23
2	plagioclase	5.36	57.33	26.12	0.60	9.64	0.76	0.06	99.87	49.85	50.15	48.07	48.37	3.56
3	plagioclase	5.20	56.88	25.95	0.49	9.83	0.68	0.07	99.10	51.09	48.91	49.59	47.47	2.94
4	plagioclase	5.07	55.94	26.76	0.50	10.26	0.72	0.09	99.34	52.79	47.21	51.22	45.80	2.97
5	plagioclase	4.96	56.61	26.50	0.42	10.30	0.74	0.09	99.62	53.44	46.56	52.08	45.39	2.53
6	plag core	5.18	56.47	26.24	0.48	10.06	0.60	0.07	99.10	51.77	48.23	50.29	46.86	2.86

Pyroxene

		Weight Percent Oxide										End-member-percentages		
		Na	Mg	Al	Si	Ca	Ti	Mn	Fe	Cr	Sum	En	Fs	Wo
1	Pyroxene	0.14	14.46	1.42	50.48	11.76	0.68	0.57	21.47	0.00	100.98	41.37	34.45	24.18
2	Pyroxene	0.19	10.56	1.45	49.46	13.30	0.75	0.63	23.96	0.00	100.30	31.47	40.05	28.48
3	Pyroxene	0.23	12.11	1.62	49.87	15.63	0.82	0.48	19.72	0.00	100.48	35.20	32.15	32.65
4	Pyroxene	0.17	14.77	1.78	50.22	12.86	0.85	0.53	19.25	0.00	100.43	42.43	31.02	26.55
5	Pyroxene	0.14	14.58	2.12	50.08	13.13	0.92	0.46	18.10	0.00	99.53	42.67	29.71	27.62
6	Pyroxene	0.15	15.55	1.25	50.48	9.90	0.62	0.58	21.39	0.00	99.92	44.86	34.61	20.52
7	Pyroxene	0.25	12.13	2.36	49.73	18.60	1.14	0.32	15.81	0.00	100.34	35.30	25.81	38.90
8	Pyroxene	0.13	14.71	1.50	48.95	11.64	0.77	0.45	20.22	0.00	98.37	42.74	32.95	24.30
9	Pyroxene	0.16	14.90	1.62	50.66	13.06	0.74	0.44	18.37	0.00	99.95	43.08	29.79	27.13
10	Pyroxene	0.15	15.37	1.53	50.72	12.00	0.78	0.43	19.48	0.00	100.46	44.02	31.29	24.70
11	Pyroxene	0.22	13.19	1.82	50.19	15.37	0.89	0.41	18.15	0.00	100.24	38.33	29.58	32.09

Oxide

		Weight Percent Oxide								
		Mg	Al	Si	Ti	Fe	Ca	Mn	Cr	Sum
1	Oxide 1	0.32	2.46	0.39	27.14	62.40	0.06	0.93	0.00	93.70
2	Oxide 2	0.71	2.37	0.21	26.33	64.80	0.08	0.89	0.00	95.39
3	Oxide 3	0.67	2.34	0.23	26.24	64.04	0.06	0.85	0.00	94.43
4	Oxide 4	0.33	2.14	2.66	32.40	54.79	0.16	1.20	0.00	93.68
5	Oxide 5	0.15	1.61	2.70	37.16	51.55	0.16	0.79	0.00	94.12
6	Oxide 6	0.30	3.30	2.88	30.32	56.06	0.13	0.71	0.11	93.81
7	Oxide 7	0.60	2.36	4.94	23.35	62.55	0.09	0.89	0.00	94.78